

DIPLOMARBEIT

Kinetic Modeling of Biomass Gasification with Steam in a Fluidized Bed

ausgeführt zum Zwecke der Erlangung des
akademischen Grades eines Diplom-Ingenieurs
unter der Leitung von

Univ. Prof. Dr. Hermann Hofbauer

Institut für Verfahrenstechnik, Umwelttechnik und
Technische Biowissenschaften
Institutsnummer: 166

eingereicht an der Technischen Universität Wien,
Fakultät Maschinenbau,
von

Josef Roider

MNr.: 9425287

Eduard Suess Gasse 17/12

1150 Wien

josef.roider@gmx.at

Wien, im April 2002

Unterschrift

Acknowledgement

I am grateful to Univ. Prof. Dr. Hermann Hofbauer, who made this project possible within the research program *RENET* which was founded on his initiative.

I owe special thanks to Dr. Sebastian Kaiser for the excellent support of this master thesis. I appreciate above all the commitment for this work beyond his Ph.D.-Thesis.

I would also like to thank Dr. Gerhard Löffler, who contributed with useful suggestions for improvements and a lot of time for discussions fundamentally important for the successful completion of this work.

Further, I appreciate the cooperative and fruitful working environment in the group for Thermal Process Engineering, which allowed me to finish the simulations quickly.

My great appreciation go to my friends, who have been accompanying me during the time at university. Special thanks to Nikolaus Keuth, Franz Nigl and Richard Simcovics for the mutual assistance during studies, and to Michaela Höllrigl for the grammatical suggestions for this manuscript.

I am grateful for the permanent support and confidence, my parents, my brother, my sister and my aunt and my grand parents have given to me.

Finally I want to thank Gema for being with me in Vienna and for her patience with my long working hours.

para mi Gema

Kurzfassung

Die Verwendung von Biomasse für die Produktion von elektrischem Strom ist ein wertvoller Beitrag zur nachhaltigen Energieproduktion. Eine der Möglichkeiten, die zur Realisierung der Verwendung von Biomasse zur Verfügung stehen, ist die Vergasung mit Wasserdampf. Neben einigen technischen Vorteilen ist vor allem die Effizienz und die relativ hohe Produkt-homogenität interessant für anschließende Prozesse.

In der vorliegenden Arbeit wurde ein mathematisches Modell für die Gaserzeugung aus Holz in einer mit Wasserdampf fluidisierten Wirbelschicht entwickelt. Charakteristisch für Wirbelschichten ist die komplexe Wechselwirkung von Gas und Feststoff im Bett. Obwohl diese Wechselwirkungen noch nicht bis ins Detail aufgeklärt sind, existiert doch ein Satz von halbempirischen Gleichungen, die eine Beschreibung der fluiddynamischen Verhältnisse erlauben. Im vorliegenden Modell wird von einem zwei-Phasen Modell für das Bett ausgegangen. Diese Annahme reduziert den Modellierungsaufwand erheblich.

Wird Holz in einen Wirbelschichtvergaser eingebracht, so laufen im Wesentlichen drei Vorgänge nacheinander ab. Zuerst erfolgt die Trocknung des Holzes, anschließend die Entgasung zu Holzkoks und letztlich die eigentliche Vergasung. Die Brennstoffentgasung wird mittels einfacher Modellannahmen berücksichtigt. Im Gegensatz zum Entgasungsschritt existieren jedoch für den Vergasungsmechanismus relativ zuverlässige mathematische Modelle zur Beschreibung der Reaktionskinetik. In dieser Arbeit liegt daher das Schwergewicht der Untersuchung auf dem Einfluss der Vergasung auf das Reaktorverhalten. Dafür werden unterschiedliche Kinetikmodelle für die Vergasung miteinander verglichen. Neben den gewöhnlichen Potenzansätzen werden auch Langmuir-Hinselwood Ansätze diskutiert. Letztere versprechen genauere Modellierungsergebnisse wenn auch unter einem erheblich größeren Mess- und Rechenaufwand. Homogene Reaktionen werden nur kurz angeschnitten, da gezeigt wird, dass ihr Einfluss an der Produktgaszusammensetzung vernachlässigbar ist.

Die Realisierung des Modelles erfolgte in FORTRAN 90. Ergänzend zum Vergasermodell wurde ein einfaches Partikelmodell entwickelt um die Stoffübergangswiderstände und die Wärmeübergangswiderstände miteinander zu vergleichen. Für den benutzten Brennstoff stellt sich der Wärmeübergangswiderstand als limitierend heraus. Er ist mehrere Male größer als der Stoffübergangswiderstand.

Für die Modellauswertung wurde ein Standard definiert auf dessen Basis Konzentrationsprofile erstellt und, Sensitivitätsanalysen sowie Parametervariationen unternommen wurden. Der Anteil der Vergasungsprodukte am Produktgasstrom erreicht nur etwa 15–20%. Der Rest entsteht durch die Entgasung, da Holz einen Anteil an flüchtigen Bestandteilen um etwa 80% besitzt.

Die Konzentrationsprofile zeigen einen starken Abfall der Wasserdampfkonzentration in der Emulsionsphase am Boden des Reaktors. Anschließend beharrt die Wasserdampfkonzentration auf niedrigem Niveau. Im Gegensatz dazu sinkt die Wasserdampfkonzentration in den

Blasen nur wenig. Das deutet auf einen starken Stoffübergangswiderstand zwischen Blasen- und Emulsionsphase hin. Die Sensitivitätsanalysen zeigen jedoch, dass für den Wasserverbrauch der diskrete relative Sensitivitätskoeffizient für den Stoffübergangskoeffizienten zwischen Blasen und Emulsionsphase nur etwa 0.1 ist. Das deutet darauf hin, dass die Stoffübergangsgeschwindigkeit und die Reaktionsgeschwindigkeit etwa die selbe Größenordnung besitzen. Generell besitzt kein Modellparameter, außer den Parametern, die die Entgasungszusammensetzung beschreiben, einen vergleichbaren Einfluss auf die Produktgaszusammensetzung wie die drei sensitivsten Anlagenparameter.

Die Betriebstemperatur, die Betthöhe und die Umlaufmenge des Bettmaterials sowie der Teillastbetrieb besitzen den größten Einfluss auf die Produktgaszusammensetzung. Die Modellparameter mit dem stärksten Einfluss sind die Parameter, die die Entgasungszusammensetzung beschreiben sowie der Frequenzfaktor der Wasserdampfvergasungsreaktion. Für den Wasserverbrauch ist jedoch der diskrete relative Sensitivitätskoeffizient des Letzteren immer noch kleiner als Eins.

Die Parametervariationen und eine Untersuchung des Teillastverhaltens zeigen, dass der gesamte Wasserverbrauch in keinem Fall bedeutend höher ist als die Wassermenge, die durch die Brennstofffeuchte eingebracht wird. Das gilt besonders für niedrige Temperaturen und Vollastbetrieb. Bezogen auf die Wassereinbringung steigt der Wasserverbrauch mit höherer Temperatur und zunehmendem Teillastbetrieb. Die Druckvariation zeigt steigenden Wasserverbrauch mit steigendem Druck. Trotzdem bleibt der Wasserverbrauch unter der Menge, die durch die Brennstofffeuchte eingebracht wird. Höherer Druck führt jedoch zu einem Verschieben der Produktgaszusammensetzung. Insbesondere der für den Brennstoffzellenbetrieb interessante Wasserstoffanteil steigt mit dem Betriebsdruck. Der Anteil an Methan und höheren Kohlenwasserstoffen sinkt hingegen.

Abstract

The utilization of biomass for the production of electrical energy can participate significantly on a sustainable energy production. One way to realize the commercialization is the steam gasification of biomass. Beside some technical advantages as for example a high product homogeneity compared to competitive processes, this process is expected to reach high efficiency.

In the present work, a mathematical model for a fluidized bed gasifier for steam gasification of wood is developed. Fluidized bed reactors are characterized by a complex interaction of the gas with the solid bed material. This interaction is not yet understood in detail. However, a large set of semi-empirical equations, which describe the fluid dynamic of the fluidized bed is available. The modeling of the fluidized bed has been done according to the two-phase model. So, it is possible to reduce the modeling effort for the fluid dynamics to an acceptable and efficient level.

Wood introduced in a fluidized bed gasifier undergoes three steps during the conversion. First, there is the drying step which results in dry wood, secondly the devolatilization step resulting into wood char and finally the gasification step. The devolatilization step is modeled by simple assumptions. Since the mechanism of wood gasification is better understood and more independent of the wood type than the mechanism of devolatilization, the main focus of this work is on the third step. For this, different results for gasification reaction kinetics are compared. The considered rate equations are of n^{th} -order type as well as of Langmuir-Hinselwood type. The latter yield to more accurate models of the gasification rate equation but the computation and measurement effort is significantly higher. Homogeneous reactions are also discussed but it is shown, that have hardly influence on the result. The implementation of the model is in FORTRAN 90.

A simple particle model has been developed later on to compare the influence of mass transfer limitations and heat transfer limitations. For the used fuel, it has been found that the heat transfer limitations exceed the mass transfer limitations several times.

For the model evaluation, a standard has been defined. Based on this standard, concentration profiles are computed. Further, sensitivity analysis and parameter variations have been performed.

The part on the product gas of this last step is just about 15–20%. The concentration profiles show a sharp decay of the steam concentration in the dense phase at the beginning of the reactor and keeps constant at low level then. The concentration of steam in the bubble phase sinks just slightly. This can be interpreted as strong mass-transfer limitation between bubble-phase and dense-phase. However, the discrete relative sensitivity coefficient of the mass transfer coefficient between bubble-phase and dense-phase is about 0.1 for the steam consumption. This indicates the presence of both, mass-transfer limitations and rate limitations for the overall conversion rate. Further sensitivity analysis show, that no investigated

model parameter but the parameters, which describe the devolatilization composition has similar influence on the result like the three most sensitive plant parameters.

The operation temperature, the bed height, the solid circulation flow and the part load operation have the main influence on the product gas composition. The model parameter with the strongest influence describe the product composition of the devolatilization. The most important model parameter for the gasification are the parameters, which describe the devolatilization composition and the rate constant of the steam gasification reaction. However, the discrete sensitivity coefficient for water consumption of the latter is still lower than unity.

Parameter variation and the investigation of the part load operation show that in no case the total consumption of water is significantly higher than the water amount loaded with fuel moisture. This is particularly valid for low temperatures and full load. Related to the water loaded with the fuel, the water consumption rises with higher temperature and with lower load. The pressure variation shows an increasing water consumption with increasing pressure. However, the water consumption does not exceed the water loaded with the fuel moisture. Higher pressure leads to a change of the volume fractions of the product components in different sense. The hydrogen fraction, which is of interest for fuel cell operation increases whereas the fraction of methane and higher hydrocarbons decreases.

Contents

Acknowledgement	ii
Kurzfassung	iv
Abstract	vi
1 Introduction	1
2 Theory	3
2.1 Fluidized Bed Technology	3
2.1.1 Bed	3
Fluidization Condition	3
Particle Classification	4
Gas Flow	5
Bubbles	7
Rising Velocity of Bubbles	7
Bubble Diameter	8
Mixing and Mass-Transfer	8
Mixing of Gas and Solids	9
Interphase Mass-Transfer	9
Particle Transport Between Bubble and Emulsion	9
Mass-Transfer Between Gas and Particles	9
Particle Mixing	10
Segregation	10
Elutriation	10
2.1.2 Freeboard	10
Entrainment	12
2.2 Reaction System	12
2.2.1 Properties of Biomass Relevant to Gasification	13
Properties of Wood	13
Properties of Char	16
2.2.2 Drying	16
2.2.3 Devolatilization	18
2.2.4 Gasification	22
n^{th} -order reaction	22
The Langmuir-Hinselwood-Approach	22
Definition of the Rate Acquired in the TGA	25

	Homogeneous and Heterogeneous Catalyzed Reactions	26
	Heterogeneous Reactions	26
2.2.5	Comparison of Drying, Devolatilization, Gasification	35
2.2.6	Particle Models	35
	Mass- and Heat- Transfer	36
	Effect of particle size	38
	Bulk temperature effect	38
	Influence of the Pore Evolution and Thermal History	38
	Characteristic Numbers for the Particle Model	39
	Damköhler Number	39
	Thiele Modulus	40
	The Shrinking Particle Model	42
	Shrinking Core Model	42
	Homogeneous Particle Model	43
3	Model Development	44
3.1	Geometry	44
3.2	Material Properties	45
3.2.1	Molecular Diffusion Coefficient	45
3.2.2	Viscosity	46
3.3	Fluid Dynamics	49
3.4	Chemical System used for Modeling	52
3.4.1	Drying	52
3.4.2	Devolatilization	52
3.4.3	Gasification	55
	Equilibrium Constants	55
	Frequency Factors and Activation Energy	58
3.5	Choice of a Suitable Particle Model	61
3.5.1	Implementation of the Particle Model in the Simulation	61
3.5.2	Particle Model with Consideration of the Heat-Transfer Limitations	65
3.6	Presumptions for the Model	72
3.6.1	Plant Parameters	72
3.6.2	Model Parameters	72
3.7	Solving Algorithm for the Balances	80
4	Model Evaluation	82
4.1	Standard Conditions	82
4.1.1	Pilot Plant Gasifier	82
4.1.2	Demonstration Plant Reactor	84
	Cross Section	84
	Bed Material Volume Fractions	84
	Velocities	87
	Volumetric Flows	87
	Steam Volumetric Flows	88
	Volume Fractions	89
	H ₂ O Volume Fraction	89
	CO and H ₂ Volume Fractions	89

CO ₂ and C _x H _y Volume Fraction	90
Volume Fractions on Particle Surface	90
Reaction Rates	94
Overall Conversion for a Species	94
Single Reaction Rates	94
Mass-Transfer Rate Bubble-Emulsion	96
Gas Consumption and Gas Generation	96
4.2 Sensitivity Analysis	100
Sensitivities for Model Parameters	101
Sensitivities for Plant Parameters	106
4.3 Parameter Variation	110
Temperature and Circulation Flow Variation	111
Solid circulation flow dependency	111
Temperature dependency	114
Pressure Variation	115
Part Load Performance	119
Product Gas Fluidization	124
4.4 Conclusion	127
5 Summary	128
Nomenclature	131

Chapter 1

Introduction

The production of energy from biomass becomes an increasing importance since it unifies several advantages, which are of interest for politics. First, it is expected to create jobs in agriculture and industry and second it is a possibility to comply with international agreements and public interest.

In the mid-1980s, first evidence of the strong influence of the atmospheric concentration of carbon dioxide as greenhouse gas was found. As a reaction of the results of a study of the Intergovernmental Panel on Climate Change (IPCC), the United Nations General Assembly agreed in 1990 to establish a process which would lead to legally binding limits on greenhouse gas emissions.

As a result, particularly of the conference of Kyoto in late 1997, the European Parliament and the European Council voted for a directive (2001/77/EC) on the promotion of electricity produced from renewable energy sources in the international energy market in September 2001. Beside the objective to introduce a system of support schemes, legislative basis for the market, etc., this directive gives a national indicative target for electricity produced from renewable energy for each member country. Austria (The European Community) has to increase the part of renewable energy from 70%(13.9%) in 1997 to 78.1%(22%) in 2010. This high value for Austria results from the high amount of electricity already produced from hydropower.

The utilization of biomass for energy production permits to decrease the carbon dioxide emission per *GWh* electrical energy drastically compared with the emissions resulting from the combustion of fossil fuels. It exist a number of methods for utilizing the biomass potential. Since solid fuels have limited applications in modern industry, a promising way is either the gasification with mainly gaseous products or the pyrolysis with mainly liquid products. Especially gases have fundamental advantages over solid fuels. Gases can be cleaned before combustion, can be burned more efficiently and with less emissions. The control over the flame is simple and possible for a wide power range. This permits the application to sensitive industrial processes like glass making or drying. Gases can be distributed easily for domestic and industrial use. The latter is appropriate just in urban regions [Reed 1981]. However, due to the transport costs of biomass the economical reasonable size of a biomass power plant is 1–20MW. This is suitable for small towns with 2000–10000 habitants [Schaller 1995]. Another possibility of the use of the gases consists in the synthesis of chemicals like methanol, gasoline or ammonia [Reed 1981].

The profitability of biomass gasification depends strongly on the quantity of biomass available for utilization. The existing resource base is comprised of agricultural residues,

manures, wood and bark mill residues, logging residues, noncommercial (cull) trees in the forests and organic municipal waste. Further, there exists the possibility to grow energy plantations on fallow land or land, which has laid waste by man. However, not all of these sources can be exploited and the amount used will depend on accompanying costs.

In Austria, the availability of wood makes it very attractive for utilization since 46.2% of Austria is covered by forest in 1992. This value is still increasing every year [Smidt 2000]. Accordingly, the wooden residues of forestry are important in quantity. The disproportionately high part of the population living in rural regions favor the utilization of wood as energy source. However, nearly all biomass power plants which are actually operated in Austria produce exclusively heat for different purposes. The absence of the production of electric energy is partly the consequence of a lack of reliable technology and partly based in economic reasons [Kaiser 2001]. An other advantage of the utilization of wood is the relative extended research work done to characterize its chemical properties. So kinetic models with the most reliable results among the biomass matter can be applied to simulation. However, still a lot of work is needed to reach a level of knowledge which is already available for coal.

Since biomass is usually available in solid form, the gasification process in a fluidized bed has several advantages. This process provides an intimate mixture of gas and solids and a nearly uniform temperature in the whole reaction zone. In fluidized bed combustion or gasification technology, just a few percent of the solid matter consists of active particles. The bulk consists of inert matter like sand. Still, there exists the possibility to substitute a part or all of the sand by reactive matter like limestone or catalysts. This permits in situ gas cleaning or the control over product gas composition. Further, it is expected to have a lower release of tar than updraft or downdraft gasifiers [Reed 1981]. The gasifier modeled in this work is a part of a reactor which uses the FICFB process (Fast Internally Circulating Fluidized Bed). With this process, it is possible to operate with two separated gas flows and one circulation solids flow. The latter can be used to transport heat but also adsorbed matter from one gas stream to the other (refer to Fig. 3.1).

The utilization of steam for fluidization is expected to have a further reduction of tar in the product gas since the steam may decompose at least a part of the tar (refer to [Hofbauer and Rauch 2000]). Further, the steam can be condensed out of the product gas. A gas with medium heating value is obtained then. The tar fraction formed by steam gasification is easier to crack compared with the tar obtained from air gasification. Further, a utilization of the dry product gas for the synthesis of basic chemical products is possible [Kaiser 2001].

New energy technologies can be developed only when it takes place in close cooperation between operators, industry and research. In Austria, such a cooperation is undertaken by the operators *EVN AG* and *Güssinger Fernwärme Ges.m.b.H.*, further the industrial partner *Babcock Borsig Power – Austrian Energy*, and finally the *Institute of Chemical Engineering* at the *Vienna University of Technology*. This cooperation is known as *RENET Austria* (Renewable Energy Network Austria) and operates already a power plant for wood gas production with a fuel thermal performance of 8MW [Hofbauer 2002]. The simulation of the FICFB process in this master thesis for the Vienna University of Technology is performed in order to use the resulting tool for process design and optimization.

Chapter 2

Theory

2.1 Fluidized Bed Technology

2.1.1 Bed

A fluidized bed is a fluid-solid mixture which is behaving fluidlike in many ways. It is realized by passing upwards a fluid through a bed of fine particles at at least such a velocity that the frictional force between the particle and fluid counterbalances the particle weight. The bed is considered to be fluidized at minimum fluidization velocity in this case. Fluidized beds are characterized by exceptionally temperature uniformity, favorable heat-transfer, mass-transfer and solid mobility. These characteristics are the motivation for the usage of fluidized beds in technical applications.

Fluidization Condition

For studying the different flow patterns or flow regimes of a fluidized bed, a column with a gas distributor like perforated or porous base plate filled with solid particles is used. By passing gas with increasing velocity through the column, a fixed bed, homogeneous fluidization, bubbling fluidization, slugging fluidization, turbulent fluidization, fast fluidization and dilute pneumatic conveying can be observed in this order. However, sometimes not all regimes may exist.

This work is focused on bubbling fluidization. For a further discussion, refer to for example Löffler or Kunii and Levenspiel [Löffler 2001, Kunii and Levenspiel 1991].

The bubbling fluidized bed is the second flow pattern which is considered already as fluidization observed with increasing gas velocity. The transition from a fixed bed to a fluidized bed occurs relatively sudden at a velocity U_{mf} , called the minimum fluidization velocity. The drag forces balance the buoyed weight of the bed in this case. This first fluidization regime is the homogeneous fluidization and exists until u_{mb} , the minimum bubbling velocity. Homogeneous fluidization, is only observed at certain combinations of particle and fluid properties. This is a gas fluidization regime at high pressure in combination with small, light particles or liquid-solid systems. Particularly for sandlike particles in combination with gaseous fluids a common approximation is $U_{mf} = u_{mb}$. The flow pattern of the homogeneous bed expansion is therefore neglected. There exist various correlations for U_{mf} as summarized in Löffler [Löffler 2001]. The correlation to derive the pressure drop due to friction at minimum fluidization conditions used in this work is based on the Carman-Kozeny equation extended

with a second order term [Ergun 1952].

$$\frac{\Delta p}{L} = 150 \frac{(1 - \epsilon)^2}{\epsilon^3} \frac{\mu_{gas} U}{(\phi_p d_p)^2} + 1.75 \frac{1 - \epsilon}{\epsilon^3} \frac{\rho_{gas} U^2}{\phi_p d_p} \quad (2.1)$$

By equilibrating the friction force and the bed weight, this leads to a formulation of the Reynolds Number at minimum fluidization conditions of the following structure:

$$Re_{mf} = \sqrt{c_1^2 + c_2 Ar_I} - c_1 \quad (2.2)$$

Eq. 2.2 can be fit to experimental data. Here $c_1 = 27.2$ and $c_2 = 0.0408$ are used. These values have been found by Grace [Grace 1982]. Therefore, Eq. 2.2 gets to

$$Re_{mf} = \sqrt{27.2^2 + 0.0408 Ar_I} - 27.2 \quad (2.3)$$

with the definition of the Reynolds Number at minimum fluidization conditions the minimum fluidization velocity is

$$U_{mf} = \frac{\mu_g}{\rho_g d_p} Re_{mf} \quad (2.4)$$

Once U_{mf} is determined the Ergun [Ergun 1952] Eq. 2.1 is used again to calculate ϵ_{mf} , the porosity at minimum fluidization conditions. This results in

$$0 = \epsilon_{mf}^3 - \frac{150}{\phi_p} \frac{Re_{mf}}{Ar_I} (1 - \epsilon_{mf}) - \frac{1.75}{\phi_p} \frac{Re_{mf}^2}{Ar_I} \quad (2.5)$$

ϵ_{mf} can be solved analytically [Bronštein et al. 1996]. The behavior towards pressure variations are controversially as discussed in [Löffler 2001]. However, ϵ_{mf} increases nearly linearly with temperature for particles in the range of $45 - 1000 \mu m$ [Formisani et al. 1998].

Particle Classification

For fluidization, the combination of particle characteristics like density, diameter or sphericity and the gas properties like density and viscosity play an important role. The influence is essential to the transition point between two flow patterns, the flow regime or even the occurrence or absence of some flow patterns like the homogeneous expansion. A basic classification which permits to estimate the principle behavior of a fluidized bed within a certain particle-fluid combination is introduced by Geldart [Geldart 1972, Geldart 1973]. It is based on the particle diameter and the density difference between particle and fluid. The groups are listed in Reed [Reed 1981] and are as follows:

- *Group C*: Very fine or cohesive powders
Fluidization turns out to be extremely difficult since interparticle forces exceed forces arising from gas flow. Face powder, starch or flour are representative of these solids.
- *Group A*: Fine and/or light, aeratable materials
Group A particles are larger than group C particles. They are easy to fluidize and show a homogeneous bed expansion at low gas velocities and controlled bubbling with small particle diameters at high gas velocities. FCC catalysts are typical of these solids.

- *Group B*: sandlike particles

The particle diameter is usually in the range $40 \mu m < \bar{d}_p < 500 \mu m$ and the density $1400 \text{ kg/m}^3 < \rho < 4000 \text{ kg/m}^3$. A vigorous bubbling action, immediate bubbling after fluidization onset, and a large bubble growth rate roughly linear to the bed excess gas velocity ($U - U_{mf}$) are characteristic of beds with this particles. Further, the bubble size is nearly independent of the mean particle size.

- *Group D*: Spoutable or large and/or dense particles.

Deep beds are difficult to fluidize. These particles readily spout and mix poorly when they are fluidized. Typical solids are coffee beans, some roasting metal ores or gasifying coals.

The main advantage of this classification is the simple application and the clear results achieved.

Gas Flow

A common model for the gas flow in a fluidized bed is the two-phase theory. It deals with a gas split into a bubble phase and an emulsion phase. Grace and Clift [[Grace and Clift 1974](#)] classified the gas flow in a fluidized bed based on experimental observations into 4 components.

- Bubble

- upward convection of the bubble, the visible bubble flow

$$Q_b = A_R \delta_b u_b \quad (2.6)$$

- the flow of gas relative to the bubbles, the through flow

$$Q_{tf} = A_R \delta_b U_{tf} \quad (2.7)$$

- Emulsion

- average net flow of interstitial voids
- average interstitial gas flow relative to particles in the dense phase

$$Q_d = A_R (1 - \delta_b) U_d \quad (2.8)$$

The third component is usually neglected since no particle net flow occurs in a stationary fluidized bed. A balance for the gas flow $Q = Q_b + Q_{tf} + Q_d$ and dividing by the reactor cross section leads to [[Toomey and Johnstone 1952](#)]:

$$U = \delta_b u_b + \delta_b U_{tf} + (1 - \delta_b) U_d \quad (2.9)$$

The ideal two-phase theory assumed the emulsion to stay in minimum fluidization conditions. The gas flow exceeding the gas flow at minimum fluidization conditions is lumped into the bubble flow $Q_{b,id}$.

$$Q_{b,id} = A_R (U - U_{mf}) \quad (2.10)$$

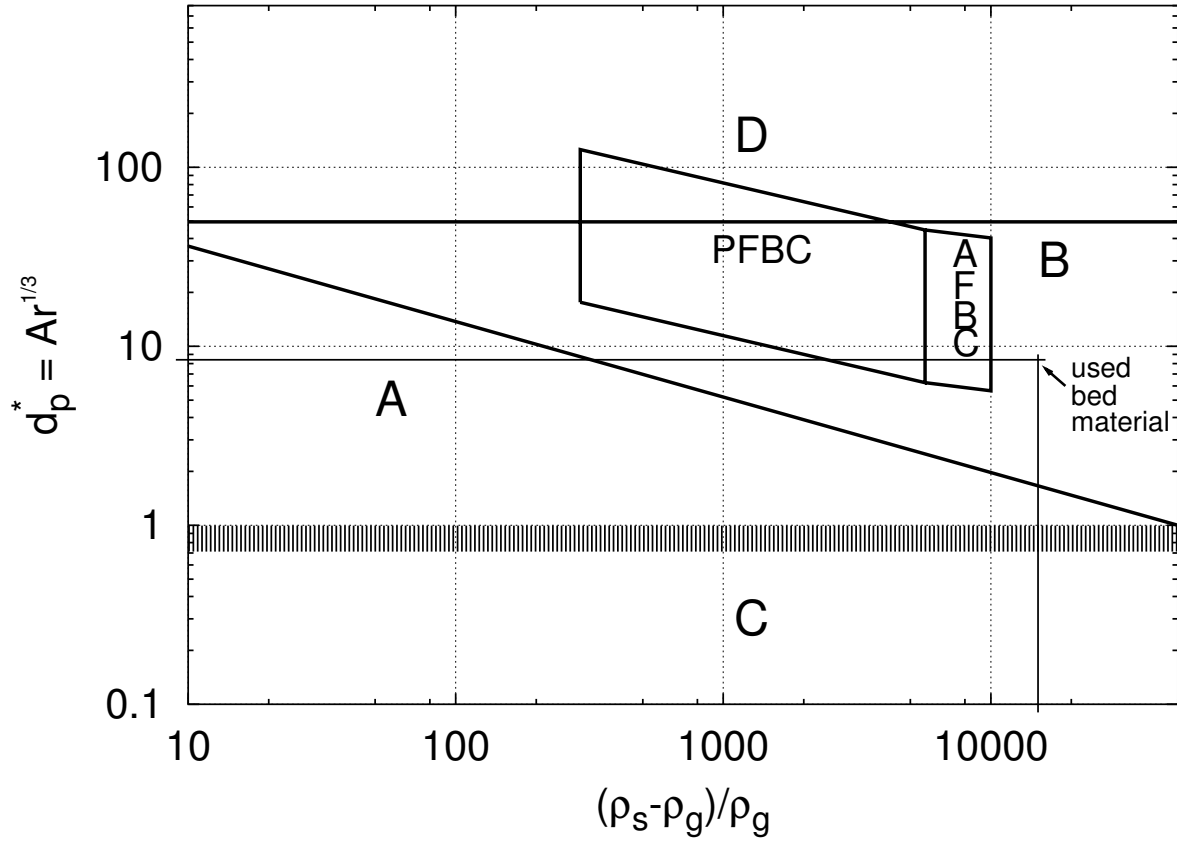


Figure 2.1: Geldart's particle classification diagram modified by Grace [Grace 1986]. Typical operating ranges for atmospheric fluidized bed combustors (AFBC) and pressurized fluidized bed combustors (PFBC) are indicated, as well [Gogolek and Grace 1995]. The used combination of the bed material (olivine $d_p = 380 \cdot 10^{-6}m$, $\rho_p = 2650 kg/m^3$) and the gas $\rho_g = 1.9 - 2.1 kg/m^3$ is clearly in the range of class B.

Experimental results show a strong evidence for a significant deviation concerning this value of the real visible bubble flow Q_b . For an explanation of $Q_b < A_R(U - U_{mf})$, different mechanisms (or a combination) have been proposed as listed in Löffler [Löffler 2001]:

- A slightly higher dense porosity than ϵ_{mf} leads to a significant increase of the interstitial velocity exceeding U_{mf} . This is especially observed in the case of elevated pressure and fine particles.
- the gas through-flow is proportional to the interstitial velocity U_d and not the minimum fluidization velocity U_{mf} . The proportionality factor also exceeds significantly unity and is further enhanced by interacting bubbles.
- High voidage shells convected with the bubbles.

The relative importance of these mechanisms is not yet known [Löffler 2001]. However, for a correction of $Q_{b,id}$ exist therefore several possibilities. Beside the determination of each velocity for Eq. 2.9 to get finally the bubble phase volume fraction, it may be useful to

determine a corrected value for Q_b by multiplying with a factor Y .

$$Q_b = A_R Y (U - U_{mf}) \quad (2.11)$$

Y is an empirical function achieved by fitting experimental data. Y is always smaller than unity and usually between 0.2 and 0.8. δ_b is evaluated directly by using the definition of Q_b . Finally, one of U_{tf} and U_d has to be fixed. Using the balance for the gas flow the other value can be computed. $U_d = U_{mf}$ corresponds to the ideal two-phase theory. However, different authors [Glicksman et al. 1987, Abrahamsen and Geldart 1980a, Abrahamsen and Geldart 1980b, Werther 1983] found $U_d = 0.8U_{mf} \dots 3U_{mf}$ and even higher. These controversial results may reflect the different gas velocities and particle shapes used in the experiments. A summary of different models and a comprehensive discussion is provided in Löffler [Löffler 2001]. Corrections for Q_b are the subject of the modified two-phase theory. For the factor Y , the following expression is used [Johnsson et al. 1991]

$$Y = \frac{0.26 + 0.7e^{-3.3 \cdot 10^3 d_p}}{0.15 + (U - U_{mf})} \left(h + 4\sqrt{A_o} \right)^{0.4} \quad (2.12)$$

Bubbles

A bubbling fluidized bed has almost solid free regions which are termed bubbles. The regions of higher solid density are called emulsion [Kunii and Levenspiel 1991].

Bubbles play an important role in the fluidized bed characteristics since they have a strong influence on the solid mixing, elutriation, mass-transfer between solid and gas and many more. Bubble formation, growth and interaction are well understood whereas the distribution of the gas flow between bubble and emulsion is still subject of controversial discussion [Löffler 2001].

Rising Velocity of Bubbles The rising velocity of a bubble ensemble is based on the rising velocity of a single bubble in a large bed. This single bubble rising velocity is often described analogous to a single bubble in a gas-liquid system as the behavior of the bubbles in both systems is similar in many ways [Kunii and Levenspiel 1991]. For a single bubble in a gas-liquid system, the rising velocity is given by

$$u_{b,\infty} = \frac{2}{3} \sqrt{g \frac{d_b}{2}} \quad (2.13)$$

as shown by Davis and Taylor [Davis and Taylor 1950]. This expression is used in a corrected form accounting for deviations of the rising velocity at low Reynolds numbers due to deformations of the spherical cap shape. For $Re > 100$, the rising velocity for a single bubble in a large fluidized bed is defined as

$$u_{b,\infty} = 0.711 \sqrt{g d_{eq}} \quad (2.14)$$

d_{eq} is the diameter of a sphere with equal volume as the deformed bubble [Davidson 1977]. Eq. 2.14 gives fair agreement to many experimental results although the Reynolds Number for the bubble typically is in the order of 10 [Löffler 2001]. Since reactor walls, bubble interactions, and solid motion influences the bubble rising velocity, correction terms accounting

for the circumstances in a reactor have been proposed. Based on the reactor geometry, the fluidization conditions and the single bubble rising velocity Werther [Werther 1978] proposed the following correlation for Geldart B particles:

$$u_b = 2.0 \sqrt{d_R} u_{b,\infty} + Y(U - U_{mf}) \quad 0.1 < d_R < 1.0 \quad (2.15)$$

where d_R is the reactor diameter. The correlation above describes an average bubble velocity. Since the bubble diameters may scatter in a wide range, the corresponding bubble rising velocities do so as well.

Bubble Diameter As already visible in Eq. 2.15, the bubble diameter plays an important role for the rising velocity and other strongly dependent values like the visible bubble flow. The bubble diameter changes due to coalescence, splitting and assimilation of excess gas during their passage through the bed [Löffler 2001].

Therefore, the determination of a characteristic bubble size is difficult since the mean volumetric size may not be suitable for very fast kinetic processes [Kunii and Levenspiel 1991]. However, the mean volumetric size is commonly used. Further, most bubble size correlations base on the initial bubble size or a certain geometry of the gas distributor, which results in fact to the problem of the unknown bubble initial size. A summary of bubble diameter correlations is given in Löffler [Löffler 2001]. The correlation of Darton et al. [Darton et al. 1977] bases on the assumption of a constant rate of pairwise coalescence. It is suitable for a perforated plate or multi-orifice distributor.

$$d_b = 0.54(U - U_{mf})^{0.4}(h + 4\sqrt{A_o})^{0.8}g^{-0.2} \quad (2.16)$$

h is the height over the distributor plate and A_o the corresponding area to each single gas inlet.

Mixing and Mass-Transfer

The two-phase theory deals with a more or less reasonable split of the bed into two phases which are interacting by mass and energy transport. This splitting permits to model the exchange phenomenons between these phases in analogy to the mass-transfer occurring between particles and the surrounding gas with a semi-empirical mass-transfer coefficient, an exchange surface and a concentration difference. Hence, the mixing of gas and particles can be divided into several mass-transport phenomenons whereof some of them are usually neglected. Mass-transfer and mixing can be classified [Löffler 2001]:

- Mixing of gas and solids in the emulsion
- Mixing of gas and solids in the bubble phase
- Mass-transfer between bubble and emulsion (interphase mass-transfer)
- Particle transport between bubble and emulsion
- Mass-transfer between gas and particles

Mixing of Gas and Solids In the dense phase, the gas is assumed to be in plug flow whereas the solid distribution is according to an ideal stirred-tank reactor. In the bubble phase, it is supposed not to occur due to the absence of particles. These extremes are commonly used, since they are a sufficient accurate approximation and permit an easy treatment in the simulation. However, recent investigations suggest a content of a few percent by volume of particles in the bubble phase [Kunii and Levenspiel 1991].

Interphase Mass-Transfer The interphase mass-transfer is essential for the two-phase theory. Mostly a significant or even dominating part of the gas passes through the reactor in the bubble phase whereas enhanced reaction rates are observed usually in the emulsion phase. The interphase mass-transfer is commonly modeled by a semi-empirical approach using a mass-transfer coefficient, the exchange area and the concentration gradient. The mass-transfer coefficient k_{be} in m/s is therefore defined by:

$$-\frac{1}{V_b} \frac{dN_{i,b}}{dt} = -\frac{Q_{be}}{A_b} \frac{dc_{i,b}}{dx} = \frac{O_{be}}{V_b} k_{be} (c_{i,b} - c_{i,e}) \quad (2.17)$$

O_{be} is the interphase exchange area and V_b the bubble volume. For spherical bubbles, the volume to surface ratio equals $6/d_b$.

$$\frac{O_{be}}{V_b} = \frac{6}{d_b} \quad (2.18)$$

The mass-transfer coefficient k_{be} is subject of many studies as listed and discussed in Löffler [Löffler 2001]. Models which lead finally to correlations for the mass-transfer coefficient differ mainly by the assumptions concerning the principal resistance to mass-transfer. This is whether or not bubble interactions may occur, the shape of the bubble and others [Löffler 2001]. A model developed by Sit and Grace [Sit and Grace 1981] allows for deformed bubbles. Later, this model was modified in order to account for an enhanced through-flow during coalescence. This is currently the best approximation available for three-dimensional beds of non-adsorbing particles [Yates 1983].

$$k_{be} = \frac{U_{mf}}{3} + \left(\frac{4D\epsilon_{mf}\bar{u}_b}{\pi\bar{d}_b} \right)^{0.5} \quad (2.19)$$

Particle Transport Between Bubble and Emulsion has not been taken into account since the bubble phase is assumed to be particle-free. However, recent investigations suggest a content of a few percent by volume of particles in the bubble phase as discussed in Löffler [Löffler 2001].

Mass-Transfer Between Gas and Particles For the gasification process, the knowledge of heat-transfer and mass-transfer to the char or wood particles is essential for computing the overall reaction rate. The char or wood concentration in a fluidized bed gasifier does not exceed a few percent of the total bed mass. Generally, the char or wood particle size, density, porosity, or the chemical reactivity are basically different to the surrounding particles. Such particles are called active particles contrarily to the inert particles forming the substance of the bed [Leckner et al. 1998]. For the Sherwood Number describing the gas-particle mass-transfer, a considerable set of semi-empirical correlation is available. Several of them are

listed in Löffler [Löffler 2001]. One of the most important influences for the mass-transfer from the particle to the surrounding gas in a fluidized bed is the ratio of the diameters of the inert particles $d_{p,I}$ to the diameters of the active particles $d_{p,A}$. For the conversion of large active particles suspended in a bed of small inert ones, it is necessary to develop correlations for the mass-transfer which takes into account for this geometrical difference. For this reason, most approaches distinguish between three regions of the $d_{p,A}/d_{p,I}$ ratio. The first case $d_{p,A}/d_{p,I} \ll 1$ and the second case $d_{p,A}/d_{p,I} \approx 1$ are frequently encountered in fluidized beds with heterogeneous catalytic reactions. The third case $d_{p,A}/d_{p,I} \gg 1$ usually concerns combustion or gasification processes. A common approach for intermediate ratios of $d_{p,A}/d_{p,I}$ is the interpolation between the mass-transfer coefficients resulting from the correlations for the special cases. Palchonok [Palchonok 1998] provides a summary for mass-transfer coefficients for particles. The structure of heat-transfer correlations are similar to the mass-transfer correlations. Therefore, the proceeding is the same. The correlations used in this work are listed in Palchonok [Palchonok 1998] and summarized in Table 2.1. Eq. 2.20 and Eq. 2.21 represent the heat and mass-transfer to surfaces of large, fixed walls in a dense, fluidized bed. They constitute the limiting case for very large active particles. It has been found experimentally that the heat and mass-transfer do not differ significantly between large fixed and large moving active particles. The semi-empirical equations Eq. 2.22 and Eq. 2.23 are based on assumptions regarding the limiting case for small particles ($Ar_I \rightarrow 0$). The additive second part represents model-free measurement data [Leckner et al. 1998].

Particle Mixing

Segregation In a fluidized bed with a homogeneous particle distribution, a segregation due to differences in particle properties can be neglected. In the case of a gasifier, at least the wood and the char particle properties differ significantly from the sand particles forming the bulk. A certain segregation as a result different particle properties may be expected then.

Elutriation Elutriation designates the separation or removal of fines from a mixture. Elutriation and feed size distribution determine the bed size distribution, which is responsible for the hydrodynamic behavior of a fluidized bed. There exist several correlations describing the phenomenon of elutriation listed in Löffler or Kunii and Levenspiel [Löffler 2001, Kunii and Levenspiel 1991]. The model used in this work takes into account for elutriation by a fixed mass distribution of the bed material as input data (refer to chapter 3.6).

2.1.2 Freeboard

In a stationary fluidized bed, the freeboard is the part of a fluidized bed reactor which is above the more or less well defined bed surface. In the freeboard, the sum of the gas flow through the dense and the bubble phase are considered as one homogeneous gas flow. For a description of the particle content in dependency of the height of the freeboard, several investigations have been undertaken as listed in [Löffler 2001]. Most of them base on an initial particle concentration on the bed surface and a decrease mechanism of the particle content vs. the height.

Expression	Range of validity	Eq. No.	Reference
$Nu_\infty = 0.85Ar_I^{0.19} + 0.006Ar_I^{0.5}Pr^{0.33}$	$d_{p,A}/d_{p,I} \gg 1$	(2.20)	[Baskakov et al. 1978]
$Sh_\infty = 0.009Ar_I^{0.5}Sc^{0.33}$	$d_{p,A}/d_{p,I} \gg 1$	(2.21)	[Baskakov et al. 1978]
$Nu_1 = 6 + 0.117Ar_I^{0.39}Pr^{0.33}$	$d_{p,A}/d_{p,I} = 1$	(2.22)	[Leckner et al. 1992]
$Sh_1 = 2\epsilon_{mf} + 0.117Ar_I^{0.39}Sc^{0.33}$	$d_{p,A}/d_{p,I} = 1$	(2.23)	[Leckner et al. 1992]
$Nu_A = \left((Nu_1 - Nu_\infty) \frac{d_{p,A}}{d_{p,I}}^{\frac{1}{3}} + Nu_\infty \frac{d_{p,A}}{d_{p,I}} \right) \phi_{p,I}^P$	$1 \leq \frac{d_{p,A}}{d_{p,I}} \leq 200$	(2.24)	[Leckner et al. 1998]
$Sh_A = (Sh_1 - Sh_\infty) \frac{d_{p,A}}{d_{p,I}}^{\frac{1}{3}} + Sh_\infty \frac{d_{p,A}}{d_{p,I}}$	$10 \leq Ar_I \leq 10^7$	(2.25)	[Leckner et al. 1998]
$P = \frac{2}{3}$	$d_{p,I} \geq 0.5 \text{ mm}$		
$P = 0$	$d_{p,I} < 0.5 \text{ mm}$		

Table 2.1: Correlations for mass- and heat-transfer for large active particles. Table from Palchonok [Palchonok 1998].

Entrainment

Entrainment is the transport of particles from the bed into the freeboard [Löffler 2001]. When bubbles burst on the bed surface, they eject particles into the freeboard. The origin of the entrained particles may be different and depend on the mechanism of entrainment. There have been proposed three ways:

- Since the bubble internal pressure is higher than bed surface pressure, they burst on reaching the surface, spraying solids from the bubble roofs into the freeboard.
- Since the bubbles rise much faster than the surrounding medium, the wake material may be thrown into the freeboard.
- During coalescence of two bubbles just as they break through the bed surface, the wake material from the trailing bubble is ejected into the freeboard. This entrainment turns out to be very effective.

Numerous studies listed in Kunii and Levenspiel [Kunii and Levenspiel 1991] show a qualitative coherent picture of the behavior in the freeboard. However, quantitatively the disagreements reach more than an order of magnitude [Kunii and Levenspiel 1991]. Some reasons for this stem from unaccounted physical conditions, unsuitable measurement methods and apparatus [Kunii and Levenspiel 1991]. The correlation used here is:

$$\varepsilon(h) = \varepsilon_{TDH} + (\varepsilon_L - \varepsilon_{TDH})e^{-f_{dy}h} \quad (2.26)$$

with the decay factor f_{dy}

$$f_{dy} = \zeta \frac{U_{t,i}}{U} \quad (2.27)$$

The constant ζ in Eq. 2.27 is 4 m^{-1} as found in experiments by [Johnsson and Leckner 1995]. The voidage of a particle class in a certain height h over the bed surface is exponentially decreasing from the voidage of the bed surface towards the voidage of the transport disengaging height TDH . Above this height, no further voidage increasing occurs. The increase of the voidage vs. the height is faster with higher terminal velocity U_t and slower with higher superficial velocity U . A representative voidage over the surface, which takes into account for effects as bubble bursting is frequently used instead of the bed surface voidage ε_L itself. However, due to the uncertainties mentioned above, the surface voidage ε_L is used here. A later step might be an introduction of experimental findings into the model. The correlation used in this work is valid for sand in the splash zone of a CFB-Furance. By increasing the operation pressure, the entrainment increases enormously and changes the size distribution towards a higher content of large particles.

2.2 Reaction System

The primary goal of gasification is to convert a solid fuel into a gaseous product. Gaseous fuel has various advantages as already discussed in the introduction.

Due to the low reaction rate of the gas in a fluidized bed reactor it is normally not possible to compute the product gas composition with sufficient accuracy just by consideration of the establishment of equilibrium. Therefore, it is necessary to develop kinetic models to

predict the conversion of the participating species. Several attempts have been made to understand and describe the reaction mechanism [Barrio and Hustad 2000, Barrio et al. 2000, Wang and Kinoshita 1993, Liliedahl and Sjöström 1997, Bandyopadhyay and Ghosh 1996]. Finally, a few different approaches have been applied to a model development.

Reed [Reed 1981] gives an overview of the terminology used in the context of gasification processes. He points out a special problem concerning the term 'pyrolysis'. Pyrolysis is the thermal destructive decomposition of biomass in the absence of oxygen, to produce char, pyrolysis oil and medium-heating-value gas. 'Pyrolysis' is also used as name of an important stage in all gasification and combustion processes for both, coal and biomass. Therefore, its meaning must be inferred from the context [Reed 1981]. In this work, the modeling is focused on the steam gasification of wood char. The thermal, destructive decomposition is a first stage and is modeled by simple assumptions as seen later. Hence, it is more appropriate to denominate this stage devolatilization rather than pyrolysis.

2.2.1 Properties of Biomass Relevant to Gasification

For a modeling of the gasification process, it is necessary to know numerous material properties. The most important are the proximate and the ultimate analysis, heats of combustion and sometimes ash analysis. The latter is only necessary, if it is expected that the ash components have a remarkable catalytic activity.

The proximate analysis of a fuel in terms of water content (W), ash (ASH), organic volatile matter (VM) and fixed carbon (FC) is determined in an inert atmosphere at high temperature. For the proximate analysis, most data is available with slow heating rate and small particles to avoid significant temperature and concentration gradients in the samples. The char and gas yield of devolatilization is of that representative for slow heating rates. Fast heating rates, as for example occur in fluidized beds, particularly with small active particles normally yield to more volatile matter (refer to Table 2.5 on page 21). In the case of fluidized beds, it is dependent of the used apparatus which its various specific parameters like *Archimedes Number*, *Reynolds Number* and others which influence strongly the heat transfer [Reed 1981, Ross et al. 2000, Mathews et al. 1997, di Blasi 1997a]. The data for the proximate analysis available for fast heating rate is thus only representative for the certain circumstances.

Using the mass of the water content, the mass of volatile matter, and the mass of the ash residue after complete combustion, the fixed carbon content can be calculated by a material balance.

$$FC = 1 - W - ASH - VM \quad (2.28)$$

Corresponding values on the basis of the dry biomass (*) are obtained by the transformation

$$material^* = \frac{material}{1 - W}$$

and yields to

$$FC^* = 1 - ASH^* - VM^* \quad (2.29)$$

Properties of Wood Compared to coal, the biomass has different chemical and physical properties which are important for modeling.

All biomass materials have a carbon content which is considerably lower than that for coal. For coal, the ratio of carbon to hydrogen is typically about unity, whereas for biomass this ratio reaches usually 1.5. Further, the bound oxygen content is higher due to the ether, acid and alcohol groups in wood. On the other hand, potential pollutants like sulfur and nitrogen are present in significantly lower quantities. However, some biomass materials as animal waste have high chlorine contents [Reed 1981].

While for coal largely a homogeneous structure can be assumed, a minute particle model for biomass demands to account for the heterogeneous physical structure of wood. Several attempts to model the pore structure have lead to more or less sophisticated models (refer to [Srinivasalu Gupta and Bhatia 2000, Raveendran and Ganesh 1998]). However, most times the particle is assumed to be homogeneous and the error undertaken is lumped into a modified diffusivity. Especially for the drying and the devolatilization step, the gas production in the particle may not be neglected. The diffusion velocity of this gases has been found to be a sensible factor for the result [Melaen and Grønli 1997, di Blasi 1997a, Reed 1981]. Further, the heat-transfer plays an important role since these processes are highly endothermic.

In softwoods, the main fluid conducting elements are the longitudinal tracheids and ray tracheids. Longitudinal tracheids form the bulk of the structure of softwoods. During gasification, the bulk of the product flow passes through these long and hollow fibers. Also, there exist longitudinal and horizontal resin canals. Perpendicularly to the principal flow through the longitudinal tracheids much smaller gas flow occurs through membrane covered pits and ray tracheids. The tracheid geometry depends on the species and varies from 15 to 80 μm in diameter and a length within the range from 1200 to 7500 μm . The diameter available for flow is typically 20 to 30 μm . The effective pit diameter varies from 0,02 to 4 μm due to the restriction created by the membrane. The volumetric composition of these elements is for softwood as follows:

Longitudinal tracheids	93%
Longitudinal resin canals	1%
Ray tracheids	6%

Hardwoods have a different structure. The dominating elements are large open vessels or pores. The vessels are short and connected by 'perforation plates' which provide low flow resistance. Tracheids are present but they show a significantly higher flow resistance. The composition is made up of:

Vessels	55%
Tracheids	26%
Woods rays	18%
Others	1%

Since the principal voidage is oriented longitudinally, the physical properties like diffusivity or thermal diffusivity are direction dependent. The difference of the order of magnitude of internal mass and heat transfer coefficients in direction to the main flow conducting longitudinal tracheids and perpendicular to them is about 4–6. Peletized, densified wood has lower permeability compared with natural woods due to the significant reduction of the voidage. Furthermore, it can be expected that the peletized wood is more or less isotropic [Reed 1981].

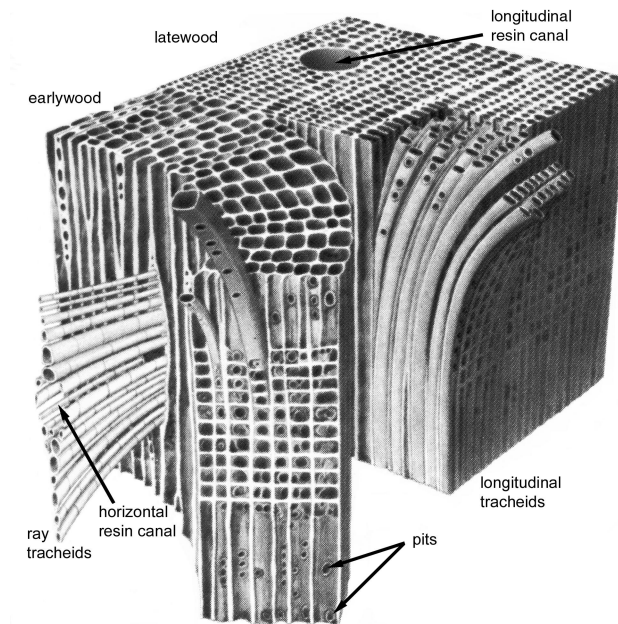


Figure 2.2: Physical structure of soft wood. The main components and the latewood (summerwood) and the earlywood (springwood) are pointed out. Figure from Taylor et al. [Taylor et al. 1978].

Beside the proximate and the ultimate analysis, an analysis of the main fractions of wood is possible. Woods can basically be separated into extractables, cell wall components and ash. The extractables represent an amount of about 4% to 20% derived from the living cell. The cell wall components constitute the bulk of wood. This bulk consists of the lignin fraction and the carbohydrate fraction which is distinguished into cellulose and hemicellulose

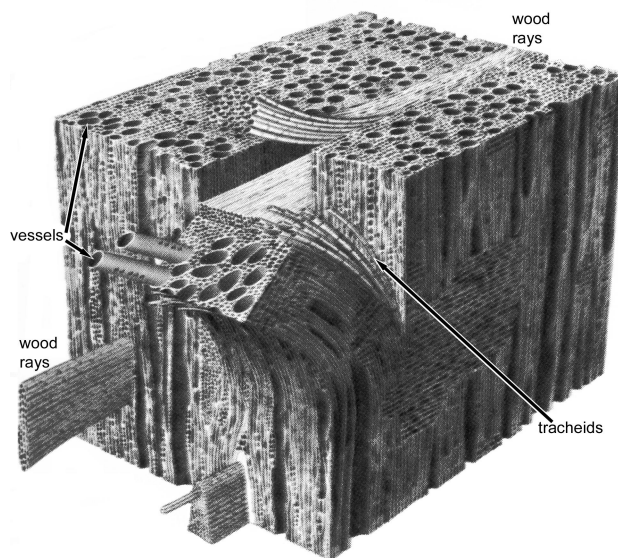


Figure 2.3: Physical structure of hard wood. The main components and the latewood (summerwood) and the earlywood (springwood) are pointed out. Figure from Taylor et al. [Taylor et al. 1978].

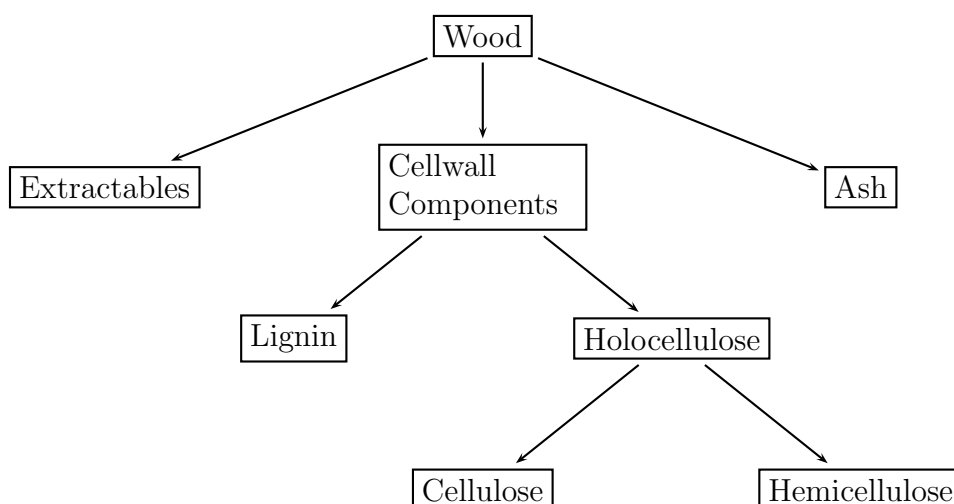


Figure 2.4: Main fractions of wood [Reed 1981].

which are summarized in the term holocellulose. Lignin is the cementing agent for cellulose fibers and is a complex polymer of phenylpropane. Cellulose and hemicellulose are based on polymers of hexose and pentose sugars. The ratio of lignin to cellulose in the cell wall fraction is about 43/57 for nearly every wood. However, sawdust, bark, and other residues of the total wood have differing ratios. Fig. 2.4 gives an overview of the main fractions.

In characterizing and correlating reactivity data especially for devolatilization it is necessary to have an idea about the chemical structure of the reacting material. Performing an analysis of the main fractions of wood is further necessary since common devolatilization models are based on this composition [di Blasi 1997b].

A more detailed description of the physical structure and the chemical composition of wood can be found for example in Reed [Reed 1981].

The permeability of air in different wood types is shown in Table 2.2. Remarkable is the influence of the location where the wood has been cut in the case of Douglas fir. The heat transfer coefficient has been shown also to depend strongly on the moisture content of the wood [Reed 1981].

Properties of Char The composition of char is varying like the composition of wood and is further dependent of the devolatilization conditions. Reed [Reed 1981] gives a summary of char compositions measured by different authors. Some results are shown in Table 2.3. For wood chars, the carbon content is about 50–80%. The ash content reaches from almost negligible quantities to about 20%. The rest is constituted by hydrogen, oxygen and traces of sulfur and nitrogen. For the physical structure, the same aspects as for wood are valid (refer to chapter 2.2.1).

2.2.2 Drying

Drying is the first stage that biomass undergoes during the thermal treatment in gasifiers, pyrolysis furnaces or combustion furnace. It means the removal of water from the fuel. Thermal degradation of the biomass does not occur during a sole drying step. However, since drying occurs in situ and is no separate process, an overlap with the following devolatilization

Permeability in $\frac{m^3}{m Pa}$	Wood type	
10^{-5}	Red Oak	<i>longitudinal direction</i>
10^{-6}	Basswood	
10^{-7}	Maple	
	Pine sapwood	
	Douglas fir sapwood (pacific coast)	
10^{-8}	Spruces (sapwood)	
	Cedars (sapwood)	
	Douglas fir heartwood (pacific coast)	
10^{-9}	White oak heartwood	
	Beech heartwood	
10^{-10}	Cedar heartwood	
	Douglas fir heartwood (intermountain)	
10^{-11}		<i>transversal direction</i>
10^{-12}	The order for the transversal direction is about the same like the longitudinal direction	
10^{-13}		

Table 2.2: Typical permeability values of wood [Reed 1981].

Material	C	H	N	S	O	Ash	gross heat of combustion in $\frac{MJ}{kg}$	Reference
Fir bark char	49.9	4.0	0.1	0.1	24.5	21.4	19.2	[Pober and Bauer 1977]
Redwood charcoal (420–550°C)	75.9	3.3	0.2	0.2	18.4	2.3	28.8	[Boley and Landers 1969]
Redwood charcoal (460–940°C)	78.8	3.5	0.2	0.2	13.2	4.1	30.5	[Boley and Landers 1969]
Oak charcoal (4400–640°C)	67.7	2.4	0.4	0.2	14.4	14.9	24.8	[Boley and Landers 1969]
Grass straw char	51.0	3.7	0.5	0.8	19.7	24.3	19.3	[Pober and Bauer 1977]
Utah coal	77.9	6.0	1.5	0.6	9.9	4.1	32.9	[Tillman 1978]

Table 2.3: Ultimate analysis data for different biomass chars [Reed 1981].

step and therefore a thermal degradation is possible. Whether these two stages overlap or not depends on the thermal conductivity of the solid. It occurs in the case of low values of the thermal conductivity [Peters and Bruch 2001]. The water content of biomass reaches values up to 150%. Moisture in solids exists in three different forms. First, there is water vapor and capillary water (free) second, water in pores and bound moisture (hygroscopic) and finally, water in the solid matrix (chemically fixed). The moisture content, which corresponds to the complete occupation of all sites where water can be chemically fixed is called Fiber Saturation Point. On the Fiber Saturation Point, there is no further free or hygroscopic water. The dynamic of drying with fast and slow heating rate is basically different. For the drying dynamic in a hot fluidized bed, only the dynamic of drying with fast heating rate is of interest. It is characterized by large spatial gradients and the propagation of a rather steep drying front through the medium is observed for the whole drying period [di Blasi 1997b, Melaaen and Grønli 1997].

Di Blasi [di Blasi 1997b] developed a mathematical model for drying dynamics. In the center of the particle, she found an overpressure which is up to 3–4 times larger than the atmospheric pressure. This dynamic of overpressure explains the still rather low evaporation rates at drying temperatures slightly over 100°C compared with a free water surface. Further, she found a significant influence of radiative heat transfer on the drying process.

Melaaen and Grønli [Melaaen and Grønli 1997] performed simulations for a particle with 25mm half-thickness. They found a moisture dependent formation of devolatilization products, namely tar (refer to Table 2.5). Whereas di Blasi [di Blasi 1997b] found a clear separation of the drying step and the consecutive devolatilization step, Melaaen and Grønli [Melaaen and Grønli 1997] found already sufficient high particle surface temperatures for a thermal degradation before the completion of drying. This is mainly due to the low drying temperature of 500K used by di Blasi and the fixed high heat flux used by Melaaen and Grønli [Melaaen and Grønli 1997]. The latter assumption allows for a particle surface temperature of about 1100K. This temperature corresponds rather to the circumstances found in a fluidized bed gasifier. So it may be expected, that in the case investigated in this work, the drying step is not yet finished when pyrolysis begins. However, the drying step is modeled very simple just by an instantaneous release of the fuel water content into the fluidized bed.

2.2.3 Devolatilization

The devolatilization step is the second stage that biomass undergoes during the thermal utilization in gasifiers. It is the first stage of thermal degradation and is of interest not only for gasification processes. Particularly for the pyrolysis process, it is important to know the product gas composition of the devolatilization step. Also, the combustion dynamics of biomass is strongly influenced by the release of the devolatilization products. Hence a lot of research projects in the field of biomass devolatilization have been done (refer to e.g. [Zanzi et al. 1994, Maschio et al. 1992, Saastamoinen 1994, Melaaen and Grønli 1997]). For modeling the devolatilization in a pyrolysis process, a common practice is to consider just the main components cellulose, hemicellulose, lignin, extractives and ash (refer to Fig. 2.4). The pyrolysis of lignocellulosic material can be distinguished in three ideal stages.

The *first stage* is the pre-pyrolysis which occurs at temperatures below 200°C . During this stage, a small weight loss is observed due to the release of mainly water, carbon monoxide and carbon dioxide. Further, a chemical rearrangement like the formation of free

radicals, carbonyl, carboxyl, etc. leads to a change of the internal structure and behavior of the biomass. Hence, a preliminary treatment like drying at high temperatures has to be considered in the whole process design.

The *second stage* corresponds to the main decomposition of biomass and is the center of pyrolysis. The main release of product gases occurs in the range of $300\text{--}600^\circ\text{C}$.

During the *third stage* the decomposition reaction slows down to a very low rate and the mass of the biomass reaches asymptotically its residual value.

In particular, the kinetics of the devolatilization process are dependent on temperature, particle size, solid residence time, composition of the feedstock and heating rate. The heating rate conditions strongly affect the progress of the process.

Maschio et al. [Maschio et al. 1994] found a higher carbon content in char obtained from large particles than for smaller particles. For large particles, they observed a lower conversion even for long process times. They interpret this as a result of longer residence times of the devolatilization products in the particle and thus secondary gas-solid reactions occurring in the char. Zanzi et al. [Zanzi et al. 1994] compared the reactivity in steam gasification of char obtained in rapid heating ($1000^\circ\text{C}/\text{s}$) with char obtained in slow pyrolysis ($0.3^\circ\text{C}/\text{s}$) to a final temperature of 900°C and 850°C , respectively. They found a 4 times higher reactivity of the char produced by rapid pyrolysis whereas the char yield reaches just the fourth part of the value of slow heating rates. They did not investigate the possible influence of the higher concentration of mineral matter on this effect although the relative ash content should be higher in the char obtained from rapid heating. Higher treating temperature favors the cracking of the hydrocarbons into the gaseous products and yields to an increased hydrogen content of the product gas [Zanzi et al. 1994].

Still, the devolatilization step of the biomass in a fluidized bed gasifier is a source of high uncertainty. Especially, for a wide spreaded particle-size distribution very different heating conditions from one particle size to another can be expected. The external mass and heat transfer resistance may have no influence on the overall rate of the devolatilization of small particle, whereas for large particles a strong influence on the overall rate is for sure.

For scale-up purposes, it may be useful to measure the devolatilization kinetics and product gas composition of the applied fuel in a fluidized bed in order to minimize this uncertainties.

Table 2.5 shows the observed effects on product gas composition and char properties on changing the devolatilization conditions.

	Conventional Pyrolysis	Fast Pyrolysis	Flash Pyrolysis
Operating Temperature in $^\circ\text{C}$	300 – 700	600 – 1000	800 – 1000*
Heating Rate in $^\circ\text{C}/\text{s}$	0.1 – 1	10 – 200	≥ 1000
Solid Residence Time in s	600 – 6000	0.5 – 5	≤ 0.5
Particle Size in mm	5 – 50	≤ 1	Dust

* Up to 2000°C in solar furnaces.

Table 2.4: Different types of pyrolysis processes [Maschio et al. 1992].

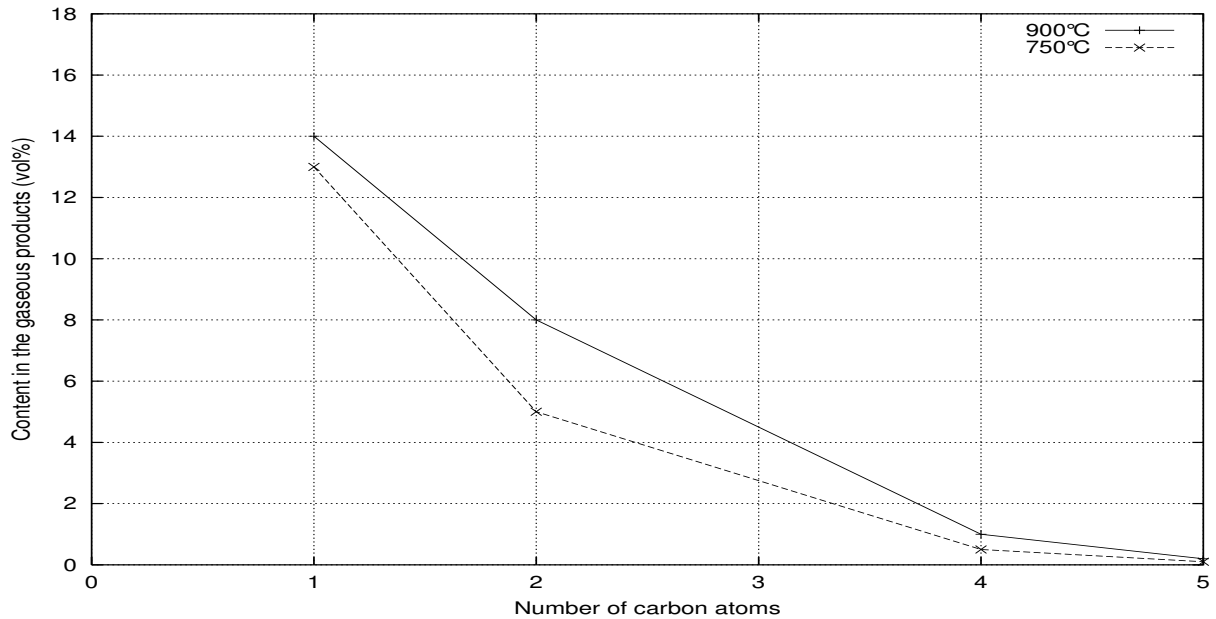


Figure 2.5: Amounts of CH_4 , $(\text{C}_2\text{H}_2 + \text{C}_2\text{H}_4 + \text{C}_2\text{H}_6)$, C_4H_{10} and C_5H_{12} obtained in the devolatilization step at 750°C and 900°C . The measurements have been performed in a free fall reactor with 1.4s residence time of small wood particles ($< 1\text{mm}$) and a pressure of 2.7bar. [Zanzi et al. 1994].

Maschio et al. [Maschio et al. 1992] give a summary for the parameters which permit distinguishing conventional (slow) pyrolysis, fast pyrolysis and flash pyrolysis (refer to Table 2.4). Later, the same research group [Maschio et al. 1994] provides devolatilization times for biomass in a moving bed reactor for different particle sizes and operating temperatures. For particle diameters in the range of 15–25mm and a bed temperature of 700°C , they found devolatilization times of 220–250s. Very large particles (50–200mm) favor char coal production and secondary reactions enrich the char coal in carbon. Thus, the cost of size reduction is reduced but the devolatilization time rises up to 40–80min (refer to Table 2.10 on page 36).

The char yield after devolatilization is about 10% (ash free) for high heating rates up to 20% (ash free) for low heating rates at an end temperature of 850°C [Maschio et al. 1992, Zanzi et al. 1994]. However, the devolatilization step seems to depend beside the fuel itself, on a complex interaction of many parameters [Jiang and Morey 1991, Maschio et al. 1992, Maschio et al. 1994, Zanzi et al. 1994, Koufopoulos et al. 1991, Ross et al. 2000, L     1994]. Hence, a reliable prediction for the product gas composition just by using biomass properties is not possible at the moment. For an accurate model of the devolatilization step in a gasifier, a preliminary measurement of the gas composition in the expected devolatilization conditions is indispensable.

	H-content product gas	char yield	carbon content in char	char reactivity with steam	tar content	char density	CO-content product gas	released gas volume	aromatic hy- drocarbons	aliphatic hy- drocarbons
rapid heating $> 10K/s$	↗	↘		↗	↗	↘	↔	↗		
increasing final temperature	↗	↘		↗↘ ***	↘		↔	↗	↘	↘
large particle $> 2mm$	↘	↗	↗		↘					
increasing residence time in a free fall reactor	↗	↗* ↔ **		↘	↘** ↔ *			↔	↗	
increasing water content of the fuel		↔			↗			↘		

* at high temperatures, ** at low temperatures, *** maximum may exist

References: [Zanzi et al. 1994, Maschio et al. 1994, Melaaen and Grønli 1997]

Table 2.5: Influence of process parameters on the products of the devolatilization step.

2.2.4 Gasification

The third stage of thermal conversion of biomass in a gasifier is the gasification. This step completes the thermal conversion of biomass. There, the residual solid, the char, which is a product of the preliminary drying and devolatilization step undergoes conversion. Char consists mainly of carbon. However, hydrogen and oxygen have been found in partly considerable amounts [Reed 1981]. Again, these results depend on the devolatilization step. The conversion of the carbon fraction of the char can be done with various gases. These are for example pure oxygen or atmospheric oxygen, hydrogen, steam or carbon dioxide. The reaction of carbon with the first three gases is exothermic, whereas the reaction with steam is endothermic. Hence, an external heat source is necessary if pure steam is used and no oxygen is added.

The following discussion is focused on gasification reactions and consecutive reactions but neglects combustion reactions. Combustion reactions are much faster than every gasification reaction and can be taken into account by instantaneous conversion of the char with oxygen [Bilodeau et al. 1993, Bettagli et al. 1995, Wang and Kinoshita 1993]. Most authors use n^{th} -order kinetics or hyperbolic kinetics as the Langmuir-Hinselwood mechanism to model the experimental results. Besides, attempts should be mentioned which use just the CO/CO₂ ratio to describe the carbon dioxide gasification reaction [Barrio et al. 2000, Reed 1981, Barrio and Hustad 2000, Cerfontain et al. 1987, Wang and Kinoshita 1993]. Still, the results of different authors scatter in a large scale (refer to Fig. 2.6 and Fig. 2.9). This might be due to influences not studied like the number of active sites or the influence of mineral matter going along with different types of wood [Barrio and Hustad 2000, Barrio et al. 2000, Reed 1981].

n^{th} -order reaction

The n^{th} -order reaction is the simplest approach to describe the gasification reactions. The utilization of this model is justified by the low effort for an implementation into a computer code, and low calculation time. Further, the largest number of reaction rate models is available for this approach since it needs by far less measurement data to provide confidential results [Barrio and Hustad 2000]. Fig. 2.9 on page 31 shows, that influences to the reaction rate which are arising from the different wood types, scatter within a range of several orders of magnitude. Fig. 2.10 on page 33 compares the n^{th} -order model and the Langmuir-Hinselwood model based on the correlations provided Barrio and Hustad [Barrio and Hustad 2000]. The reaction rate of the carbon dioxide gasification is several times reduced due to the CO inhibition. However, this deviation is clearly less than the deviations of the reaction rates resulting from the use of different wood types. Therefore, using n^{th} -order approach provides still sufficient good results if the fuel type is not explicitly fixed. As it is widespread used, a further discussion is renounced here.

The Langmuir-Hinselwood-Approach

The Langmuir-Hinselwood mechanism accounts for the intrinsic conversion of the participating species as well as for the pre- and post-surface reactions adsorption and desorption. It has been investigated many times, since due to the supposed reaction scheme the model seems to be physically well-founded and it is expected to achieve more accurately results as discussed in Froment and Bischoff [Froment and Bischoff 1990].

For this mechanism, the gasification reactions on the char surface are related to a certain number of surface sites, which are disponibel for a chemical reaction. The total number of these active sites in S_Γ . If a part of the active sites is covered by a unique species \mathcal{A} , the fractional coverage $\Theta_{\mathcal{A}}$ is defined by:

$$\Theta_{\mathcal{A}} = \frac{S_\Gamma - S_l}{S_\Gamma} \quad (2.30)$$

where S_l stands for the number of free active sites [Budde 1988]. As stated in Froment and Bischoff [Froment and Bischoff 1990], Langmuir also assumed that the usual mass action laws could describe the individual steps. For the associative adsorption and desorption of the gaseous species \mathcal{A} on the free active sites S_l of the solid, one can write:



$$\bar{r}_{ad} = k_{ad}p_{\mathcal{A}}(1 - \Theta_{\mathcal{A}}) \quad (2.32)$$

$$\bar{r}_{des} = k_{des}\Theta_{\mathcal{A}} \quad (2.33)$$

Assuming the equilibrium state, the fractional coverage of the species \mathcal{A} leads to the Langmuir adsorption isotherm:

$$\Theta_{\mathcal{A}}^e = \frac{K_{\mathcal{A}}p_{\mathcal{A}}}{1 + K_{\mathcal{A}}p_{\mathcal{A}}} \quad (2.34)$$

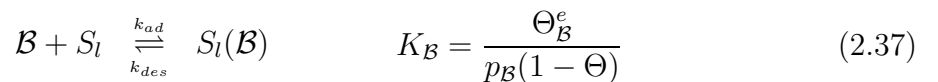
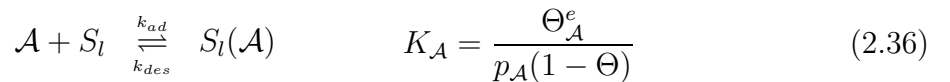
The classical theory of Langmuir is based on the following hypothesis:

- Uniformly energetic adsorption sites
- Monolayer coverage
- No interaction between adsorbed molecules

Especially, the second assumption is suitable for describing chemisorption or low-coverage physisorption. Based on the adsorption isotherm of Langmuir, Hinselwood developed a surface kinetics for chemical reactions of the type [Reed 1981]:

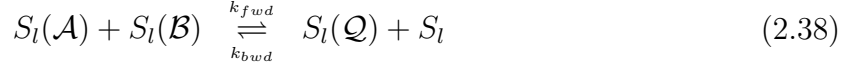


- i.) The first step is the adsorption of the reacting gaseous species on the free active sites l of the solid.



p_i denotes the partial pressures of the gaseous species i and K_i the adsorption equilibrium constants of the species i on the solid surface. It is assumed that the *equilibrium* of adsorption and desorption is hold during the whole surface reaction.

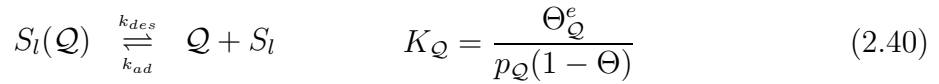
- ii.) As a second step, the *rate-controlling* reaction between the adsorbed species takes place.



$$\bar{r} = k_{fwd}\Theta_{\mathcal{A}}\Theta_{\mathcal{B}} - k_{bwd}\Theta_{\mathcal{Q}}(1 - \Theta) \quad (2.39)$$

\bar{r} denotes the reaction rate and is the difference of the forward and the backward reaction rate.

- iii.) The final step consists in the desorption of the product:



$$(2.41)$$

Again, the equilibrium of adsorption and desorption reaction is assumed. A balance for the active sites leads finally to the overall rate equation. For this, a constant total number of active sites is assumed.

$$\bar{r} = \frac{k(p_{\mathcal{A}}p_{\mathcal{B}} - \frac{p_{\mathcal{Q}}}{k^e})}{(1 + K_{\mathcal{A}}p_{\mathcal{A}} + K_{\mathcal{B}}p_{\mathcal{B}} + K_{\mathcal{Q}}p_{\mathcal{Q}})^2} \quad (2.42)$$

where

$$k = k_{fwd}K_{\mathcal{A}}K_{\mathcal{B}}$$

$$k^e = \frac{k_{fwd}K_{\mathcal{A}}K_{\mathcal{B}}}{k_{bwd}K_{\mathcal{Q}}}$$

The power of the denominator appearing in Equation 2.43 is included in the adsorption group (refer to Eq. 2.43) and depends as well on the presumption of the rate determining step. In the previous example, the reaction between the adsorbed species is the rate controlling step. This leads to the square appearing in the adsorption group. The power turns out to be one if the adsorption step of \mathcal{A} is rate determining [Froment and Bischoff 1990, Budde 1988]. With this procedure, it is possible to develop a considerable variety of different equations just by choosing a rate-controlling step. These equations are all of the structure:

$$\bar{r} = \frac{\text{kinetic factor} * \text{drivingforce group}}{\text{adsorption group}} \quad (2.43)$$

But already for other than first order reactions or if no assumption on the rate controlling step is undertaken, a general solution is exceedingly tedious or even impossible to derive. The similar construction of the equations of Langmuir-Hinselwood type and the difficulties in deriving a general result leads to a systematic treatment performed by Hougen and Watson as briefly reviewed in Froment and Bischoff [Froment and Bischoff 1990]. This formalism based on the Langmuir-Hinselwood mechanism deals with a large set of parameters. These parameters correspond to a combination of several rate constants of the set of consecutive

reactions constituting the mechanism which are lumped into one coefficient. Hence, contrary to the equation derived by analyzing the reaction mechanism, the latter is incapable to reflect the true mechanism. However, it is still a strong belief that this approach is only a systematic, but nevertheless an empirical formalism leading to a better fit of the experimental results [Froment and Bischoff 1990].

To obtain the kinetic rate constants in the Langmuir-Hinselwood based model, two methods can be applied. The first method is the two-steps calculation. The intention of the first step is to reduce the system in such a way that in the second step a linear regression analysis can be done. The second method is the direct calculation with a powerful statistic tool which is capable to solve an equation system of higher order with six and more kinetic constants. The input for this calculation is the result from numerous experiments. Compared with the n^{th} -order kinetics a Langmuir-Hinselwood model needs a considerably higher number of experiments to obtain trustful results [Barrio et al. 2000].

Barrio et al. [Barrio et al. 2000] applied both methods to the experimental results obtained from carbon dioxide gasification of different biomass chars. They found partly strong differences and a high level of uncertainty in the calculation for the kinetic factor for carbon monoxide in the denominator.

This dependency on the used mathematical method for the evaluation of the experiments has to be considered if different results of various authors are compared.

Definition of the Rate Acquired in the TGA

There are two definitions of the reactivity commonly used:

$$\bar{r} = -\frac{1}{m(t) - m(t_\omega)} \frac{d(m(t) - m(t_\omega))}{dt} \quad (2.44)$$

$$\bar{\bar{r}} = -\frac{1}{m(t_0) - m(t_\omega)} \frac{d(m(t) - m(t_\omega))}{dt} \quad (2.45)$$

where $m(t_\omega)$ represents the ash content or the residual matter after gasification and $m(t_0)$ the initial mass. With the definition of the degree of conversion

$$X(t) = 1 - \frac{m(t) - m(t_\omega)}{m(t_0) - m(t_\omega)} \quad (2.46)$$

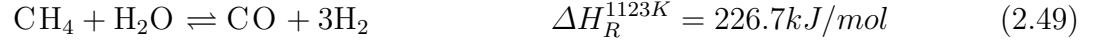
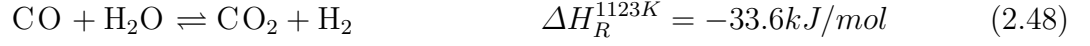
the relation between the two definitions is $\bar{\bar{r}} = \bar{r}(1 - X)$. Thus, if analyzing the reactivity according to the two rate definitions, the difference in the frequency factor should be a constant since the representative reactivity definition is related to a fixed degree or an interval of conversion [Barrio et al. 2000]. With these definitions, the reaction rate for carbon can be calculated. Using the time dependent carbon concentration $\frac{m(t) - m(t_\omega)}{V_{cont}}$ in a control volume V_{cont} , the reaction rate in terms of $\frac{mol}{m^3s}$ for the carbon is:

$$R_C = \frac{dc_C(t)}{dt} = \frac{m(t) - m(t_\omega)}{M_C V_{cont}} \bar{r} \quad (2.47)$$

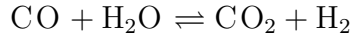
Once evaluated this carbon conversion rate for a certain reaction, the gravimetric factor are used to compute the reaction rates for the other species.

Homogeneous and Heterogeneous Catalyzed Reactions

The heat of reaction is computed at a temperature of $1123K$. Assuming the absence of oxygen, the following homogeneous reactions are participating on gasification:

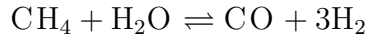


•Water-Gas-Shift Reaction:



Since combustion reactions (if present), the producer-gas equilibrium and the steam gasification are forming carbon monoxide, the water-gas-shift reaction can take place in the presence of steam. This reaction occurs in form of heterogeneous catalysis on the carbon surface at temperatures below $1350K$. At higher temperatures, it is possible to occur as homogeneous reaction in significant quantities [Reed 1981].

•Methane Decomposition Reaction:



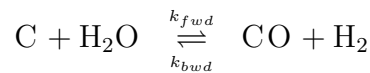
The kinetic study of methane thermal decomposition seems to be a very complicated chain reaction on the carbon surface [Wang and Kinoshita 1993].

Heterogeneous Reactions

The heat of reaction is computed at the operating temperature of $1123K$. Assuming the absence of oxygen, the following heterogeneous reactions are participating on the gasification:

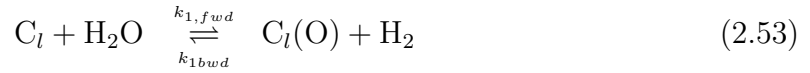


•Steam Gasification Reaction:



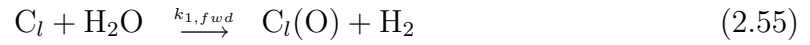
In the steam gasification reaction, the catalytic activity of the ash plays an important role. [Moilanen and Mühlen 1996, Turn et al. 1998, Tancredi et al. 1996b]. Furthermore, this reaction is considerably more complicated than the carbon dioxide gasification because the three different gaseous species appearing in the reaction above are participating on consecutive reactions. Further, the product gases hydrogen and carbon monoxide are inhibiting the forward reaction due to the occupation of active sites on the carbon surface [Barrio et al. 2000, Gururajan et al. 1992, Reed 1981, Mühlen 1983].

Carbon dioxide also influences the kinetics of this reaction due to the equilibrium of the water-gas-shift reaction [Barrio et al. 2000]. In spite of this, many authors determine the kinetics in pure steam or for the carbon dioxide gasification, in carbon dioxide atmospheres. Although this can be useful to examine the catalytic activity of inorganic components or to rank the coals according to their reactivity, reaction rates obtained in this way can not be used for the modeling of gasifiers with gas mixtures [Gururajan et al. 1992]. Hüttinger and Merdes [Hüttinger and Merdes 1992] give a comprehensive description of the models for the carbon - steam reaction proposed in the literature. Basically there is the oxygen exchange model and the hydrogen inhibition model. The oxygen exchange model is described by the following reactions [Barrio et al. 2000, Reed 1981]:



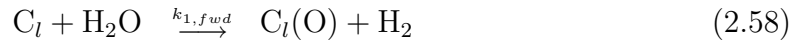
where C_l is an active site and $C_l(O)$ an occupied site on the the carbon surface. Here, the dissociation reaction of oxygen (2.53) is supposed to be in equilibrium.

There are basically two different hydrogen inhibition models which are distinguished by different explanations of the inhibition mechanism by the hydrogen [Barrio et al. 2000]. The first model is based on the following reactions [Barrio et al. 2000, Reed 1981]:



The reason for the inhibition is the formation of the $C_l(H)_2$ complex (reaction 2.57). This complex occupies the active sites C_l for the first reaction 2.55.

The second model presented in Barrio et al. [Barrio et al. 2000] is as follows:



For the second form of the inhibition model, the dissociative chemisorption of the hydrogen on the active sites (reaction 2.60) is supposed to be the reason for the inhibition.

On this bases the reaction rate equations for the reaction schemes above are presented as follows in the corresponding order:

$$\bar{r} = \frac{k_{1,fwd}p_{H_2O}}{1 + \frac{k_{1,fwd}}{k_2}p_{H_2O} + \frac{k_{1,bwd}}{k_2}p_{H_2}} \quad (2.61)$$

$$\bar{r} = \frac{k_{1,fwd}p_{H_2O}}{1 + \frac{k_{1,fwd}}{k_2}p_{H_2O} + \frac{k_{3,fwd}}{k_{3,bwd}}p_{H_2}} \quad (2.62)$$

$$\bar{r} = \frac{k_{1,fwd}p_{H_2O}}{1 + \frac{k_{1,fwd}}{k_2}p_{H_2O} + \frac{k_{4,fwd}}{k_{4,bwd}}p_{H_2}^{0.5}} \quad (2.63)$$

Wood species	$E_{a,1,fd}$ kJ/mol	$k_{0,1,fd}$ $s^{-1}bar^{-1}$	$E_{a,1,bwd}$ kJ/mol	$k_{0,1,bwd}$ $s^{-1}bar^{-1}$	$E_{a,2}$ kJ/mol	$k_{0,2}$ s^{-1}	Reference
Beech	199	$2.0 \cdot 10^7$	146	$1.8 \cdot 10^6$	225	$8.4 \cdot 10^7$	[Barrio et al. 2000]
Birch	214	$7.6 \cdot 10^7$	284	$2.1 \cdot 10^{12}$	273	$1.6 \cdot 10^{10}$	[Barrio et al. 2000]

$$k_{v} = k_{0,v} \exp(-E_{a,v}/(RT))$$

Table 2.6: Langmuir-Hinselwood order Kinetics of Steam Gasification [Barrio et al. 2000]. The reaction mechanism is according Eq. 2.53 and Eq. 2.54 which leads to the rate equation Eq. 2.61. For a graphical representation refer to Figure 2.7.

Char origin	E_a kJ/mol	k_0	n	Reference
Birch*	237 ± 0.4	$2.62 \cdot 10^8 \pm 5 \cdot 10^6 s^{-1}bar^{-n}$	0.57 ± 0.03	[Barrio et al. 2000]
Beech**	211 ± 6.1	$1.71 \cdot 10^7 \pm 1 \cdot 10^7 s^{-1}bar^{-n}$	0.51 ± 0.05	[Barrio et al. 2000]
Wood char	138	$1.79 \cdot 10^3 s^{-1}atm^{-n}$	1.00	[Capart and Gél 1988]
Wood char	198	$1.23 \cdot 10^7 s^{-1}atm^{-n}$	0.75	[Hemati and Laguerie 1988]
Fir wood	104.5 ± 8			[Richard et al. 1982]
Black liquor	210 ± 10			[Li and van Heiningen 1991]
Black liquor	230		0.56	[Whitty 1997]
Poplar	271			[Timpe and Hauserman 1992]
Cattails	262			[Timpe and Hauserman 1992]
Wood	196, 217			[Moilanen et al. 1993]
Black liquor	226			[Moilanen et al. 1993]
Straw	151	$4.77 \cdot 10^7 \%/min$	~ 0.5	[Stoltze et al. 1994]
Black liquor	119	$1.76 \cdot 10^6 \%/min$	~ 0.5	[Stoltze et al. 1994]
Poplar wood	182	$1.2 \cdot 10^8 min^{-1}$		[Rensfelt et al. 1978]
Straw	182	$5.9 \cdot 10^7 min^{-1}$		[Rensfelt et al. 1978]
Wood char	217	$10^6 - 10^7 s^{-1}m^{2.1}mol^{-0.7}$	0.7	[Groeneveld 1980]

$$* R_{sqr} = 0.9919, ** R_{sqr} = 0.9784$$

Table 2.7: n^{th} order Kinetics of Steam Gasification [Barrio et al. 2000]. For a graphical representation of some values refer to Figure 2.6.

The structure of the so obtained rate equations is similar with the exception of the power for the hydrogen partial pressure. It is not possible to determine the dominating mechanism just by consideration of the reaction rate since the structure of the oxygen exchange model and the first hydrogen inhibition mechanism is identical [Hüttinger and Merdes 1992].

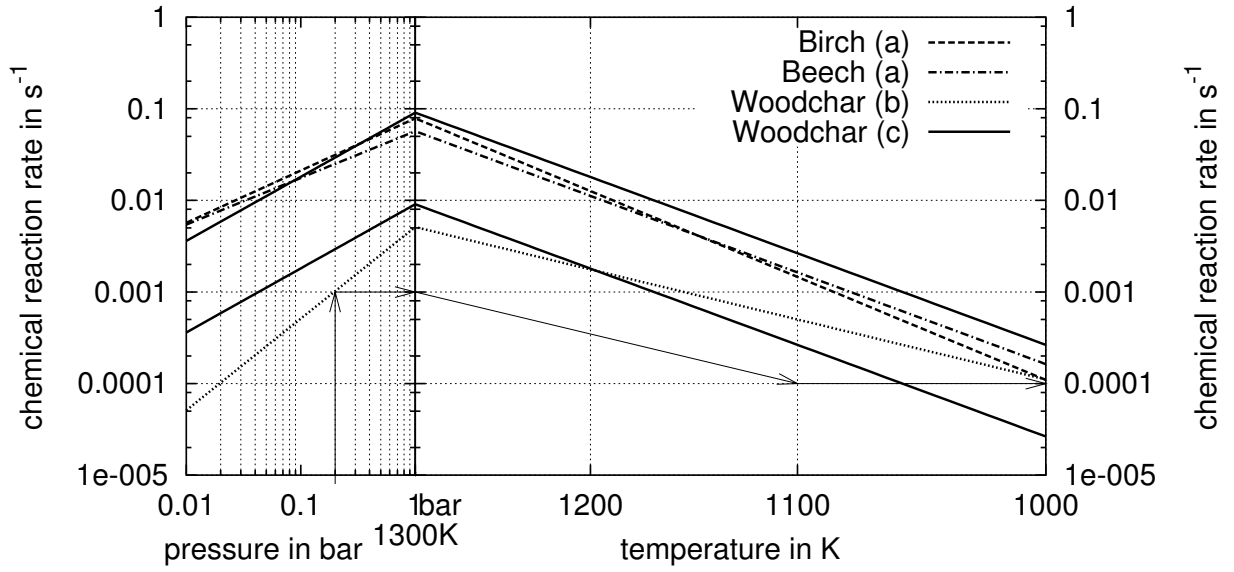


Figure 2.6: n^{th} order kinetics of steam gasification (refer to Table 2.7). The example shows a reaction rate of about $0.0001s^{-1}$ for $0.2bar$ steam pressure and $1100K$ for wood char measured by Capart and Gélus [Capart and Gél 1988]. Groeneveld [Groeneveld 1980] found a range for the reaction rate, in which nearly all other results are situated. References: (a) [Barrio et al. 2000], (b) [Capart and Gél 1988], (c) [Groeneveld 1980].

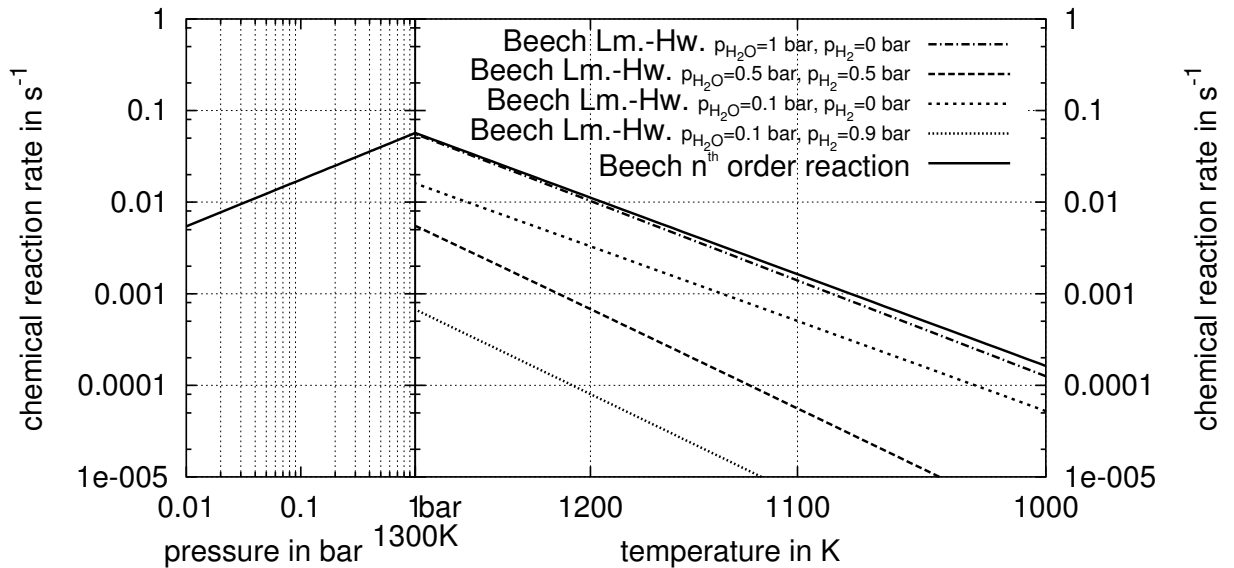
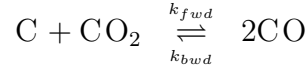


Figure 2.7: Comparison n^{th} order kinetics and Langmuir-Hinselwood kinetics of steam gasification (refer to Table 2.6). The figure shows, the reaction rate for several different partial pressures of steam and hydrogen. The hydrogen inhibiting effect for the steam gasification reaction is considerable for high hydrogen partial pressures. The reaction rate by less than one order of magnitude [Barrio et al. 2000].

•Carbon Dioxide Gasification Reaction:



This reaction has been studied most extensive of all gasification reactions because the examination is more easy since the products do not enter into side reactions. However, the activation energy of carbon gasification with carbon dioxide is strongly influenced by the type of the carbon [Dutta et al. 1987, Reed 1981] A common representation for the reaction mechanism is as follows [Reed 1981, Barrio et al. 2000, Mühlen 1983]:



The rate equation of this system is therefore:

$$\bar{r} = \frac{k_{1,fwd} p_{\text{CO}_2}}{1 + \frac{k_{1,fwd}}{k_2} p_{\text{CO}_2} + \frac{k_{1,bwd}}{k_2} p_{\text{CO}}} \quad (2.66)$$

The inhibition effect of CO consists in lowering the steady-state concentration of the carbon-oxygen complexes $\text{C}_l(\text{O})$ (also transitional surface oxide) by the backwards reaction (Eq. 2.64) [Barrio et al. 2000].

The reaction rates for the carbon dioxide and the steam gasification behave similar for the most chars. So, any of the gasification reactions can serve as an indicator for the reactivity of chars. The steam gasification is several times faster but is more difficult to investigate since competitive and consecutive reactions occur (see above).

Reed [Reed 1981] gives some results from mechanistic studies for the carbon dioxide gasification:

- The exchange of oxygen by the Eq. 2.64 occurs reversible at all temperatures investigated, including those below those required for gasification.
- Interchange of carbon between carbon dioxide and the solid carbon occurs only at temperatures at about 1500°C
- Deposition of carbon on the surface by decomposition of carbon monoxide (refer to Eq. 2.65) occurs at an insignificant rate.
- Eq. 2.65 is rate controlling at low temperatures.
- Eq. 2.64 is rate controlling at high temperatures due to the lower activation energy.

Cerfontain et al. [Cerfontain et al. 1987] found that the reaction rate for carbon dioxide gasification of activated carbon only depends on the CO/CO_2 ratio. Barrio et al. [Barrio et al. 2000] found as well a strong correlation for the reaction rate and the CO/CO_2 ratio for the wood chars investigated.

Some research groups [Barrio et al. 2000, Reed 1981] evaluated the values obtained from the measurements according the n^{th} order kinetics as well as for Langmuir-Hinselwood approach. A comparison shows little differences between these two approaches for temperatures above 1100K and atmospheric pressure. For lower temperatures, the fit of the Langmuir-Hinselwood approach is somewhat better than the results for the n^{th} order kinetics (refer to Fig. 2.10, Fig. 2.7, and Fig. 2.8).

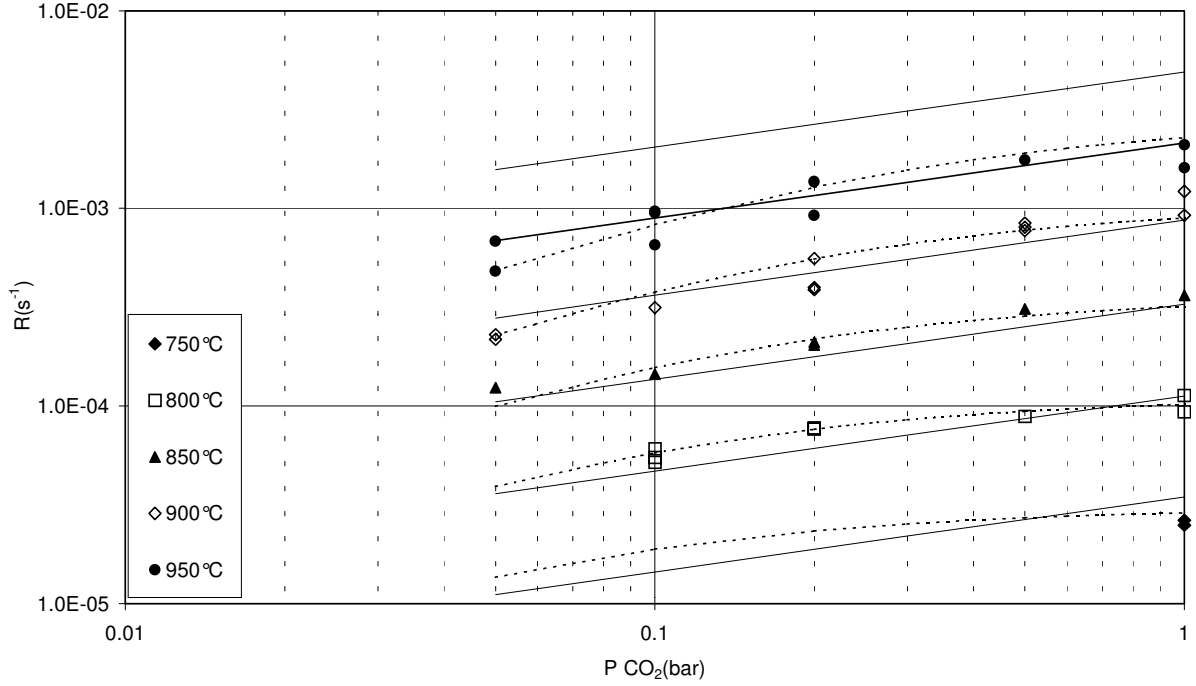


Figure 2.8: Influence of CO_2 partial pressure and temperature on char reactivity. For lower temperatures, the Langmuir-Hinselwood rate equation fits the data visibly better. Figure from Barrio and Hustad [Barrio and Hustad 2000].

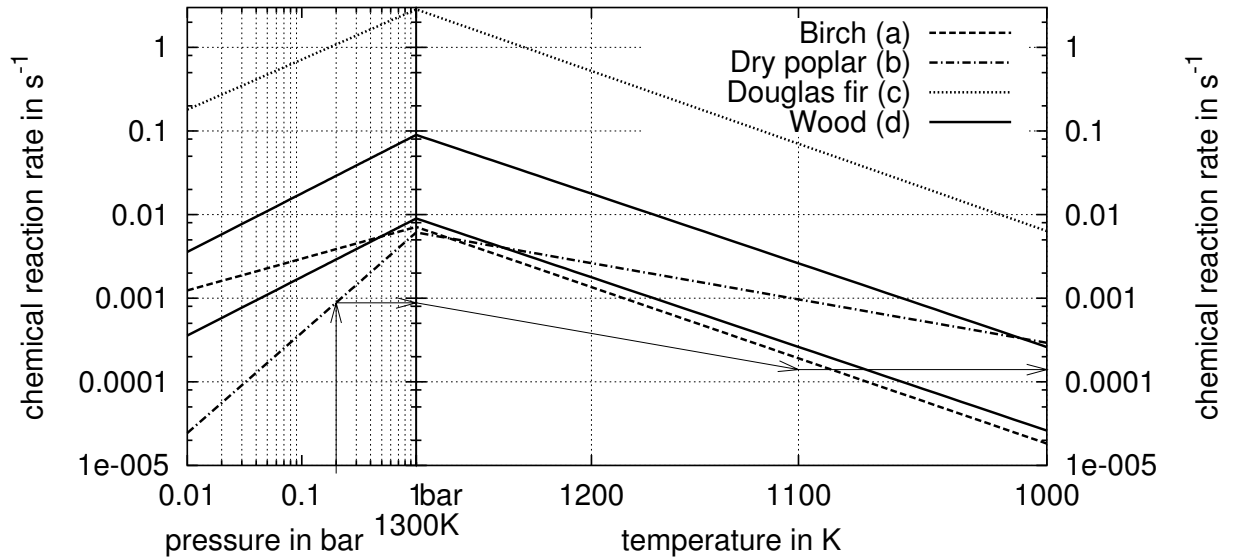


Figure 2.9: n^{th} order kinetics of carbon dioxide (refer to Table 2.9). The example shows a reaction rate of about 0.00015s^{-1} for 0.2bar CO_2 pressure and 1100K for char from dry poplar measured by Plante et al. [Plante et al. 1988]. The reaction rates scatter more than for steam gasification (refer to Fig. 2.6). References: (a) [Barrio and Hustad 2000], (b) [Plante et al. 1988], (c) [De Groot and Shafizadeh 1984], (d) [Groeneveld 1980].

Wood species	$E_{a,1, fwd}$ kJ/mol	$k_{0,1, fwd}$ $s^{-1}bar^{-1}$	$E_{a,1, b}$ kJ/mol	k_{01b} $s^{-1}bar^{-1}$	$E_{a,2}$ kJ/mol	$k_{0,2}$ s^{-1}	Reference
Birch	165	$1.3 \cdot 10^5$	20.8	$3.6 \cdot 10^{-1}$	236	$3.23 \cdot 10^7$	[Barrio and Hustad 2000]

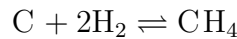
$$k_v = k_{0,v} \exp(-E_{a,v}/(RT))$$

Table 2.8: Langmuir-Hinselwood order kinetics of carbon dioxide gasification [Barrio and Hustad 2000]. The reaction mechanism is according Eq. 2.64 and Eq. 2.65 which leads to the rate equation Eq. 2.66. For a graphical representation refer to Figure 2.10.

Char origin	E_a kJ/mol	k_0	n	Reference
Birch	215	$3.1 \cdot 10^6 s^{-1}bar^{-0.38}$	0.38	[Barrio and Hustad 2000]
Eucalyptus	230 – 260			[Tancredi et al. 1996a]
Wheat	152			[Illerup and Rathmann 1995]
Coconut	250			[Bandyopadhyay et al. 1991]
Dry poplar	109.5	$153.52 s^{-1}bar^{-1}$	1.2	[Plante et al. 1988]
Cotton wood	196	$4.85 \cdot 10^8$	0.6	[De Groot and Shafizadeh 1984]
Douglas fir	220	$1.97 \cdot 10^9$	0.6	[De Groot and Shafizadeh 1984]
Wood	217.1	$10^6 - 10^7 s^{-1}m^{2.1}mol^{0.7}$	0.7	[Groeneveld 1980]
Spruce	220	$2.1667 \cdot 10^7 s^{-1}$	0.36	[Risnes et al. 2000]

Table 2.9: n^{th} order kinetics of carbon dioxide gasification [Barrio and Hustad 2000]. For a graphical representation of some values refer to Figure 2.9.

•Hydrogasification Reaction:



The methane formation by hydrogasification (Eq. 2.52) is for two reasons important for air and oxygen gasification. First, the energy content of the synthesis gas is increased due to the presence of methane. Second, the oxygen necessary for gasification is reduced because of the heat released in methane formation. For coal chars, Johnson [Johnson 1974] observed two methane-forming processes.

Highly reactive, freshly devolatilized char forms methane at a high rate but with the beginning of graphitization which stabilizes the carbon the reaction rate drops to a very low value. To obtain significant quantities of conversion by hydrogasification, it is necessary to operate at high pressures and rapid heating. Low pressure and dilution of the hydrogen by other gases lead to a total elimination of methane production according Eq. 2.52 [Reed 1981].

Wang et al. [Wang and Kinoshita 1993] measured the reaction rate of the hydrogasification and computed the rate constant and the activation energy using a shrinking particle model and a Langmuir-Hinselwood mechanism with a rate controlling adsorption step. The used adsorption constants are cited in Reed [Reed 1981].

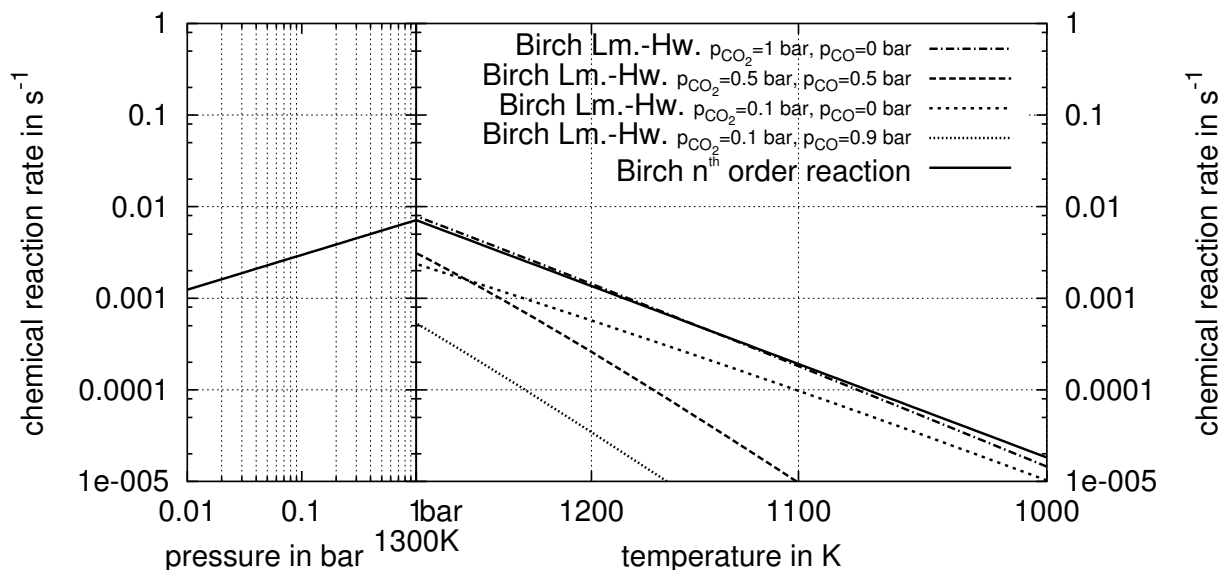


Figure 2.10: Comparison n^{th} order kinetics and Langmuir-Hinselwood kinetics of carbon dioxide gasification (refer to Table 2.8). The figure shows, the reaction rate for several different partial pressures of carbon dioxide and carbon monoxide. The carbon monoxide inhibiting effect for the carbon dioxide gasification reaction is not as high as the hydrogen inhibition effect for the steam gasification reaction (refer to Fig. 2.7). However, the effect slows down the reaction rate by less than one order of magnitude [Barrio and Hustad 2000].

For the steam gasification and the carbon dioxide gasification, the reactivity increases always with increasing conversion (refer to Fig. 2.11). An elevated reaction rate is observed especially during the last stages of conversion. This may be due to the enrichment of catalytic active species in the char as well as due to the evolution of the pore structure [Gururajan et al. 1992, Moilanen et al. 1994, Reed 1981].

Moilanen et al. [Moilanen et al. 1994] found a decreasing gasification rate with increasing conversion for peat char in a fixed bed reactor. This stands in contrast to other biomass chars. The microscopic study shows that the gasification shifts towards the particle surface when conversion reaches about 40%. They supposed the reason to be carbon deposition on reaction surfaces inside the particle blocking the pore-structure. Other explanations deal with mass-transfer limitation due to an ash layer or with the heterogeneity of the peat char (refer to Fig. 2.12). However, a similar behavior could not be observed in a fluidized bed reactor. This is indicating the absence of similar phenomena on the surface probably due to attrition in the fluidized bed. Thus, the results obtained in TGA have to be used very carefully for a modeling of a fluidized bed. Using an appropriate, exact particle model for TGA and the fluidized bed may solve this problem. Introducing a new parameter in the rate equation to describe the ash layer or similar effects in TGA can improve the accuracy of the results and achieve the applicability to other physicochemical circumstances. Nevertheless, for the validation of models with an increased number of parameters, considerable more measurements are required in order to reach sufficient statistical significance [Moilanen et al. 1994].

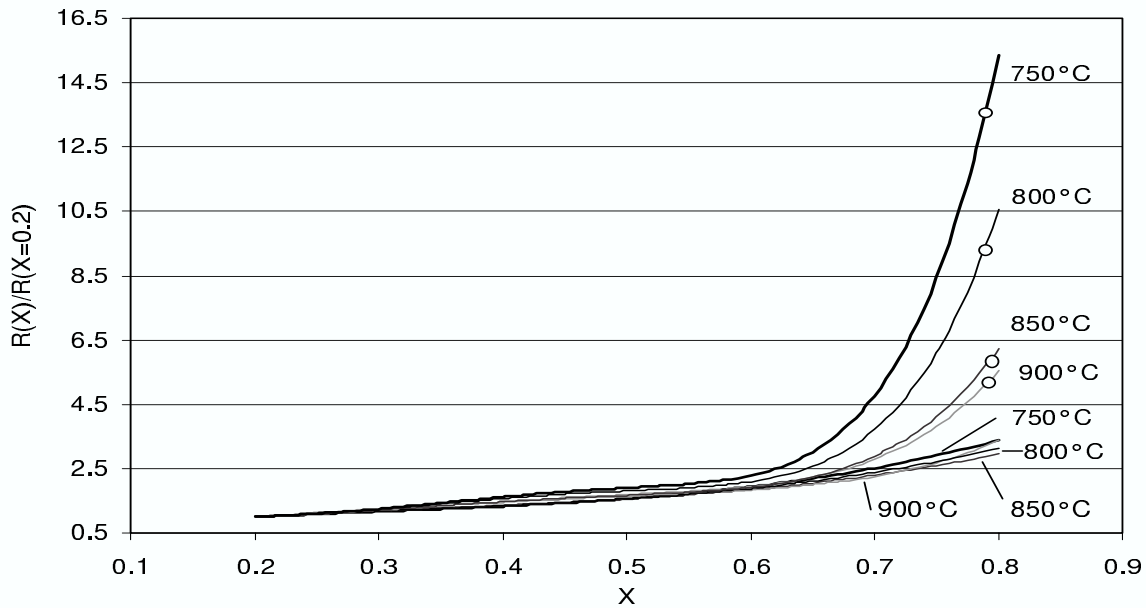


Figure 2.11: Reactivity profiles vs. the conversion for steam gasification of birch and beech (o). Especially for low temperatures, the char reactivity increases very strong at higher conversions. This effect levels for higher temperatures. Also, the effect of increasing reactivity is much more significant for beech. Figure from Barrio et al. [Barrio et al. 2000].

Still, there is no agreement how to quantify the conversion dependent reactivity for the gasification reactions although it has been found by many researchers [Barrio et al. 2000, Barrio and Hustad 2000, Gururajan et al. 1992, Reed 1981, Moilanen et al. 1994]. To achieve a representative reaction rate, most frequently an average of the reaction rate between two degrees of conversion is used [Barrio and Hustad 2000]. However, due to the different definitions of the representative reaction rate, a comparison of the obtained results is problematic. Stoltze et al. [Stoltze et al. 1993] proposed to apply a mass weighed mean reactivity to attach less importance to the reactivity of the last stages of conversion.

The gasification temperature shows an influence on the reactivity profile vs. conversion, as well [Barrio et al. 2000, Reed 1981]. For steam gasification, the effect of the sudden increase of the reaction rate at the end of conversion levels off for higher temperatures [Barrio and Hustad 2000]. This underlines the suggestion of a catalytic activity of the ash. For carbon dioxide gasification, Barrio et al. [Barrio et al. 2000] found a contrary behavior of the temperature influence. However, the reactivity profiles found at the same temperature scatter relatively large and therefore, no quantitative conclusion may be taken [Barrio et al. 2000]. The influence of the temperature history on the gasification process has been reported by several other authors as discussed in Barrio et al. [Barrio et al. 2000]. A variation of the reactant concentration shows no systematic influence on the shape of

reactivity profiles [Barrio et al. 2000].

Squires [Squires 1961] discussed the difference between the gasification rate measured in fixed bed reactors and the one, observed in fluidized bed reactors. He stated that the intensive solid circulation between the oxidizing and reducing zones in the fluidized bed gasifier might increase the reactivity of the surface of the carbon particles.

An other problem is the uncertainty of the number of active sites participating on the reaction. According to a summary in Reed [Reed 1981], it has been proposed not to use the total surface of carbon but the edge carbon atoms. These are for example the atoms present along crystal defects but as well atoms in the proximity to mineral matter deposits particularly CaO, MgO and FeO₄. In investigations, where the chemisorption areas of carbon monoxide, hydrogen and oxygen have been compared with the total surface area of the char, it was found, that just a small part of a few percent of the total surface area of the char participates on the reaction [Laine et al. 1963, Ergun 1956, Menster and Ergun 1973]. Further, Ergun [Ergun 1956] and Menster and Ergun [Menster and Ergun 1973] suggest that the activation energy of the elementary reaction steps of the gasification reaction is independent of the char type. This reduces the considerable differences of the reaction rates in the common models to a difference of the number of active sites, only. Using this approach, the problem changes to the determination of this number of active sites which does not facilitate the problem of a correct description of the reaction rate at all. The evolution of the number of active sites and the evolution of the porosity, pore structure and activity of the carbon during the gasification has been the subject of several studies [Sørensen et al. 1996, Srinivasalu Gupta and Bhatia 2000, Moilanen et al. 1994]

2.2.5 Comparison of Drying, Devolatilization, Gasification

Table 2.10 gives a short overview of the time for drying, devolatilization and gasification. It shows the high importance of the devolatilization step since the largest part of the fuel mass is released during this step. The drying step is very sensitive to the heat transfer coefficient [Peters and Bruch 2001]. Therefore, the drying time is closely connected with the process and operating conditions. Most data for the drying time is available as a result of investigating the pyrolysis process. However, these values are not representative for the drying stage in fluidized bed gasifiers since the heat transfer coefficients which characterize these processes, are basically different. In fluidized bed gasifiers, a higher heat transfer coefficient and consequently lower drying times can be expected.

2.2.6 Particle Models

The particle model describes the evolution of the temperature and the concentration profiles of every participating species. The chemical reactions occurring between the gaseous species and the porous char have to be considered as well as the mass and heat transport. These profiles are important in determining both, the overall and the local reaction rates [Chen and Gunkel 1987].

	Drying	Devolatilization	Gasification
Reaction time	$\sim 140s$ (a), $\sim 220s$ (b)	$\sim 250s$ (c), $\sim 660s$ (d)	$> 3000s$ (e)
Mass fraction converted in the step	depending on the water content 0.1–0.5	0.8–0.9	0.1–0.2

- (a) [Peters and Bruch 2001] wood $\phi 40mm$ at $1000K$, $30 \frac{W}{m^2K}$ heat transfer coefficient and 30% initial water content
 (b) [di Blasi 1997b] wood $\phi 20mm$ at $600K$, $4.2 \frac{W}{m^2K}$ heat transfer coefficient and 50% initial water content
 (c) [Maschio et al. 1994] beech $\phi 25mm \times 100mm$ length at $973K$
 (d) [Larfeldt et al. 2000] dry birch $\phi 25mm \times 300mm$ length at $973K$ in N_2 atmosphere
 (e) [Chen and Gunkel 1987]

Table 2.10: Examples of the time necessary for a complete drying, devolatilization, and gasification.

Effect of Mass- and Heat- Transfer on Global Reaction Rate

To calculate the distribution of the species and the temperature within the particle the differential material and energy balances are used. In a particle with the porosity ε_p , the mole balance for \bar{n} gaseous species and char which participate on \bar{m} chemical reactions can be expressed by:

$$\frac{\partial}{\partial t}(\varepsilon_p c_i) + \text{div}(\varepsilon_p u c_i + J_i) = \sum_{j=1}^{\bar{m}} \bar{\nu}_{i,j} R_j \quad i = 1 \dots \bar{n} \quad (2.67)$$

$$\frac{\partial}{\partial t}((1 - \varepsilon_p) c_{ch}) = \sum_{j=1}^{\bar{m}} \bar{\nu}_{ch,j} R_j \quad (2.68)$$

J_i denotes the diffusive mole flow of the species i and $\bar{\nu}_{i,j} R_j$ is the source of the species i due to the reaction rate R_j of the chemical reaction j . $\bar{\nu}_{i,j}$ is the corresponding gravimetric factor. Analogous to the mass balance, the energy balance for \bar{n} gaseous species leads to:

$$\frac{\partial}{\partial t}(T c_{ch}(1 - \varepsilon_p) c_{p,ch}) + \frac{\partial}{\partial t}(T \varepsilon_p \sum_{i=1}^{\bar{n}} c_i c_{p,i}) + \text{div}(T u \varepsilon_p \sum_{i=1}^{\bar{n}} c_i c_{p,i} + T \sum_{i=1}^{\bar{n}} J_i c_{p,i} + \Phi) = \sum_{j=1}^{\bar{m}} (-\Delta H_j) R_j \quad (2.69)$$

Φ denotes the conductive heat flow and ΔH_j the reaction enthalpy due to the chemical reaction j . The diffusive flows are expressed by Fick's (Eq. 2.70) and Fourier's law (Eq. 2.71).

$$J_i = -D_{e,i} \text{grad}(c_i) \quad (2.70)$$

$$\Phi = -\lambda_e \text{grad}(T) \quad (2.71)$$

For spherical particles and spherically symmetrical material properties, the concentration and temperature profiles are as well spherically symmetrical. Under this conditions Eq. 2.67

and Eq. 2.69 reduce to:

$$\frac{\partial}{\partial t}(\varepsilon_p c_i) + \frac{1}{r^2} \frac{\partial}{\partial r}(r^2 \varepsilon_p u c_i) + \frac{1}{r^2} \frac{\partial}{\partial r}(r^2 J_i) = \sum_{j=1}^{\bar{m}} \bar{v}_{i,j} R_j \quad i = 1 \dots \bar{n} \quad (2.72)$$

$$\begin{aligned} \frac{\partial}{\partial t}(T c_{ch}(1 - \varepsilon_p) c_{p,ch}) + \frac{\partial}{\partial t}(T \varepsilon_p \sum_{i=1}^{\bar{n}} c_i c_{p,i}) + \frac{1}{r^2} \frac{\partial}{\partial r}(r^2 \varepsilon_p T u \sum_{i=1}^{\bar{n}} c_i c_{p,i}) \\ + \frac{1}{r^2} \frac{\partial}{\partial r}(r^2 T \sum_{i=1}^{\bar{n}} J_i c_{p,i}) + \frac{1}{r^2} \frac{\partial}{\partial r}(r^2 \Phi) = \sum_{j=1}^{\bar{m}} (-\Delta H_j) R_j \end{aligned} \quad (2.73)$$

In order to simplify the system to an analytically solvable set of equations, the following presumptions are undertaken:

- Neglect of the convective transport terms which are $\frac{1}{r^2} \frac{\partial}{\partial r}(r^2 \varepsilon_p u c_i)$ in the mass balance and $\frac{1}{r^2} \frac{\partial}{\partial r}(r^2 \varepsilon_p T u \sum_{i=1}^{\bar{n}} c_i c_{p,i})$ in the heat balance. This neglect is exactly valid if no gas formation occurs within the particle or if these terms are small compared to the diffusive flows. Although this is not the case for gasification reactions, this simplification is necessary to achieve a system of equations, which is analytically solvable. If this simplification is not acceptable for a certain application, the system has to be solved numerically.
- Neglect of the heat transported with the diffusive flow $\frac{1}{r^2} \frac{\partial}{\partial r}(r^2 T \sum_{i=1}^{\bar{n}} J_i c_{p,i})$.
- Constant material properties D_e and λ_e

This leads to the following system:

$$\frac{\partial(\varepsilon_p c_i)}{\partial t} = D_{e,i} \frac{1}{r^2} \frac{\partial}{\partial r}(r^2 \frac{\partial c_i}{\partial r}) + \sum_{j=1}^{\bar{m}} \bar{v}_{i,j} R_j \quad i = 1 \dots \bar{n} \quad (2.74)$$

$$\frac{\partial(\bar{c}_p T)}{\partial t} = \lambda_e \frac{1}{r^2} \frac{\partial}{\partial r}(r^2 \frac{\partial T}{\partial r}) + \sum_{j=1}^{\bar{m}} (-\Delta H_j) R_j \quad (2.75)$$

Where $\bar{c}_p = (1 - \varepsilon_p) c_{ch} c_{p,ch} + \varepsilon_p \sum_{i=1}^{\bar{n}} c_i c_{p,i}$ denotes the average mole-specific heat capacity of the gas-solid matrix. Assuming quasi-steady state ($\frac{\partial(\varepsilon_p c_i)}{\partial t} = 0$, $\frac{\partial(\bar{c}_p T)}{\partial t} = 0$), Chen and Gunkel [Chen and Gunkel 1987] solved this system of differential equations analytically with the Fredholm integral technique for the mass as well as for the heat transfer with simultaneous chemical reaction. Then they did a time discretization in order to obtain a time dependent concentration and temperature profile within particle. The material properties they used for the simulation correspond to biomass char gasification. To acquire an image of the interactions of the physicochemical system in a particle, a summary of the results is presented below.

Effect of particle size Chen and Gunkel [Chen and Gunkel 1987] performed the calculations for the temperature profile for a bulk temperature of $1500K$ and carbon concentration remaining constant on initial concentration. A constant carbon concentration is necessary in order to exclude the effect of local carbon concentration on the temperature profile. For particles less than $0.2cm$ in diameter, the temperature within the particle remains nearly constant. The significant temperature difference of the particle temperature to the bulk temperature of up to $250K$ is entirely reached in the boundary layer. Under this circumstances, the isothermal particle is a good approximation and every thermal resistance may be lumped into the boundary layer.

The temperature drop within the particle becomes significant in particles up to $1-4cm$ in diameter. Since the reaction rate depends exponentially on local temperature, a reasonable overall reaction rate demands for the consideration of the particle model. The particle size affects as well the surface temperature. Under gasification conditions, the endothermic reactions are volumetric while the heat is transferred through the particle surface. This results in a lower surface temperature for large particles since a large temperature drop as driving force is required. This effect levels off with further increasing diameter due to diffusion limitations in the particle.

The concentration profiles are similar to the temperature profiles since the reaction rate is coupled with the temperature in the same sense. The particle consumption time in a bulk with constant temperature increases slightly nonlinear with particle size. A linear approximation in a wide range of particle sizes may be justified.

Bulk temperature effect Investigating the influence of the bulk temperature two extremes may be observed. First, the homogeneous model, where the entire char participates on the reaction (proportional to the cube of the diameter). Second the shrinking core model, where a thin surface layer participates on the reaction and which is proportional to the square of the diameter.

Chen and Gunkel [Chen and Gunkel 1987] evaluated the effect of bulk temperature on gas concentration profiles for particles with $2cm$ in diameter. They found at low temperatures up to $1000K$ the chemical reaction to be the rate determining step. In this case, the concentration profile is nearly uniformly within the particle. With increasing temperature, the reaction rate increases much faster than the diffusion process. Neglecting diffusional limitations over $1200K$ and higher temperatures causes a significant kinetic error.

High reaction rates are generally observed at bulk temperatures between $1200K$ and $1600K$ for moving bed gasifiers. Chen and Gunkel [Chen and Gunkel 1987] conclude that neither the homogeneous model nor the shrinking particle model is applicable in this case since the temperature and the concentration distribution are in an intermediate state.

Influence of the Pore Evolution and Thermal History The evolution of the pore structure during thermal conversion of char has been subject of several studies. Therefore, more or less sophisticated pore models have been investigated [Froment and Bischoff 1990, Srinivasalu Gupta and Bhatia 2000, Borelli et al. 1996, Kantorovich and Bar-Ziv 1999]. Srinivasalu Gupta and Bathia [Srinivasalu Gupta and Bhatia 2000] investigated a discrete random pore model where they introduced a parameter to allow for an adjustment of the initial surface. The intention is, to account for inhibitory groups on the initial char surface as well as for the formation and degradation of surface complexes as reaction proceeds.

A reduced number of initial active sites may also be explained by the exclusive participation of the edge atoms on reaction (refer to page 35). A comparison of the model with experimental data for air gasification shows a significant improvement for the model of the reaction rate as well as for the evolution of the intrinsic surface respective to the conversion. However, for steam gasification the initial surface is not important for modeling [Srinivasalu Gupta and Bhatia 2000].

It is widely accepted, that the thermal history has strong influence due to graphitization and other structural modifications on the gasification kinetics (refer to chapter 2.2.2 and chapter 2.2.3). However, it is rather complicated to quantify this fact and so it is neglected or the range of validity of the measured kinetics is restricted to a certain pretreatment [Tancredi et al. 1996b]. Tancredi et al. [Tancredi et al. 1996b] investigated the influence of the thermal history on the reactivity of chars which were obtained by carbonizing at different temperatures. They determined the BET surface area and the reactivity in carbon dioxide per BET surface area at different conversion levels. For eucalyptus wood char and carbon dioxide gasification at low and intermediate conversion, they found the evolution of the reactivity to be basically a result of the increasing surface and pore opening. At higher conversion they suggested an increasing contribution of catalytic effects which leads to a step increase in reactivity at advanced stages of conversion.

Characteristic Numbers for the Particle Model

For the modeling of a particle conversion in a reactor, as occurring in a fluidized bed gasifier, the system of heat and mass-transport equations Eq. 2.67 and Eq. 2.69 is rather unwieldy. Therefore, two characteristic numbers, the Damköhler Number and the Thiele Modulus have been defined to characterize the physico-chemical circumstances of the system. With these numbers, it is possible to determine the limiting steps for the overall reaction rate. Once known which rate limitations take place, it is possible to undertake reasonable simplifications for the evaluation of the overall reaction rate. Further, the computation of an effectiveness factor based on these numbers permits an easy handling of the particle model in the overall reaction rate. For reasons of simplification, the heat transfer is usually not considered. This is common for both, the Damköhler Number and the Thiele Modulus. It exist attempts to apply similar procedures for systems with limitations of heat and mass-transfer. However, the simplification achieved is of minor relevance since the need for an iterative solution can not be avoided (for details refer to Froment and Bischoff [Froment and Bischoff 1990]).

Damköhler Number The *Damköhler Number* sets two extreme situations of the rate controlling step into relation and permits to know the importance of the chemical reaction rate relative to the external mass-transfer rate. It is dimensionless and is the ratio between the reaction rate without mass-transfer limitations, which implies that the surface concentration equals the ambient concentration, and the reaction rate with the maximum mass-transfer limitation which implies that the particle surface concentration is zero.

$$Da_{II} = \frac{\text{reaction rate without mass-transfer limitations}}{\text{reaction rate with the maximum mass-transfer limitation}} \quad (2.76)$$

Be the chemical reaction of the form:



where \mathcal{C} denotes the carbon reacting with species \mathcal{A} to species \mathcal{B} and \mathcal{D} . Further, a law of the form

$$\frac{1}{m_C} \frac{dm_C}{dt} = -\bar{r}(c_A, T) \quad (2.78)$$

describes the kinetics. With the molar mass of carbon M_C and the density of char $\rho_{ch} = \frac{m_C}{V_{ch} w_C}$, Eq. 2.78 equals for sphere particles and a uniform concentration distribution within the particle the following form:

$$\frac{dn_{A,S}}{dt} = \frac{\bar{v}_A \rho_{ch} w_C d_p^3 \pi}{6M_C} \bar{r}(c_{A,S}, T) \quad (2.79)$$

Using the *Sherwood Number* $Sh_A = \frac{k_{m,A} d_p}{D_A}$, the molar flux on the particle surface due to the external concentration gradient is:

$$\frac{dn_{A,S}}{dt} = \frac{Sh_A D_A}{d_p} d_p^2 \pi (c_{A,\infty} - c_{A,S}) \quad (2.80)$$

As a next step, $c_{A,S}$ is replaced by $c_{A,\infty}$ in Eq. 2.79 and by 0 in Eq. 2.80. This corresponds to no external mass-transfer limitation and the maximum mass-transfer limitation, respectively. Finally, the ratio of these equations leads to the *Damköhler Number*:

$$DaII_A = \frac{\bar{v}_A \rho_{ch} w_C d_p^2}{6M_C Sh_A D_A} \frac{\bar{r}(c_{A,\infty}, T)}{c_{A,\infty}} \quad (2.81)$$

For high *Damköhler Numbers* (mass-transfer is rate controlling), the overall reaction rate can be modeled by regarding the mass-transfer with surface concentration zero. For intermediate and low $DaII$, it is necessary to do further investigation on the concentration profile within the particle [Froment and Bischoff 1990]. In the presented procedure, the particle temperature is assumed to stay constant at ambient temperature. The concentration of the single species in the particle is assumed to stay at surface concentration. This is only valid, if internal mass-transfer resistances can be neglected or the entire amount of reactants diffusing to the particle surface is consumed immediately without appreciable penetration into the particle. Furthermore, no convective terms are considered. This may cause a significant error, if gas generating reactions take place.

It is possible, to obtain an effectiveness factor η_{ext} directly from the *Damköhler Number*. η_{ext} relates the reaction rate with external limitations to the reaction rate with ambient conditions. It has the form [Budde 1989]:

$$\eta_{ext} = 1/(1 + DaII) \quad (2.82)$$

In order to use η_{ext} for the computation of the overall reaction rate, the reaction rate is preliminary evaluated with ambient conditions. Then, the obtained result is multiplied by the effectiveness factor.

Thiele Modulus If a chemical reaction occurs on the pore walls of a particle, the diffusion rate, the reaction rate, and if necessary, thermal effects must be considered simultaneously. For this purpose, the mass-transport equation (Eq. 2.74) for spherical particles is used again. Neglecting the time dependent and the convective terms, one gets:

$$0 = D_{e,i} \frac{1}{r^2} \frac{\partial}{\partial r} (r^2 \frac{\partial c_i}{\partial r}) + \sum_{j=1}^{\bar{m}} \bar{v}_{i,j} R_j \quad i = 1 \dots \bar{n} \quad (2.83)$$

The boundary conditions are as follows:

$$c_i(r) \big|_{(r=a_p)} = c_{S,i} \quad \text{at the surface} \quad (2.84)$$

$$\frac{\partial c_i(r)}{\partial r} \big|_{(r=0)} = 0 \quad \text{at the center} \quad (2.85)$$

This equation system permits to compute the concentration of a species i in a particle as a function of the radius. Once achieved a solution for the concentration profile, the evaluation of the reaction rate at each point is straight forward.

A rather flat concentration profile implies a rather low reaction rate compared to the diffusion rate. This is notably the case of steam-, carbon dioxide- or hydrogasification as seen later on. For autothermic gasification with oxygen or air, or for high temperatures, an increasing domination of the chemical reaction can be expected. In this case, the concentration of the species i may drop towards zero within a small distance after penetrating the particle. Since the chemical reaction rate is more temperature sensitive ($\sim e^{\frac{1}{T}}$) than the diffusion rate ($\sim T^{1.75}$), the relative importance of the latter on the overall rate can vary considerably. To characterize the diffusion resistance, the overall reaction rate with pore diffusion is related to the reaction rate without internal diffusion resistance. Hence, for the latter case, the concentration of every species equals the particle surface concentration within the whole particle. This leads to the definition of the effectiveness factor η_{int} , which is:

$$\eta_{int} = \frac{\text{reaction rate with pore diffusion resistance}}{\text{reaction rate with surface conditions}} \quad (2.86)$$

The *Thiele Modulus* ϕ is derived for the example of the conversion of a species i . The reaction occurs within a porous particle which consists of a pure solid with density ρ_s and mole mass M_s . The heterogeneous reaction j is of first order with the frequency factor k_j :

$$k_j c_i \frac{\rho_s}{M_s} = R_i \quad (2.87)$$

$$\phi_{i,j} = \frac{a_p}{3} \sqrt{\frac{k_j \rho_s}{D_{e,i} M_s}} \quad (2.88)$$

$$\eta_{int,i,j} = \frac{1}{\phi_{i,j}} \frac{3\phi_{i,j} \coth 3\phi_{i,j} - 1}{3\phi_{i,j}} \quad (2.89)$$

The effectiveness factor η_{int} (Eq. 2.89) is a function of the *Thiele Modulus* ϕ only. Parameters like the geometry or the temperature influence η_{int} just through ϕ . This permits to characterize the shape of the concentration profile within a particle just by regarding the ϕ . If ϕ tends towards zero, the effectiveness tends towards one (no internal diffusion limitations) and conversely for very large ϕ the effectiveness factor tends towards zero (high internal diffusion limitations, the reaction occurs just on the particle surface). The latter can occur for small diffusivity, large pellet size or very rapid reaction rate.

It is possible to derive an analytic solution for the *Thiele Modulus* of n^{th} -order reactions and any particle shapes.

$$\phi_{i,j} = \frac{V_p}{O_p} \sqrt{\frac{n+1}{2} \frac{k_j c_{S,i}^{n-1} \rho_s}{D_{e,i} M_s}} \quad n > -1 \quad (2.90)$$

Where V_p denotes the particle volume, O_p the particle surface and n the reaction order. The relation between *Thiele Modulus* and effectiveness factor given by Eq. 2.89 is still approximately valid for intermediate values of the *Thiele Modulus* and exactly valid for extreme values ($\phi \ll 1$ or $\phi \gg 1$) [Froment and Bischoff 1990]. This procedure assumes the knowledge of the surface concentration and the particle temperature. To verify the influence of external mass-transfer limitations, the *Damköhler Number* can be used. If the *Damköhler Number* indicates external mass-transfer resistance an external heat-transfer resistance can also be expected. In this case it is essential to consider the thermal balance if the heat of reaction is high. Furthermore, every convective term has been neglected which is problematic for gas generating reactions as gasification reactions, devolatilization or drying. Therefore, the equations presented here can give an image of the situation but they are not applicable for an accurate calculation of highly heat consuming, gas producing gasification reactions in large heterogeneous particles. The calculation of an effectiveness factor which takes into account for the combination of external and internal mass-transfer resistances is explained elsewhere [Froment and Bischoff 1990].

The Shrinking Particle Model

The shrinking particle model is a special case of a particle model. The rapid reaction rate compared to the external mass transfer rate prevents the reacting species from penetrating the particle to a large depth. Therefore, the carbon conversion occurs within a thin surface layer. This results in a shrinking particle diameter during conversion. Further, the reaction rate is proportional to the square of the particle diameter. Small penetration depths of the reacting species can be accomplished in two cases. First, in the case of very high values of the *Damköhler Number*, which is identical to a high external diffusion resistance. Second, in the case of very low internal effectiveness factors η_{int} , which is equal to high values of the *Thiele Modulus*. The *Thiele Modulus* does not play a role in the first case whereas the *Damköhler Number* has no influence in the second case (refer to Fig. 2.12).

Shrinking Core Model

The shrinking core model is similar to the shrinking particle model. In addition to this a residual ash layer after the complete conversion is assumed. So, an additional mass-transfer resistance through this ash layer must be taken into account. This leads to a shrinking reacting core with the initial external mass-transfer conditions due to the constant particle diameter.

Sørensen et al. [Sørensen et al. 1996] evaluated the char reactivity by different shrinking-core models for coal char and air gasification. They conclude that the shrinking core model is not appropriate for low temperatures ($< 900^\circ\text{C}$) because the penetration depth of oxygen is not sufficiently thin over a large burnoff interval. This result has been found as well by other authors [Chen and Gunkel 1987, Reed 1981].

Extrapolated to the by far slower steam gasification and common gasification temperatures it can be suggested that a shrinking core model is not an appropriate model for this process.

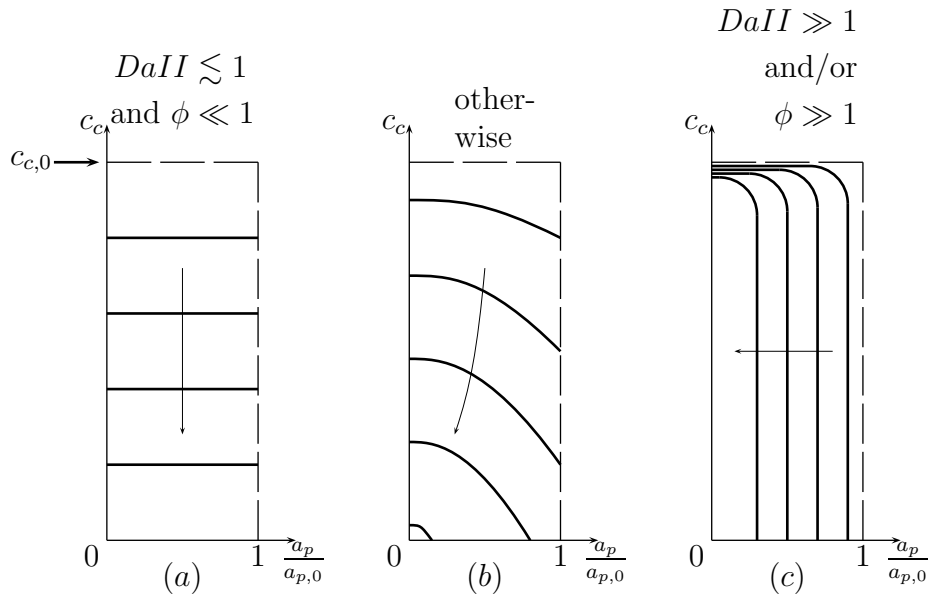


Figure 2.12: The first Figure (a) shows the concentration profile for slow reaction rates and high internal diffusion rates. In this case, no significant external diffusion limitation may be present. The carbon concentration decreases homogeneous in the whole particle. Figure (b) shows the concentration profile if no dominating limitation can be fixed. The concentration profile according Figure (c) corresponds to a very fast chemical reaction rate related to the diffusion rate. The flash shows the direction of increasing time.

Homogeneous Particle Model

The homogeneous particle model is a special case of a particle model which is appropriate to use at low values of the *Thiele Modulus* and moderate or low *Damköhler Numbers* [Froment and Bischoff 1990]. Essentially is the homogeneous concentration profile of the species within the particle (refer to Fig. 2.12). This equals a high internal diffusion rates and a low reaction rate.

Chapter 3

Model Development

3.1 Geometry

The principal parts of the FICFB-plant constitute the fluidized bed gasifier and a slender riser (refer to Fig. 3.1). In the gasifier, there is a stationary fluidized bed with steam fluidization. The riser is operated with a fast air fluidized bed. These two parts are communicating by two facilities. First, by a tube on the bottom, where the bed material withdrawn from the gasifier is passed to the riser. Second, by a syphon slightly above the bed surface, where the bed material is withdrawn from the riser and passed back to the gasifier.

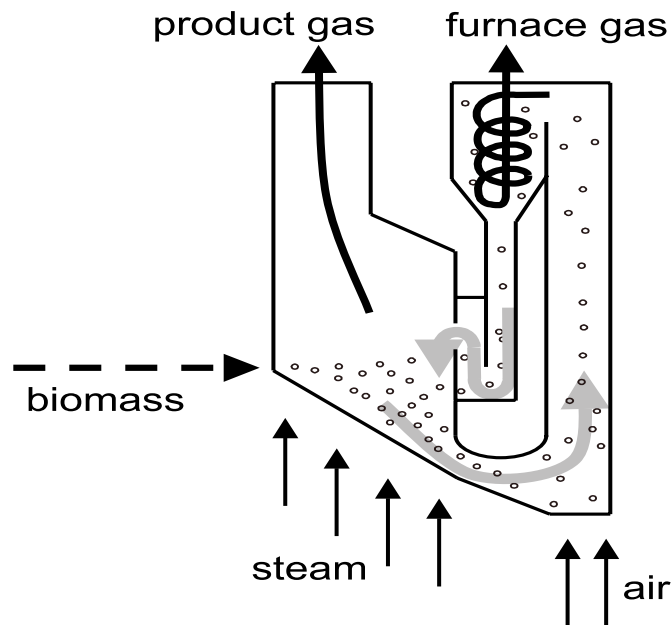


Figure 3.1: On the left-hand side, it is shown the gasifier unit with steam fluidization flow, biomass feed and product gas flow. The riser on the right-hand side is fluidized with air. The cyclone on the top of the riser separates the furnace gases from the particles of the circulating bed material. The two reactors communicate by a syphon slightly above the bed surface and by a chute on the bottom. Figure from Kaiser [Kaiser 2001]

In the riser, the bed material is heated up by air combustion of the residual char and additional fuel. Second, by a cyclone separator and a siphon where the hot bed material is fed back to the gasifier. The control over the bed temperature is done by an additional combustible fed in the riser in order to heat up the solid circulation flow. To handle the geometry of the gasifier in the mathematical model, it is simplified in a reasonable way. Fig. 3.2 and Fig. 3.3 show the simplified geometry used for the simulation for the pilot plant gasifier and the demonstration plant. It consists of a cylinder followed by a rotation-symmetrical cone and again a cylinder. The inlet for the fluidizing gas as well as the drain for the bed material are situated on the bottom of the first cylinder. The external solid circulation flow through the combustion unit is supposed to intermix instantaneous with the rest of the bed as passed in the gasifier again. Further, it does not affect any process in the freeboard (refer to idealizations for the fluid dynamics on page 49). So it is not important where it is fed into the gasifier but it is symbolized to be on the top of the reactor. The bed in the pilot plant gasifier reaches into the upper cylindric part whereas the bed in the demonstration plant terminates already in the cone.

Related to the bed height, the pilot plant reactor is much higher. However, the enlargement of the freeboard beyond the bed surface increases the residence time of the gases in the freeboard of the demonstration plant reactor. Therefore, the difference between the residence time of the gases of the demonstration plant and the pilot plant reactor approach each other. The idealizations regarding the geometry are summarized in the following list:

- Geometry according Fig. 3.2 for the pilot plant gasifier and according Fig. 3.3 for the demonstration plant reactor.
- Horizontal bottom plate
- Symmetrical to main axis
- Withdrawal of bed material at the bottom plate level
- Recharge of the heated bed material at the level of the bed surface

3.2 Material Properties

3.2.1 Molecular Diffusion Coefficient

The calculation uses the method of Fuller, Schettler and Giddings, which is described in 'Properties of Gases and Liquids' [Reid et al. 1986]. The method of Fuller et al. is the correlation, which is recommended since it has been found that this correlation yield the smallest average error of the methods discussed there [Reid et al. 1986]. Based on Table 3.1, the diffusion volume of CH_4 is 25.14. The molecular diffusion coefficient of component \mathcal{A} in component \mathcal{B} , $D_{\mathcal{A},\mathcal{B}}$ in m^2/s is

$$D_{\mathcal{A},\mathcal{B}} = \frac{45220.6 T^{1.75}}{p \sqrt{M_{\mathcal{A},\mathcal{B}}} \left((\sum_v)_{\mathcal{A}}^{1/3} + (\sum_v)_{\mathcal{B}}^{1/3} \right)^2} \quad (3.1)$$

with

$$M_{\mathcal{A},\mathcal{B}} = 2 \left(M_{\mathcal{A}}^{-1} + M_{\mathcal{B}}^{-1} \right)^{-1} \quad (3.2)$$

The term \sum_v is found for each component by summing atomic diffusion volumes in Table 3.1.

3.2.2 Viscosity

The calculation for the viscosity uses 3rd order polynomial correlation for each pure species. All the correlations but the ones for CO and O₂ are based on a table out of 'VDI-Wärmeatlas' [VDI-GVC 1997]. The correlations for CO and O₂ are according to the 'Handbook of Chemistry and Physics' [The Chemical Rubber Co. 1977]. The Viscosity of the mixture is calculated by the Method of Wilke which is described in 'Properties of Gases and Liquids' [Reid et al. 1986]. These correlations are derived from the rigorous kinetic theory of Chapman-Enskog by neglecting second order effects. The rather unwieldy equations are therefore simplified by Wilke to a practicable form. The equations for the 3rd order polyoma are given in Table 3.2. The viscosity for a mixture μ_m of \bar{n} species is

$$\mu_m = \sum_{i=1}^{\bar{n}} \frac{y_i \mu_i}{\sum_{h=1}^{\bar{n}} y_h \bar{\phi}_{i,h}} \quad (3.3)$$

where

$$\bar{\phi}_{i,h} = \frac{\left(1 + \left(\frac{\mu_i}{\mu_h}\right)^{1/2} \left(\frac{M_h}{M_i}\right)^{1/4}\right)^2}{\left(8\left(1 + \frac{M_i}{M_h}\right)\right)^{1/2}} \quad (3.4)$$

Atomic and Structural Diffusion Volume Increments			
C	15.9	F	14.7
H	2.31	Cl	21.0
O	6.11	Br	21.9
N	4.54	I	29.8
Aromatic ring	−18.3	S	22.9
Heterocyclic ring	−18.3		
Diffusion Volumes v for Simple Molecules			
He	2.67	CO	18.0
Ne	5.98	CO ₂	26.9
Ar	16.2	N ₂ O	35.9
Kr	24.5	NH ₃	20.7
Xe	32.7	H ₂ O	13.1
H ₂	6.12	SF ₆	71.3
D ₂	6.84	Cl ₂	38.4
N ₂	18.5	Br ₂	69.0
O ₂	16.3	SO ₂	41.8
Air	19.7		

Table 3.1: Atomic diffusion volumes [Reid et al. 1986].

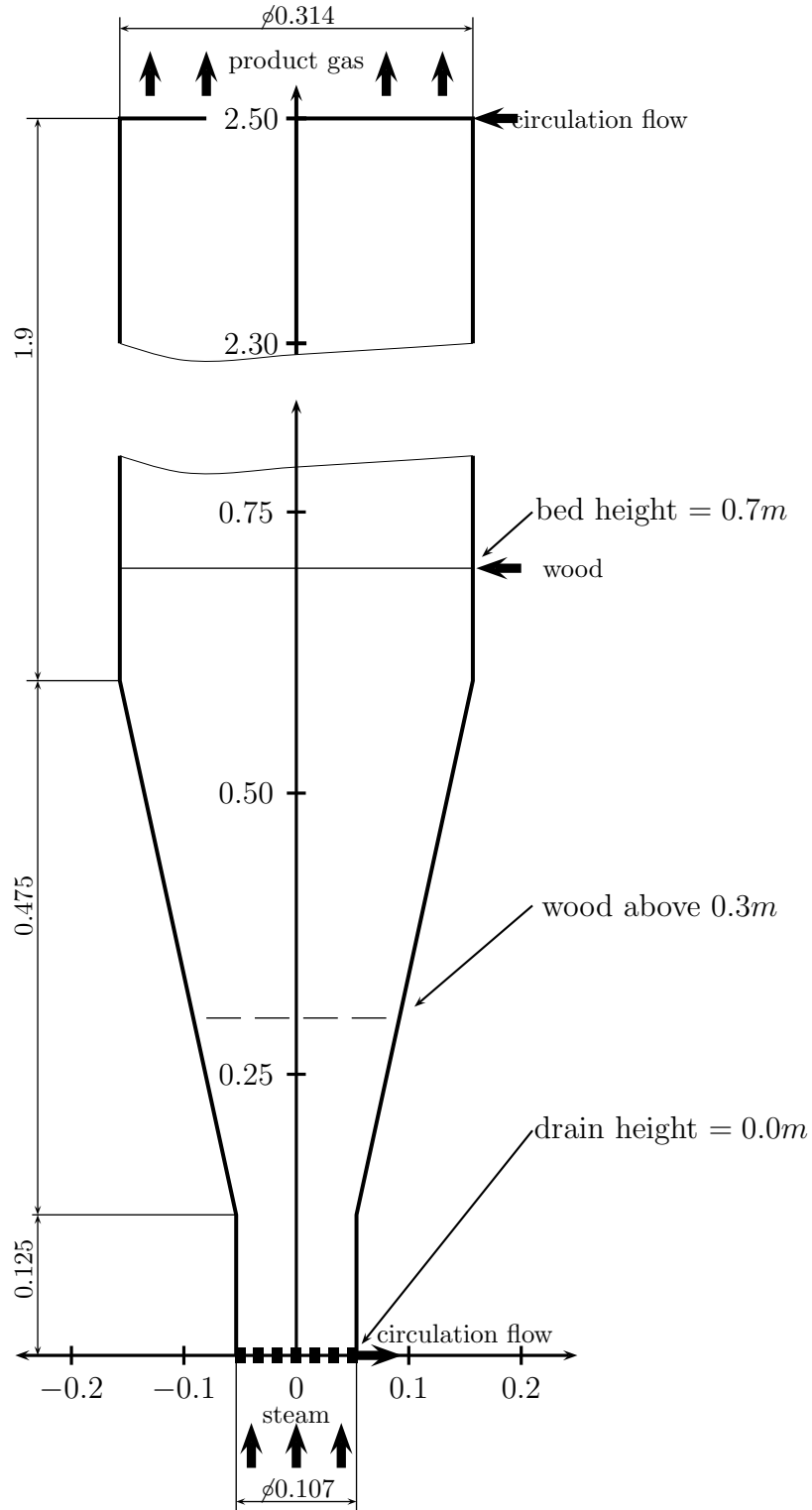


Figure 3.2: Simplified geometry of the pilot plant reactor. Especially the inlet sheet is modeled in horizontally position which differs from the pilot plant reactor. Since the correlations for the fluid dynamics do not account for asymmetry the reactor is simplified to rotation-symmetrical geometry. The depth of the wood submergence is assumed to be about $0.4m$ for the model. Hence, it is encountered just above a height of $0.3m$. The total bed height is $0.7m$.

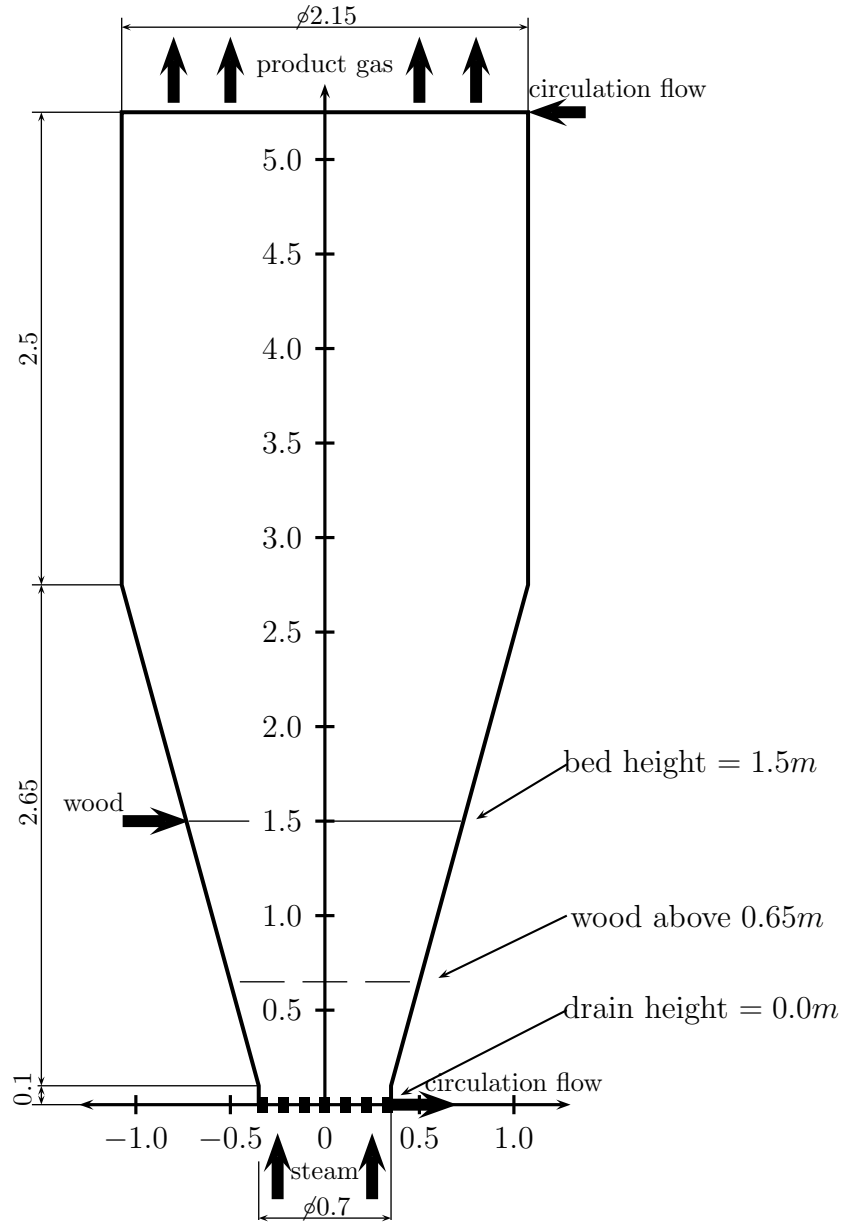


Figure 3.3: Simplified geometry of the demonstration plant gasifier. The depth of the wood submergence is assumed to be about $0.85m$ for the model. The total bed height is $1.5m$. A significant difference is the bed height relative to the geometry compared to the pilot plant reactor. The bed in the demonstration plant ends already in the conical part whereas the bed height in the pilot plant reactor passes beyond the conical section (refer to figure 3.2).

$\mu_{N_2} = 10^{-6}(1.89696 \cdot 10^{-8}T^3 - 4.99074 \cdot 10^{-5}T^2 + 7.22905 \cdot 10^{-2}T + 1.66136 \cdot 10^{-1})$
$\mu_{O_2} = 10^{-6}(1.39088 \cdot 10^{-8}T^3 - 4.49772 \cdot 10^{-5}T^2 + 7.72693 \cdot 10^{-2}T + 9.85268 \cdot 10^{-1})$
$\mu_{CH_4} = 10^{-5}(9.83710 \cdot 10^{-11}T^3 - 1.82433 \cdot 10^{-6}T^2 + 4.28954 \cdot 10^{-3}T - 2.00742 \cdot 10^{-2})$
$\mu_{H_2} = 10^{-5}(4.58331 \cdot 10^{-10}T^3 - 1.37650 \cdot 10^{-6}T^2 + 2.73110 \cdot 10^{-3}T + 1.88272 \cdot 10^{-1})$
$\mu_{CO} = 10^{-6}(6.12430 \cdot 10^{-8}T^3 - 9.58389 \cdot 10^{-5}T^2 + 8.48528 \cdot 10^{-2}T - 6.97080 \cdot 10^{-1})$
$\mu_{CO_2} = 10^{-6}(4.87022 \cdot 10^{-9}T^3 - 2.34095 \cdot 10^{-5}T^2 + 6.11504 \cdot 10^{-2}T - 1.33587)$
$\mu_{H_2O} = 10^{-6}(-5.99161 \cdot 10^{-9}T^3 + 1.15667 \cdot 10^{-5}T^2 + 3.37086 \cdot 10^{-2}T - 1.677664)$

Table 3.2: Viscosity for pure species in *Pas*.

$\bar{\phi}_{h,i}$ is found by interchanging subscripts or by

$$\bar{\phi}_{h,i} = \frac{\mu_h}{\mu_i} \frac{M_i}{M_h} \bar{\phi}_{i,h} \quad (3.5)$$

3.3 Fluid Dynamics

For the modeling of the bed fluid dynamic, the semi-empiric correlations listed in Table 3.3 are used. However, these equations can not describe the fluid dynamic system completely. Further, some reactor specific features have to be modeled in an appropriate way. The bed material distribution and the neglect of the fluid dynamic system of the large active particles as constitute the char and the wood fraction are an example of these simplifications. The presumptions regarding these simplifications are listed here:

- One dimensional fluid dynamics. So the bed is supposed to be perfectly mixed perpendicularly to the main flow direction within the dense phase and the bubble phase.
- No back-mixing of the gases. Further, the axial diffusivity is assumed to be zero.
- The bubbles are solid-free.
- The dense phase is kept at minimum fluidization conditions.
- The mass-transfer of a single species between the dense-phase and bubble-phase is modeled by a mass-transfer coefficient (k_{be}).
- In the freeboard the solid fraction is homogeneously mixed with the gas perpendicularly to the main flow direction.
- The correlations used for the fluid dynamic models are evaluated entirely with the material properties of sand. The different material properties and size of the wood and char particles are not considered.
- The mass distribution of char and wood is an input (refer to page 74).

Expression	Eq. No.	Remarks	Reference
$\varepsilon_{mf}^3 - \frac{150}{\phi_p^2} \cdot \frac{Re_{mf}}{Ar_I} \cdot (1 - \varepsilon_{mf}) - \frac{1.75}{\phi_p} \cdot \frac{Re_{mf}^2}{Ar_I} = 0$	(2.5)	for ε_{mf}	[Ergun 1952]
$Q_b = \delta_b u_b A_R$	(2.6)	for δ_b	
$Ar_I = \frac{d_p^3 \rho_g (\rho_p - \rho_g) g}{\mu_g^2}$	(3.6)		
$Sh_\infty = 0.009 Ar_I^{0.5} Sc^{0.33}$	(2.21)	$d_{p,A}/d_{p,I} \gg 1$	[Baskakov et al. 1978]
$Sh_1 = 2\varepsilon_{mf} + 0.117 Ar_I^{0.39} Sc^{0.33}$	(2.23)	$d_{p,A}/d_{p,I} = 1$	[Leckner et al. 1992]
$Sh_A = (Sh_1 - Sh_\infty) \frac{d_{p,A}}{d_{p,I}}^{\frac{1}{3}} + Sh_\infty \frac{d_{p,A}}{d_{p,I}}$	(2.25)	in bed (refer to Table 2.1)	[Leckner et al. 1998]
$U_{mf} = \frac{\mu_g}{\rho_g d_p} (\sqrt{27.2^2 + 0.0408 Ar_I} - 27.2)$	(2.4)		[Grace 1982]
$Y = \frac{0.26 + 0.7e^{-3.3 \cdot 10^3 d_p}}{0.15 + (U - U_{mf})} (h + 4\sqrt{A_o})^{0.4}$	(2.12)		[Johnsson et al. 1991]
$d_b = 0.54(U - U_{mf})^{0.4} (h + 4\sqrt{A_o})^{0.8} g^{-0.2}$	(2.16)		[Darton et al. 1977]
$u_{b,\infty} = 0.71 \sqrt{g \bar{d}_{eq}}$	(2.14)	it is used $d_b = d_{eq}$	
$u_b = 2.0 \sqrt{\bar{d}_R} u_{b,\infty} + Y(U - U_{mf})$	(2.15)	group B, $0.1 < d_R < 1$	[Bauer et al. 1981]
$Q_b = Y A_R (U - U_{mf})$	(2.11)		
$k_{be} = \frac{U_{mf}}{3} + \left(\frac{4D\varepsilon_{mf}\bar{u}_b}{\pi \bar{d}_b} \right)^{0.5}$	(2.19)		[Sit and Grace 1981]

A_o distributor section per orifice in m^2 ; $u_{b,\infty}$ single bubble velocity in m/s ; $\bar{u}_b = u_b$ and $\bar{d}_b = d_b$ because of recalculation in every instance

Table 3.3: Summary of the equations used to calculate the bed fluid dynamic.

Expression	Eq. No.	Remarks	Reference
$Sh_A = 2\varepsilon_{FB} + \left(\frac{Re_t}{\varepsilon_{fb}}\right)^{0.5} Sc^{0.33}$	(3.7)		[Baskakov et al. 1978]
$U_t^2 = \frac{4}{3} \frac{\rho_p - \rho_g}{\rho_g} \frac{d_p g}{c_w}$ with $c_w = \begin{cases} \frac{24}{Re_t} & \text{for } Re_t < 1 \\ \frac{24}{Re_t} + \frac{4}{\sqrt{Re_t}} + 0.4 & \text{for } 1 < Re_t < 3000 \\ 0.43 & \text{for } 3000 < Re_t \end{cases}$	(3.8)	for U_t	
$f_{dy} = 4 \frac{U_t}{U}$	(2.27)		[Johnsson and Leckner 1995]
$\varepsilon(h) = \varepsilon_{TDH} + (\varepsilon_L - \varepsilon_{TDH})e^{-f_{dy}h}$	(2.26)		[Johnsson and Leckner 1995]

Table 3.4: Summary of the correlations used in the freeboard.

- By drying, devolatilization and gasification generated gas is split between dense-phase and bubble-phase in the way presented in Table 3.5.
- The through-flow is lumped into the bubble flow (refer to chapter 2.1.1)
- The bed height is fixed.
- Plug-flow in freeboard
- The bed material withdrawn for the riser has the composition of the stage where the material is discharged.

The gasifier is split up into control volumes along the main axis in order to model the fluid dynamics. Each control volume itself is split up into a bubble-phase and a dense-phase, where the gas production occurs. The amount of the produced gas in the dense-phase would soon lead to an exceed of the maximum flow given by the minimum fluidization conditions. This is the case because the mass-transfer correlations between bubble and dense-phase can not compensate the effect of gas production. To avoid this error in modeling, which would lead to a serious distortion of the gasification kinetics, the generated gas is first mixed with the gas in the dense-phase. Then, a part of the gas in the emulsion is passed directly into the bubble-phase such that the fluid dynamic equations in Table 3.3 are satisfied. The equations which are used for the described procedure are sequentially listed in Table 3.5.

3.4 Chemical System used for Modeling

3.4.1 Drying

For the drying step, no kinetic modeling is done. The only criteria which is to fulfill, is the satisfaction of the molar balances over the reactor. Therefore, the drying time is assumed to equal the devolatilization time to simplify the model development.

3.4.2 Devolatilization

The problem to acquire confidential compositions of the gases released in the devolatilization step is already discussed in chapter 2.2.3. Although the char composition still contains partly considerable amounts of hydrogen and oxygen (refer to Table 2.3), for the model, a complete devolatilization to a char particle of pure carbon and ash is assumed. The ash is considered as inert. Therefore, it is assumed, that the entire hydrogen and oxygen content of the wood is released with the devolatilization gases. This is either in pure form like hydrogen or within a carbon compound like carbon dioxide or as water. This eliminates the problem how to handle the elements which remain in the char and eases a material balance over the whole reactor. Hence, the devolatilization compositions listed in literature can not be used directly for this model since in the experiment always remains a non carbon residue in the char. Therefore, not the product gas concentration from the experiment are used, but the proximate analysis, the ultimate analysis, and certain important product gas concentration ratios. With these data, a correction of the released product gas concentration is possible. However, for large solid circulation flows, neglecting the residual content of non carbon elements, the computed product gas composition may have a significant deviation towards

Step i:	$\dot{n}_{b,i}^k = \dot{n}_{gr,b,i}^k + \dot{n}_{rel,b,i}^k$	mole flow vector, bubble-phase
Step ii:	$\dot{n}_{e,i}^k = \dot{n}_{gr,e,i}^k + \dot{n}_{rel,e,i}^k$	mole flow vector, dense-phase
Step iii:	$\dot{n}_{R,i}^k = \dot{n}_{e,i}^k + \dot{n}_{b,i}^k$	mole flow vector, reactor
Step iv:	$Q_R^k = \frac{\mathcal{R}T}{p} \sum_i (\dot{n}_{R,i}^k)$	volumetric flow, reactor
Step v:	$U^k = Q_R^k / A_R^k$	superficial velocity
Step vi:	$\delta_b^k = Y^k \frac{(U^k - U_{mf}^k)}{u_b^k}$	bubble fraction
Step vii:	$A_e^k = A_R^k (1 - \delta_b^k)$	cross section dense-phase
Step viii:	$A_b^k = A_R^k \delta_b^k$	cross section bubble-phase
Step ix:	$Q_b^k = Y^k A_R^k (U^k - U_{mf}^k)$	volumetric flow, reactor
Step x:	$Q_e^k = A_e^k U_{mf}^k$	volumetric flow, dense-phase
Step xi:	$Q_{tf}^k = Q_{tot}^k - Q_b^k - Q_e^k$	volumetric flow, through-flow
Step xii:	$Q_b^{k+1} = Q_b^k + Q_{tf}^k f_{tf,b}^k$	new volumetric flow, bubble-phase
Step xiii:	$Q_e^{k+1} = Q_e^k + Q_{tf}^k (1 - f_{tf,b}^k)$	new volumetric flow, dense-phase
Step xiv:	$\dot{n}_b^{k+1} = \frac{p}{\mathcal{R}T} Q_b^k$	new mole flow, bubble-phase
Step xv:	$\dot{n}_e^{k+1} = \frac{p}{\mathcal{R}T} Q_e^k$	new mole flow, dense-phase
Step xvi:	$\dot{n}_{eb} = \dot{n}_{tot,e,i}^k - \dot{n}_{tot,e,i}^{k+1}$	corrective flow
Step xvii:	$\dot{n}_{eb,i} = \dot{n}_{eb} \frac{c_{e,i}^k}{\sum_i (c_{e,i}^k)}$	for $n_{eb} > 0$
Step xviii:	$\dot{n}_{eb,i} = \dot{n}_{eb} \frac{c_{b,i}^k}{\sum_i (c_{b,i}^k)}$	for $n_{eb} < 0$
Step xix:	$\dot{n}_{e,i}^{k+1} = \dot{n}_{e,i}^k - \dot{n}_{eb,i}$	new mole flow vector, dense-phase
Step xx:	$\dot{n}_{b,i}^{k+1} = \dot{n}_{b,i}^k + \dot{n}_{eb,i}$	new mole flow vector, bubble-phase

Table 3.5: Split for excess gas.

lower contents of devolatilization products.

	Equation	Remark	White Fir	Pine	Douglas Fir
x_1	$= \frac{n_{CO_2}}{n_{CO}}$	used: $x_1 = 1.35$	0.82	3.05	0.42
x_2	$= \frac{n_{CH_4}}{n_{CO}}$	used: $x_2 = 1.1$	0.07	0.67	1.18
m_{waf}	$= m_w(1 - w_{wt} - w_{ash})$				
n_i	$= w_i \frac{m_{waf}}{M_i}$	$i = H, O$			
n_C	$= w_C \frac{m_{waf}}{M_C} - m_{waf} \frac{1-w_{VM}}{M_C}$	for carbon			
n_C	$= (1 + x_1 + x_2)n_{CO}$				
n_H	$= 4x_2n_{CO} + 2n_{H_2} + 2n_{H_2O}$				
n_O	$= (1 + x_1)n_{CO} + n_{H_2O}$				

Table 3.6: Equations used for the calculation of the devolatilization composition. The system of equations is complete. The computation of the composition of the devolatilization product is straight forward. The values and references are taken from Reed [Reed 1981]. The ratios scatter in a very large scale. Higher hydrocarbons are lumped into the methane fraction.

White Fir: fast heating [Brink 1978]; Douglas Fir: fast heating [Hileman et al. 1976]; Pine: slow heating [Knight 1976]

The following procedure allows to compute the devolatilization composition by using material balances, measurement results and a few assumptions concerning the composition. The composition of the devolatilization products is computed based on the elementary analysis (refer to Table 3.14), the content of volatile matter (refer to Table 3.15) and a set of species, which is expected to be released by the devolatilization step. The elementary composition is reduced to the three elements C, H and O. The composition of volatile matter includes only CO, CO₂, CH₄, H₂ and H₂O. The higher hydrocarbons are lumped into the methane fraction. Since the elementary composition and the amount of volatile matter fix three degrees of freedom for the elements in the devolatilization products, the two remaining degrees of freedom are fixed by the ratios n_{CO_2}/n_{CO} and n_{CH_4}/n_{CO} . So, the system of equations for the five species for the composition of the devolatilization product is determined. Table 3.6 lists the equations used for this calculation. A summary of the idealizations used for the devolatilization step is provided below. The results for the calculation with $x_1 = 1.35$ and $x_2 = 1.1$ are presented in Table 3.13. Since the ratios x_1 and x_2 scatter in a very large scale, the values used for simulation are chosen somewhere in the range presented in Table 3.6 in order to get reasonable values for the hydrogen and water content as well. The dependency of the composition of the gases released by devolatilization on x_1 and x_2 is traced in Fig. 3.4 to Fig. 3.8.

- The elementary composition of the combustible part of wood is just hydrogen, carbon and oxygen.

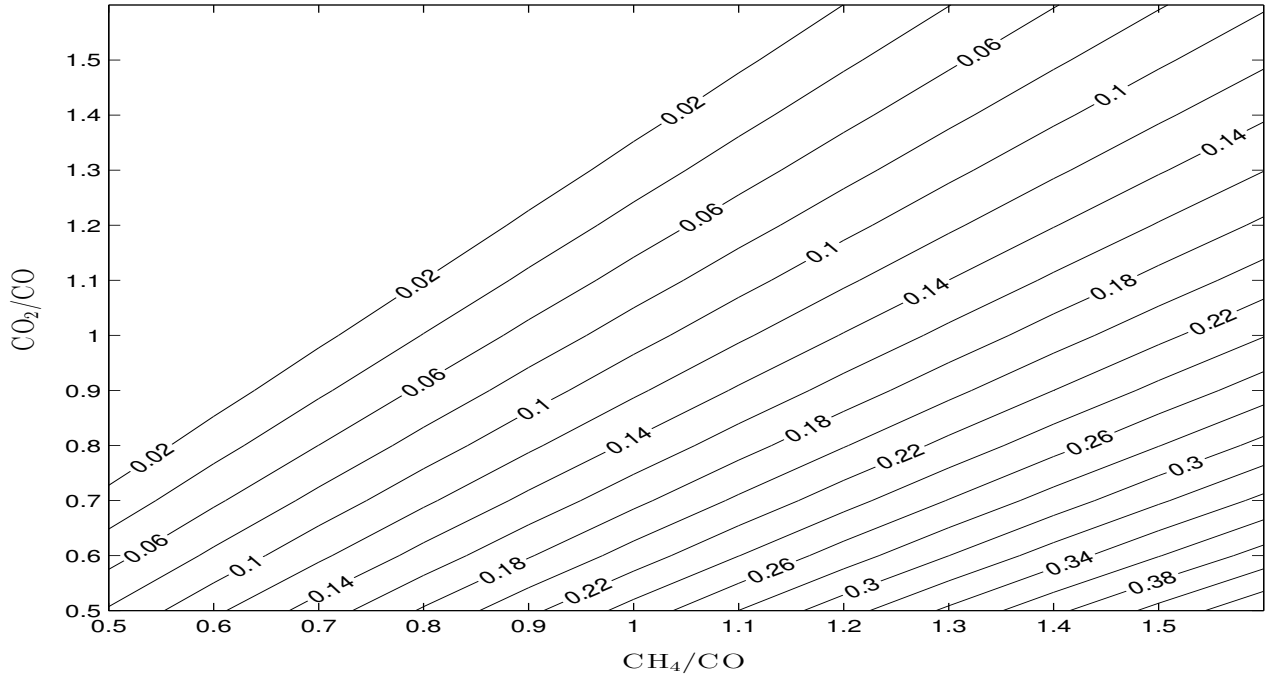


Figure 3.4: H_2O volume fraction of the gases released by devolatilization. With a fixed ratio of either $n_{\text{CO}_2}/n_{\text{CO}}$ or $n_{\text{CH}_4}/n_{\text{CO}}$ the H_2O content can be adjusted by the variation of the other.

- The devolatilization of the wood is complete before gasification onset. Hence, the residual char consists entirely of carbon and ash. Therefore, no element but carbon is transported into the riser for combustion.
- The ash is inert.
- The gases released by devolatilization consist only of CO , CO_2 , CH_4 , H_2 and H_2O .
- Methane, tar and higher hydrocarbons are lumped into the methane fraction. The carbon content is held constant in this procedure. For the chemical reactions Eq. 2.48, Eq. 2.49, and Eq. 2.52 this fraction is treated as if it consisted just of methane.
- The devolatilization composition can be computed by using the equations listed in Table 3.6.

Figures 3.4 to 3.8 show the composition of volatile matter. On the abscissa, the $x_2 = n_{\text{CH}_4}/n_{\text{CO}}$ ratio and on the ordinate the $x_1 = n_{\text{CO}_2}/n_{\text{CO}}$ ratio is plotted.

3.4.3 Gasification

Equilibrium Constants

The thermochemical equilibrium constants are computed using the thermodynamic data for formation entropy at operation temperature $S_{f^*,T}$, formation enthalpy at operation tem-

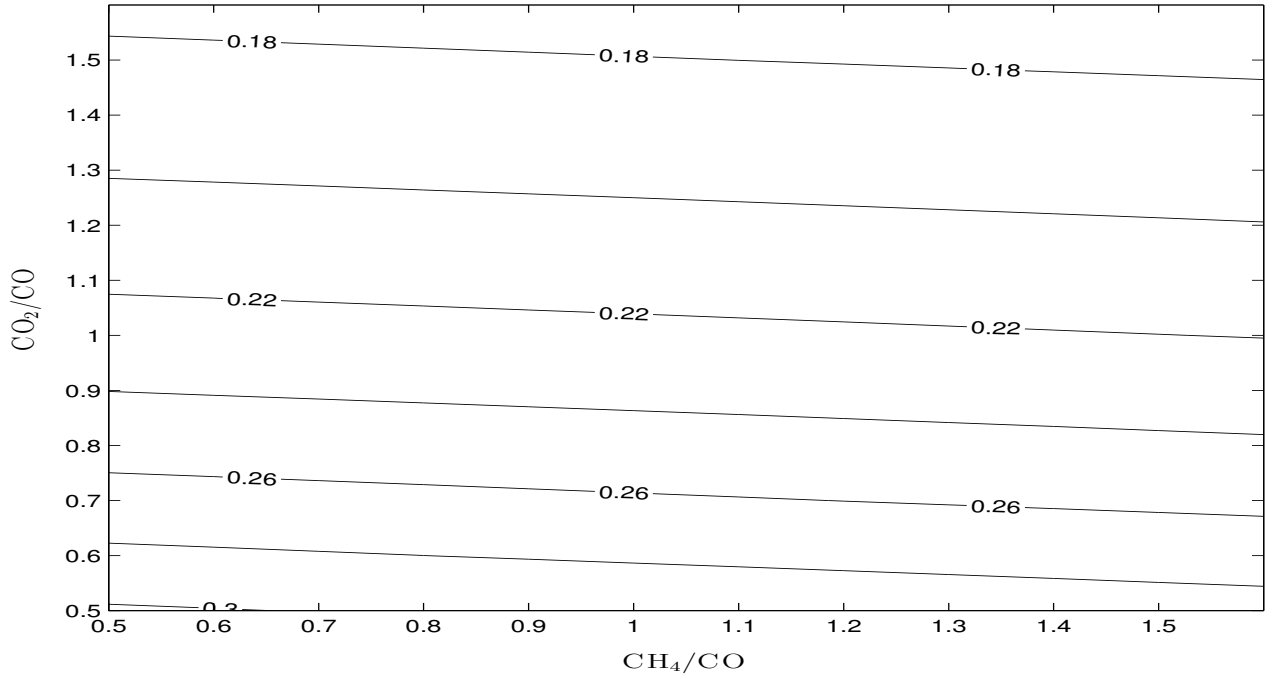


Figure 3.5: CO volume fraction of the gases released by devolatilization. With a fixed ratio of $n_{\text{CH}_4}/n_{\text{CO}}$ the CO content can be adjusted by the variation of the ratio $n_{\text{CO}_2}/n_{\text{CO}}$. This is hardly possible the other way round since the CO volume fraction does not change significantly on a variation of $n_{\text{CH}_4}/n_{\text{CO}}$.

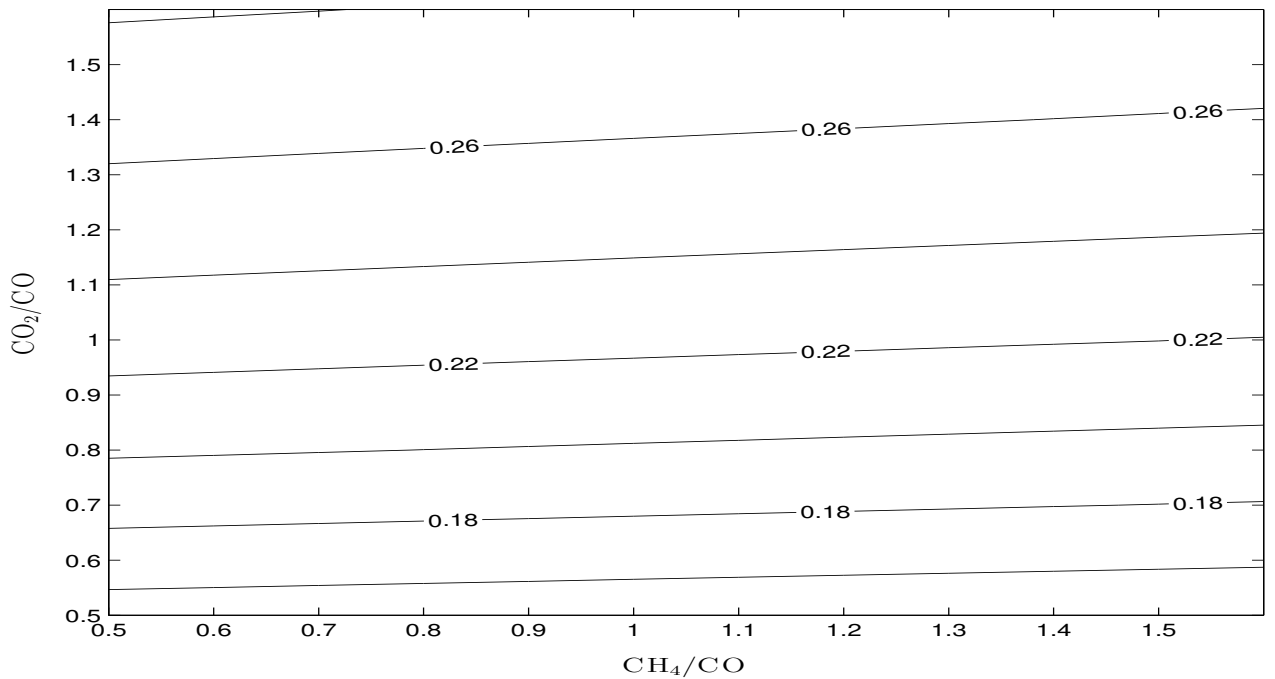


Figure 3.6: CO₂ volume fraction of the gases released by devolatilization. Similarly to Fig. 3.5, presuming a fixed ratio of $n_{\text{CH}_4}/n_{\text{CO}}$ the CO₂ content can be adjusted by the variation of the ratio $n_{\text{CO}_2}/n_{\text{CO}}$. This is hardly possible the other way round since the CO₂ volume fraction does not change significantly on a variation of $n_{\text{CH}_4}/n_{\text{CO}}$.

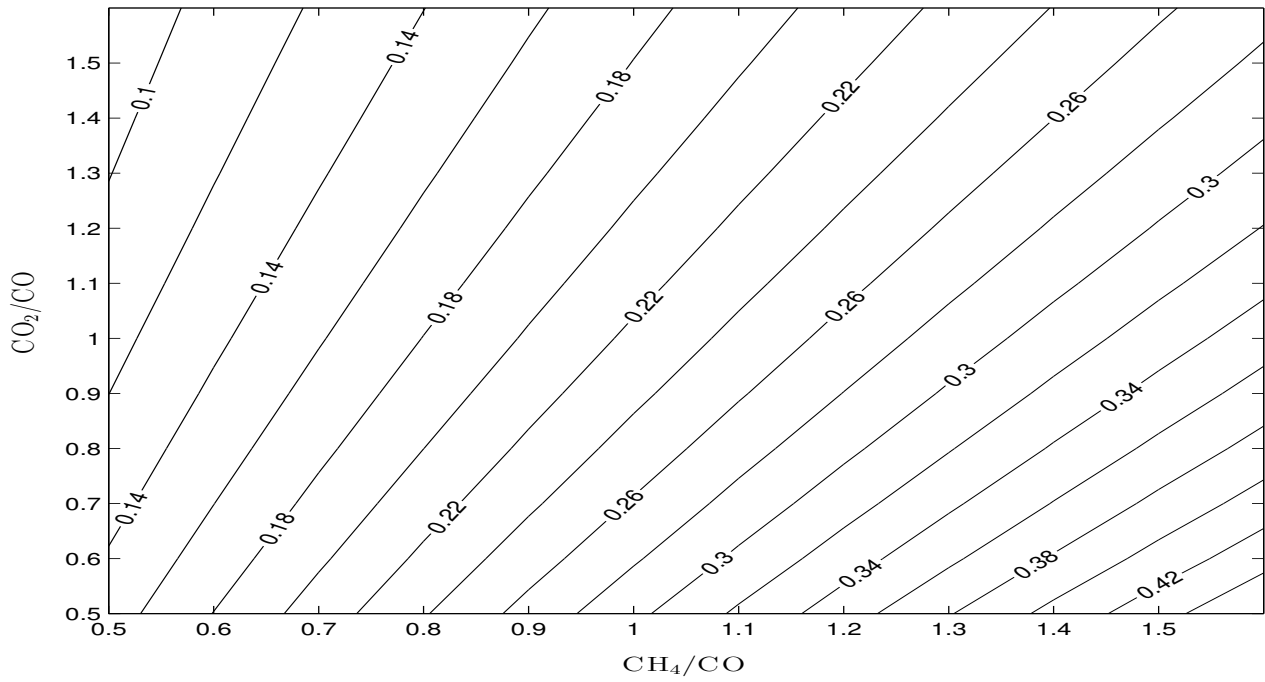


Figure 3.7: CH_4 volume fraction of the gases released by devolatilization. Persuming a fixed ratio of either $n_{\text{CO}_2}/n_{\text{CO}}$ or $n_{\text{CH}_4}/n_{\text{CO}}$ the CH_4 content can be adjusted by variation of the other.

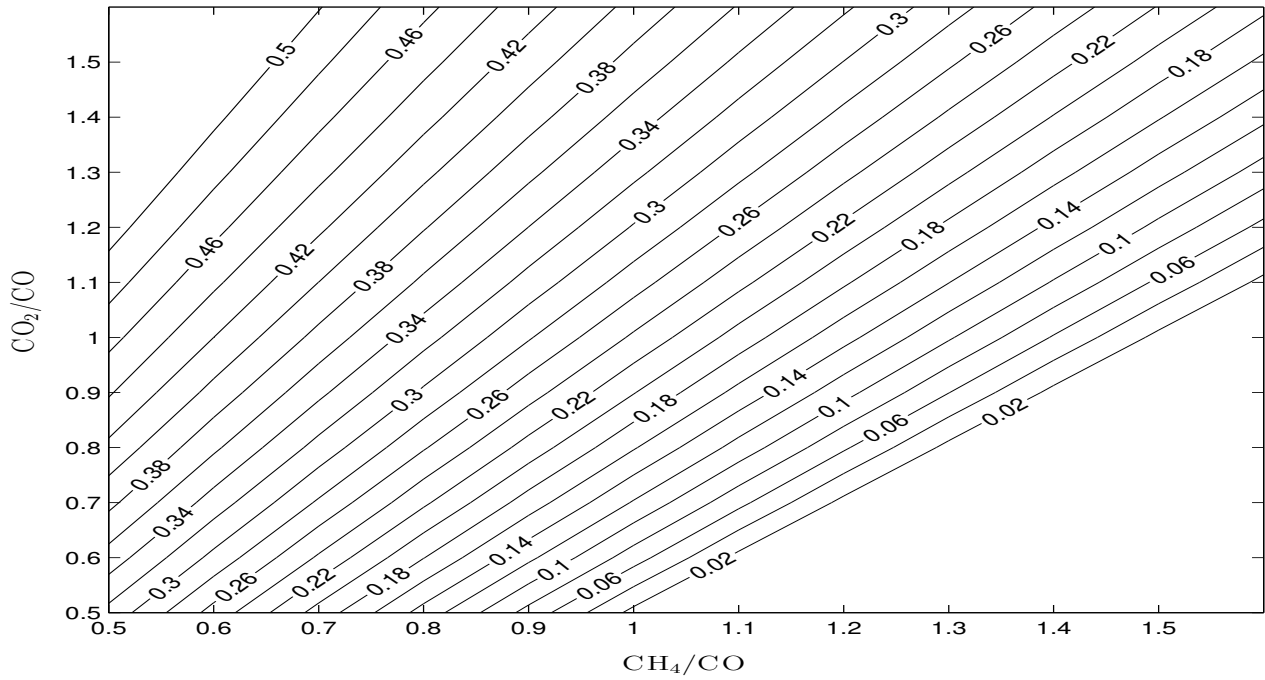


Figure 3.8: H_2 volume fraction of the gases released by devolatilization. With a fixed ratio of either $n_{\text{CO}_2}/n_{\text{CO}}$ or $n_{\text{CH}_4}/n_{\text{CO}}$ the H_2 content can be adjusted by variation of the other.

perature $H_{f*,T}$. The equations for this computation are presented in Table 3.7 and the coefficients in Table 3.8. Thermochemical properties can be found in form of the NASA polynomials in the Chemkin Thermodynamic Database [Kee et al. 1993]. One main source for thermodynamical properties state the JANAF tables [Stull and Prohet 1971].

Frequency Factors and Activation Energy

For the model, different kinetic equations are used. For the gasification reaction with steam and carbon dioxide, as well as for the water-gas-shift reactions (homogeneous and heterogeneous), a n^{th} -order equation is used. The usage of the n^{th} -order equation for the gasification reactions are justified by the faster computer code compared to a hyperbolic function.

The water-gas-reaction, both, the homogeneous and the heterogeneous are measured by Weimer et al. [Weimer and Clough 1981]. The minimum fluidization porosity appearing in the heterogeneous equation is used to account for the gas mass displaced by the solid fraction in the dense phase.

For the hydrogasification and the methane decomposition, a Langmuir-Hinselwood mechanism is chosen. If the coefficients in the denominator of the latter are interpreted as adsorption constants, which is already an assumption on the reaction mechanism (refer to chapter 2.2.4), these should satisfy some conditions which are characteristic for adsorption constants. For example, the adsorption constants should be independent of pressure, origin, porosity, crystallinity and particle size of the carbon but they should depend on temperature. A few authors [Barrio and Hustad 2000, Barrio et al. 2000, Wang and Kinoshita 1993, Reed 1981] provide a Langmuir-Hinselwood model. However, the temperature dependency is frequently lumped into the temperature dependency frequency factor of the rate constant [Wang and Kinoshita 1993]. An exception constitute the rate equations provided by Barrio et. al. [Barrio et al. 2000] and Barrio and Hustad [Barrio and Hustad 2000].

Wang and Kinoshita [Wang and Kinoshita 1993] fix the adsorption constants due to insufficient information on temperature dependence. For the hydrogasification reaction and the methane decomposition reaction, their reaction kinetics is used in this model. Still, they did a parameter fitting to their measurement data in order to obtain the rate equations. However, it was the only source, which provided data for a wood char hydrogasification reaction and the char catalyzed methane decomposition.

The idealizations made for the chemical reaction system are listed below

- No catalytic activity of char accompanying substances.
- In the devolatilization step, the higher hydrocarbons are lumped into the methane fraction. This fraction is considered to be methane for the chemical reactions Eq. 2.52, Eq. 2.49, and Eq. 2.48. However, it has to be kept in mind, that it is C_xH_y rather than CH_4 .
- Calculation of the *energy balance* just in freeboard but fixed temperature in bed.

$$(3.9): H_{f^*,T,i} = (\bar{C}_{1,i} + \frac{\bar{C}_{2,i}}{2}T + \frac{\bar{C}_{3,i}}{3}T^2 + \frac{\bar{C}_{4,i}}{4}T^3 + \frac{\bar{C}_{5,i}}{5}T^4 + \frac{\bar{C}_{6,i}}{T})T\mathcal{R}$$

$$(3.10): S_{f^*,T,i} = (\bar{C}_{1,i} \log_{10}(T) + \bar{C}_{2,i}T + \frac{\bar{C}_{3,i}}{2}T^2 + \frac{\bar{C}_{4,i}}{3}T^3 + \frac{\bar{C}_{5,i}}{4}T^4 + \bar{C}_{7,i})\mathcal{R}$$

$$(3.11): \Delta S_{f^*,T,j} = \sum_i (\bar{\nu}_{i,j} S_{f^*,T,j})$$

$$(3.12): \Delta H_{f^*,T,j} = \sum_i (\bar{\nu}_{i,j} H_{f^*,T,j})$$

$$(3.13): k_{therm,j}^e = \exp(\frac{\Delta S_{f^*,T,j}}{\mathcal{R}} - \frac{\Delta H_{f^*,T,j}}{\mathcal{R}T})$$

$$(3.14): k_{c,j}^e = k_{therm,j}^e \left(\frac{p}{\mathcal{R}T}\right)^{\Delta_g n}$$

$$(3.15): k_{pp,j}^e = k_{therm,j}^e p^{\Delta_g n}$$

Table 3.7: Equations for chemical equilibrium of Eq. j with participating species i . $\Delta_g n$ is the mole change of gaseous species in a chemical reaction. For the coefficients \bar{C}_1 to \bar{C}_7 , refer to Table 3.8.

	Species			
	C	CO	CO ₂	CH ₄
\bar{C}_1	$0.01490166 \cdot 10^2$	$0.03025078 \cdot 10^2$	$0.04453623 \cdot 10^2$	$0.01683479 \cdot 10^2$
\bar{C}_2	$0.01662126 \cdot 10^{-1}$	$0.01442689 \cdot 10^{-1}$	$0.03140169 \cdot 10^{-1}$	0.01023724
\bar{C}_3	$-0.06687204 \cdot 10^{-5}$	$-0.05630828 \cdot 10^{-5}$	$-0.01278411 \cdot 10^{-4}$	$-0.03875129 \cdot 10^{-4}$
\bar{C}_4	$0.01290880 \cdot 10^{-8}$	$0.01018581 \cdot 10^{-8}$	$0.02393997 \cdot 10^{-8}$	$0.06785585 \cdot 10^{-8}$
\bar{C}_5	$-0.09205334 \cdot 10^{-13}$	$-0.06910952 \cdot 10^{-13}$	$-0.01669033 \cdot 10^{-12}$	$-0.04503423 \cdot 10^{-12}$
\bar{C}_6	$0.07074019 \cdot 10^4$	$-0.01426835 \cdot 10^6$	$-0.04896696 \cdot 10^6$	$-0.01008079 \cdot 10^6$
\bar{C}_7	$-0.08717785 \cdot 10^2$	$0.06108218 \cdot 10^2$	$-0.09553959 \cdot 10^1$	$0.09623395 \cdot 10^2$
	H ₂	H ₂ O	O ₂	N ₂
\bar{C}_1	$0.02991423 \cdot 10^2$	$0.02672146 \cdot 10^2$	$0.03697578 \cdot 10^2$	$0.02926640 \cdot 10^2$
\bar{C}_2	$0.07000644 \cdot 10^{-2}$	$0.03056293 \cdot 10^{-1}$	$0.06135197 \cdot 10^{-2}$	$0.01487977 \cdot 10^{-1}$
\bar{C}_3	$-0.05633829 \cdot 10^{-6}$	$-0.08730260 \cdot 10^{-5}$	$-0.01258842 \cdot 10^{-5}$	$-0.05684761 \cdot 10^{-5}$
\bar{C}_4	$-0.09231578 \cdot 10^{-10}$	$0.01200996 \cdot 10^{-8}$	$0.01775281 \cdot 10^{-9}$	$0.01009704 \cdot 10^{-8}$
\bar{C}_5	$0.01582752 \cdot 10^{-13}$	$-0.06391618 \cdot 10^{-13}$	$-0.01136435 \cdot 10^{-13}$	$-0.06753351 \cdot 10^{-13}$
\bar{C}_6	$-0.08350340 \cdot 10^4$	$-0.02989921 \cdot 10^6$	$-0.01233930 \cdot 10^5$	$-0.09227977 \cdot 10^4$
\bar{C}_7	$-0.01355110 \cdot 10^2$	$0.06862817 \cdot 10^2$	$0.03189166 \cdot 10^2$	$0.05980528 \cdot 10^2$

Table 3.8: Coefficients for chemical equilibrium calculation (refer to Table 3.7).

Reaction	Frequency Factor k_0	Activation Energy E_a in J/mol	Power n	Structure	Remarks	Reference
(3.16): $C + CO_2 \xrightarrow{k_{fwd}} 2CO$	$3.1 \cdot 10^6 \frac{1}{bar^{0.38}s}$	215000	0.38	$\frac{\bar{v}_i}{m_C} \frac{dm_C}{dt} = kp_{CO_2}^n$	Birch, fw.	[Barrio and Hustad 2000]
(3.17): $C + H_2O \xrightarrow{k_{fwd}} H_2 + CO$	$2.62 \cdot 10^8 \frac{1}{bar^{0.57}s}$	237000	0.57	$\frac{\bar{v}_i}{m_C} \frac{dm_C}{dt} = kp_{H_2O}^n$	Birch, fw.	[Barrio et al. 2000]
(3.18): $CO + H_2O \xrightarrow{k_{fwd}} H_2 + CO_2$	$2.978 \cdot 10^9 \frac{m^3}{mol s}$	369000		$\bar{v}_i \frac{dc}{dt} = kc_{CO} c_{H_2O}$	non-cat., fw.	[Weimer and Clough 1981]
(3.19): $H_2 + CO_2 \xrightarrow{k_{fwd}} CO + H_2O$	$7.245 \cdot 10^{11} \frac{m^3}{mol s}$	398300		$\bar{v}_i \frac{dc}{dt} = kc_{H_2} c_{CO_2}$	non-cat., fw.	[Weimer and Clough 1981]
(3.20): $CO + H_2O \xrightarrow{k_{fwd}} H_2 + CO_2$	$0.03 \cdot \varepsilon_{mf} \frac{m^3}{mol s}$	60270		$\bar{v}_i \frac{dc}{dt} = kc_{CO} c_{H_2O}$	cat., fw.	[Weimer and Clough 1981]
(3.21): $H_2 + CO_2 \xrightarrow{k_{fwd}} CO + H_2O$	$1.362 \cdot \varepsilon_{mf} \frac{m^3}{mol s}$	94920		$\bar{v}_i \frac{dc}{dt} = kc_{H_2} c_{CO_2}$	cat., fw.	[Weimer and Clough 1981]
(3.22): $C + 2H_2 \xrightleftharpoons[k_{fwd}]{k_{fwd}} CH_4$	$4.189 \cdot 10^{-3} \frac{1}{s}$	19210		$\frac{\bar{v}_i}{n_C} \frac{dn}{dt} = k \frac{p_{H_2}^2 - \frac{p_{CH_4}}{k^e}}{denom}$	Lm.-Hw., fw.+bw.	[Wang and Kinoshita 1993]
(3.23): $CH_4 + H_2O \xrightleftharpoons[k_{fwd}]{k_{fwd}} CO + 3H_2$	$7.301 \cdot 10^{-2} \frac{1}{s}$	36150		$\frac{\bar{v}_i}{n_C} \frac{dn}{dt} = k \frac{p_{CH_4} p_{H_2O} - \frac{p_{CO} p_{H_2}^3}{k^e}}{denom}$	Lm.-Hw., fw.+bw.	[Wang and Kinoshita 1993]

cat.: Kinetic data for the catalyzed water-gas-shift reaction in the interstitial gas; non-cat.: Kinetic data for the non-catalyzed water-gas-shift reaction in the dilute phase; Lm.-Hw.: Langmuir-Hinselwood kinetics. Adsorption constants see Table 3.10; fw.: Forward reaction only; fw.+bw.: Forward- and backward reaction (computed by chemical equilibrium) $denom = 1 + (K_{pb,H_2} p_{pb,H_2} + K_{pb,CO} p_{CO} + K_{pb,CO_2} p_{CO_2} + K_{pb,H_2O} p_{H_2O} + K_{pb,CH_4} p_{CH_4})$ (pressure in bar); refer to Table 3.10 for the adsorption equilibrium constants K_{pb} ; $k = k_0 \exp(\frac{-E_a}{RT})$

Table 3.9: Summary of the used chemical kinetic equations.

Species	H ₂	CO	H ₂ O	CO ₂	CH ₄
Adsorption equilibrium constant K_{pb} in bar^{-1}	32.57	23.06	2.507	2.309	unknown and fixed to 0.0

Table 3.10: Summary of the used adsorption constants at according Reed [Reed 1981]. The temperature dependency is neglected since the equation is fitted to gasification results by Wang et al. [Wang and Kinoshita 1993].

3.5 Choice of a Suitable Particle Model

3.5.1 Implementation of the Particle Model in the Simulation

A particle model permits to compute the concentration profile of the species from the ambient gaseous atmosphere to the center of the particle. It considers the chemical reaction as well as the external and internal mass-transfer. Since the reaction kinetics is strongly temperature dependent, it is necessary for the modeling of chemical systems including reactions with high reaction enthalpy, to consider also the thermal balance (refer to discussion below).

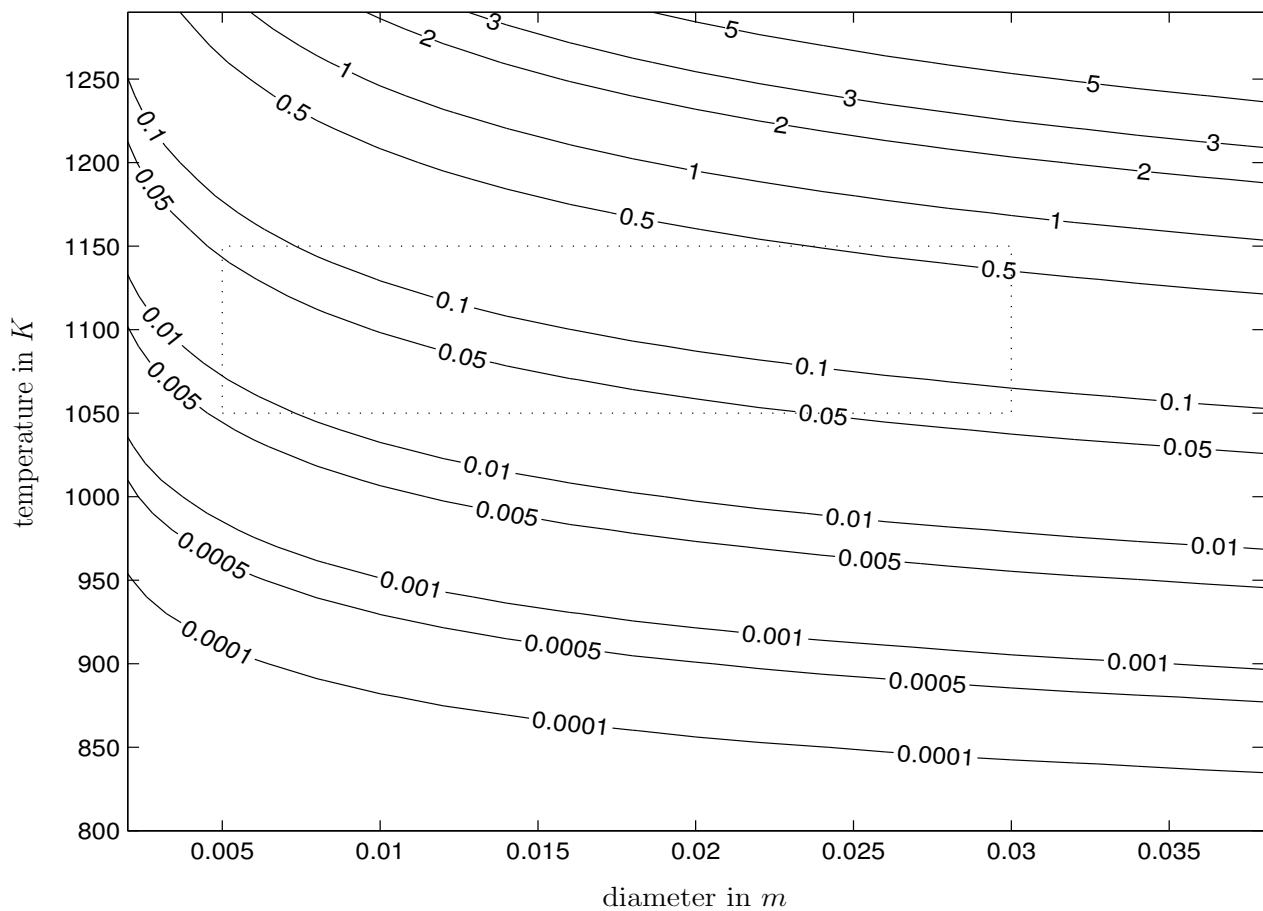


Figure 3.9: The dependency of the *Damköhler Number* Da_{II} on the particle temperature T_p and the particle diameter d_p for steam gasification. The marked area shows the region relevant to the large particles used for this process. The Da_{II} shows small to intermediate values in the interesting range. This indicates a low to a moderate mass-transfer limitation.

To get an image of the external and the internal mass-transfer limitations of the chemical system of the gasifier the steam gasification reaction (Eq. 3.17) in a 100% steam environment and different particle diameters and temperatures is plotted in Fig. 3.9, 3.10 and 3.11. The Sherwood Number has been taken from the Table 3.3 for emulsion conditions. The

Damköhler Number indicates a very low external mass-transfer limitation and for the used particle geometries. Fig. 3.10 and Fig. 3.11 show largely insignificant internal diffusion limitation. For the calculation here, it is assumed that the porous char consists of carbon, only.

$$DaII_{H_2O} = \frac{\rho_{ch} w_C d_{p,A}^2}{6M_C Sh_{A,H_2O} D_{H_2O}} \frac{2.62 \cdot 10^8 \exp \frac{-237000}{RT} p_{H_2O}^{0.57}}{\frac{p_{H_2O}}{RT}}$$

For the computation of the Thiele Modulus, the absence of external mass-transfer limitations is assumed. Hence, for steam, the partial pressure on the particle surface equals the ambient partial pressure.

$$\phi_{H_2O} = \frac{d_{p,A}}{6} \sqrt{\frac{1.57 \cdot 2.62 \cdot 10^8 \exp \frac{-237000}{RT} p_{H_2O}^{0.57} \rho_{ch}}{2 D_{e,H_2O} M_C \frac{p_{H_2O}}{RT}}}$$

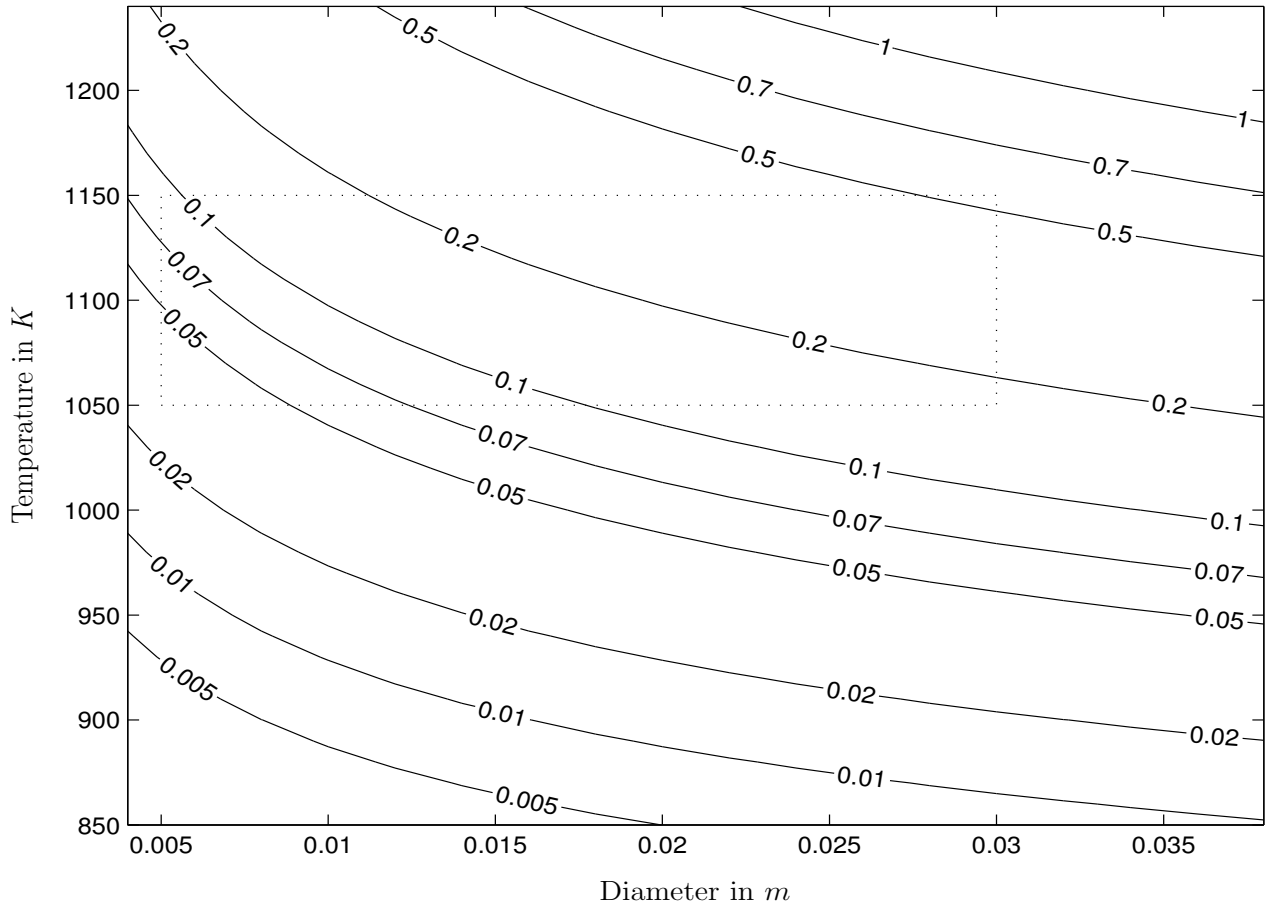


Figure 3.10: The dependency of the *Thiele Module* ϕ on particle temperature T_p and particle diameter d_p for steam gasification. The marked area shows the region relevant to the large particles used for this process.

For the modeling of the internal and external mass-transfer limitation of a particle in the program, the following procedure have been chosen. To compute the surface concentration the reaction rate is equated with the external mass-transfer rate.

$$\frac{Sh_i D_i}{d_p} d_p^2 \pi (c_{i,\infty} - c_{i,s}) = \frac{\bar{v}_i \rho_{Ch} w_C d_p^3 \pi}{6 M_C} r_C(c_{i,s}, T) \quad (3.24)$$

Where i stands for each reacting specie ($i = \text{CO}, \text{CO}_2, \text{CH}_4, \text{H}_2, \text{H}_2\text{O}$). The considered reactions for this equation system are the steam gasification reaction (Eq. 3.17), the carbon dioxide gasification reaction (Eq. 3.16) and the hydrogasification reaction (Eq. 3.22). Homogeneous reactions have not been taken into account in the boundary layer and within the particle. The mass-transfer rate is calculated with the Sherwood Number according to Table 3.3. The solution of this system gives the surface concentration on a particle without

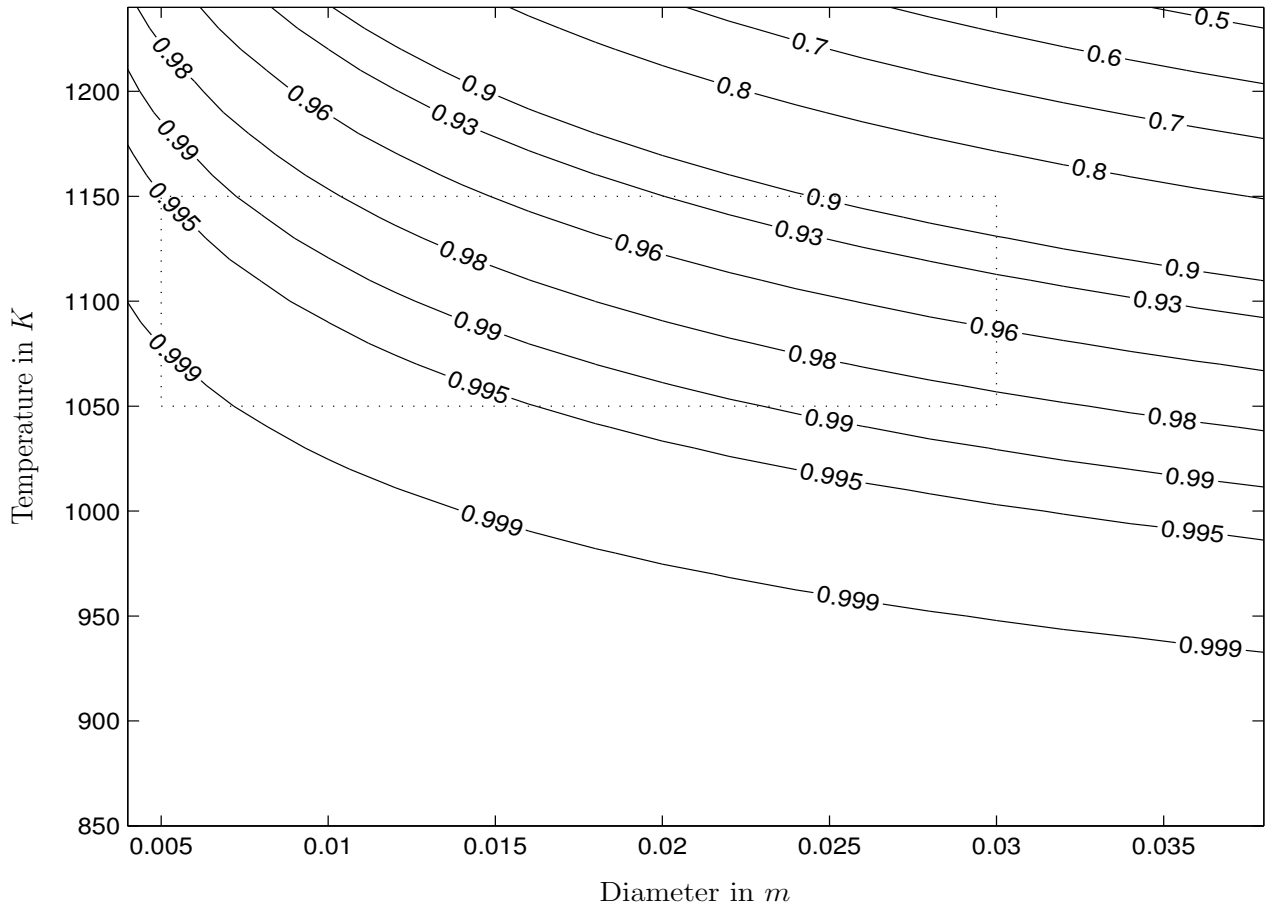


Figure 3.11: The dependency of the *effectiveness factor* η_{int} (refer to 2.86) on the particle temperature T_p and the particle diameter d_p for steam gasification. The marked area shows the region relevant to the large particles used for this process. Hence, η_{int} is in the range of 0.9–1 which is in fact equivalent to the absence of internal mass-transfer limitations.

consideration of the internal mass-transfer limitation which previously has been shown to be low. To compute the reaction rate rather this surface concentration than the bed concentration is used. The internal mass-transfer limitations are taken into consideration by multiplying the reaction rate by the effectiveness factor, which is about 0.9–1.0 (refer to Fig. 3.11).

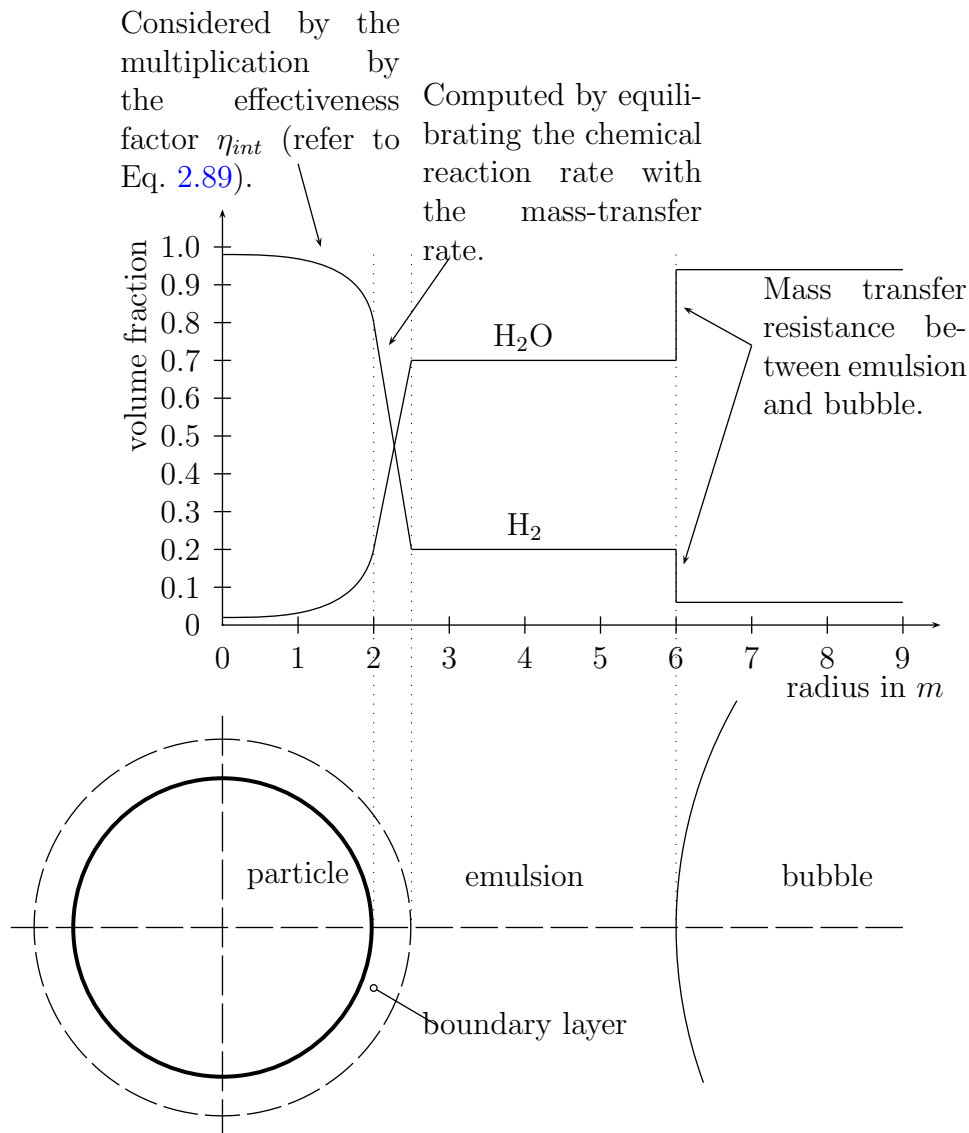


Figure 3.12: Qualitative concentration profile for the example of H₂O and H₂ from the bubble through the emulsion, the boundary layer to the center of the particle. The particle temperature is assumed to stay constant at ambient temperature.

The diameter used for this calculation is $0.0133m$. It is the representative diameter for the complete consumption of the particle (refer to discussion below). The problem of this approach consists of the neglect of the gas formation in the particle. The simple equation of the reaction rate with the mass-transfer rate without consideration of the convective mass-transfer due to gas formation results formally into a higher pressure in the particle than the ambient pressure. The result of the overestimation of the partial pressures of the participating gases is a shift of the chemical equilibrium. This leads to a

distortion of the reaction rates of the gasification reactions in an intricate way especially if the backward reaction is computed by using the chemical equilibrium. Nevertheless, this modeling is applied because it is a compromise between an exact solution and the computing capacity. An exact study of the error committed may be the subject of further investigations. The idealizations made for the particle model are as follows

- Unique representative particle diameter.
- The *mass-transfer resistance* between particle and emulsion phase is taken into account just for *gasification reactions* but not for char catalyzed reactions.
- No heat-transfer limitation to the particle. Possible limitations are considered in the effectiveness factor.

3.5.2 Particle Model with Consideration of the Heat-Transfer Limitations

The aim of this investigation is to achieve effectiveness numbers taking into account for the thermal situation as well. Further, to quantify the relative influence of mass-transfer limitations and heat-transfer limitations. Third, a representative particle diameter for the calculation of the surface concentration is fixed.

As already seen in previous discussion, the Thiele Modulus, which is a measure for the internal mass-transfer resistance is nearly independent of the temperature for the circumstances considered here. The value evaluated for this system is nearly unity, which justifies the neglect of internal mass-transfer limitations. Effectiveness numbers, which account for the thermal balance as well, demand for iteration. Further, they are just applicable to a single n^{th} -order reaction (refer to [Froment and Bischoff 1990]). Therefore, the determination of such effectiveness numbers has been renounced in this work.

Nevertheless, a detailed investigation of the thermal influence has been undertaken. For this purpose, a system of two chemical reactions (Eq. 3.17 and Eq. 3.16) interacting with the external mass-, and heat-transfer is solved. Transfer terms are modeled with Sherwood and Nusselt correlations (refer to Table 2.1).

According to the previously discussed particle models, the change of particle properties (diameter, carbon concentration, porosity etc.) due to carbon consumption can be modeled in one of the following way:

1. Reduction of the particle diameter with constant initial carbon concentration within the particle during the whole conversion.
2. Reduction of the carbon concentration within the particle and constant particle diameter during the whole conversion.
3. Solving the mass- and heat-transport equations resulting in a continuous consumption distribution of carbon within the particle.

In the *first approach* presented here, the *whole* particle is involved in reaction. This is justified by the high internal effectiveness numbers η_{int} of about unity. Hence, it is a modification of the case of the shrinking particle model presented in chapter 3.5.1. There, just a surface proportional part, which corresponds to a thin surface layer, participates on chemical

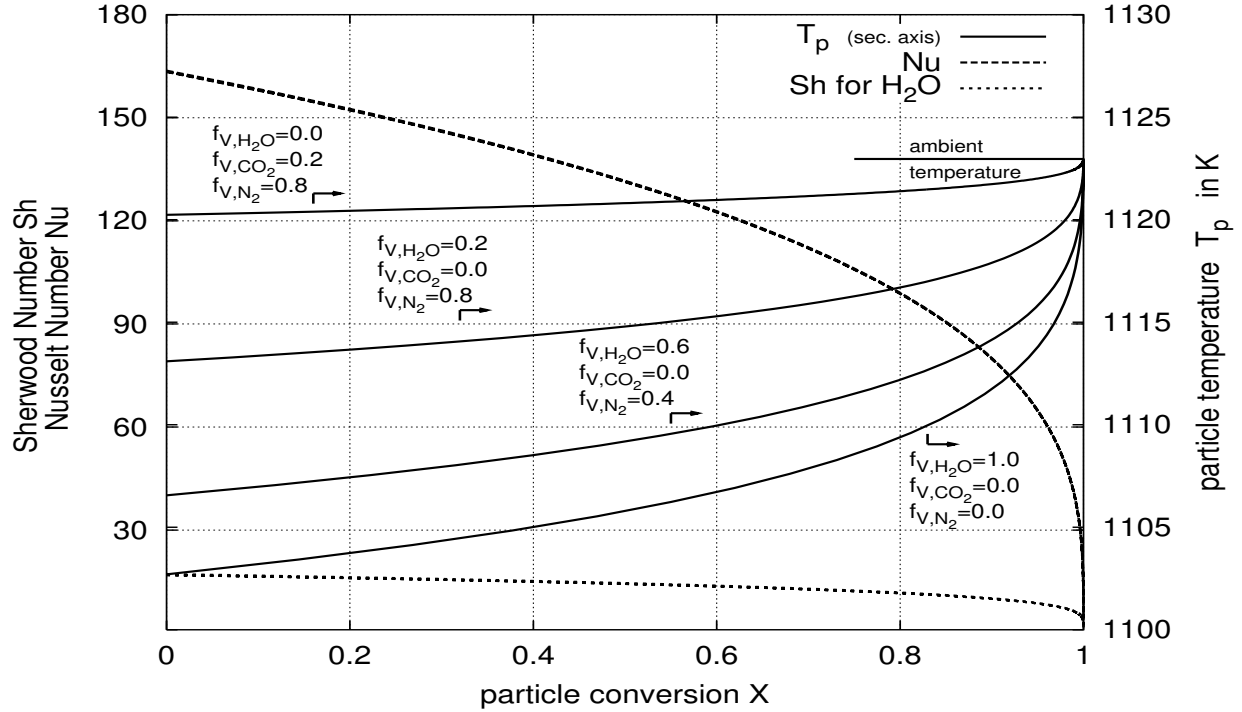


Figure 3.13: Sherwood Number Sh , Nusselt Number Nu on the primary axes and particle temperatures T_p on the secondary axes vs. the conversion X . Remarkable is the Nusselt Number, which exceeds the Sherwood Number about eight times. As expected, the carbon dioxide gasification reduces the temperature least of all. This is due to the lower reaction rate and the lower heat of reaction for the carbon dioxide gasification.

reaction. However, according to it, the consumed carbon is lumped into a thin surface layer which is contradictory to the over the whole particle occurring reaction. This approach eases computation for a model, which takes into account for a decreasing diameter. Allowing for a decreasing diameter was the primary objective in this approach since a shrinking particle includes several side effects going hand in hand with this diameter reduction. The Sherwood and the Nusselt Number decrease for example with a shrinking diameter as well. Further, the also decreasing particle volume decreases the total amount of carbon available for reaction and slows down the conversion rate. However, surface dependent mechanisms become decreasing influence on the overall reaction rate. Therefore, the particle temperature and the surface concentrations converge to the ambient conditions.

The *second approach* is a pure homogeneous particle model. Since the particle diameter does not change in this case, the Nusselt Number and the Sherwood Number do not change during the whole reaction, neither. These values correspond to the initial value of the first approach. Therefore, during the whole reaction period, the average mass- and heat-transfer limitations are *larger* than in the first approach. Solely the decreasing carbon concentra-

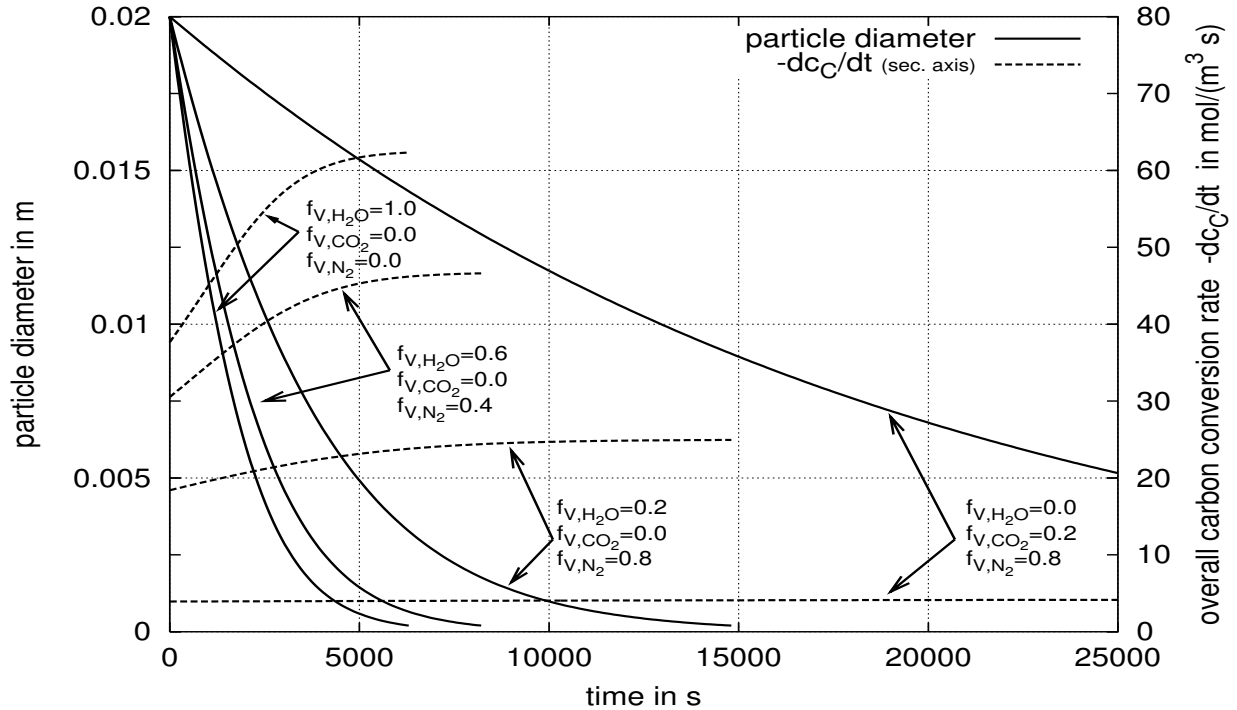


Figure 3.14: Carbon reaction rate and evolution of the particle diameter versus time. The slope of the carbon conversion rate is highest at the beginning of the conversion and the conversion rate is highest at the end of the conversion. The consumption of the particle is completed in the range of 5000–15000s for steam gasification. The carbon dioxide gasification needs many times more.

tion decreases the conversion rate of the carbon and therefore the difference to the ambient conditions of the species concentration and the particle temperature. So, surface limitations become decreasing influence on the overall reaction rate not because of the disappearance of the external heat and mass-transfer resistance factors but due to the increasing participation of the limitations of the chemical reaction rate on the overall reaction rate. However, this case is not presented here since an idea of the result can be acquired on regarding the beginning of gasification in the first case. There, the particle diameter is still about the initial value at the first percents of conversion. In the second approach, the external rate limitations dominate until the chemical reaction rate slows down significantly due to the decreasing carbon concentration. But at this point, the major part of the carbon will already be consumed. Hence, the external limitations dominate nearly the whole reaction.

The *third approach* is already a very minute modeling. It have to be considered the changing particle properties due to particle porosity changing (thermal conductivity, diffusivity, ...) as well as the gas volume formation. Contrary to the first two cases, these changing particle properties should not be neglected if the effort of this precise modeling is accepted. Since this quality of a particle model is not subject of this work, the modeling of

ρ_A	=	$300 \frac{kg}{m^3}$	$d_{A,0}$	=	$0.02m$	ν	=	$200 \cdot 10^{-6} \frac{m^2}{s}$
ρ_I	=	$2300 \frac{kg}{m^3}$	d_I	=	$0.38 \cdot 10^{-3}m$	ε_{mf}	=	0.4
ϵ_p	=	0.8	Ar_I	=	550	p_∞	=	$101325Pa$
c_{p,N_2}	=	$1.038 \frac{kJ}{kg K}$	$c_{p,CO}$	=	$1.110 \frac{kJ}{kg K}$	c_{p,CO_2}	=	$1.089 \frac{kJ}{kg K}$
c_{p,CH_4}	=	$1.200 \frac{kJ}{kg K}$	c_{p,H_2}	=	$1.464 \frac{kJ}{kg K}$	c_{p,H_2O}	=	$2.343 \frac{kJ}{kg K}$
λ_g	=	$0.1 \frac{W}{m K}$	λ_A	=	$80.0 \frac{W}{m K}$	T_∞	=	$1123K$

Table 3.11: Presumptions for the material properties for the particle model.

Parameter	1 st case	2 nd case	3 rd case	4 th case
$f_{V,H_2O,\infty}$	1.0	0.6	0.2	0.0
$f_{V,CO_2,\infty}$	0.0	0.0	0.0	0.2
$f_{V,N_2,\infty}$	0.0	0.4	0.8	0.8

Table 3.12: Volume fraction of the ambient gas used for the particle model.

the third approach is not further discussed.

The presumptions for the material properties used for the particle model are listed in Table 3.11. The ambient conditions used for computation are listed in Table 3.12. The Sherwood correlation, the Nusselt correlation, and the fluid dynamic equations are taken from Table 3.3. The particle diameter and the carbon reaction rate versus the time are plotted in Fig. 3.14. This gives a first image of the situation but more appropriate for practical use is the dependency on the particle conversion. Fig. 3.13 shows the Sherwood and the Nusselt Number over the conversion X . The Nusselt Number exceeds the Sherwood Number about eight times. The evolution of the particle diameter d_p (Fig. 3.15) shows a decreasing reaction rate with decreasing ambient concentrations of H_2O .

The evolution of the particle diameter for the carbon dioxide gasification suggests a four times slower reaction rate than for the steam gasification. Fig. 3.13 shows the evolution of the particle temperature T_p and the species volume fraction f_{V,H_2O} and f_{V,CO_2} in the particle versus the conversion X . The initially over a wide range nearly constant surface conditions converge suddenly at the last stages of conversion towards ambient conditions. This is a result of the transition of the dominant mechanisms from surface proportional to volume proportional for small particles. Using Fig. 3.15, a representative diameter for the computation of the surface concentration can be estimated. Similarly to the reaction kinetics, the average overall carbon conversion rate between $X_1 = 0.2$ and $X_2 = 0.8$ (refer to [Barrio and Hustad 2000, Barrio et al. 2000]) is used as representative conversion rate.

$$\overline{\frac{dc_C}{dt}} = \frac{1}{X_H - X_L} \int_{X_L=0.2}^{X_H=0.8} \frac{\partial c_C}{\partial t} dX \quad (3.25)$$

The value of the particle diameter corresponding to the conversion rate which equals the average conversion rate is used for the representative diameter. For a correct integration

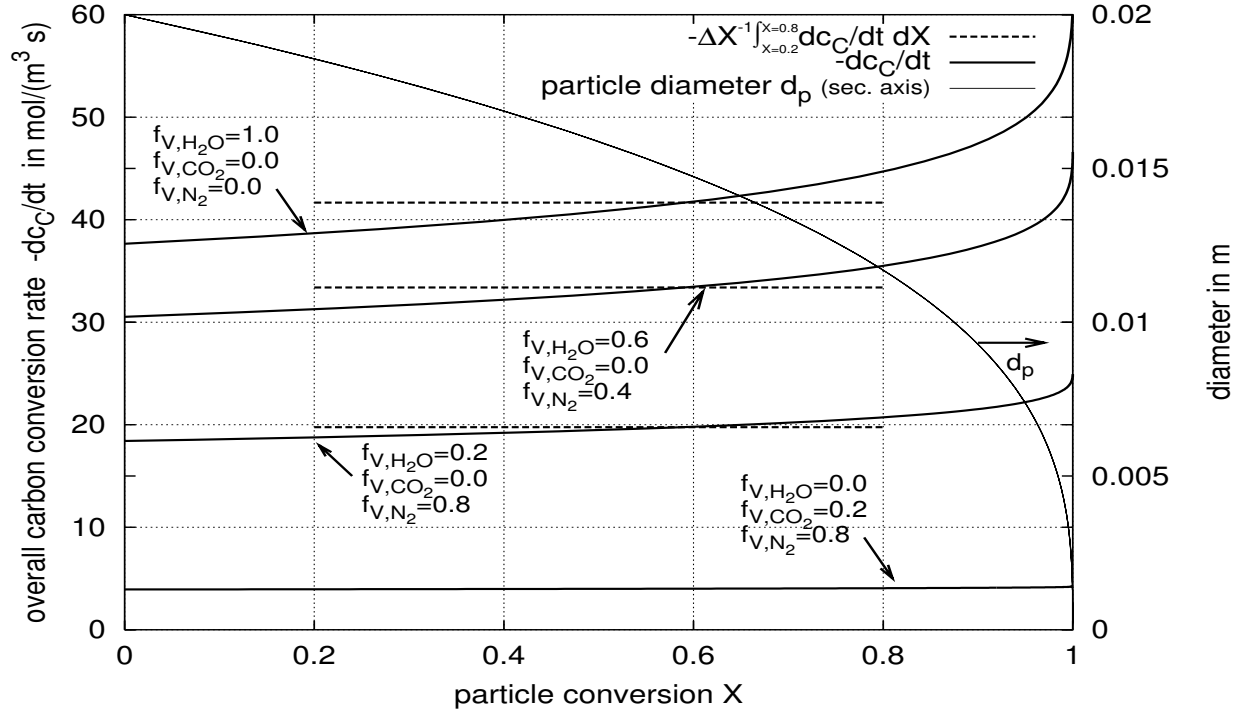


Figure 3.15: Particle diameter d_p and carbon reaction rate versus the particle conversion X . The average conversion rates between a conversion of $X_1 = 0.2$ and $X_2 = 0.8$ are sketched out here. Whereas the conversion rate for carbon dioxide gasification is more or less constant over the whole interval, the carbon reaction rate for steam gasification changes rapidly particularly at the end of the particle conversion.

of the representative diameter into the simulation, the representative diameter has to be calculated at every instance or it has to be computed with an over the reactor representative ambient steam concentration. Since the representative steam volume fraction can be expected to be in the range of 0.2 – 0.4 (refer to Fig. 4.8), the representative diameter is about 0.013–0.015m. This value can be acquired from Fig. 3.15 and is situated at the intersection of the curve for the overall carbon conversion rate for a desired gas composition and the curve for the corresponding representative conversion rate. Hence, the representative particle conversion is about 0.6 which corresponds to the (representative) diameter of the value mentioned above. For the simulation 0.0133m is used. For the given conditions, this representative diameter is suitable just for a fuel with a particle diameter of $d_p = 0.02m$. The effectiveness number, which relates the reaction rate in the particle at surface conditions to the hypothetical reaction rate at ambient conditions is plotted in Fig. 3.17.

The dotted lines stand for the situation with present mass-transfer limitations and no heat-transfer limitations. The solid lines consider heat-transfer limitations as well as mass-transfer limitations. It is clear, that the first case is consistent with the Damköhler Numbers Da_{III} in chapter 3.5.1 and nearly negligible. But the slightly reduced temperature of not

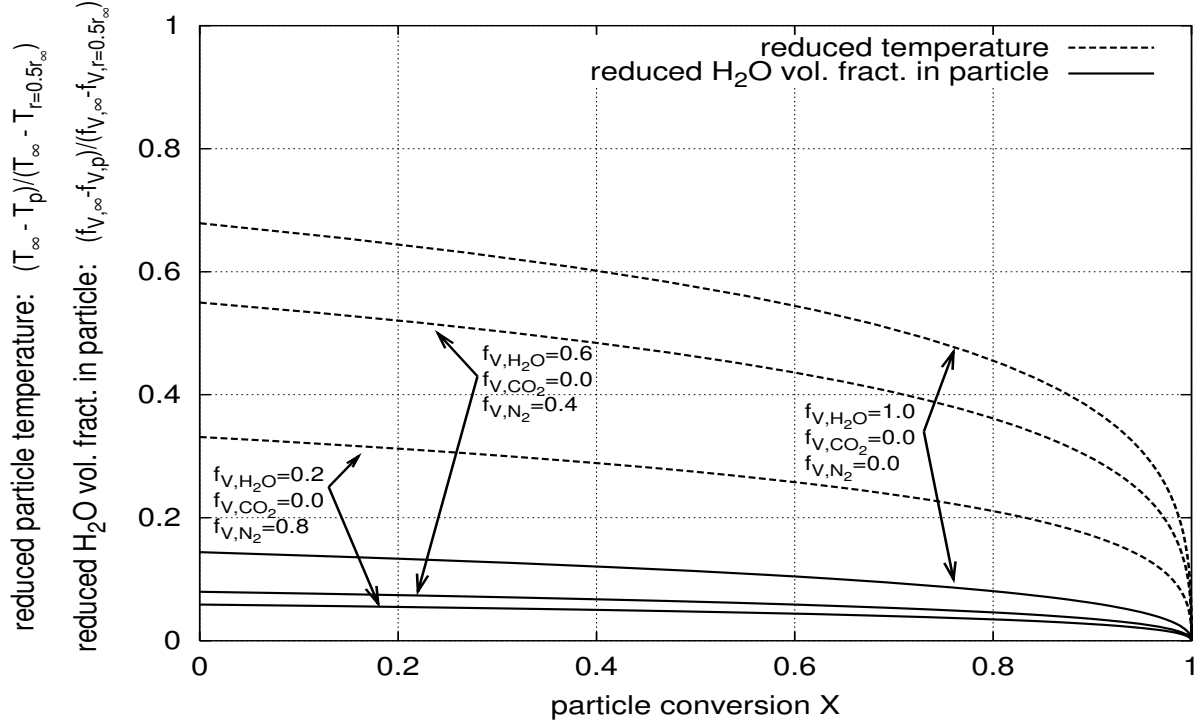


Figure 3.16: The actual concentration difference is related to the concentration difference, which would halve the reaction rate. An analogous plot is performed for the temperature difference. The influence of the heat-transfer limitations are therefore dominating the influence of the mass-transfer limitations.

more than 25°C in the second case leads to a significant reduction of the effectiveness number to 0.6–0.7. To quantify finally the relative importance of the reduced surface concentration and the reduced surface temperature, the concentration difference and the temperature difference to ambient conditions are related to the hypothetical surface conditions which lead to the half reaction rate:

$$\frac{T_{\infty} - T_S}{T_{\infty} - T_{r=0.5r_{\infty}}} \quad \text{and} \quad \frac{c_{\text{H}_2\text{O},\infty} - c_{\text{H}_2\text{O},S}}{c_{\text{H}_2\text{O},\infty} - c_{\text{H}_2\text{O},r=0.5r_{\infty}}} \quad (3.26)$$

The results of this relations are sketched in Fig. 3.16. The dotted lines represent the temperature effect which is found out to be quite important and may not be neglected in future investigations for large particles. It exceeds the reduction of the reaction rate due to lower species surface concentration as a result of external mass-transfer limitations several times.

Here, the whole system is determined by external heat transfer limitations rather than the chemical reaction rate. Hence, every circumstance, which reduces during conversion the chemical reaction rate respective to the transfer rate, increases the external effectiveness number. During the gasification process, a combination of a decreasing particle diameter and a decreasing carbon concentration will slow down the chemical conversion rate and

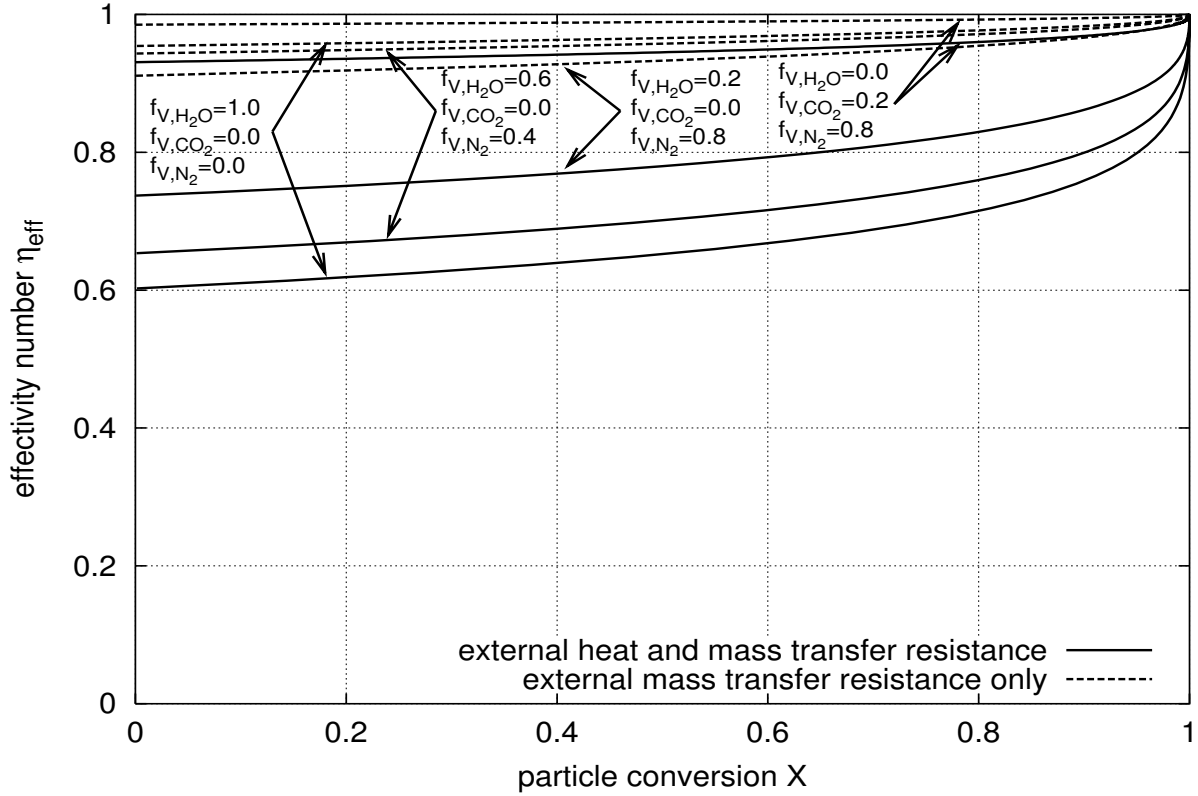


Figure 3.17: The effectiveness factors obtained by consideration of heat and mass-transfer limitations are considerably lower than the effectiveness factors for mass-transfer limitations, only. The latter correspond well with the values obtained in chapter 3.5.1. The internal effectiveness number is set to unity.

therefore, the effectiveness number increases. For a simple particle model, one of the border cases, a shrinking particle model or a homogeneous particle model can be applied. The model developed here, is a combination. While the whole particle participates on the conversion it allows for a particle shrinking. The former is justified by the low Thiele Modulus which results in a high internal effectiveness factor (refer to Fig. 3.10 and Fig. 3.11). The latter is justified by the mechanical stress on the particle surface. The worst case for the effectiveness factor is therefore equal to the initial effectiveness factor. The best effectiveness factor for this Thiele Modulus is therefore the result of this particle model. Regarding again Fig. 3.15, the representative conversion can be acquired on the intersection point of the overall carbon conversion rate $-\frac{dc_C}{dt}$ and the corresponding average overall carbon conversion rate. For a pure steam atmosphere, the representative particle conversion is about $X = 0.6$. However, the value is approximately valid for all investigated compositions of the ambient gas. With this value, the external effectiveness number can be determined using Fig. 3.17. However, since the internal effectiveness number is unity, the external effectiveness number is identical to the overall effectiveness number. For a pure steam atmosphere, an effectiveness number

in the range from 0.6 to 0.7 can be determined. However, for an ambient atmosphere which contains 20% steam, an effectiveness number in the range from 0.75 to 0.8 is figured out. This is rather representative for the conditions in the gasifier than a pure steam atmosphere.

If the particle diameter is larger than $0.02m$, then the so acquired effectiveness number is too high. This is mainly the case because a higher diameter results in a further increase of the heat and mass transfer limitation. Also, the assumption of the absence of internal heat and mass transfer limitations may not be valid anymore. If fuel with a broad particle size distribution is used, the computation of the representative particle diameter and the effectiveness number for the overall conversion rate is considerably more costly in work. For this, the fuel has to be split up into particle classes with a uniform size distribution. Then, the procedure of the present work can be applied to each class. The overall conversion rate for the fuel is the mass weighted average of the representative overall conversion rate of each particle class. Then, the representative overall conversion rate for the fuel is used to chose a representative particle diameter and a corresponding effectiveness number.

3.6 Presumptions for the Model

3.6.1 Plant Parameters

Table 3.19 contains parameters which have to be fixed to operate the plant successfully. These parameters can be influenced by changing the operating conditions, gasifier geometry, the fuel composition, etc. Some of the plant parameters are, once fixed, not or hardly changeable. One of these parameters is for example the number of nozzles for the fluidization. Other parameters can easily be changed and are therefore interesting for a performance optimization. Some of them are investigated in the sensitive analysis. For the most sensitive parameters as the bed temperature, a parameter variation is performed.

3.6.2 Model Parameters

Beside the plant parameters above, there have to be fixed some model parameters. This includes first of all the fluid dynamic equations like the correlations for the bed expansion which are still a high source of incertitude and reaches to the chemical reaction system. Especially, for these parameters one encounter widely scattering, not yet investigated or simply unknown values like the catalytic activity of char accompanying substances or the pore structure and the active surface of the char. The discretization intervals for the fluid dynamic equations are chosen according to stability of the differential equation solver. Too large intervals cause side effects which lead finally to an instability although the solver has primary nothing to with this discretization.

The bed material distribution in the freeboard is calculated with correlations using an exponential decay of the bed material voidage with increasing height (refer to Table 3.4). The initial value for the voidage of a certain material in the freeboard is the voidage of the respective material on the bed surface. The final value of the voidage is calculated form the solid content in the product gas listed in Table 4.4.

Species	H ₂ O	CH ₄	H ₂	CO	CO ₂
Composition in volume-%	4.18	21.02	29.90	19.10	25.80

Table 3.13: Devolatilization composition

Species	C	H	O
Composition in $\frac{kg}{kg_{waf}}$	0.5018	0.0566	0.4416

Table 3.14: Elementary analysis of the used fuel on a water and ash free basis

$\frac{kg_{VM}}{kg_{w,waf}}$	$\frac{kg_{ch}}{kg_{w,waf}}$	$\frac{kg_{ash}}{kg_{w,wet}}$	$\frac{kg_{wt}}{kg_{w,wet}}$
0.79	0.21	$0.729 \cdot 10^{-2}$	0.10

Table 3.15: Proximate analysis of the used wood

Height in m		Interval in m
Begin	End	
0.0	0.4	$1.0 \cdot 10^{-4}$
0.4	0.7	$5.0 \cdot 10^{-4}$
0.7	0.701	$1.0 \cdot 10^{-4}$
0.701	2.5	$5.0 \cdot 10^{-4}$

Table 3.16: Discretization for the computation of the bed fluid dynamic for the pilot plant gasifier. The small values are chosen because higher ones cause stability problems of the solving algorithm.

Height in m		Interval in m
Begin	End	
0.0	0.1	$5.0 \cdot 10^{-5}$
0.1	0.65	$2.0 \cdot 10^{-3}$
0.65	0.8	$1.0 \cdot 10^{-4}$
0.8	1.5	$1.0 \cdot 10^{-3}$
1.5	1.8	$1.0 \cdot 10^{-4}$
1.8	2.5	$5.0 \cdot 10^{-2}$
2.5	5.25	$2.5 \cdot 10^{-1}$

Table 3.17: Discretization for the computation of the bed fluid dynamic for the demonstration plant gasifier. The small values are chosen because higher ones cause stability problems of the solving algorithm.

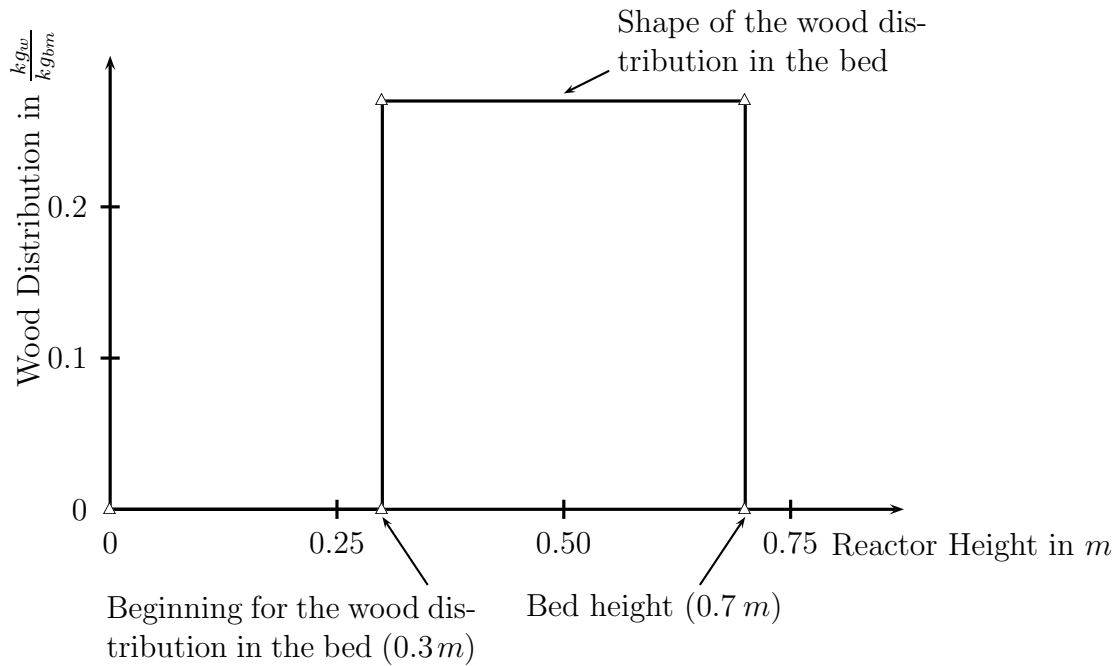


Figure 3.18: The wood distribution in the fluidized bed is modeled by a step beginning at the bed height of 0.3 m for the pilot plant gasifier and 0.65 m for the demonstration plant gasifier. The bed height is 0.7 m for the pilot plant gasifier and 1.5 m for the demonstration plant gasifier. This is justified by the hydrostatic buoyancy of the large, low dense wood particles.

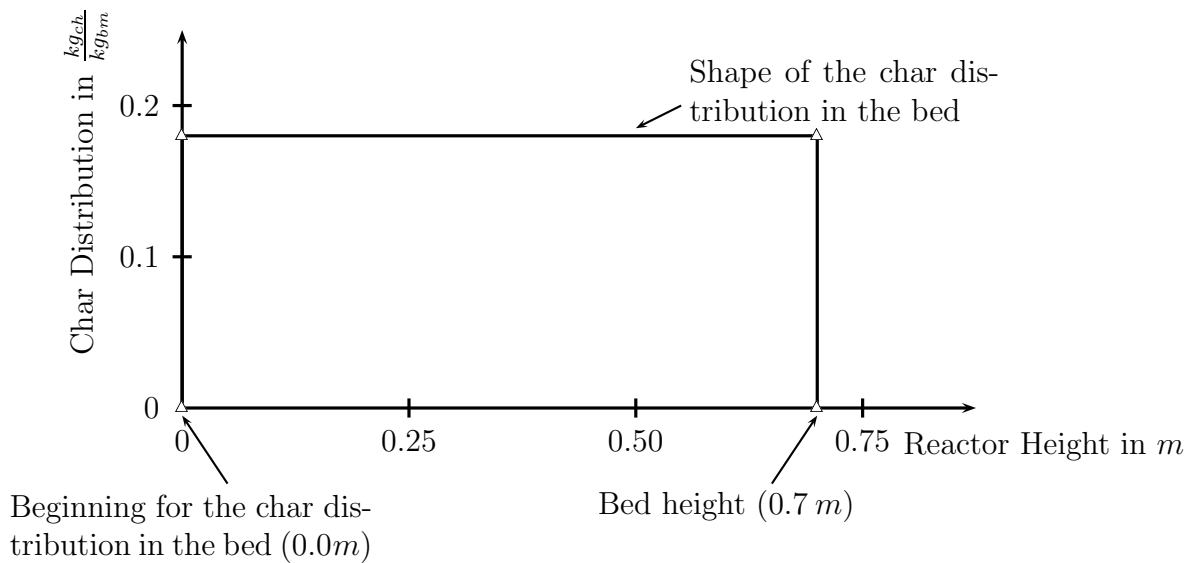


Figure 3.19: The char distribution in the fluidized bed is supposed to be uniform for both, the pilot plant gasifier and the demonstration plant gasifier. The char distribution in the freeboard is analogous to the other bed material (refer to chapter 3.6.2).

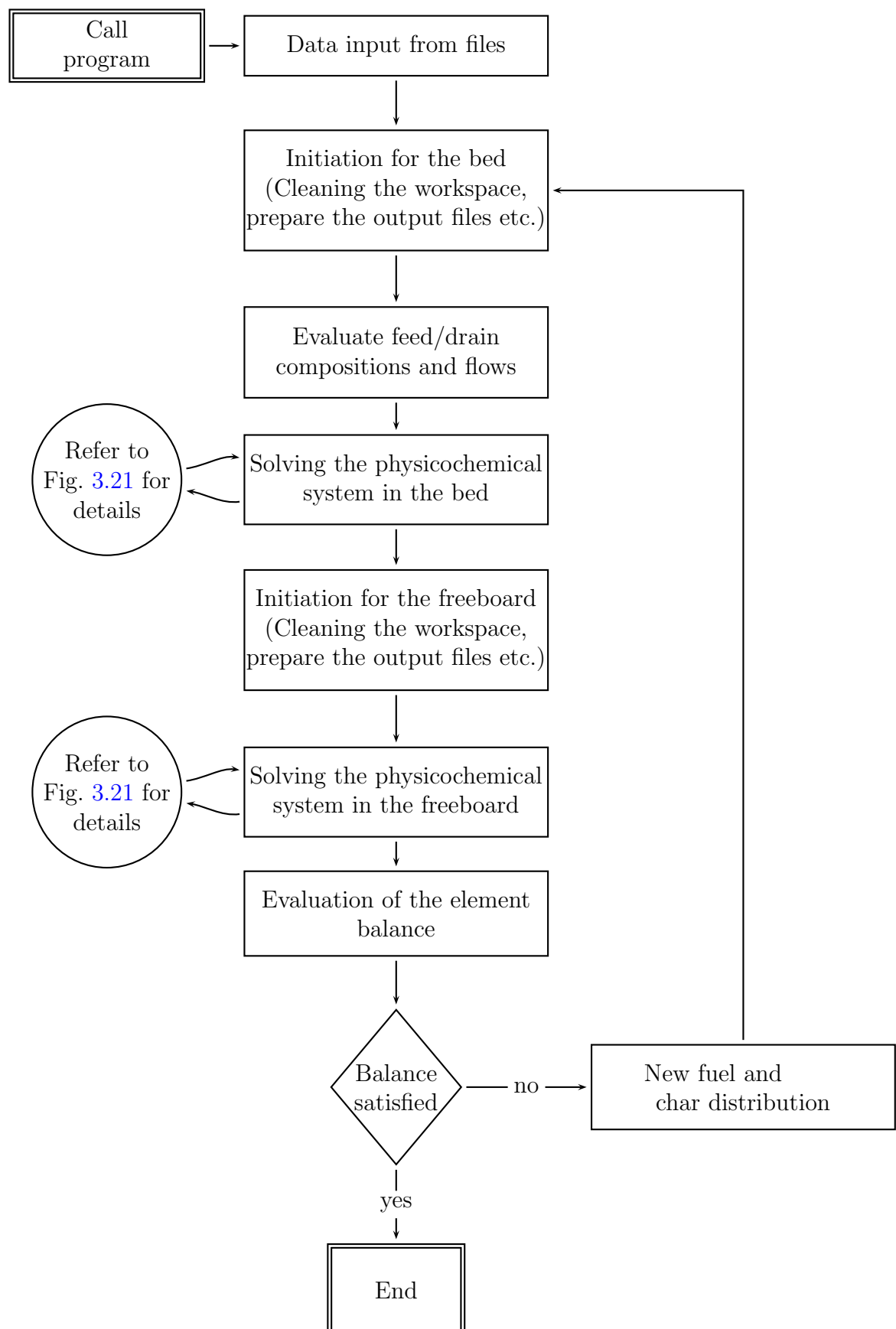


Figure 3.20: Overview for the solving scheme

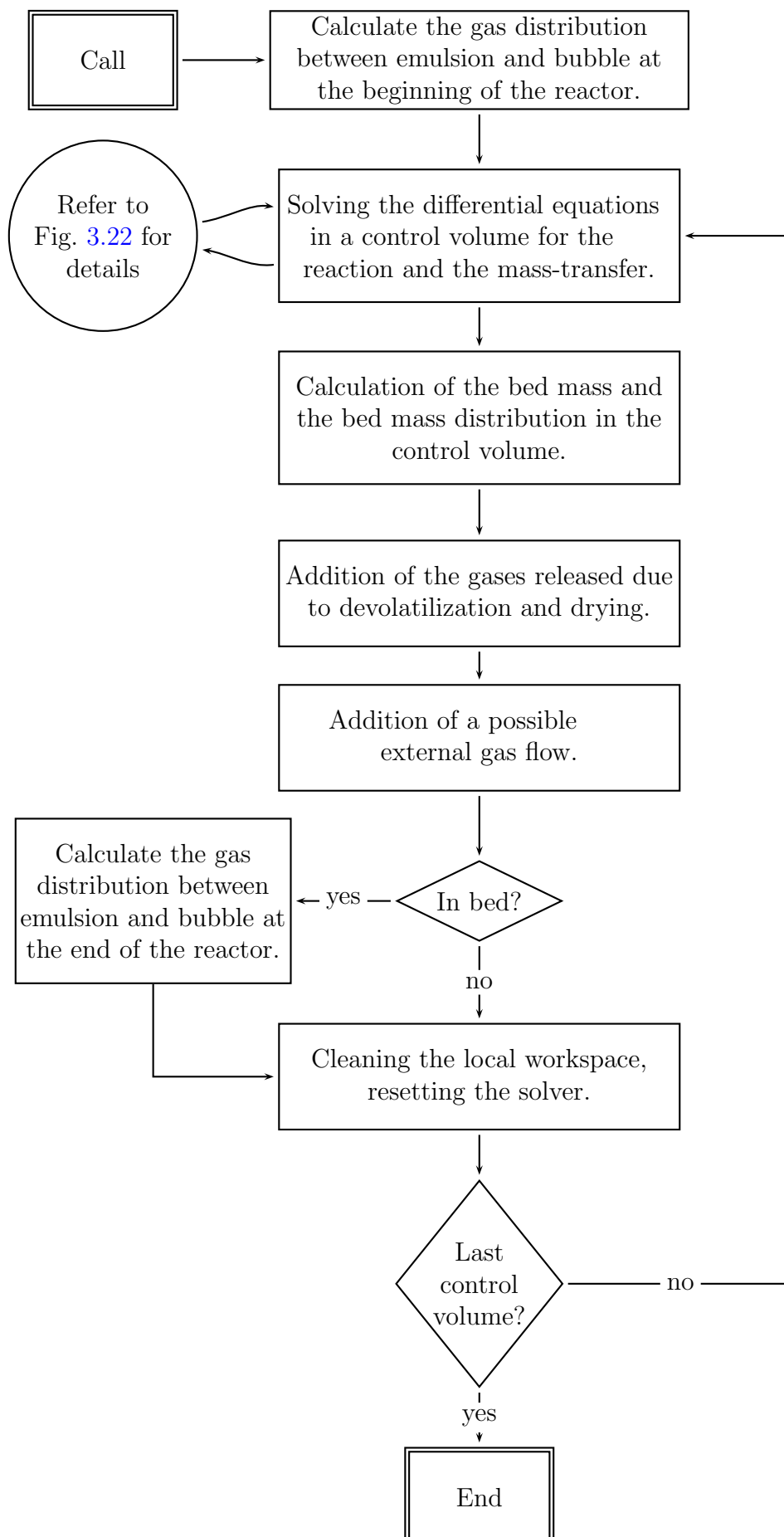


Figure 3.21: Flowsheet for the bed and the freeboard

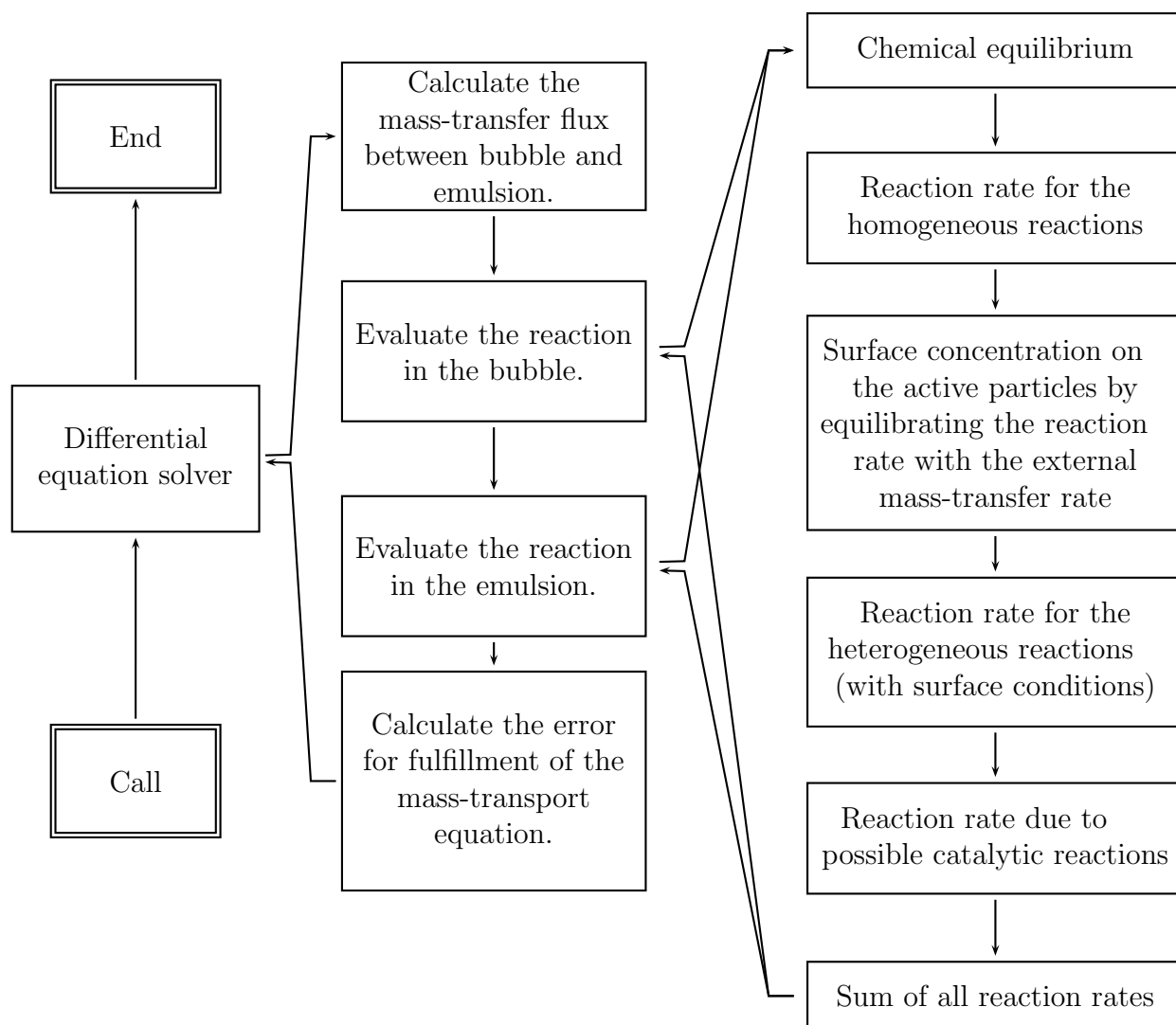


Figure 3.22: Flowsheet for the differential equation solver

Value	Pilot Plant Reactor	Demonstration Plant
Area of the bottom plate per orifice A_o	$3.98 \cdot 10^{-4} m^2$	$4.58 \cdot 10^{-4} m^2$
Fluidization gas mass flow	$2.5 \cdot 10^{-3} \frac{kg_{wt}}{s}$	$1.37 \cdot 10^{-1} \frac{kg_{wt}}{s}$
Fuel mass flow \dot{m}_f	$5.887 \cdot 10^{-3} \frac{kg_w}{s}$	$4.69 \cdot 10^{-1} \frac{kg_w}{s}$
Circuit mass flow	$50.0 \frac{(kg/s)_{bm}}{(kg/s)_{f,waf}}$	$50.0 \frac{(kg/s)_{bm}}{(kg/s)_{f,waf}}$
Bed temperature (homogeneous)	$850^\circ C$	$850^\circ C$
Pressure in the reactor (uniform)	$10^5 Pa$	$10^5 Pa$
External temperature	$293^\circ C$	$293^\circ C$
Overall heat transfer coefficient through the reactor walls	$3.0 \frac{W}{m^2 K}$	$0.0 \frac{W}{m^2 K}$
Devolatilization time	$200s$	$200s$
Bed height	$0.7m$	$1.5m$
Particle diameter (active matter)	$0.02m$	$0.02m$
Representative particle diameter (active matter)	$0.0133m$	$0.0133m$
Particle diameter (inert matter)	$380 \cdot 10^{-6}m$	$380 \cdot 10^{-6}m$
Particle density (active matter)	$300 \frac{kg}{m^3}$	$300 \frac{kg}{m^3}$
Particle density (inert matter)	$2650 \frac{kg}{m^3}$	$2650 \frac{kg}{m^3}$
Sphericity active matter	1	1
Sphericity inert matter	1	1
Composition of the fluidization gas	100% H ₂ O	100% H ₂ O
Geometry refer to	Fig. 3.2	Fig. 3.3
Fuel composition refer to	Table 3.14	Table 3.14
Devolatilization composition refer to	Table 3.13	Table 3.13
Particle mass flow of unburned combustibles in product gas	$2 \cdot 10^{-5} kg/m_N^3$	$2 \cdot 10^{-5} kg/m_N^3$

Table 3.19: Summary of the used plant parameters.

Value	Pilot Reactor	Plant	Demonstration Plant
Wood penetration depth	0.40m		0.85m
Effectiveness number for gasification (refer also to Fig. 3.11 and 3.17)	1		1
Char composition	carbon and ash		carbon and ash
Kinetic parameters for chemical reaction E_a , k_0 , n refer to	Table 3.9		Table 3.9
Adsorption constants K refer to	Table 3.10		Table 3.10
Discretization for the computation of the fluid dynamic	Table 3.16		Table 3.17
Chemical reactions involved in the computation of the particle surface concentration	Eqs. 3.17, 3.22, 3.16		Eqs. 3.17, 3.22, 3.16
Decay constant f_{dy} refer to	Table 3.4		Table 3.4
Maximal tolerable error of the carbon mole balance	$2.0 \cdot 10^{-6} mol/s$		$1.0 \cdot 10^{-5} mol/s$
Maximal tolerable error of the hydrogen and oxygen mole balance	$5.0 \cdot 10^{-6} mol/s$		$5.0 \cdot 10^{-5} mol/s$
Absolute error for the differential equation solver	$1.0 \cdot 10^{-6} mol/m^3$		$1.0 \cdot 10^{-6} mol/m^3$
Relative error for the differential equation solver	$1.0 \cdot 10^{-6}$		$1.0 \cdot 10^{-6}$
Fraction of gases formed by devolatilization, which is released into emulsion phase	1		1
Fraction of through-flow in bubble phase $f_{tf,b}$ (refer to chapter 2.1.1)	1		1

Table 3.20: Summary of the used model parameters.

3.7 Solving Algorithm for the Balances

Fig. 3.20 gives an overview of the solving method. To achieve a solution for the whole process, an iteration algorithm turns out to be necessary. The estimation is the mass fraction of the char and the wood at each bed height. This is done by modifying the height of the shape shown in Fig. 3.18 and Fig. 3.19. The input of necessary data is done via text files. This includes also the first estimation of the bed material distribution which has to be done manually. Then all values are set to initial values, which are the values for the bottom. Further, the species and element molar flows for the fuel flow and the solid circulation flow are computed. Subsequently, the whole physicochemical system is solved in the bed. This step is described in detail in Fig. 3.21. The same procedure is repeated in the freeboard. Once solved, the element balance over the whole reactor is done. These balances of carbon, hydrogen and oxygen permit to correct the char distribution shape with the carbon balance error and the shape for the wood distribution with the hydrogen and oxygen mass balance error. If it is not satisfied within the tolerances listed in Table 4.3, the bed material distributions are modified and the calculation is repeated. As the correction algorithm of the bed material shape, the Newton algorithm is applied.

Fig. 3.21 shows the scheme which permits to compute the physicochemical system in the bed and the freeboard, respectively. The difference between bed and freeboard is the different algorithm of the solid material distribution and the absence of a bubble-phase since the solids are supposed to be homogeneous mixed with the gas perpendicularly to the main flow direction (refer to chapter 3.3).

$$\begin{aligned} \frac{Q_b^k}{A_b^k} \frac{dc_{b,i}}{dh} &= R_{b,i} + k_{be,i} \frac{6}{d_b} (c_{e,i} - c_{b,i}) && \text{for bubble phase} \\ U_e^k \frac{dc_{e,i}}{dh} &= R_{e,i} - k_{be,i} \frac{6}{d_b} (c_{e,i} - c_{b,i}) \frac{A_b^k}{A_e^k} && \text{for dense phase} \end{aligned}$$

Table 3.21: Differential equation system for the control volume at instance k for each species i ($i = \text{CO}, \text{CO}_2, \text{CH}_4, \text{H}_2, \text{H}_2\text{O}$).

As a first step, the gas distribution between the dense and the bubble phase at the begin of a control volume is done. The equations used for this are listed in Table 3.3 and the procedure is similarly to the procedure which is used to calculate the gas redistribution (refer to Table 3.5). The resulting fluid dynamic values are kept constant within the whole control volume. So neither velocities nor cross sections change. The next change of these values occurs at the beginning of the next control volume. Then, the differential equations listed in Table 3.21 on page 80 are applied within the control volume. This step is described in detail in Fig. 3.22. After solving, the reaction system in a control volume CV , the mass of wood, which is undergoing devolatilization and drying is computed. Subsequently, the gases from the devolatilization step and the drying step are added to the volumetric gas flow of the bubble. Finally, the gas redistribution is calculated as already presented earlier (refer to Table 3.5). This solving algorithm is applied sequentially to all control volumes CV since the result of CV^k is the initial condition for CV^{k+1} .

The differential equation solver solves a first order differential-algebraic system of equations,

$g(t, y, y') = 0$, using the Petzold-Gear BDF method [Petzold 1982, Brenan et al. 1989]. The equations provided to the solver are listed in Table 3.21 on page 80. Variables with a superscript k do not change within the control volume. Other values, like the mass-transfer rate change during the solving procedure of the differential equation solver. First, the mass-transfer flow between bubble phase and dense phase is computed. Then the reaction rate in the bubble phase and the reaction rates for the homogeneous and the heterogeneous reactions are computed. The latter are evaluated under the consideration of mass transfer limitations between gas and particle. The reaction rates in the dense phase are computed in the same way. Finally, the error to the fulfillment of the differential equation system is computed. The result provided by the differential equation solver is the concentration with the first derivations at an adjustable number of instances.

Chapter 4

Model Evaluation

4.1 Standard Conditions

The following discussion is focused on the standard reactor which was previously defined in chapter 3.6. Subsequently, based on this standard, the sensitivity of various parameters is investigated. For parameters where the influence on the solution is shown to be significant, a variation over a larger range of values is performed.

4.1.1 Pilot Plant Gasifier

For the pilot plant gasifier, just one run for the defined standard is performed. The results of this simulation are summarized in Table 4.1. This is done above all for a verification of the assumptions of the devolatilization composition. As already discussed, this composition is a highly uncertain one (refer to chapter 2.2.3). However, since a large series of measurements has been undertaken on this reactor, results for the product gas composition are already available (refer to [Kaiser 2001, Hofbauer and Rauch 2000, Fercher et al. 1998, Hofbauer and Rauch 2001, Schuster et al. 2001])

Species	
Carbon monoxide CO in volume-% (dry)	28.2
Carbon dioxide CO ₂ in volume-% (dry)	19.4
Hydrocarbons C _x H _y in volume-% (dry)	15.7
Hydrogen H ₂ in volume-% (dry)	36.7
Water H ₂ O in volume-%	37.6
Product gas volumetric flow Q_{pr} in m_N^3/h	21.8
Carbon in solid circulation flow $\frac{w_{C,cir}}{w_{C,f}}$ in $\frac{kg_{C,cir}}{kg_{C,f}}$	0.283

Table 4.1: Simulation results for the product gas composition for the pilot plant gasifier in percent by volume of the steam free product gas for every species but steam. The value of the product gas composition for steam is in percent by volume of the product gas. Further, there is listed the product gas volumetric flow in m_N^3/h and carbon mass in solid circulation flow.

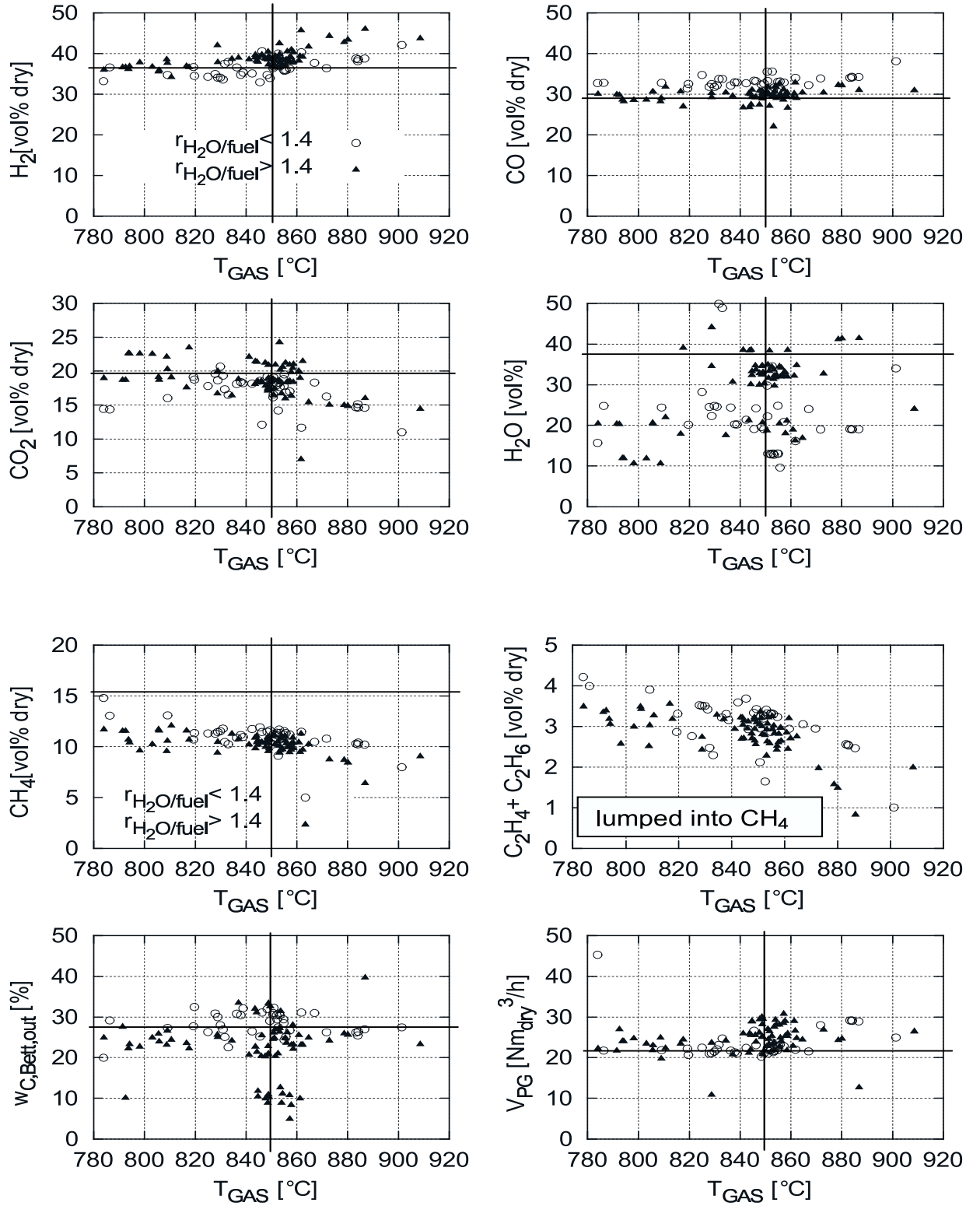


Figure 4.1: The measurement results of the product gas composition in pilot plant gasifier compared with the computed results show slight deviations of the simulation results (for the simulation: $r_{\text{H}_2\text{O}/\text{fuel}} = \frac{\dot{m}_{\text{wt},f} + \dot{m}_{\text{wt},fl}}{\dot{m}_{f,\text{dry}}} < 1.4$). However, this is mainly due to the composition of the devolatilization gases. Figure from Kaiser [Kaiser 2001].

The results of the simulation and measurements at the pilot plant gasifier are presented in Fig. 4.1. They are good within the range of the measurement results. The measured water content scatters in a wide scale, but the result of the simulation seems to overestimate the water content by a few percents. C_xH_y is representative for the methane fraction plus the higher hydrocarbons which are lumped into the CH_4 fraction. So the simulation result shows an about 6% higher methane content than the measured results for methane. However, to obtain qualitative simulation results, an analysis of the used fuel regarding the devolatilization composition is necessary. The results of the simulation are presented in Table 4.1.

4.1.2 Demonstration Plant Reactor

The demonstration plant reactor is presented in detail here. The evolution of the volume fractions is discussed as well as the fluid dynamics. All the plots are performed as a function of the height, which is the abscissa of all plots in this section.

Cross Section

The cross section of the plant reactor can be seen in Fig. 4.2. Further, the cross section occupied by the bubble phase is plotted. The cross section of the dense phase is visible between the two curves. The ratio of dense phase cross section and bubble phase cross section is about 3.5 at the beginning, rises up to 8.0 until 0.65m reactor height due to reactor cross section enlarging and sinks again to about 7.0 at the bed surface. From the beginning of the devolatilization, the volume of the released gases, which is assimilated almost entirely by the bubble phase lead to this increase of the bubble cross section.

Bed Material Volume Fractions

The volume fractions $f_{V,q}$ of the single bed materials q are plotted in Fig. 4.3. The differential volume dV of a bed material q at a certain height h is defined by $dV_q(h) = A_q(h) dh$, where $A_q(h)$ is the cross section occupied by the bed material q . The volume fraction of a bed material at a certain height is therefore

$$f_{V,q} = \frac{\text{cross section occupied by the bed material } q}{\text{reactor cross section}} \quad (4.1)$$

All volume fractions remain almost constant in the initial cylindric section. The enlarging cross section of the conic part deviates the volume fraction of the emulsion towards higher values. According to Eq. 2.5, the minimum fluidization porosity hardly changes. The only influences which lead to an observable deviation, arise as a result of a changing gas viscosity and a changing gas density due to a changing composition (refer to Fig. 4.4). Hence, the volume fraction of the bed material increases with the same characteristic as the emulsion volume fraction.

The distribution of the char volume fraction is uniform from the beginning to a step decrease at 0.65m height and remains again constant until the end of the reactor. The volume fraction of sand shows similar behavior. Wood shows a step behavior as well, but it is absent at the bottom of the reactor and is present above a height of 0.65 m. For the model development, the *mass fraction distribution* of the bed components are fixed (refer to Fig. 3.19 and 3.18).

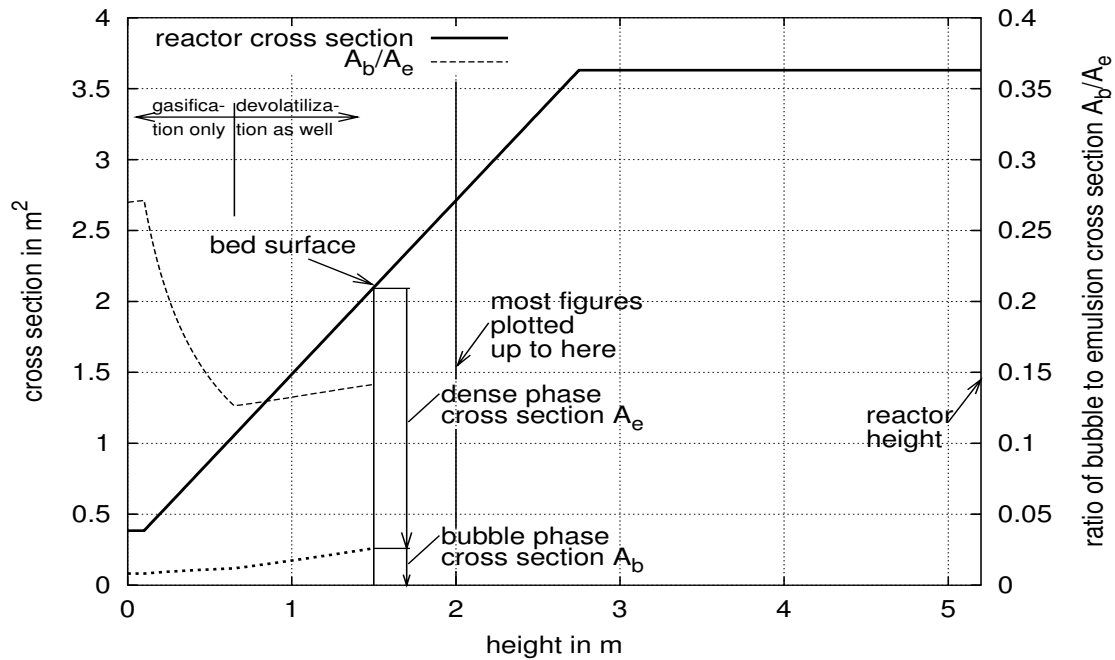


Figure 4.2: The Figure shows the cross sections of the reactor, the bubble and the dense phase for standard conditions. The bed surface is sketched at a height of 1.5 m . Most figures are plotted just up to a height of 2.0 m because above this height no conversion occurs for the investigated reactions (standard conditions).

The step in the bed material *volume fraction distribution* arises due to the sudden change of the mass fraction distribution and the different densities of the bed materials (refer to Fig. 4.3). With the appearance of wood, the average bed material density changes. Therefore, the mass fraction of the char stays constant within the whole bed, whereas the volume fraction is changing.

Above 0.65 m , the volume fractions of the bubble and the emulsion change hardly. The additional gases released by the drying and the devolatilization step change the fluid dynamic conditions in such a way that the bubble fraction and the minimum fluidization porosity remain more or less unchanged up to the end of the bed (Fig. 4.3).

The transition from the bed volume fraction to the freeboard volume fraction of each bed material is steady. In the freeboard, the volume fractions decrease according to an exponential law towards the final volume fractions. The presence of sand can be seen up to 0.3 m over the bed surface, whereas the char fraction penetrates the freeboard just a few centimeters and the wood is in fact absent. For the entrainment, the same correlation has been used for wood, char and sand. To account for their differences in density and size, their terminal velocity is used.

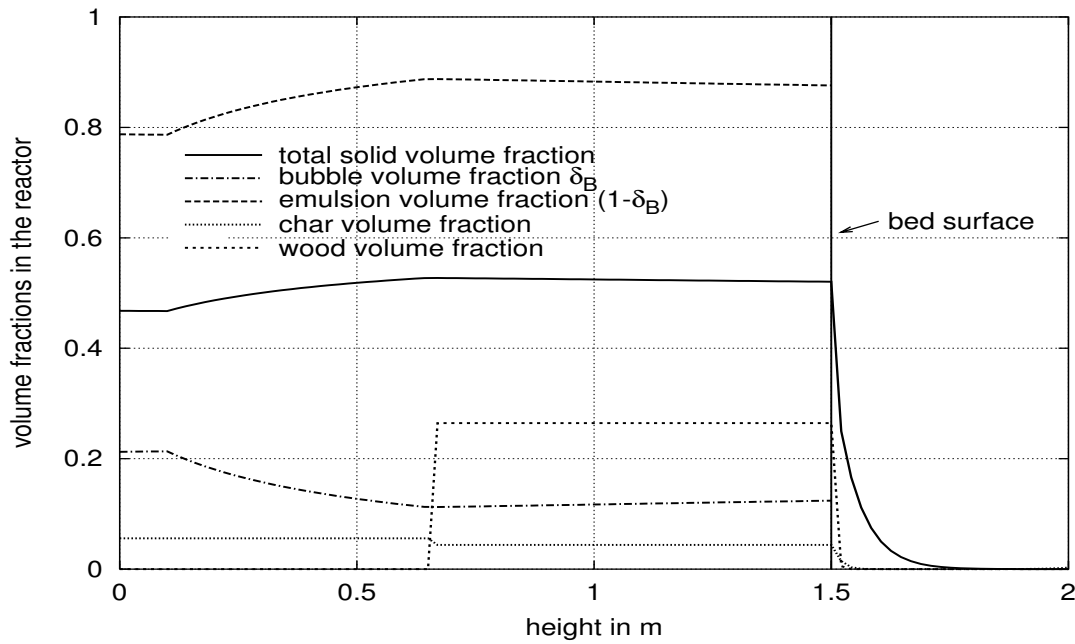


Figure 4.3: The volume fractions stay constant at the beginning. With the increasing reactor cross section in the cone, the volume fraction of the dense phase increases and remains constant again with the beginning of devolatilization. The step in the char distribution is due to the fixed *mass fraction* whereas this Figure shows the volume fractions. The interval of the result output is 0.02 m which results in the deviation of the smooth plot in the freeboard and the inexact step behavior at 0.65 m (standard conditions).

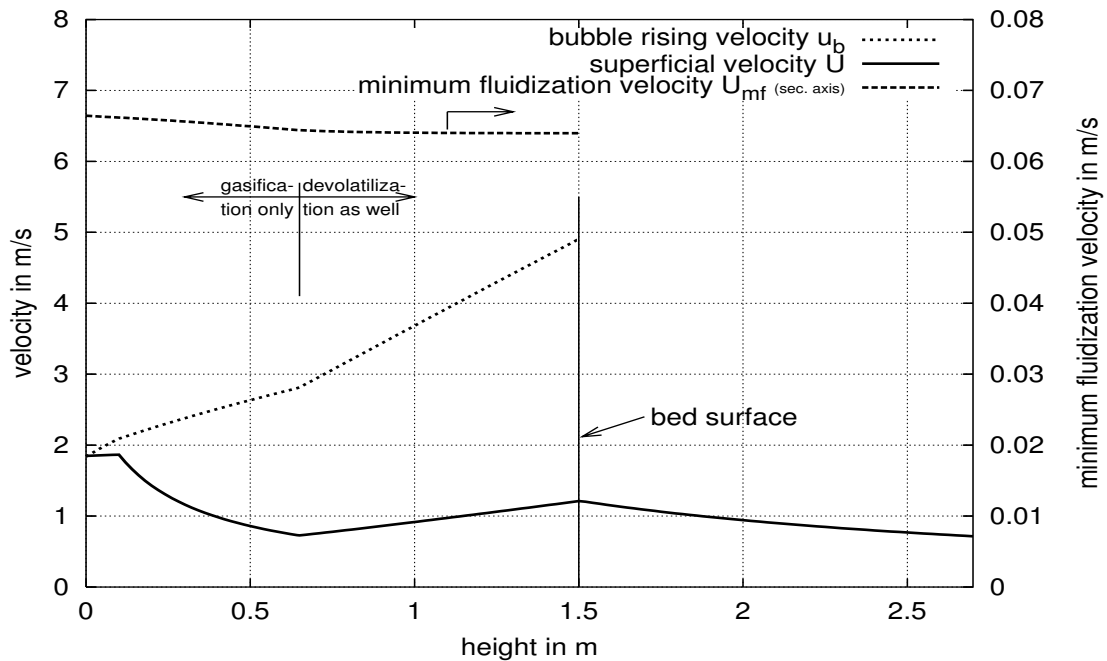


Figure 4.4: The minimum fluidization velocity U_{mf} , the superficial velocity U , the bubble velocity u_b and the gas velocity in the dense phase U_d , which is equal to the minimum fluidization velocity (standard conditions).

Velocities

The minimum fluidization velocity U_{mf} , the superficial velocity U , the bubble velocity u_b , and the gas velocity in the dense phase U_d , which is equal to the minimum fluidization velocity, are plotted in Fig. 4.4. The minimum fluidization velocity remains almost constant at about $0.065 \frac{m}{s}$ within the whole bed. The only deviation is arising due to a change of the gas composition and therefore the viscosity and density. The bubble rising velocity and the superficial velocity undergoes a significant change versus the reactor height. At the bottom of the reactor, both are about 28 times the minimum fluidization velocity. The bubble rising velocity increases continually, whereas the superficial velocity sinks due to the enlarging reactor cross section until the beginning of the devolatilization at a height of $0.65m$ height where it begins to rise again. The smallest value of the superficial velocity is about $0.738 \frac{m}{s}$ which is slightly over 11 times the minimum fluidization velocity. After an almost linear increase up to the bed surface, the superficial velocity reaches $19U_{mf}$.

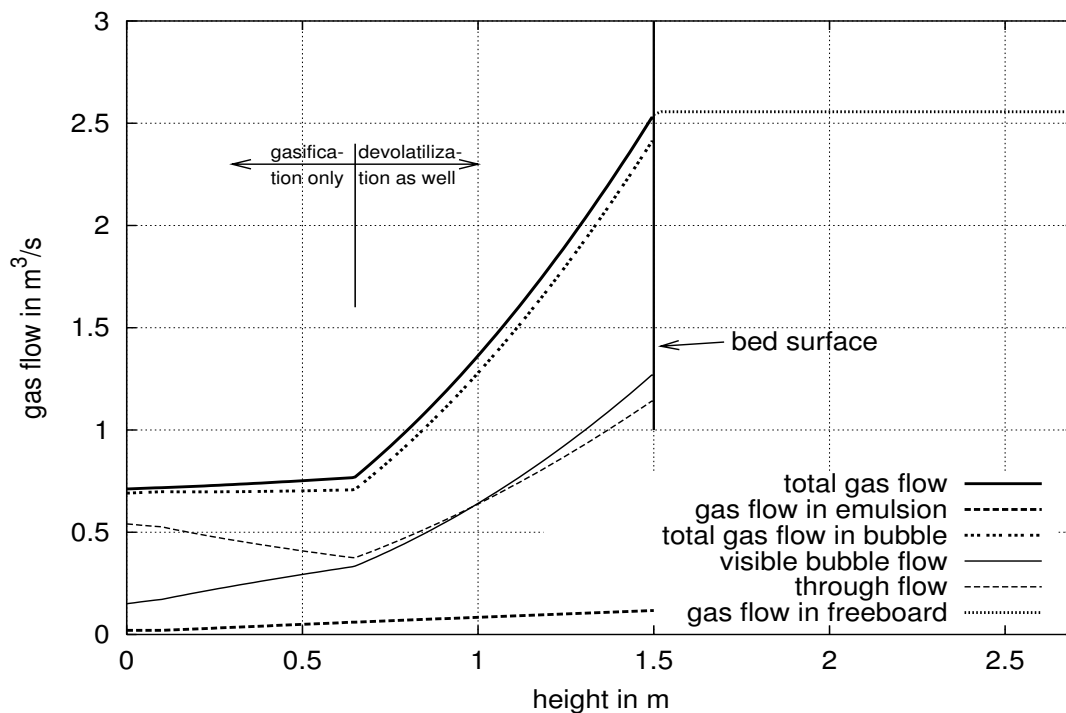


Figure 4.5: Total gas flow, gas flow in emulsion, total gas flow in bubble which is the visible bubble flow plus through-flow, visible bubble flow, through-flow and gas flow in freeboard (standard conditions).

Volumetric Flows

Several volumetric flows are plotted in figures 4.5 and 4.6. The first Figure shows the total volumetric gas flow as well as the volumetric flow in the bubble and the emulsion. The volumetric flow in the emulsion stays constant in the cylindric initial part and rises almost linearly in the conic part. Since the emulsion is supposed to stay in minimum fluidization

conditions which are changing just within a small range, the deviation is entirely due to the enlarging cross section of the reactor and thus emulsion as well. For the standard conditions, the through-flow is lumped into the bubble phase. Therefore, the total volumetric gas flow equals the sum of the volumetric flow of the emulsion and the bubble. The visible bubble flow and the through-flow are plotted in Fig. 4.5 with thin lines. Initially, the through-flow is about 3.5 times higher than the visible bubble flow. With increasing height, the visible bubble flow increases due to the increasing bubble rising velocity and an increasing *factor Y* (refer to Fig. 4.6). In contrary, to fulfill the gas flow balance, the through-flow decreases. At a height of 0.65m the ratio of the through-flow and visible bubble flow reaches and stays at about unity. This is a direct result of the evolution of the *factor Y* which is increasing continuously from 0.23 to a value of about 0.5 at a reactor height of 0.65m . Above this height, this factor increases only slightly and stays almost constant.

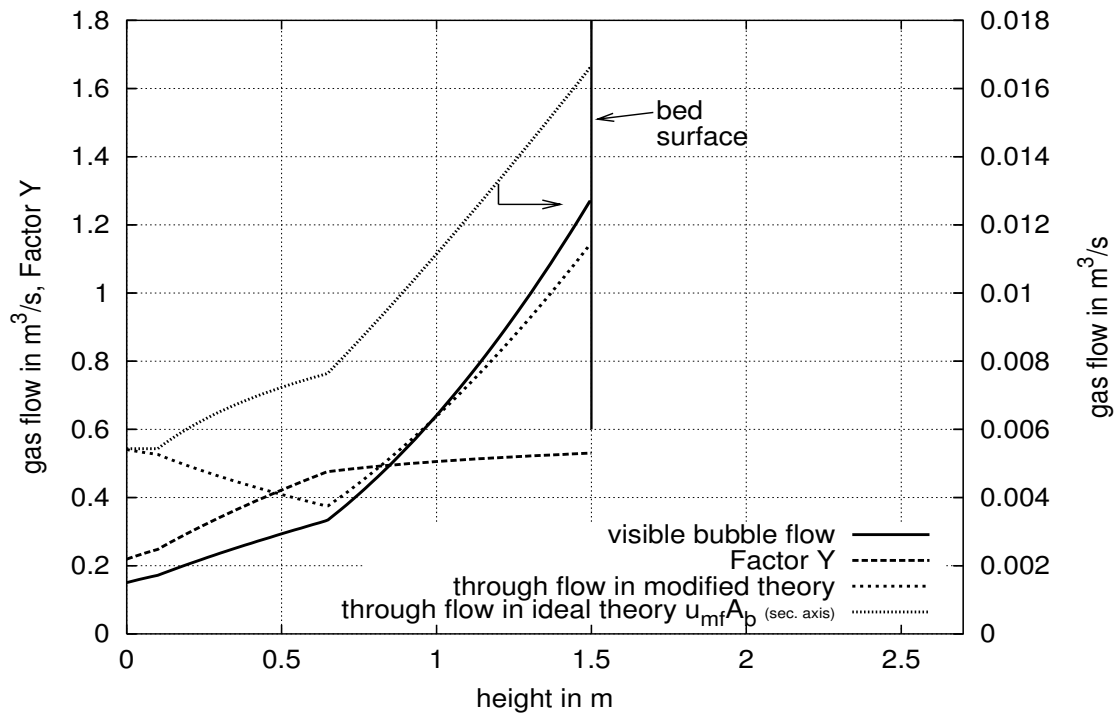


Figure 4.6: The visible bubble flow, the factor Y and the through-flow for the original two-phase theory and the modified two-phase theory. Remarkable is the difference of several orders of magnitude between the last two (standard conditions).

Steam Volumetric Flows The steam volumetric flows can be seen in Fig. 4.7. As expected, the H_2O volumetric flow in the emulsion decreases as a result of the rapidly decreasing concentration of steam in the first cylindric part of the reactor, whereas the H_2O volumetric flow in the bubble increases, which is not that clear. The change relative to the emulsion volumetric flow is significant, in contrary to the change relative to the bubble volumetric flow, which is only marginal. With the transition to the conic part of the reactor the tendencies of the gas flows change immediately. Similarly to the dense phase volume fraction the gas flow

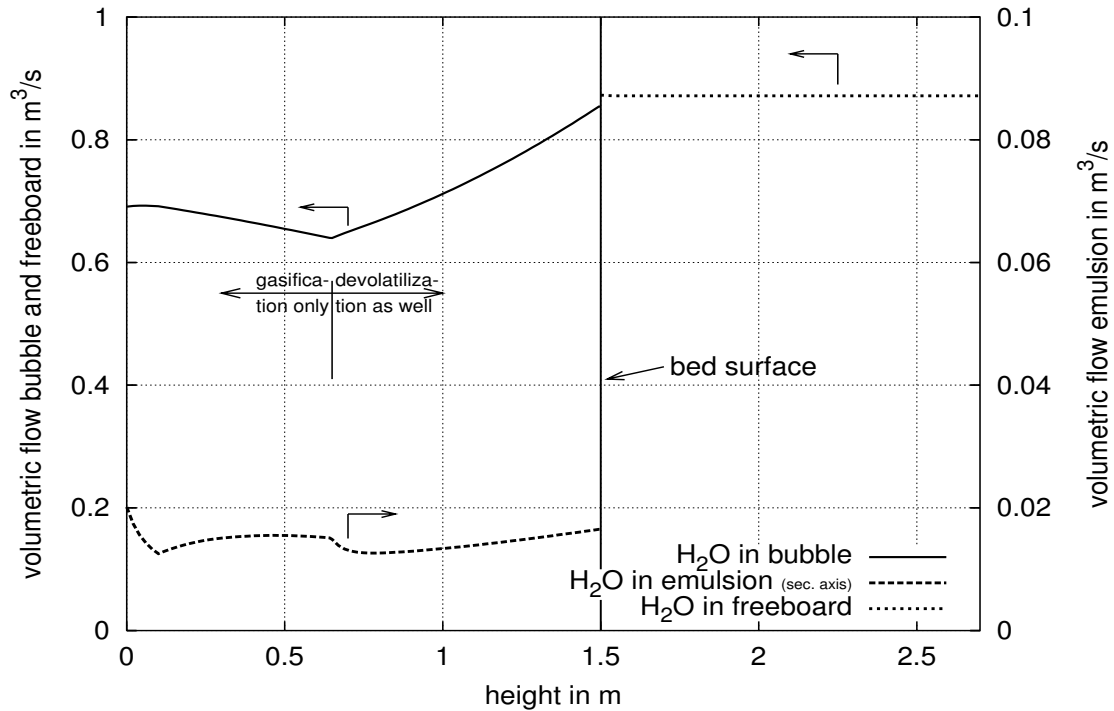


Figure 4.7: Volumetric flow of the H_2O fraction in the bubble and the dense phase. The combination of the evolution of the H_2O concentration and the geometry leads to the graph with several local extreme values (standard conditions).

through the dense phase increases, whereas the bubble flow decreases now. Finally, at the beginning of devolatilization, the steam content increases significantly due to the released steam of wood drying.

Volume Fractions

H_2O Volume Fraction The volume fraction of H_2O is plotted in Fig. 4.8. The three curves show the volume fraction of steam in the bubble phase, in the dense phase and the average volume fraction. The difference between the volume fraction of the two phases indicate a large mass-transfer resistance. The proximate position of the average volume fraction and the volume fraction in the bubble phase demonstrate the high gas volumetric flow passing through the bubble phase related to the gas volumetric flow through the dense phase. In the first half of the bed, the steam volume fraction sinks slightly below 20% and remains nearly constant afterwards. This is approximately the volume fraction of steam in the gases released by devolatilization. The gas volume, which is released by devolatilization is therefore dominating the gas composition in the dense phase. The H_2O volume fraction in the bubble phase shows a strong dilution above 0.65m . This is reducing the mass-transfer to the dense phase and enhances therefore the decrease of the conversion rate by steam.

CO and H_2 Volume Fractions The volume fractions of CO and H_2 are shown in Fig. 4.9 and Fig. 4.10. The evolution of these volume fractions is basically the same. The only

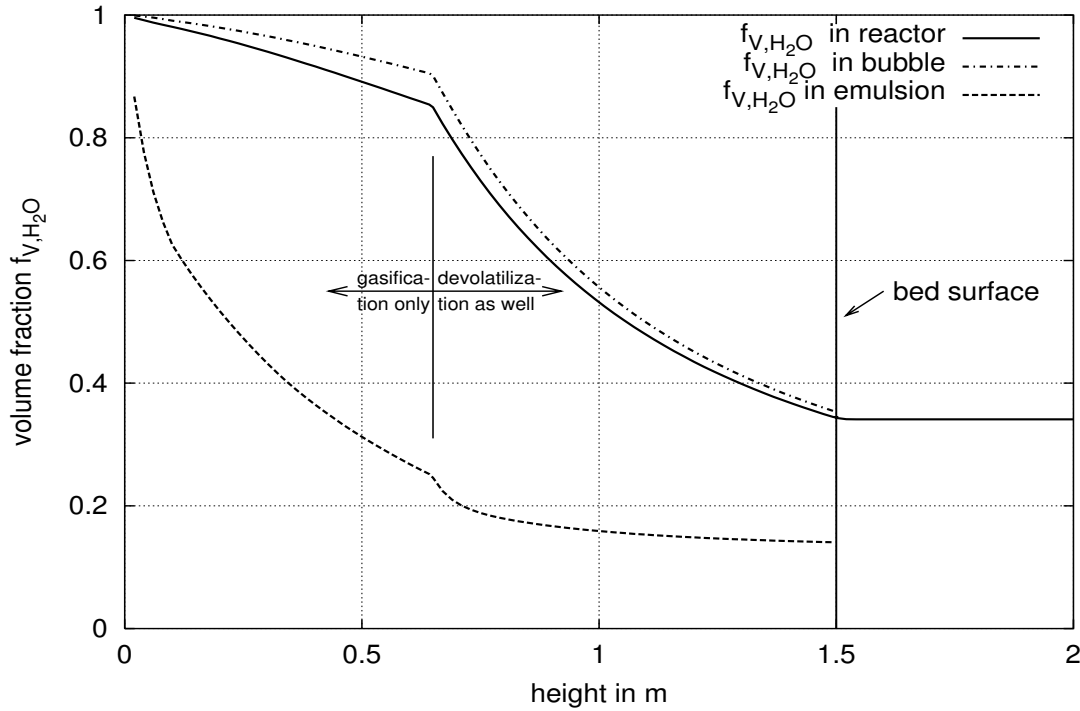


Figure 4.8: Evolution of the volume fraction of steam in the dense phase, the bubble phase and the reactor average (standard conditions).

difference arises due to a higher diffusivity of the hydrogen. Thus, in the emulsion, the hydrogen concentration is lower related to the carbon dioxide concentration. Above $0.65m$ reactor height, the composition of the gases released by devolatilization dominate again the overall composition.

CO₂ and C_xH_y Volume Fraction The volume fractions of CO₂ and C_xH_y are sketched in Fig. 4.11 and Fig. 4.12. Again, the evolution of the volume fractions is basically the same. Differences arise due to the composition of the gases released by devolatilization. It can be seen that the hydrogasification has no visible influence on the C_xH_y volume fraction since C_xH_y is absent up to a height of $0.65m$. However, the methane decomposition by the inverse hydrogasification reaction takes place since the equilibrium constant is $k_{pb}^{e,1123K} \sim 0.92$ derived from the pressure in *bar* at a temperature of $1123K$ (refer to Eq. 3.22 on page 60).

Volume Fractions on Particle Surface The volume fractions on the surface of the active particles are plotted in Fig. 4.13. Further, the composition of the ambient gas in the dense phase is plotted with thin lines of the same type. The concentration difference between the gas concentrations on the particle surface and the ambient gas is not large. This is coherent with the computed Damköhler Number and the external effectiveness factor respectively (refer to chapter 3.5.1). In the simulation, it has not been accounted for the influence of the heat-transfer resistance. This influence is discussed in chapter 3.5.2. Assuming a lower particle temperature, the concentration difference can be expected to be still lower.

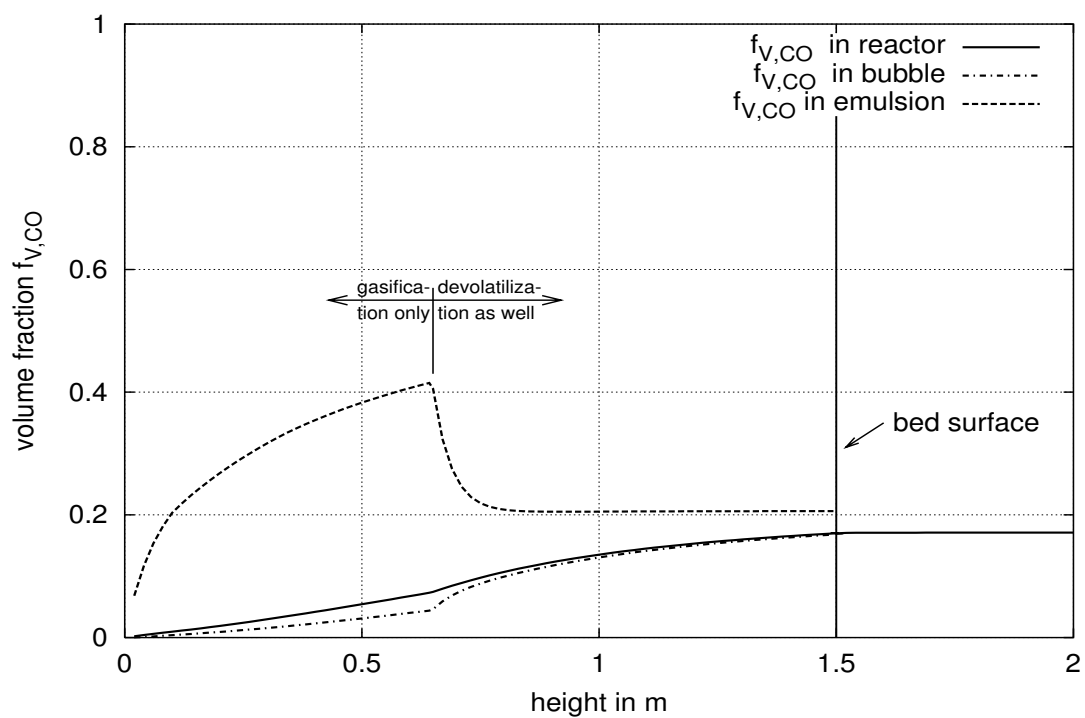


Figure 4.9: Evolution of the volume fraction of carbon monoxide in the dense phase, the bubble phase and the reactor average (standard conditions).

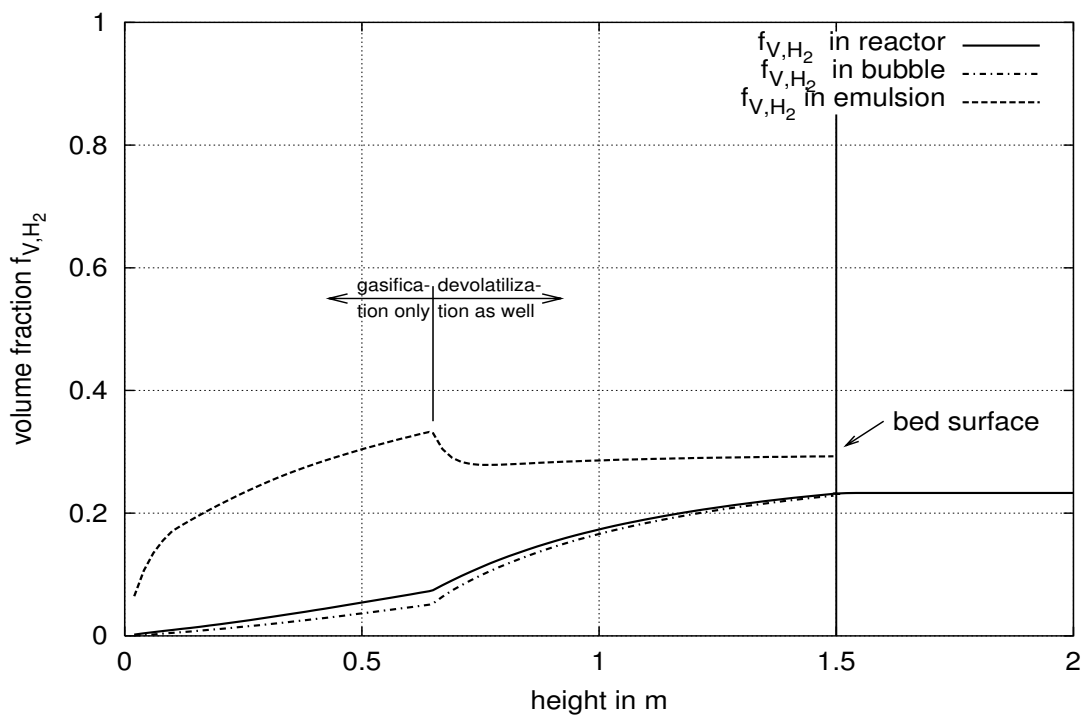


Figure 4.10: Evolution of the volume fraction of hydrogen in the dense phase, the bubble phase and the reactor average (standard conditions).

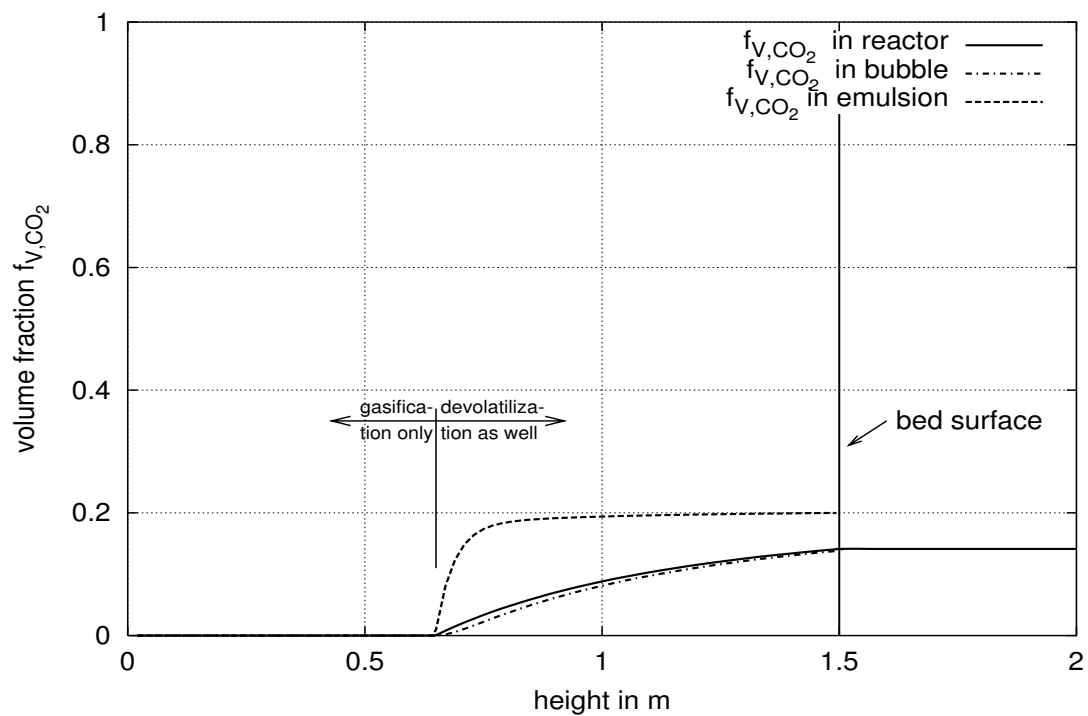


Figure 4.11: Evolution of the volume fraction of carbon dioxide in the dense phase, the bubble phase and the reactor average (standard conditions).

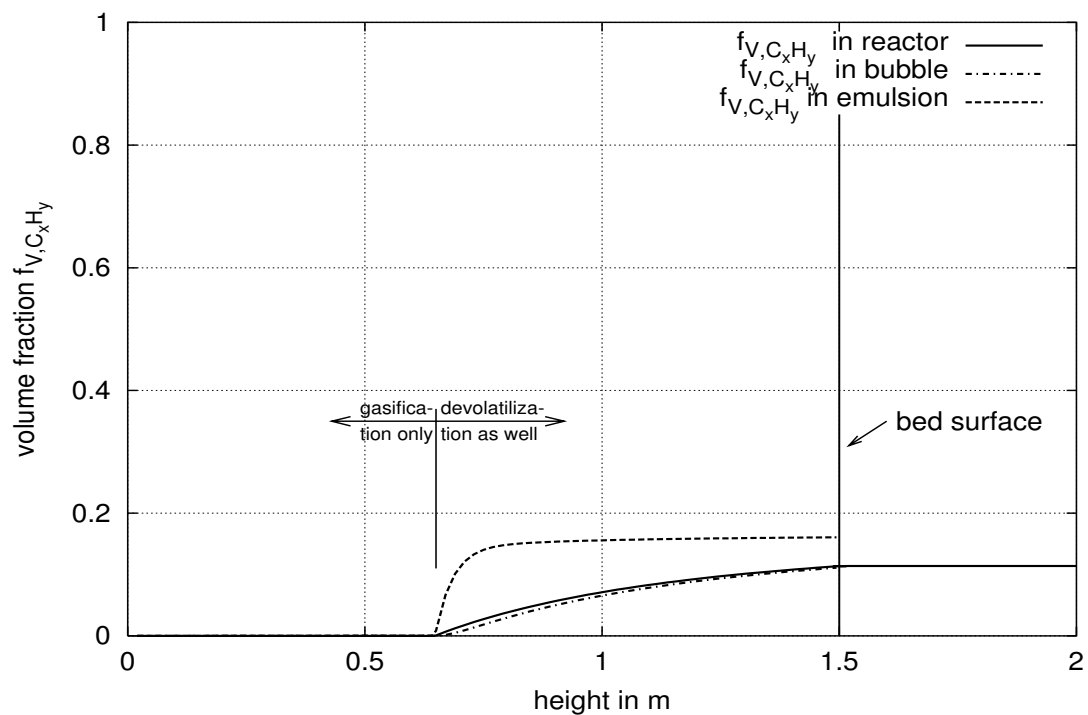


Figure 4.12: Evolution of the volume fraction of C_xH_y in the dense phase, the bubble phase and the reactor average (standard conditions).

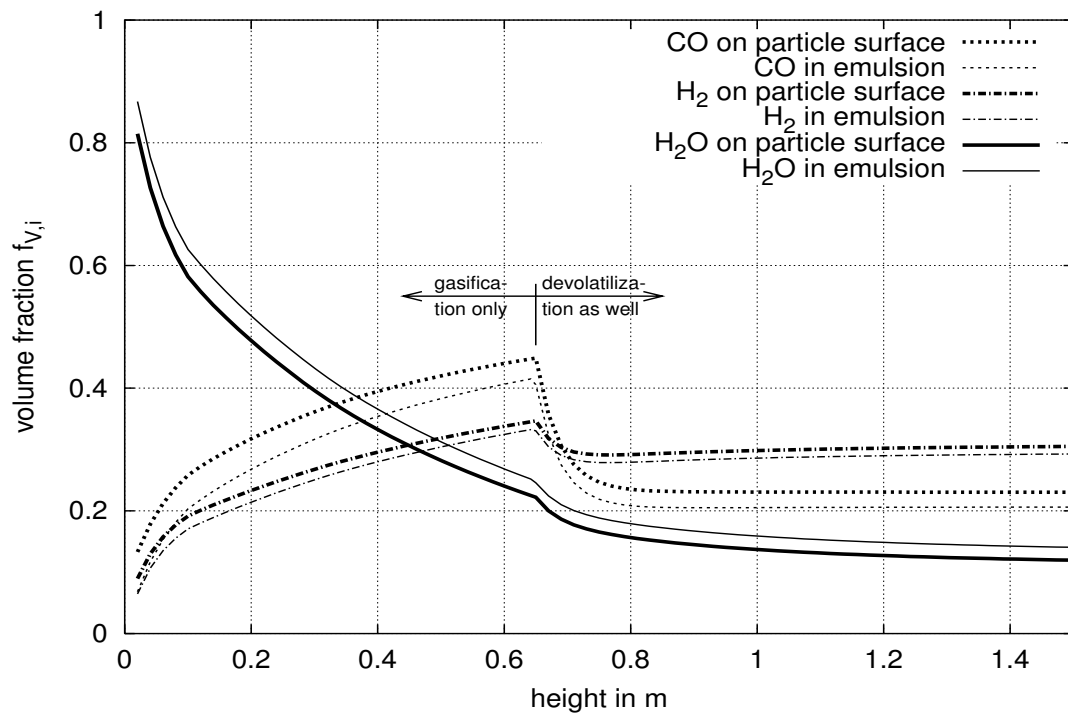


Figure 4.13: Species volume fraction on the particle surface (standard conditions).

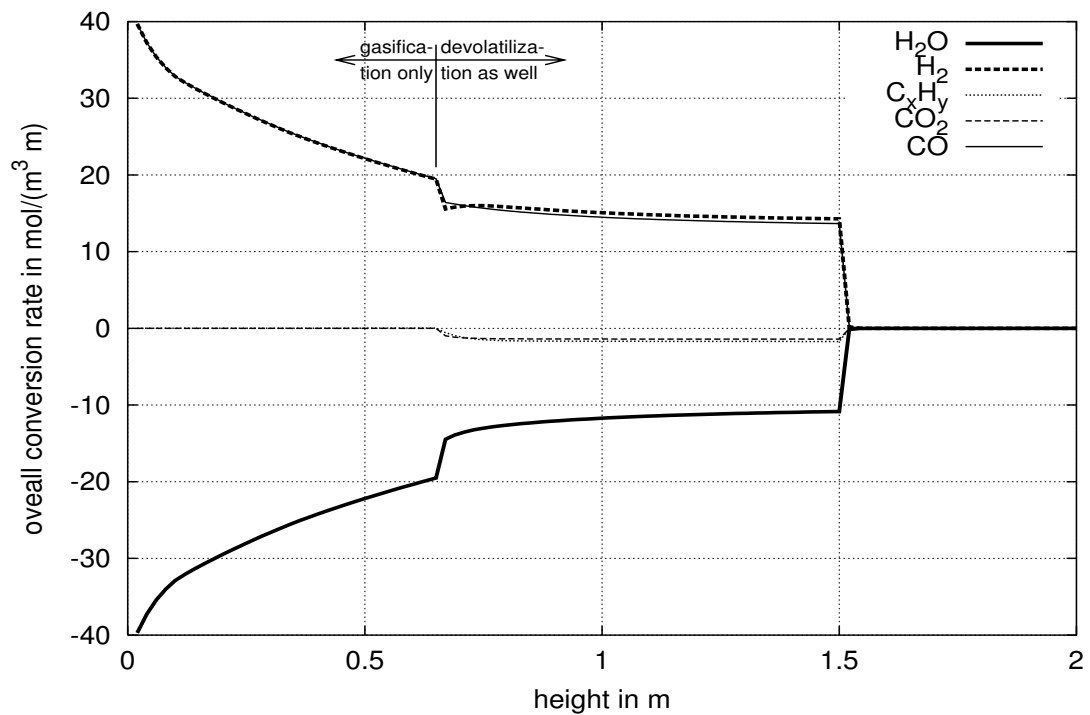


Figure 4.14: Overall conversion rate of the single species in the dense phase. The step behavior due to the beginning release of the devolatilization products is very clear observable. Remarkable is the by far dominating influence of the steam gasification reaction (standard conditions).

Reaction Rates

Overall Conversion for a Species The reaction rates $R_{gt,i} = \sum_{j=1}^{\bar{m}} (\bar{v}_{i,j} \bar{r}_i)$ in terms of $\frac{\text{mol}}{\text{m}^3 \text{s}}$ reflect the chemical conversion of a species i as a result of the sum of every reaction j where i is involved. By contrast, the reaction rates $R_{gh,i}$ in terms of $\frac{\text{mol}}{\text{m}^3 \text{m}}$ take into account for the different gas velocities within the phases. To distinguish the two rates the former is called *overall reaction rate* and the latter *overall conversion rate*. The corresponding rates for a single chemical reaction are called *reaction rate* and *conversion rate* respectively. Therefore, reactor specific characteristics as the velocities or the phase cross sections play an important role for the conversion rate. The model for the flow pattern has been chosen according to a plug flow reactor. Hence, the velocity of the volumetric flow in the bubble phase or the emulsion phase determines the residence time in the volume of a slice with the height ΔH at a certain height. For *steam*, the overall conversion rate has its maximum of about $40 \frac{\text{mol}}{\text{m}^3 \text{m}}$ at the bottom of the reactor, since there, the gas in the dense phase consists entirely of steam. However, since the steam in the emulsion is consumed rapidly, the conversion slows down. The reduction of the conversion rate is considerably at the reactor bottom. From a height of about 0.15m on, the conversion rate slows down nearly linearly with a slope of $20 \frac{\text{mol}}{\text{m}^3 \text{m}}$. Again, at a height of 0.65m , a step behavior in the trace of the overall conversion rates is observable. This conduct is due to the dilution of the steam content in the dense phase with steam-poor gases released by devolatilization into the emulsion. Finally, the lower total carbon content as previously discussed (refer to Fig. 4.3) participates as well on this step decrease. Every conversion rate reaches an almost constant value at this point. Again, this indicates the by far dominating participation of the devolatilization products on the gas composition. From the existence of *carbon dioxide* and C_xH_y on, a low conversion due to the carbon dioxide gasification, and the producer-gas reaction is also present. These reaction rates reach about 10% of the lowest value of the reaction rate of steam gasification.

Single Reaction Rates The reaction rates of the different reactions are plotted in Fig. 4.15 and 4.16. The evolution of the curves is similar to the evolution of the overall conversion rates. The conversion of CO_2 and C_xH_y begins at a height of 0.65m . Despite the dilution of steam in the emulsion due to the gases released by devolatilization and the resulting lower reaction rate, the steam gasification reaction stays several times faster than the carbon dioxide gasification or the methane decomposition by the backward reaction of the hydrogasification. The latter is due to the equilibrium of the reaction. According literature [Barrio and Hustad 2000, Barrio et al. 2000, Reed 1981], the carbon dioxide gasification is about 4 times slower than the steam gasification. The larger difference pointed out in Fig. 4.15 is due to the lower concentration of carbon dioxide in the emulsion.

The reaction rate of methane decomposition with steam and the heterogeneous water-gas-shift reaction shown in Fig. 4.16 are about 100 times slower than the carbon dioxide gasification reaction rate and several hundred times slower than the steam gasification reaction rate. In fact, the homogeneous water-gas-shift reaction does hardly occur at all. Due to the position of the equilibrium, the heterogeneous water-gas-shift reaction indicates a production of carbon dioxide up to a height of 0.65m and runs in the other direction above. The kinetics of methane decomposition does not allow for a backward reaction. An inaccuracy for the heterogeneous water-gas-shift reaction in the freeboard can be seen in Fig. 4.16. The presence of the solid catalyst is modeled by the minimum fluidization porosity (refer to Table 3.9). It has not been accounted for the actual porosity of the active particles. Thus,

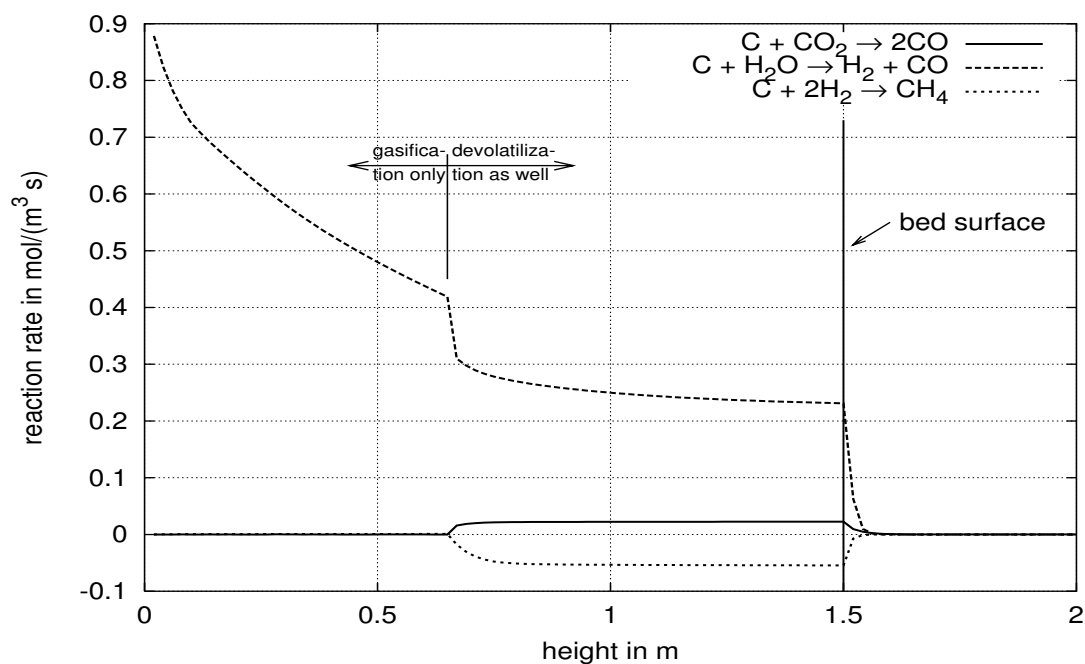


Figure 4.15: Reactions 3.16, 3.17 and 3.22 which are dominating the whole reaction system.

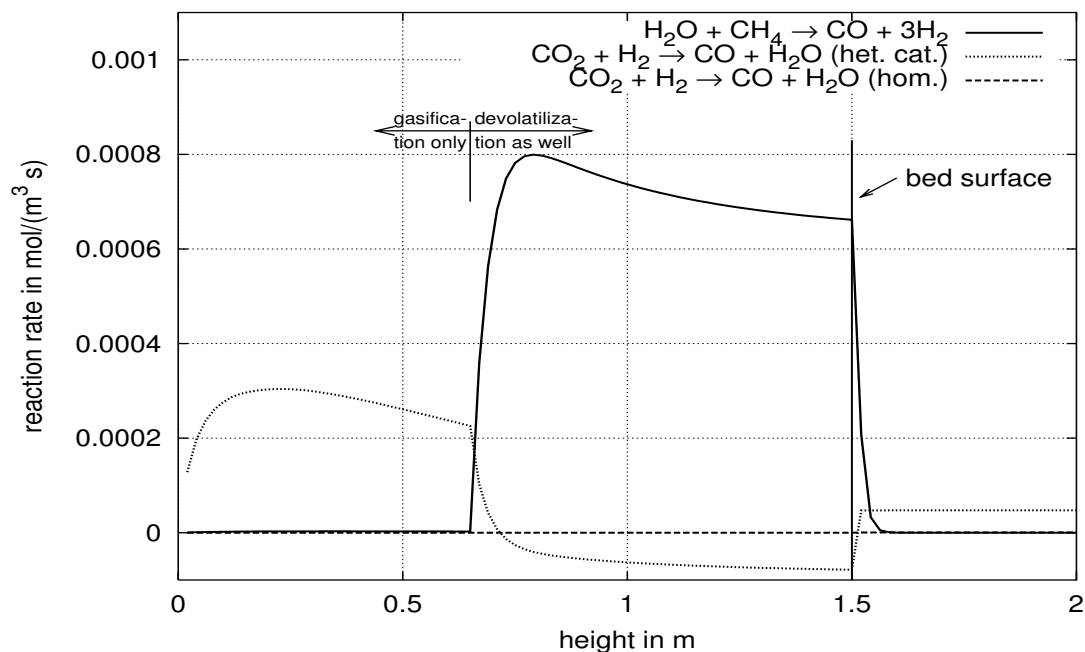


Figure 4.16: Homogeneous and the heterogeneous water-gas-shift reaction and the C_xH_y decomposition reaction. The homogeneous water-gas-shift reaction is not visible even in the nearly 1000 times smaller scale (standard conditions).

the reaction rate does not reach zero when no more char for catalytic activity is present in the freeboard. Since the reactions plotted in Fig. 4.16 do not affect the solution at all (as discussed in chapter 4.2), this is not significant for the simulation result.

Mass-Transfer Rate Bubble-Emulsion

The mass-transfer rate in $\frac{\text{mol}}{\text{m}^3 \text{m}}$ from the bubble phase into the emulsion phase is plotted in Fig. 4.17. The mass-transfer rate of steam is positive for a transport into the dense phase, and reaches with $10-30 \frac{\text{mol}}{\text{m}^3 \text{m}}$ about the same order as the overall conversion rate. At the bottom, the mass-transfer rate increases rapidly according to the growing concentration difference between bubble phase and dense phase (refer to Fig. 4.8). At a height of $0.1m$, the mass-transfer rate begins to decrease steadily. This is a result of the enlarging cross section in the conic part. There, the mass transfer decreases because of the decrease of the term $\frac{6A_b}{d_b A_e U_e} k_{be}$ which is essential coefficient for the mass transfer into the dense phase (refer to Table 3.21 on page 80). In addition, the growth of the steam concentration difference is stagnating up to $0.65m$ bed height. In Fig. 4.17, both curves are sketched. The factor $\frac{Q_{be}}{V_b} k_{be}$ which is $\frac{6}{d_b} k_{be}$ is plotted, as well. The decay of the former has the highest value at the bottom of the reactor. On the other hand at the reactor bottom, the growth of the concentration difference is still higher. The mass transfer rate from the bubble phase to the emulsion phase increases therefore at the bottom of the reactor. At a height slightly over $0.1m$, the mass transfer rates reach their maximum. Afterwards, they are falling continuously because of decay of the factor $\frac{6A_b}{d_b A_e U_e} k_{be}$ exceeds the growth of the steam concentration difference. At the height of devolatilization onset, the steam concentration difference is falling, as well. Hence, the mass transfer rates show a sudden interruption in the smooth evolution of the graph. Comparing the two terms $\frac{6A_b}{d_b A_e U_e} k_{be}$ and $\frac{6}{d_b} k_{be}$, a strong influence of the ratio of the cross sections A_b/A_e is suggested since U_e is largely constant. This can be verified in Fig. 4.2 on page 85. Fig. 4.18 shows a comparison of the mass transfer rate and the overall chemical conversion rate for steam.

Gas Consumption and Gas Generation

The consumption and the formation of the participating gases is shown in Fig. 4.19 for steam, in Fig. 4.20 for hydrogen and in Fig. 4.21 for carbon dioxide. Carbon monoxide is not presented because its evolution is similarly to the evolution of hydrogen. The relation of the generated to the introduced quantity is slightly higher in the case of carbon monoxide. This is due to the lower amount released by devolatilization. Carbon dioxide and C_xH_y have similar shapes, as well. Therefore, just the curve for the carbon dioxide is shown. The consumed water (Fig. 4.19) is the difference between the steam introduced into the reactor by fluidization, by the water released by drying and devolatilization and the actual steam flow, which is also plotted. Up to $0.65m$ the graph for the consumed water increases fairly parabolic. Above the height of $0.65m$ the consumption slows down and the graph shows a nearly linear behavior. The percentage of the consumed water can be seen on the secondary axis at the bed surface. It is about 16% of the introduced water.

The consumption of carbon dioxide begins above $0.65m$ where it appears for the first time due to the gases released by devolatilization. The consumed carbon dioxide is about 3% of the total amount of CO_2 released by devolatilization.

The formation of hydrogen is 100% of the up to $0.65m$ present H_2 because the only possibility

for hydrogen formation is the steam gasification reaction. Passing the height of 0.65m , hydrogen released by devolatilization is also present. Therefore, the amount of hydrogen generated by the chemical conversion of steam, C_xH_y , etc. reaches about 28% at the end of the bed. Since the values for H_2 , CO , CO_2 and C_xH_y are based on the (uncertain) values for the devolatilization composition, they may be regarded with caution. A summary of the consumed or formed gases by the gasification reactions shows Table 4.2.

Species	% by Volume Consumed	% by Volume Generated
Water H_2O	16.0	
Hydrogen H_2		27.6
Carbon monoxide CO		36.8
Carbon dioxide CO_2	2.7	
Methane CH_4	1.2	

Table 4.2: Consumed water in % of the introduced amount. By gasification reactions consumed and generated gases (H_2 , CO , CO_2 , C_xH_y) in % of the obtained amount. The remainder to 100% is released by devolatilization.

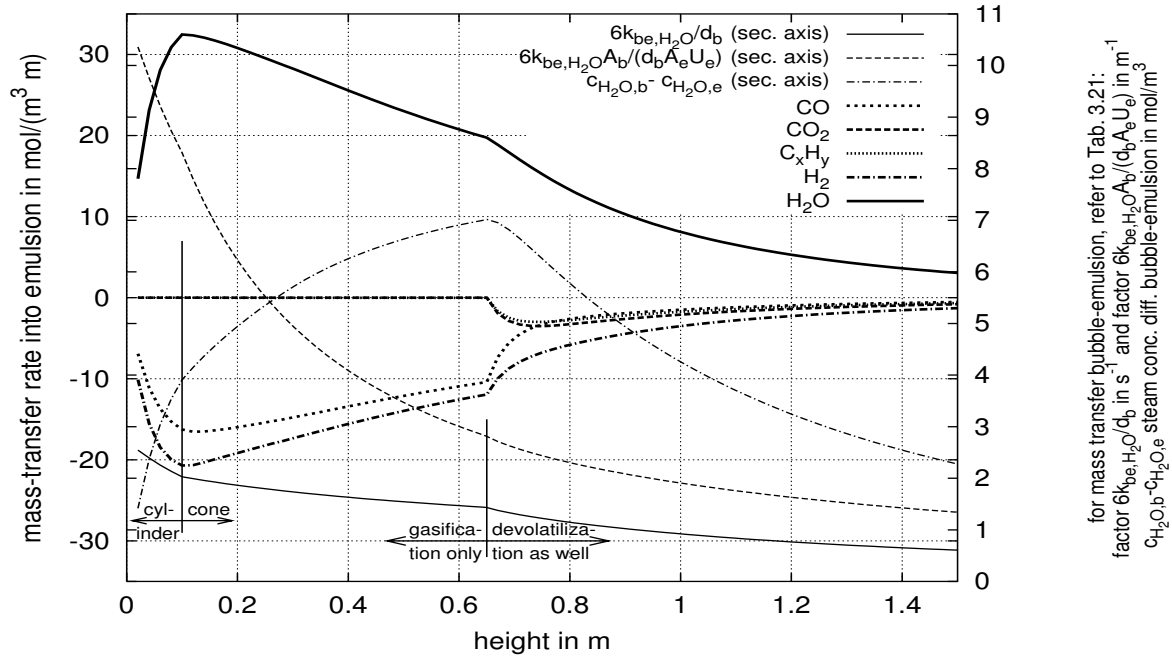


Figure 4.17: Mass-transfer rate in $\frac{\text{mol}}{\text{m}^3 \text{m}}$ from the bubble phase into the dense phase. Further, the concentration difference of steam between the bubble phase and the dense phase and the factors $\frac{6A_b}{d_b A_e U_e} k_{be}$ and $\frac{6}{d_b} k_{be}$ (refer to Table 3.21; standard conditions).

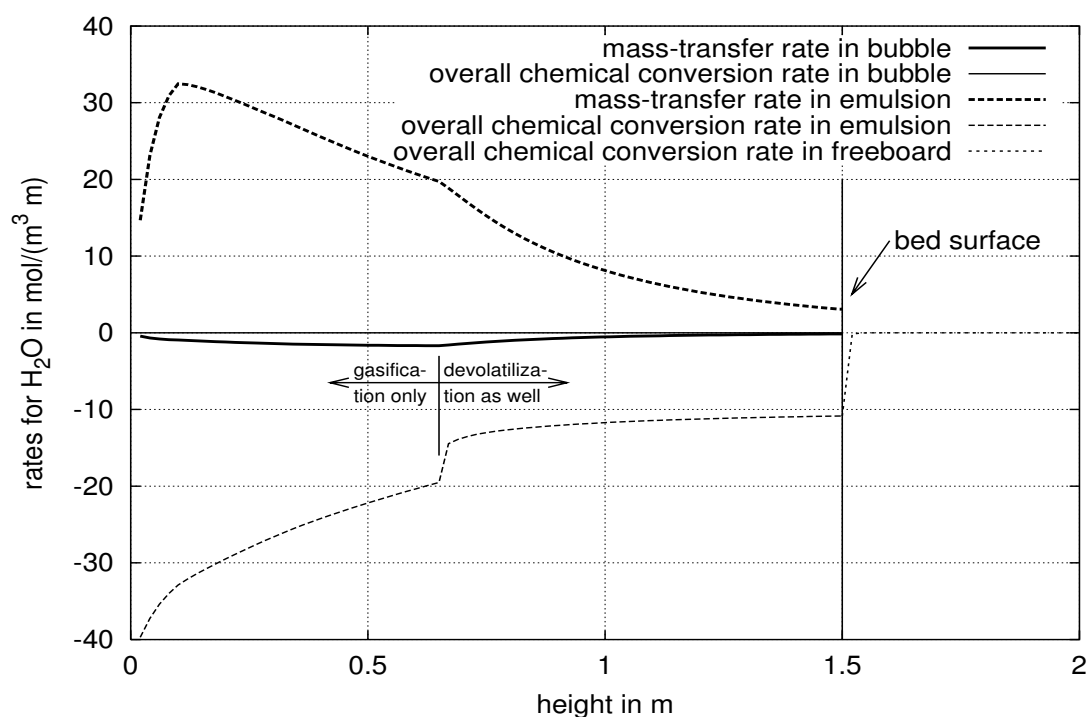


Figure 4.18: Evolution of the overall conversion rates of steam in the dense phase and the bubble phase due to the chemical reactions in the bubble phase, the chemical reactions in the dense phase and the mass-transfer rates between bubble phase and dense phase (standard conditions).

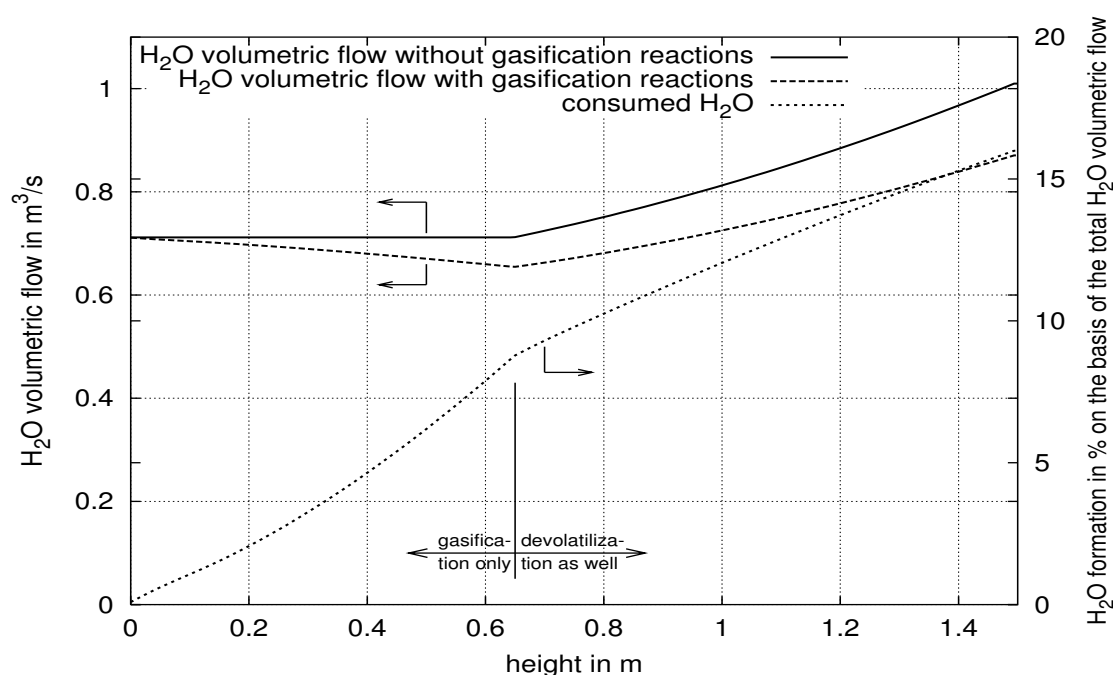


Figure 4.19: Consumed steam vs. the reactor height. It is about 16.0% at the end of the bed. In fact, it does not change in the freeboard.

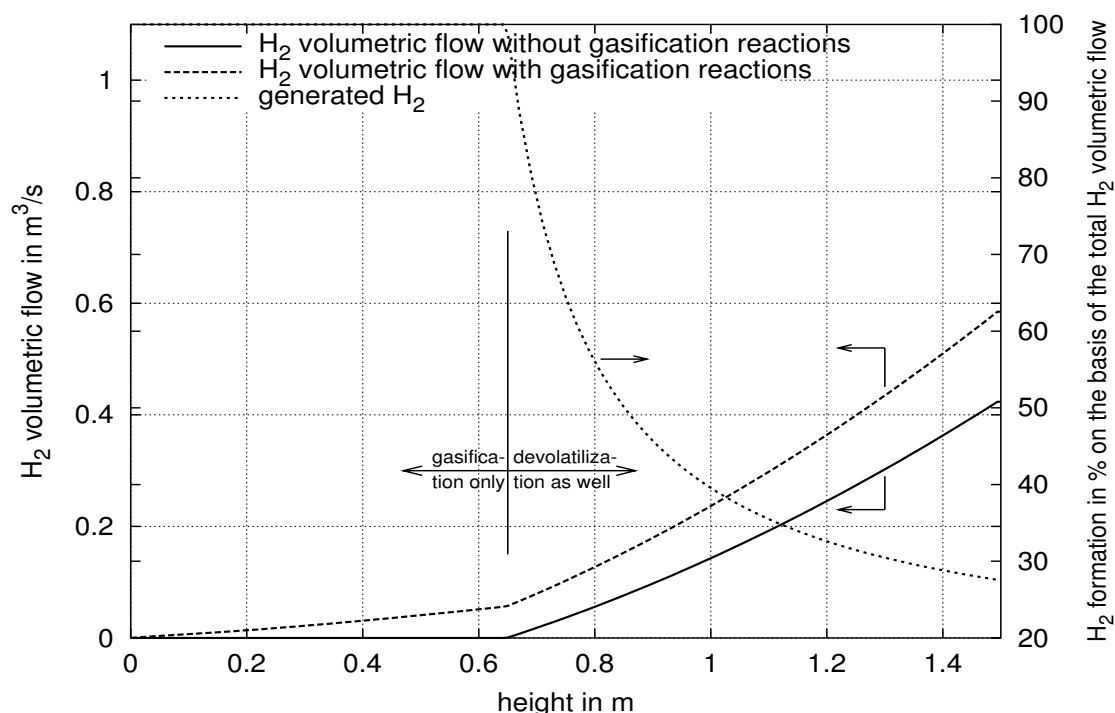


Figure 4.20: Generated hydrogen vs. the reactor height. Finally, about 27.6% of the hydrogen obtained is generated by chemical conversion of steam or C_xH_y . The rest is a direct devolatilization product (standard conditions).

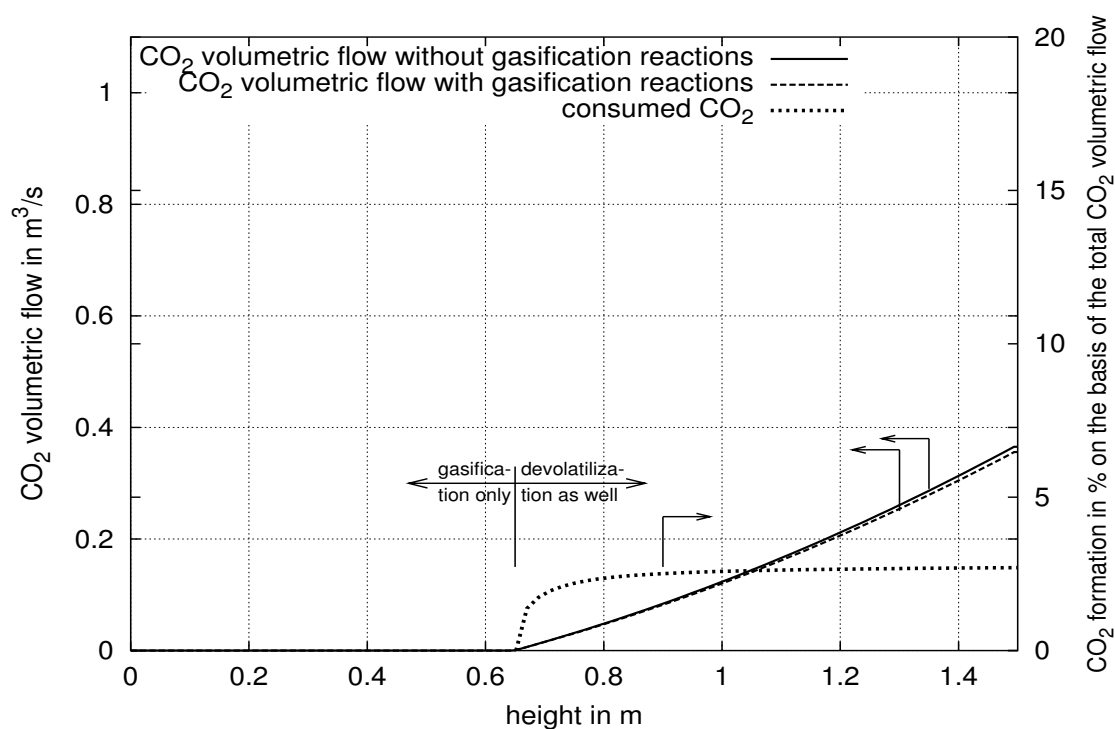


Figure 4.21: Consumed carbon dioxide vs. the reactor height. Finally, a 2.7% part of the carbon dioxide obtained is converted by carbon dioxide gasification. The rest is a direct devolatilization product (standard conditions).

4.2 Sensitivity Analysis

The developed model depends on a number of constants as for example constants for the chemical system, initial conditions, constants for transport phenomena or operation conditions. Usually, a part of them are fairly known or can be adjusted. The objective of sensitivity analysis is to determine systematically the effect of chosen parameters on the solution. A general representation of the system is

$$f(x_1, x_2, \dots, x_i, \dots, x_{\bar{n}^*}; \xi_1, \xi_2, \dots, \xi_j, \dots, \xi_{\bar{m}^*}) = 0 \quad (4.2)$$

Beside the variables x_i which stand for the concentrations, spatial coordinates, or the time, exist the parameters ξ_j , which are fixed for the simulation. The linear sensitivity coefficient ω_j for the system f with regard to the parameter ξ_j is defined as

$$\omega_j = \frac{\partial f}{\partial \xi_j} \quad (4.3)$$

The linear sensitivity coefficient describes a linear system, whereas the original system is in general non-linear. Therefore, the linear sensitivity coefficient can reflect the influence of only small deviations of the parameters. The relative or logarithmic sensitivity coefficients are defined by:

$$\omega_j^{rel} = \frac{\xi_j}{f} \frac{\partial f}{\partial \xi_j} = \frac{\partial \ln f}{\partial \ln \xi_j} \quad (4.4)$$

For the evaluation of the simulation results, the following discrete formulation is used:

$$\bar{\omega}_j^{rel} = \frac{\xi_j}{f} \frac{\Delta f}{\Delta \xi_j} = \frac{\xi_j}{f} \frac{f(x_i, \xi_j) - f(x_i, \kappa \xi_j)}{\xi_j - \kappa \xi_j} = \frac{1 - \frac{f_\kappa}{f}}{1 - \frac{\kappa \xi_j}{\xi_j}} = \frac{1 - \frac{f_\kappa}{f}}{1 - \kappa} \quad (4.5)$$

where $f_\kappa = f(x_i, \kappa \xi_j)$. The parameter κ is 0.9 for the -10% variation and 1.1 for the $+10\%$ variation. With a preliminary defined standard (refer to chapter 3), the solution of the standard system $f(x_i, \xi_j)$ is evaluated. Afterwards, the solution $f_\kappa(x_i, \kappa \xi_j)$ resulting from a variation of $+10\%$ and/or -10% of the interesting parameters is computed. The results of this variations are evaluated with respect to the standard. Therefore, the relative system response $\bar{\sigma}^{rel}$ is defined as

$$\bar{\sigma}_j^{rel} = \frac{f_\kappa(x_i, \kappa \xi_j)}{f(x_i, \xi_j)} \quad (4.6)$$

With this definition, the system reactions of the different variations are already comparable if $|1 - \kappa|$ is the same. However, by dealing with $\bar{\sigma}_j^{rel}$, it has to be kept in mind, that a remarkable sensitivity is present for $|1 - \bar{\sigma}_j^{rel}| \geq 0.1$. This corresponds to a discrete relative sensitivity coefficient of $|\bar{\omega}_j^{rel}| \geq 1$ (refer to Eq. 4.6). A parameter variation, which provokes an opposing evolution of a result value is reflected by a negative discrete relative sensitivity coefficient for this value. A higher rate constant for the steam gasification reaction leads to a positive discrete relative sensitivity coefficient for the steam conversion rate, which indicates an enhanced steam conversion (positive sensitivity coefficient). Contrary to this, the carbon mass in the solid circulation flow decreases. Therefore, this result has a negative discrete relative sensitivity coefficient.

Table 4.3 and Table 4.4 show the discrete relative sensitivity coefficients for the gas conversion, the volumetric flows in the product gas, and the carbon mass flow within the circulation bed material.

Sensitivity analysis is performed for model parameters, which are fairly known or are expected to have a higher influence, respectively. Other sensitivity analysis concern the plant parameters, which can be influenced by the process conducting or fuel preparation.

Sensitivities for Model Parameters

For the development of the model, numerous model parameters are chosen according literature or according observations on the pilot plant reactor.

A summary of the relative discrete sensitivity coefficients for the parameters where a sensitivity analysis is performed is presented in Table 4.3. The top line shows the results for the standard situation. The first five values represent the amount of the converted gas volume in m_N^3/h . Negative values indicate a gas consumption, whereas positive values stand for a gas formation. The following five values represent the volumetric flows of the investigated species in the product gas flow in m_N^3/h . Again, higher hydrocarbons are lumped into the methane fraction. The last value in the top line shows the carbon mass flow with the circulation bed material in kg/h . The subsequent lines show the discrete relative sensitivity coefficients $\bar{\omega}_j^{rel}$ for the variations described in the second column. The first column describes the parameters for the standard reactor. Discrete relative sensitivity coefficients, which have an absolute value in the vicinity and above unity ($|\bar{\omega}_j^{rel}| \geq 0.9$) are marked by an underline. Discrete relative sensitivity coefficients, which have an absolute value over or equal 0.5 are bold-faced.

In Table 4.3 can be clearly seen that all investigated model parameters but the devolatilization parameter $x_2 = \frac{n_{CH_4}}{n_{CO}}$ have a disproportionate low influence on the total carbon mass in the reactor as well as to the consumed water. The splitting of the through-flow and the case of the uniformly distributed wood in the bed can not be considered as model parameter. The former is an assumption of the two-phase-theory and the latter results from a deviation of the standard, which is too large that the obtained discrete relative sensitivity coefficient can be considered as valid in this range. This can be seen by comparing line <17> and line <10> in Table 4.3, which do not have the same sensitivities. Especially for the hydrogen fraction and the carbon dioxide fraction, $\bar{\omega}_j^{rel}$ differs about 100%. However, both parameters are presumptions for the model and therefore mentioned here, as well.

The more sensitive model parameters within the investigated ones are all gasification reactions, the wood penetration depth into the bed, the devolatilization parameters x_1 and x_2 , and the gas-split of the through-flow (refer to Table 4.3). However, just a few of them are of further interest since sensitivities for the carbon dioxide and the hydrocarbons are elevated basically due to the small amount converted in the case of the standard conditions. Therefore, if the reaction rate for the carbon dioxide gasification (refer to line <1> and line <2> in Table 4.3) changes slightly, the effect to the part of the carbon dioxide which is converted, is considerably $\bar{\omega}_j^{rel} \sim 0.97$. This means, that a 10% percent higher frequency factor results in a nearly 10% enhanced carbon dioxide conversion. On the other hand, the total volumetric flow decreases just slightly ($\bar{\omega}_j^{rel} \sim -0.03$). An analogous conclusion can be taken for the hydrogasification reaction. Thus, if just the effects to the product gas flow are regarded, the unique model parameter which has a disproportional high influence, is the devolatilization parameter x_2 . Considering the definition of $x_2 = n_{CH_4}/n_{CO}$, the influence on the methane content (representative for C_xH_y) of the product gas is found to be direct. The strong influence of this factor to the H_2 content can be explained by the dependency of the whole devolatilization composition on just one of these two factors (refer to Fig. 3.8). Still, there

Standard flow:		Converted by Gasification Reactions					Volume Flow of Product Gas					$\dot{m}_{ch,cir}$
gases in m_N^3/h , char mass		CO	CO ₂	C _x H _y	H ₂	H ₂ O	CO	CO ₂	C _x H _y	H ₂	H ₂ O	C
in solid circulation flow $\dot{m}_{ch,cir}$ in kg/h)		152.8	-10.1	-11.2	154.9	-133.4	411.6	339.3	273.5	559.9	819.5	251.3
RELATIVE SENSITIVITY												
Standard	Variation	CO	CO ₂	C _x H _y	H ₂	H ₂ O	CO	CO ₂	C _x H _y	H ₂	H ₂ O	C
⟨1⟩ Reaction C + CO ₂ → 2CO (refer to Eq. 3.16)	10% lower chemical rate constant ↓	0.118	0.974	-0.025	-0.014	-0.013	0.044	-0.029	0.001	-0.004	0.002	-0.017
⟨2⟩ Reaction C + CO ₂ → 2CO (refer to Eq. 3.16)	10% higher chemical rate constant ↑	0.117	0.970	-0.025	-0.014	-0.013	0.044	-0.029	0.001	-0.004	0.002	-0.017
⟨3⟩ Reaction C + H ₂ O → CO + H ₂ (refer to Eq. 3.17)	10% lower chemical rate constant ↓	0.528	-0.068	-0.257	0.492	0.615	0.196	0.002	0.010	0.136	-0.100	-0.165
⟨4⟩ Reaction C + H ₂ O → CO + H ₂ (refer to Eq. 3.17)	10% higher chemical rate constant ↑	0.493	-0.064	-0.236	0.460	0.574	0.183	0.002	0.010	0.127	-0.093	-0.154
⟨5⟩ Reaction C + 2H ₂ → CH ₄ (refer to Eq. 3.22)	10% lower chemical rate constant ↓	0.009	0.003	0.930	0.143	0.010	0.003	0.000	-0.038	0.040	-0.002	0.018
⟨6⟩ Reaction C + 2H ₂ ⇌ CH ₄ (refer to Eq. 3.22)	10% higher chemical rate constant ↑	0.009	0.004	0.922	0.141	0.010	0.003	0.000	-0.038	0.039	-0.002	0.018
⟨7⟩ Reaction H ₂ O + CH ₄ ⇌ CO + 3H ₂ (refer to Eq. 3.23)	10% lower chemical rate constant ↓	0.000	0.000	0.006	0.001	0.001	0.000	0.000	0.000	0.000	0.000	0.000
⟨8⟩ Mass-transfer bubble- emulsion according to Eq. 2.19	10% higher mass- transfer rate form bubble to emulsion ↑	0.120	-0.026	-0.046	0.115	0.141	0.044	0.001	0.002	0.032	-0.023	-0.037

To be continued on next page.

Continued from previous page.

Standard flow:		Converted by Gasification Reactions					Volume Flow of Product Gas					$\dot{m}_{ch,cir}$
gases in m_N^3/h , char mass		CO	CO ₂	C_xH_y	H ₂	H ₂ O	CO	CO ₂	C_xH_y	H ₂	H ₂ O	C
in solid circulation flow $\dot{m}_{ch,cir}$ in kg/h)		152.8	-10.1	-11.2	154.9	-133.4	411.6	339.3	273.5	559.9	819.5	251.3
RELATIVE SENSITIVITY												
Standard	Variation	CO	CO ₂	C_xH_y	H ₂	H ₂ O	CO	CO ₂	C_xH_y	H ₂	H ₂ O	C
⟨9⟩ 0.85m wood penetration into bed	10% lower wood penetration into bed ↓	-0.023	0.519	0.589	-0.005	-0.108	-0.009	-0.015	-0.024	-0.002	0.018	0.030
⟨10⟩ 0.85m wood penetration into bed	10% higher wood penetration into bed ↑	-0.046	0.455	0.513	-0.031	-0.120	-0.017	-0.014	-0.021	-0.009	0.020	0.034
⟨11⟩ release of all gases from devolatilization into emulsion	10% of the devolatilization gases in bubble ↓	0.038	0.055	0.253	0.067	0.035	0.014	-0.002	-0.010	0.018	-0.006	-0.005
⟨12⟩ entire through-flow in bubble-phase	10% of the through-flow in emulsion ↓	-0.513	0.172	0.420	-0.468	-0.614	-0.191	-0.005	-0.017	-0.129	0.100	0.166
⟨13⟩ devolatilization parameter $x_1 = 1.35$	10% lower devolatilization parameter $x_1 = \frac{n_{CO_2}}{n_{CO}}$ ↓	-0.265	0.293	-0.845	-0.421	-0.348	-0.354	0.644	-0.389	0.900	-0.355	0.067
⟨14⟩ devolatilization parameter $x_1 = 1.35$	10% higher devolatilization parameter $x_1 = \frac{n_{CO_2}}{n_{CO}}$ ↑	-0.255	0.263	-0.721	-0.390	-0.331	-0.331	0.595	-0.362	0.832	-0.327	0.066
⟨15⟩ devolatilization parameter $x_2 = 1.1$	10% lower devolatilization parameter $x_2 = \frac{n_{CH_4}}{n_{CO}}$ ↓	0.304	-0.115	1.319	0.505	0.366	-0.094	-0.336	0.678	-1.139	0.325	-0.065
⟨16⟩ devolatilization parameter $x_2 = 1.1$	10% higher devolatilization parameter $x_2 = \frac{n_{CH_4}}{n_{CO}}$ ↑	0.281	-0.109	1.409	0.495	0.339	-0.090	-0.315	0.630	-1.063	0.306	-0.056
⟨17⟩ 0.85m wood penetration depth ($\kappa = 1.765$ refer to Eq. 4.6)	wood uniformly distributed within bed	-0.092	0.399	0.461	-0.076	-0.163	-0.034	-0.012	-0.019	-0.021	0.027	0.045

Table 4.3: Relative discrete sensitivity coefficients $\bar{\omega}_j^{rel}$ for the model parameters.

is the problem of the large scattering values of these ratios (refer to Table 3.6).

The devolatilization parameter x_1 shows less influence on the product gas volumetric flows but this influence is still larger than the influence of the frequency factor of the steam gasification reaction.

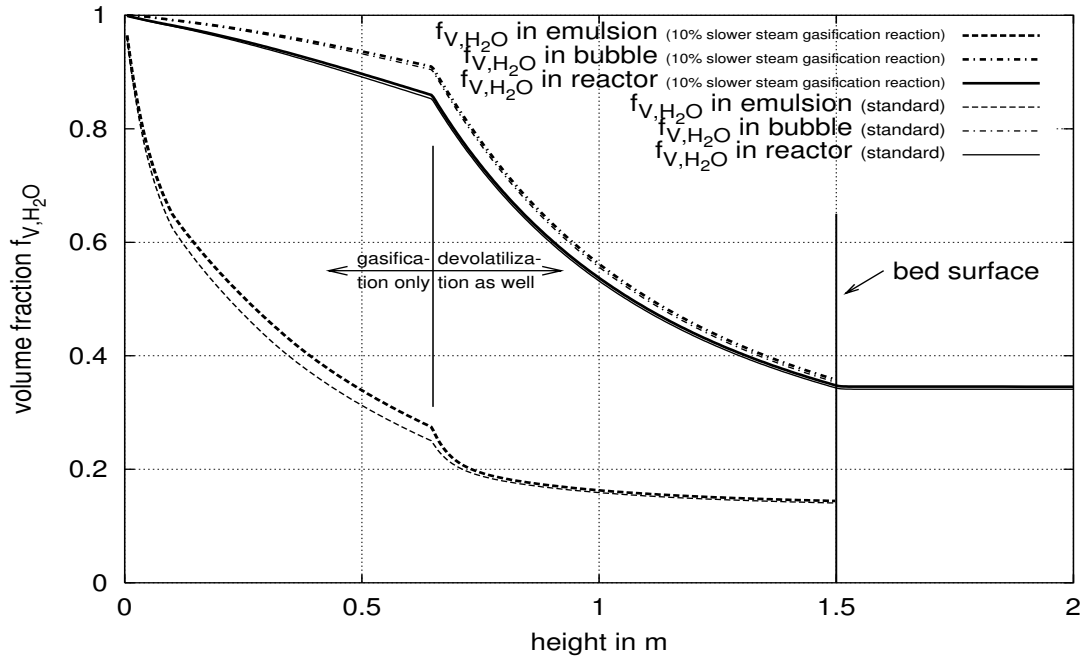


Figure 4.22: Volume fractions for steam in the bubble-phase, the emulsion-phase, and in the reactor. The thin lines correspond to the standard case, and the thick lines to a steam gasification reaction which is slower by 10%.

The frequency factor of the *steam gasification reaction* is the only reaction, which shows an enhanced influence on species, which undergo a conversion in quantitative amounts. For all species, which are participating on the steam gasification reaction, the discrete relative sensitivity of the converted amount is in the vicinity of 0.5. This is still disproportionate low but it exceeds the discrete relative sensitivity coefficients for the other reaction rates several times. Therefore, the steam gasification reaction is the clear dominating reaction. For the volumetric gas flows of the considered species in the product-gas, $\bar{\omega}_j^{rel}$ is within the range from 0.1 to 0.2. This is still quite low, but reaches already close to the values which are obtained for various important plant parameters like the circulation flow of the bed material. The evolution of the steam volume fractions for a 10% lower frequency factor are depicted in Fig. 4.22. Solely the steam volume fraction in the dense-phase shows a significant deviation from standard conditions. At the height of beginning devolatilization, even this difference to the standard levels off.

The *through-flow* is lumped into the bubble phase which is an assumption of the used theory. The variation has been undertaken to investigate the sensitivity of this simplification. For high fluidization velocities, the assumption that the dense phase remains in minimum fluidization conditions should be revised since slight deviations from the minimum fluidiza-

tion porosity lead to a significant increase of the dense phase volumetric flow. Therefore, other correlations for the gas velocity in the dense phase than $U_d = U_{mf}$ could be more appropriate (refer to chapter 2.1.1).

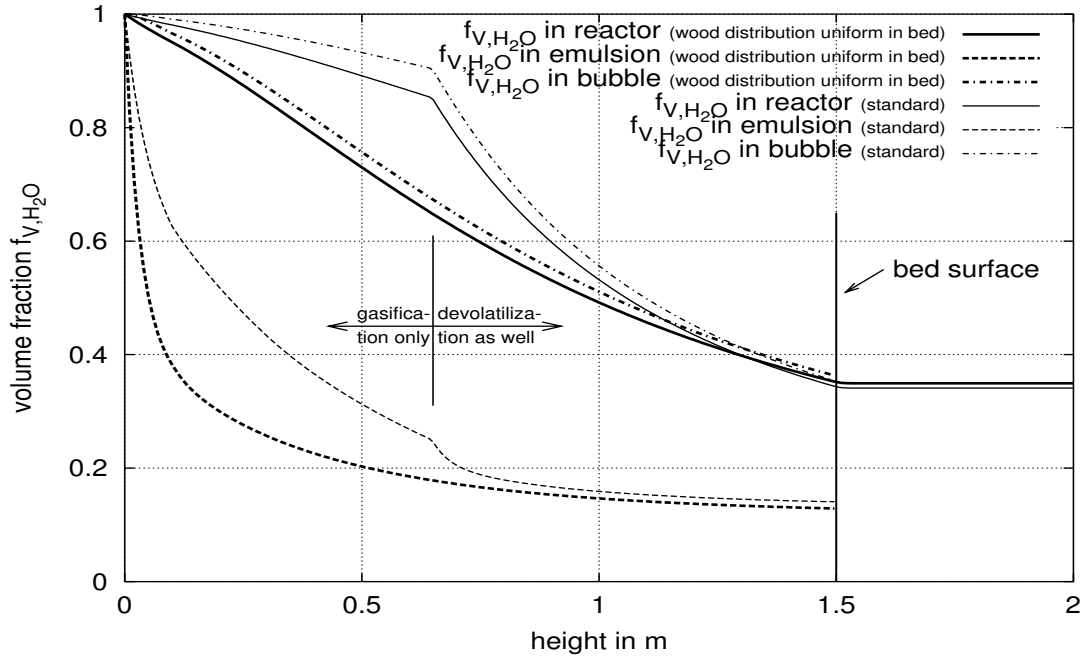


Figure 4.23: Volume fractions of steam in the bubble-phase, the emulsion-phase and in the reactor. The thin lines correspond to the standard case (0,85m wood penetration into bed) and the thick lines to the case of uniformly distributed wood in the emulsion.

The last result listed in Table 4.3 is the case of *uniform wood distribution* within the bed and therefore a uniform release of the devolatilization products within the bed. Hence, the average H_2O concentration in the emulsion is lower already from the reactor bottom on. The result is a lower steam consumption and a higher char mass flow within the circulation bed material flow. On the other hand, the carbon dioxide and the methane consumption is enhanced due to the longer contact of these gases with the char fraction in the emulsion. Variations of the assumed penetration depth of the wood fraction are rather insensitive as line <9> and line <10> in Table 4.3 show. However, a significant influence of a homogeneous wood distribution can be expected since the discrete relative sensitivity coefficients in line <17> of Table 4.3 are calculated with $\kappa = 1.765$. This is a too high value for a calculation of the discrete relative sensitivity (refer to Eq. 4.6). The high κ is also the reason for the small discrete relative sensitivity coefficients of the uniform wood distribution. Especially the steam gasification rate is just slightly reduced despite the large deviations of the volume fractions of steam in the dense phase from standard (refer to Fig. 4.23). The concentration profiles for the standard (thin lines) and the uniform wood distribution (thick lines) are sketched in Fig. 4.23. It is clearly visible, that the uniform wood distribution and therefore

the uniform release of the devolatilization gases dilutes the steam concentration in the dense phase considerably. After a strong decrease at the first instances of the reactor, the steam volume fraction keeps almost constant in the dense phase. This reduces the steam conversion from 16% of the fluidization gas flow to 13.5% of the fluidization gas flow.

The investigated parameters discussed above, are the only model parameter which have an influence on the solution, which is comparable to the more sensitive plant parameters as the bed height (refer to Table 4.4). The case of a split of the devolatilization products into 10% which goes into the bubble-phase and the residue, which goes into the dense-phase shows no remarkable sensitivity. The even lower reaction rates of the other reactions listed in Table 3.9 have not been investigated for their sensitivity.

Sensitivities for Plant Parameters

The discrete relative sensitivity coefficient of the plant parameters are listed in Table 4.4. The important sensitive plant parameters are the operating temperature, the solid circulation flow, load variations, and the variation of the bed height. The other plant parameters investigated are listed in Table 4.4 but not further discussed.

The dependency on the *temperature* underlines the necessity of a detailed modeling of the heat-balance in the particle model. On the other hand, a $\pm 10\%$ variation of the temperature is about $\pm 110K$, which is beyond the situations occurring during normal operation. However, it is one of the few parameters, which have a disproportionate high influence on the volumetric flows of all species but C_xH_y in the product gas. Also, the char mass flow with the solid circulation flow is affected significantly by temperature variations. The discrete relative sensitivity coefficients are higher for an enhanced temperature than for a reduced temperature (refer to Table 4.4 line <11> and line <12>). The evolution of the water volume fraction for an enhanced temperature and standard temperature is depicted in Fig. 4.24. Contrary to the standard case, the minimum steam volume fraction is reached *before* the height of beginning devolatilization. Therefore, the gases released by devolatilization have a higher steam volume fraction than the gases in the dense-phase before the height of the beginning devolatilization. Since the devolatilization gases enrich the dense-phase with steam, for higher temperatures the conversion of carbon is enhanced in the zone of devolatilization and not retarded like in the standard case. With regard to the conversion rate, a uniform wood distribution in the bed is therefore preferable at high temperatures, whereas an accumulation of the wood on the bed surface because of floating is preferable at low temperatures.

The *bed material circulation flow* shows a discrete relative sensitivity, smaller than unity for all values investigated (refer to Table 4.4 line <9> and line <10>). Contrary to a temperature deviation, a difference of more than $\pm 10\%$ of the standard conditions will be part of every day operation. So, a discrete relative sensitivity coefficient of 0.5–0.7 for the conversion is already important. For a reduced solid circulation flow by 10%, the conversion of all species enhances. This is a result of a higher char content in the reactor.

For the *variation of the bed height*, the penetration depth of the wood fraction is the same as for standard conditions (refer to Fig. 4.25). For a higher bed, the water consumption increases because the height where the devolatilization products do not reduce the steam concentration by dilution, increases. Further, the carbon mass which is transported out of the reactor with the solid circulation flow decreases. An increase of the CO and H₂ formation is the direct result of an enhanced steam conversion. The discrete relative sensitivity coefficients for the conversion rates are roughly unity for bed height variations (refer to Table 4.4 line <1>

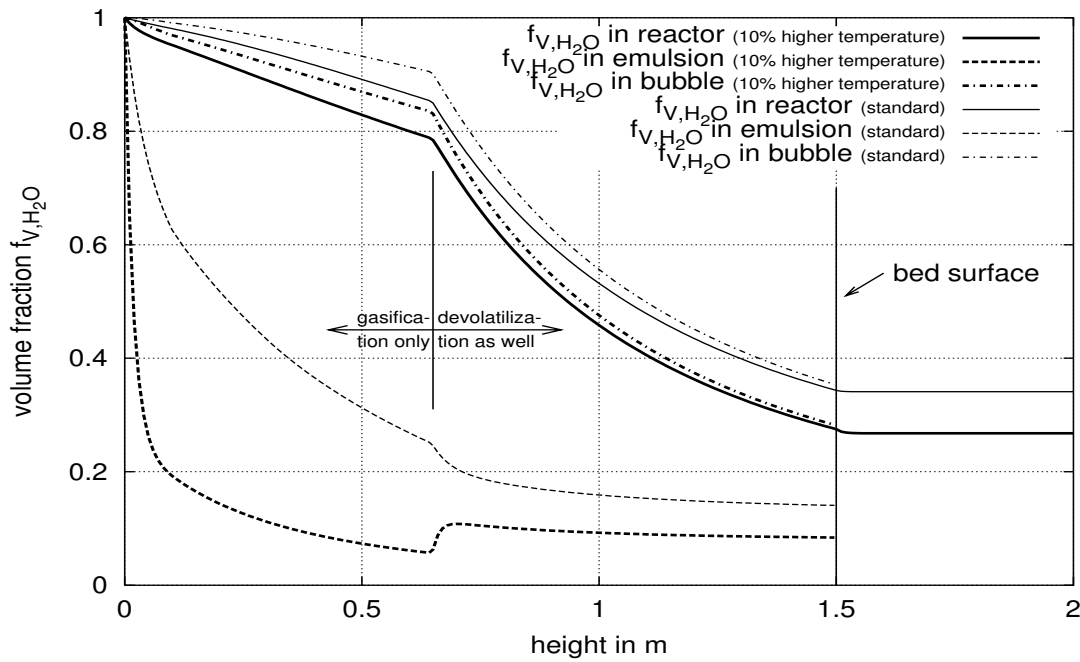


Figure 4.24: The temperature sensitivity of the steam volume fraction is distinct. Contrary to the standard case, the minimum steam volume fraction is reached *before* the height of beginning devolatilization. Since the gases released by devolatilization enrich the dense-phase with steam, the conversion of carbon is enhanced for higher temperatures and not retarded like in the standard case.

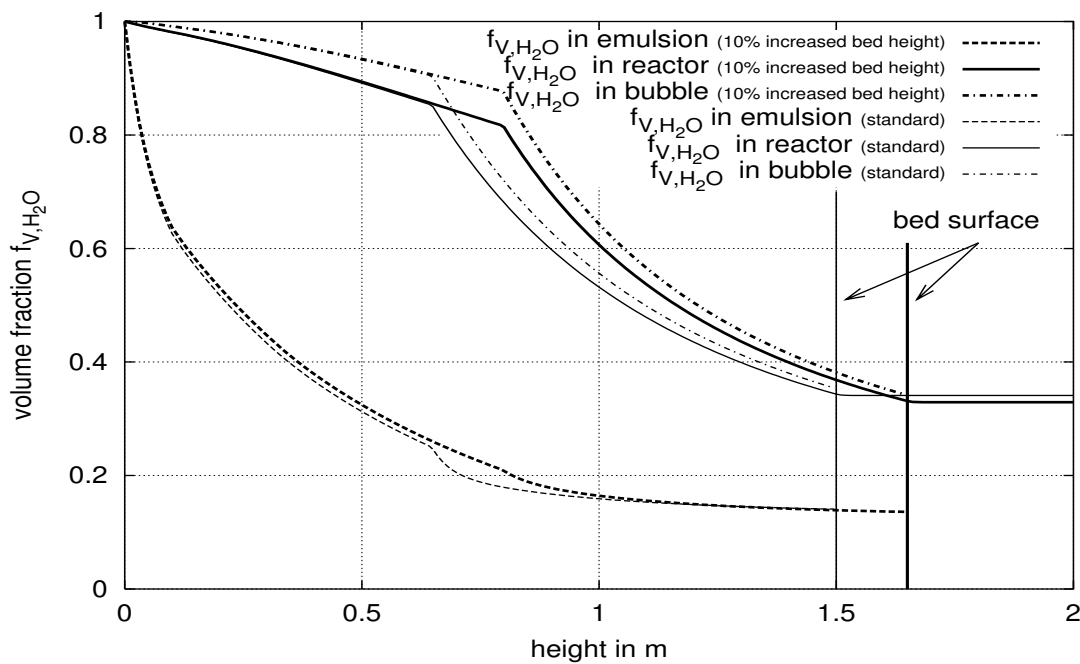


Figure 4.25: The high sensitivity of the steam conversion and the steam volumetric flow in the product gas for bed height variations is a result of a larger steam rich height at the reactor bottom. This is due to the same wood penetration depth assumed in the variation and standard conditions.

Standard flow:		Converted by Gasification Reactions					Volume Flow of Product Gas					$\dot{m}_{ch,cir}$
gases in m_N^3/h , char mass		CO	CO ₂	C_xH_y	H ₂	H ₂ O	CO	CO ₂	C_xH_y	H ₂	H ₂ O	C
in solid circulation flow $\dot{m}_{ch,cir}$ in kg/h		152.8	-10.1	-11.2	154.9	-133.4	411.6	339.3	273.5	559.9	819.5	251.3
RELATIVE SENSITIVITY												
Standard	Variation	CO	CO ₂	C_xH_y	H ₂	H ₂ O	CO	CO ₂	C_xH_y	H ₂	H ₂ O	C
⟨1⟩ 0.7m bed height	10% lower bed height ↓	<u>1.578</u>	<u>1.034</u>	0.861	<u>1.546</u>	<u>1.639</u>	0.586	-0.031	-0.035	0.428	-0.267	-0.434
⟨2⟩ 0.7m bed height	10% higher bed height ↑	<u>1.517</u>	<u>1.096</u>	0.801	<u>1.468</u>	<u>1.588</u>	0.563	-0.032	-0.033	0.407	-0.259	-0.416
⟨3⟩ 10% water content in fuel	10% lower water content in fuel ↓	0.140	-0.129	-0.187	0.128	0.170	-0.018	-0.111	-0.108	-0.045	0.243	-0.191
⟨4⟩ 10% water content in fuel	10% higher water content in fuel ↑	0.130	-0.008	-0.093	0.115	0.172	-0.022	-0.114	-0.112	-0.048	0.243	-0.184
⟨5⟩ representative char particle diameter: 0.0133m	10% lower char particle diameter ↓	-0.063	-0.020	-0.005	-0.060	-0.069	-0.023	0.001	0.000	-0.017	0.011	0.018
⟨6⟩ representative char particle diameter: 0.0133m	10% higher char particle diameter ↑	-0.079	-0.053	-0.015	-0.074	-0.083	-0.029	0.002	0.001	-0.020	0.013	0.022
⟨7⟩ char particle density: $300 \frac{kg}{m^3}$	10% lower char density ↓	-0.012	0.000	0.037	-0.007	-0.014	-0.005	0.000	-0.002	-0.002	0.002	0.004
⟨8⟩ char particle density: $300 \frac{kg}{m^3}$	10% higher char density ↑	-0.017	0.001	0.032	-0.012	-0.019	-0.006	0.000	-0.001	-0.003	0.003	0.006

To be continued on next page.

Continued from previous page.

Standard flow:		Converted by Gasification Reactions					Volume Flow of Product Gas					$\dot{m}_{ch,cir}$
gases in m_N^3/h , char mass		CO	CO ₂	C _x H _y	H ₂	H ₂ O	CO	CO ₂	C _x H _y	H ₂	H ₂ O	C
in solid circulation flow $\dot{m}_{ch,cir}$ in kg/h)		152.8	-10.1	-11.2	154.9	-133.4	411.6	339.3	273.5	559.9	819.5	251.3
RELATIVE SENSITIVITY												
Standard	Variation	CO	CO ₂	C _x H _y	H ₂	H ₂ O	CO	CO ₂	C _x H _y	H ₂	H ₂ O	C
$\langle 9 \rangle$ circulation flow: $50.0 \frac{(kg/s)_{bm}}{(kg/s)_{f,waf}}$	10% lower circulation flow of the bed material ↓	-0.568	-0.292	-0.693	-0.622	-0.607	-0.211	0.009	0.028	-0.172	0.099	0.149
$\langle 10 \rangle$ circulation flow: $50.0 \frac{(kg/s)_{bm}}{(kg/s)_{f,waf}}$	10% higher circulation flow of the bed material ↑	-0.501	-0.259	-0.598	-0.546	-0.534	-0.186	0.008	0.024	-0.151	0.087	0.132
$\langle 11 \rangle$ 1123K bed temperature	10% lower bed temperature ↓	<u>8.935</u>	<u>8.991</u>	<u>5.617</u>	<u>8.452</u>	<u>8.872</u>	<u>3.318</u>	-0.266	-0.229	<u>2.340</u>	<u>-1.445</u>	<u>-2.381</u>
$\langle 12 \rangle$ 1123K bed temperature	10% higher bed temperature ↑	<u>15.283</u>	<u>53.079</u>	<u>4.858</u>	<u>8.891</u>	<u>9.537</u>	<u>5.676</u>	<u>-1.571</u>	-0.198	<u>2.462</u>	<u>-1.553</u>	<u>-3.434</u>
$\langle 13 \rangle$ full load	90% load ↓	0.066	0.065	0.248	0.092	0.071	0.653	<u>1.028</u>	<u>1.031</u>	0.749	<u>1.151</u>	<u>1.245</u>
$\langle 14 \rangle$ full load	110%load ↑	0.022	0.039	0.164	0.040	0.025	0.637	<u>1.029</u>	<u>1.034</u>	0.734	<u>1.159</u>	<u>1.256</u>
$\langle 15 \rangle$ $0.1372 \frac{kg}{s}$ fluidization steam flow	10% lower fluidization steam flow ↓	0.005	-0.049	-0.028	0.007	0.013	0.002	0.001	0.001	0.002	0.813	-0.003
$\langle 16 \rangle$ $0.1372 \frac{kg}{s}$ fluidization steam flow	10% higher fluidization steam flow ↑	0.002	-0.045	-0.027	0.004	0.009	0.001	0.001	0.001	0.001	0.814	-0.002
$\langle 17 \rangle$ 1bar operation pressure	1.5bar operation pressure	0.153	-0.005	-0.028	0.135	-0.470	0.153	-0.005	-0.028	0.135	-0.078	-0.116

Table 4.4: Relative discrete sensitivity coefficients $\bar{\omega}_j^{rel}$ for the plant parameters.

and line <2>). Since $\bar{\omega}_j^{rel}$ is about 1.6 for the steam conversion, an enhancement of the char conversion could be easily achieved. However, this result is strongly dependent on other operation conditions. For high operation temperatures, and a floating wood fraction, a lower bed leads to the elimination of the part just below the height of the beginning wood devolatilization. Since there, the steam concentration in the dense phase is a minimum, a lower bed height had no significant influence (refer to Fig. 4.24). On the other hand, a smaller pressure drop over the bed could have advantages. However, if the wood fraction is distributed uniformly within the whole dense-phase at high operating temperatures, a high bed would have a significantly enhanced conversion rate compared to lower beds. This is the case, because the steam released by drying and devolatilization maintains a higher steam concentration in the dense phase as it would be just due to the mass-transfer between bubble and emulsion.

Concerning the char conversion, a high bed is always preferable for low temperatures. In this case, it depends on other factors like the moisture content whether a floating wood fraction leads to an enhanced conversion rate compared to a uniformly distributed wood fraction or not.

The analysis for the *lower load* was performed in the same way as the part load operation of the plant. Therefore, a reduction of the fuel flow goes along with a reduction of the total water feed. This is realized in reducing the fluidization steam flow at the reactor bottom. The ratio of the total dry fuel feed to the total water feed is held constant. As sensitivity analysis show, the reduction of the fuel flow by 10% results in a slightly reduced water consumption. However, the volumetric flow of steam within the product gas is significantly reduced. This is a result of the huge excess of steam in the reactor. Therefore, a reduction of the introduced water by 10% shows still little effect to the steam concentration in the bubble phase which results in a hardly reduced mass-transfer rate between bubble-phase and dense-phase. However, the volumetric flows of the single species in the product gas show a significant sensitivity (refer to Table 4.4 line <13> and line <14>). This is due to the change of the amount of gases released by devolatilization since the fuel flow is reduced.

A similar situation is found for the *fluidization steam* variation. Contrary to the part load operation, the fuel mass flow is not reduced. The low discrete relative sensitivity coefficients for the volumetric flow of all species but steam in the product gas indicates the huge excess of steam. The relatively large deviation from unity towards lower values of $\bar{\omega}_j^{rel}$ for the steam volumetric flow in the product gas is due to the water content of the fuel (refer to Table 4.4 line <15> and line <16>). However, the huge excess of steam is justified by the enhanced tar decomposition [Hofbauer and Rauch 2000] which has not been considered here.

4.3 Parameter Variation

A variation of parameters within a large range is done with the demonstration plant model for the more sensitive plant parameters. Further, a variation of the operation pressure from 1 bar to 3 bar and an operation with product-gas fluidization is performed. For the demonstration plant gasifier, there is no data available yet. Therefore, the results for the variations are presented without comparing it with measurement results.

temperature in K	1073				1123				1173	
solid circulation flow ratio in kg_{cir}/kg_f	90	70	50	30	70	50	30	10	50	30
product gas composition in percent by volume										
CO (dry)	22.2	22.6	23.2	24.2	25.8	26.7	28.1	30.7	30.8	32.1
CO ₂ (dry)	24.8	24.4	23.9	22.8	21.6	20.8	19.5	17.0	17.4	16.2
C _x H _y (dry)	20.0	19.7	19.0	18.0	17.6	16.8	15.6	13.1	14.7	13.7
H ₂ (dry)	33.0	33.3	33.9	35.0	35.0	35.7	36.8	39.2	37.1	38.0
H ₂ O	39.6	39.0	38.0	36.2	34.6	33.0	30.5	24.9	27.4	24.8
consumed species in $10^{-3}kg/s$										
C	5.5	6.7	8.6	12.2	36.9	44.0	17.1	20.7	26.7	40.4
H ₂ O	7.5	9.5	12.7	18.7	51.1	61.8	24.2	29.8	39.4	61.5

Table 4.5: Product gas composition in percent by volume and converted carbon and H₂O at different temperatures and solid circulation flows. The graphical representation is in figures 4.26, 4.27, 4.30, 4.28 and 4.29.

Temperature and Circulation Flow Variation

The temperature and the circulation flow are presented together, since combinations of different values are evaluated. So, a family of curves is obtained. The results are sketched in figures 4.26, 4.27, 4.30, 4.28 and 4.29 and listed in Table 4.5. Below $\approx 5 kg$ total carbon mass in the reactor, the algorithm has stability problems and for a circulation flow of $10 kg_{cir}/kg_f$ the only temperature investigated is $1123 K$.

Solid circulation flow dependency The carbon mass-flow discharging with the solid circulation flow and the carbon consumed by gasification reactions are sketched in relation to the fixed carbon in Fig. 4.26. The absolute values are presented on the secondary axis. As independent variable, the solid circulation flow is chosen. With the idealization made for this simulation, the fixed carbon mass is corresponding to the char mass. The part of the charged char, which is consumed by gasification reactions increases with decreasing values of the solid circulation flow. This increase occurs faster at low values of the solid circulation flow. The evolution of the portion of the charged char, which is discharged by the circulation flow is in the opposite direction.

Fig. 4.27 shows a rapid increase of the total carbon content in the reactor with a decrease of the solid circulation flow. This is due to the high ratio of carbon discharged with the solid circulation flow to the consumed carbon, which is $\frac{\dot{m}_{C,cir}}{\dot{m}_{C,cons}} > 3$ for standard conditions (refer to Fig. 4.26). Only for an operating temperature of $1123K$ and a solid circulation flow of $30 kg_{cir}/kg_f$, this ratio becomes unity. For the standard operation temperature of $1123K$, the solid circulation flow is below $10 kg_{cir}/kg_f$ when $\frac{\dot{m}_{C,cir}}{\dot{m}_{C,cons}}$ becomes unity. Therefore, for low solid circulation flow, the water consumption increases and the water concentration in the product gas flow decreases (refer to Fig. 4.27 and Fig. 4.30). The water consumption is in the order of magnitude of the water flow introduced by the fuel feed flow and below. Fig. 4.30 shows, that the consumed water exceeds the water flow which is charged with just at a solid circulation flow of about $10-20 kg_{cir}/kg_f$ the fuel feed. For standard conditions, the water flow charged with the fuel feed flow is approximately the double of the consumed water. Beside the total water flow ($0.0573 kg/s$), which includes water in the volatiles (refer to chapter 2.2.2), the water charged as free water only ($0.0469 kg/s$), is sketched as well in

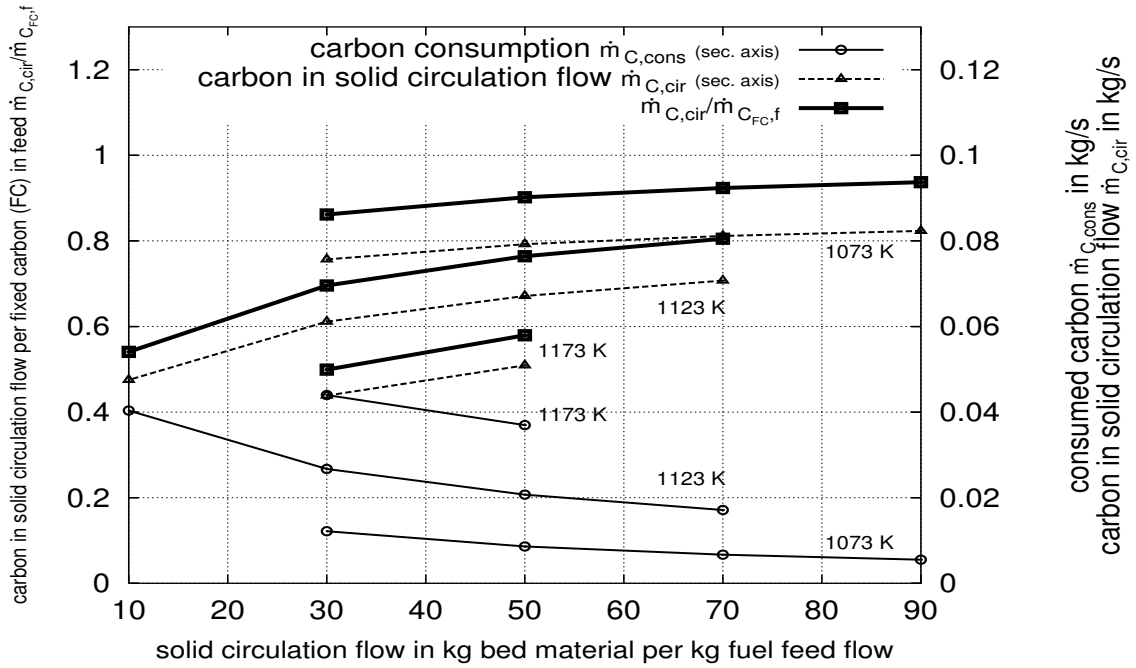


Figure 4.26: Carbon consumption and carbon discharged with the solid circulation flow on temperature and solid circulation flow variation. On the main axis, the values are related to the fixed carbon in the feed. The total carbon mass-flow and the absolute consumption can be read off on the secondary axis.

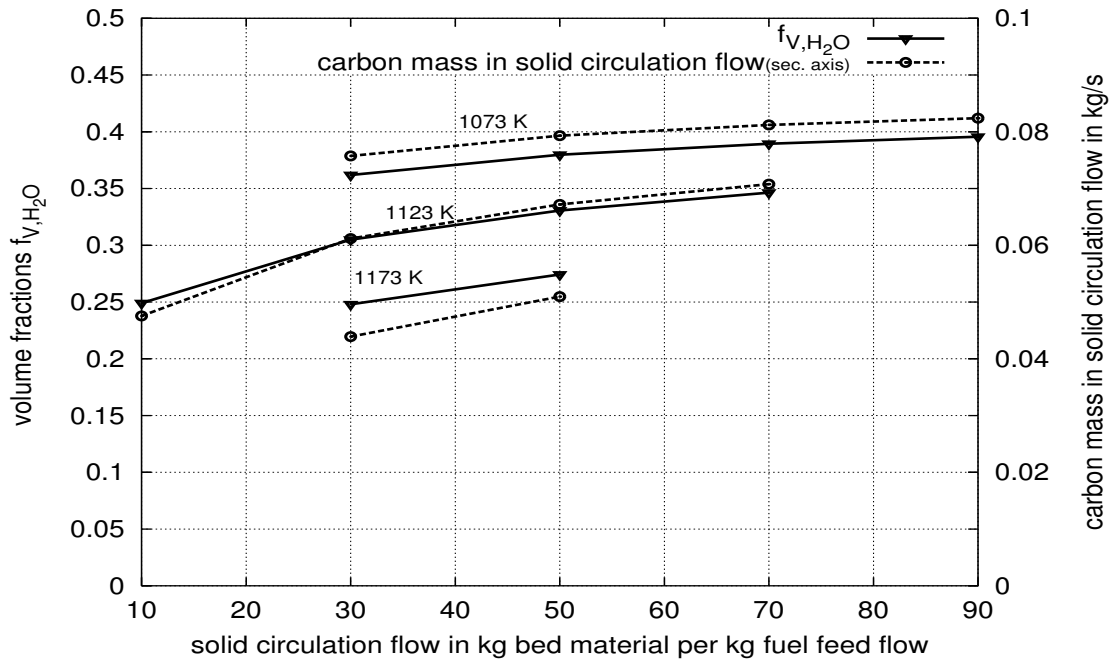


Figure 4.27: Volume fraction of H₂O in the product gas and carbon mass discharged in the solid circulation flow. With increasing temperature, the carbon mass in the solid circulation flow and the water volume fraction in the product gas decreases. Lower solid circulation flows cause a higher carbon content in the reactor and therefore a lower water volume fraction in the product gas.

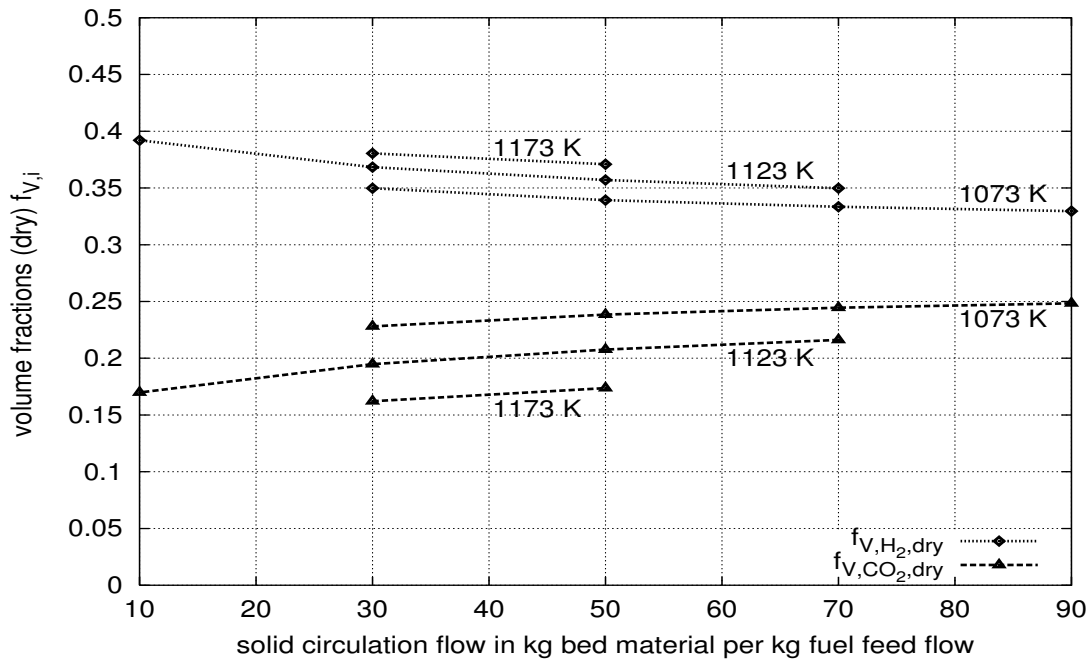


Figure 4.28: Volume fractions of H_2 and CO_2 in product gas on variations of the temperature T and the solid circulation flow \dot{m}_{cic} .

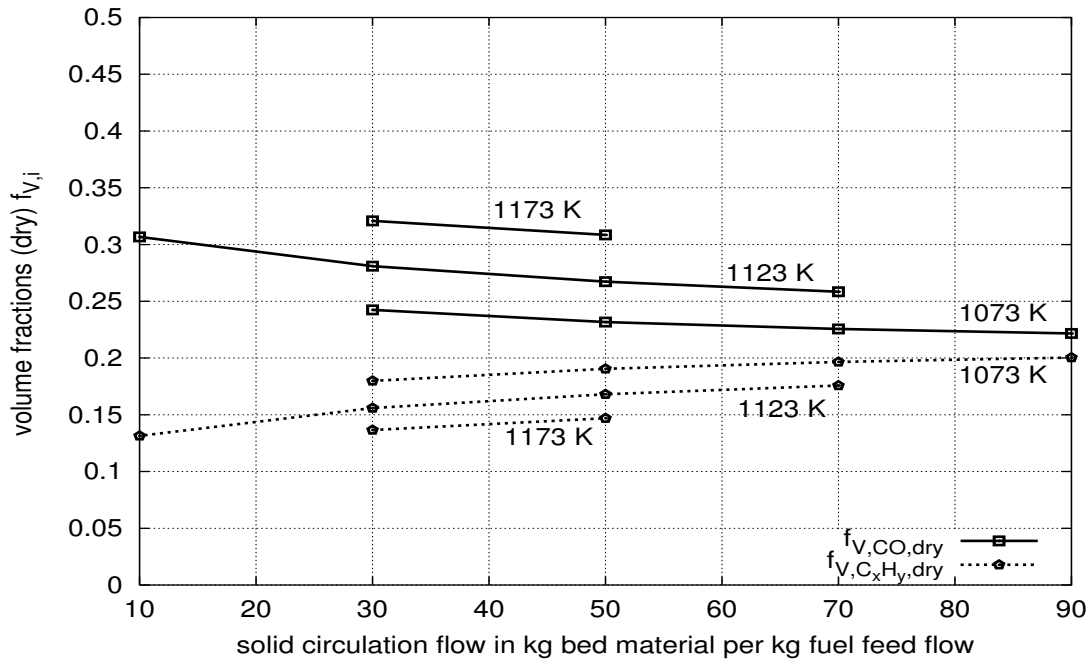


Figure 4.29: Volume fractions of CO and C_xH_y in product gas on variations of the temperature T and the solid circulation flow \dot{m}_{cic} .

Fig. 4.30. However, even this part is not consumed by gasification reactions for operating temperatures below $1173K$ and solid circulation flows above $20\text{ kg}_{cir}/\text{kg}_f$.

The volume fractions for carbon dioxide and C_xH_y are sketched in figures 4.28 and 4.29 show a dependency upon the solid circulation flow, which is similar to the evolution of the steam volume fraction. According to Eq. 3.16, CO_2 is increasingly consumed with a higher carbon content and an increasing operation temperature. The consumption of C_xH_y is basically a result of the equilibrium position of the hydrogasification reaction (Eq. 3.22) since the methane decomposition is also admitted. For this reaction, the equilibrium constant is $k_{pb}^{e,1123K} \sim 0.92$ based on the pressure in *bar* at a temperature of $1123K$. The influence of the reaction rate of this process is in the same order of magnitude as the carbon dioxide gasification reaction (refer to Table 4.3). Hydrogen and carbon monoxide are produced according to the conversion of water, carbon dioxide and C_xH_y . Their evolution depending on the solid circulation flow is therefore in the opposite direction to the consumed species.

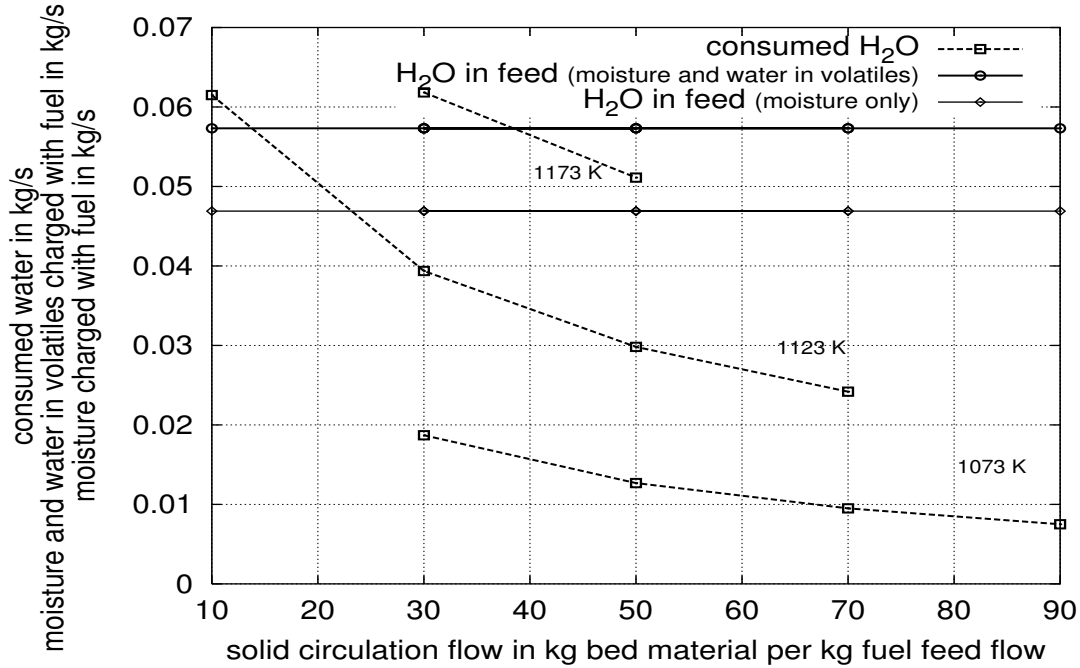


Figure 4.30: Water and carbon consumption on temperature and circulation flow variations. The water consumption exceeds the water charged by the fuel feed just in case of very low solid circulation flows and/or high temperatures. Beside the water charged by the fuel feed (0.0573 kg/s) the moisture (0.0469 kg/s) is sketched as reference in this figure.

Temperature dependency Fig. 4.26 shows a rapid increase of char which is consumed by gasification reactions with increasing temperature. For low solid circulation flows, this increase is still more significant. Increasing temperature results in a decreasing carbon mass flow with the circulation flow and an increasing water consumption (refer to Fig. 4.27). Based on the standard conditions of $1123K$ at a solid circulation flow ratio of $50\text{ kg}_{cir}/\text{kg}_f$, for an

	1073K	1123K	1173K
Carbon content in reactor	8.055kg (117%)	6.904kg	5.319kg (77%)
Frequency factor for			
H ₂ O gasification in $bar^{-0.57}s^{-1}$	$7.60 \cdot 10^{-4}$ (30.6%)	$24.81 \cdot 10^{-4}$	$73.36 \cdot 10^{-4}$ (295%)
CO ₂ gasification in $bar^{-0.38}s^{-1}$	$1.06 \cdot 10^{-4}$ (34.2%)	$30.97 \cdot 10^{-4}$	$82.77 \cdot 10^{-4}$ (267%)
H ₂ gasification in s^{-1}	$4.86 \cdot 10^{-4}$ (90.9%)	$5.36 \cdot 10^{-4}$	$5.86 \cdot 10^{-4}$ (109%)

Table 4.6: Frequency factor for steam, carbon dioxide and hydrogasification at different temperatures. Further, the carbon content in the reactor is presented here, as well. The value in parentheses is the value in percent derived from the value at 1123K. The change of the total carbon mass is higher than the change due to the frequency factor in the case of the hydrogasification reaction.

operating temperature increased by 50K, the water conversion increases by about 70% and the carbon consumption even more due to other gasification reactions. The deviations for a change towards higher temperature is stronger as the deviations for a change towards lower temperatures. This is clearly visible in the sensitivity analysis (refer to Table 4.4) and in the figures presented in this section. For a high char and steam conversion, it is preferable to operate with low circulation flows and high bed temperatures. However, the combination of low solid circulation flows and high bed temperature is problematic to maintain since the high temperature accelerates endothermic reactions which consume the thermal energy provided by the hot solid circulation flow. In order to fulfill this balance, the solid circulation flow has to be heated up considerably over the bed temperature. This can cause technological problems with the biomass ash.

Generally, the frequency factor in the kinetic equations of the chemical reactions and the lower carbon concentration in the bed derive the conversion rates in a contrary direction. The influence of the frequency factor is dominating in the case of the steam and carbon dioxide conversion, whereas the C_xH_y conversion is dominated by the decreasing carbon content in the reactor. This is a consequence of the small activation energy for the hydrogasification reaction ($E_a = 19210J/mol$) which is much inferior to the steam gasification reaction ($E_a = 237000J/mol$) and the carbon dioxide gasification reaction ($E_a = 215000J/mol$) (refer to Table 4.6). The latter reaction produces therefore more CO than the former reaction H₂. This results in a shift towards relatively lower hydrogen volume fractions in the dry product gas (refer to Fig. 4.28 and Fig. 4.29).

Pressure Variation

A pressure variation is done because the gasification under elevated pressure is of interest for downstream process stages which need to be operated on enhanced pressures. These are for example a gas turbine or fuel cells. All the parameters, particularly the molar flow for the fluidization are kept constant for this variation. Hence, the volumetric flow is smaller at enhanced pressures. This leads to smaller bubbles. Therefore, the term $\frac{6}{d_b}k_{be}$ (in s^{-1}) is higher for enhanced pressures. However, the term $\frac{6A_b}{d_bA_eU_e}k_{be}$ (in m^{-1}), which is the essential factor for the mass transfer into the emulsion (refer to Table 3.21 on page 80) is lower for enhanced pressures. This is due to the decreasing ratio of the cross sections of the bubble phase to the emulsion phase $\frac{A_b}{A_e}$ for higher pressures (refer to Fig. 4.31). Despite of this, the mass transfer rate is enhanced for higher operating pressure since the

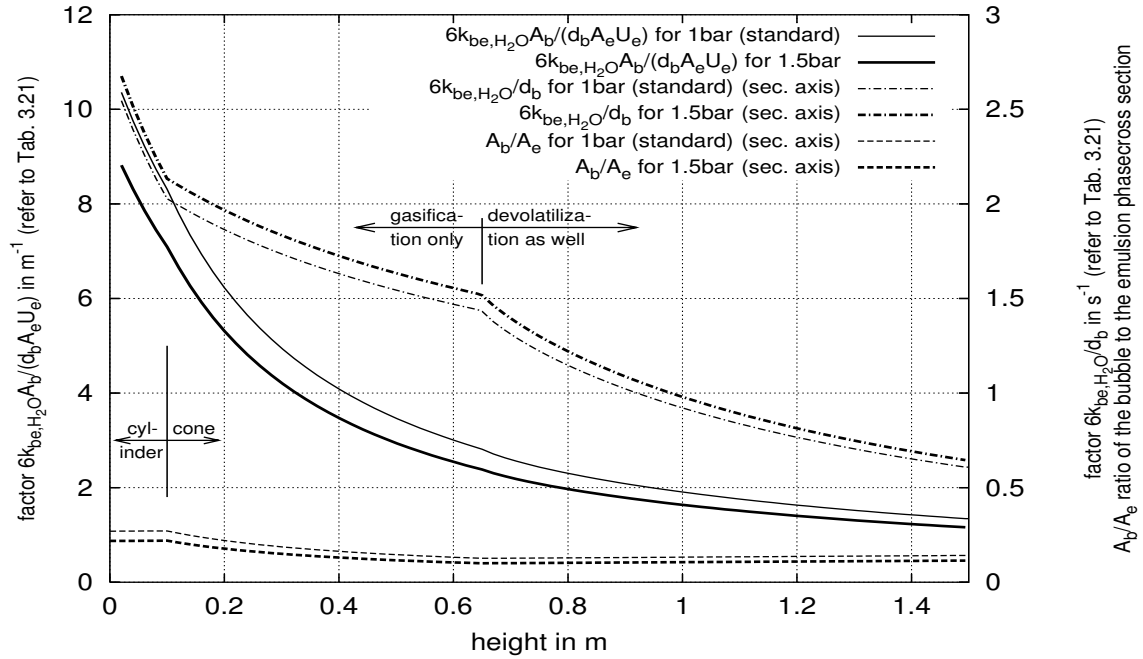


Figure 4.31: The terms $\frac{6}{d_b}k_{be}$ (in s^{-1}), $\frac{6A_b}{d_bA_eU_e}k_{be}$ (in m^{-1}), and the ratio of the cross sections of the bubble phase to the dense phase $\frac{A_b}{A_e}$ at enhanced pressure. The first two terms are important for the mass transfer rate from the bubble to the emulsion phase (refer to Table 3.21 on page 80).

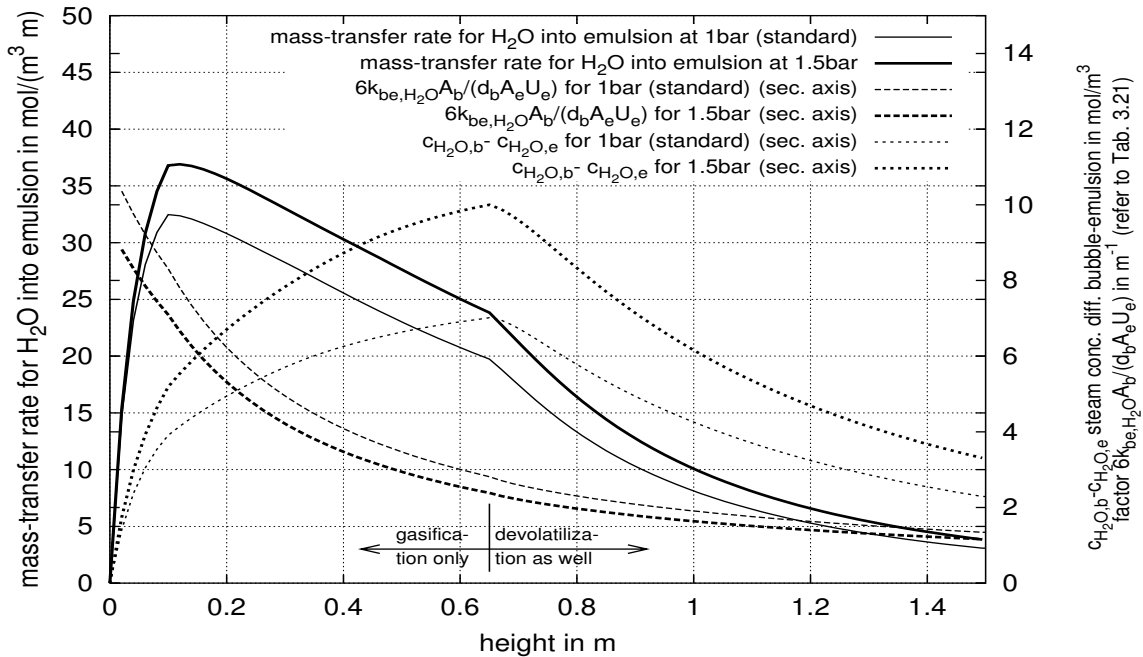


Figure 4.32: The mass transfer rate from the bubble to the emulsion phase for steam at enhanced pressure. This is the product of the term $\frac{6A_b}{d_bA_eU_e}k_{be}$ (in m^{-1}) with the concentration difference between the bubble and the emulsion phase.

concentration difference between bubble and emulsion phase is considerably higher than for the standard case (refer to Fig. 4.32). This enhanced mass transfer rate and the higher partial pressure leads finally to the enhanced conversion of carbon. The volume fractions for pressure operation and for standard conditions are compared in Fig. 4.33. Nevertheless, a higher operating pressure shows not much effect (refer to Table 4.4, line (17)). This is basically because the power of most gasification reactions is smaller than unity. However, a high pressure operation results in a distortion of the product gas composition since these powers are different and therefore the behavior towards enhanced pressure, as well. The correlations describing the fluid dynamic behavior are also affected by the pressure deviations (refer to [Löffler 2001, Kunii and Levenspiel 1991] and chapter 2.1.1). However, since most of these correlations take into account for the material and gas properties, useful simulation results can be expected in vicinity of normal pressure.

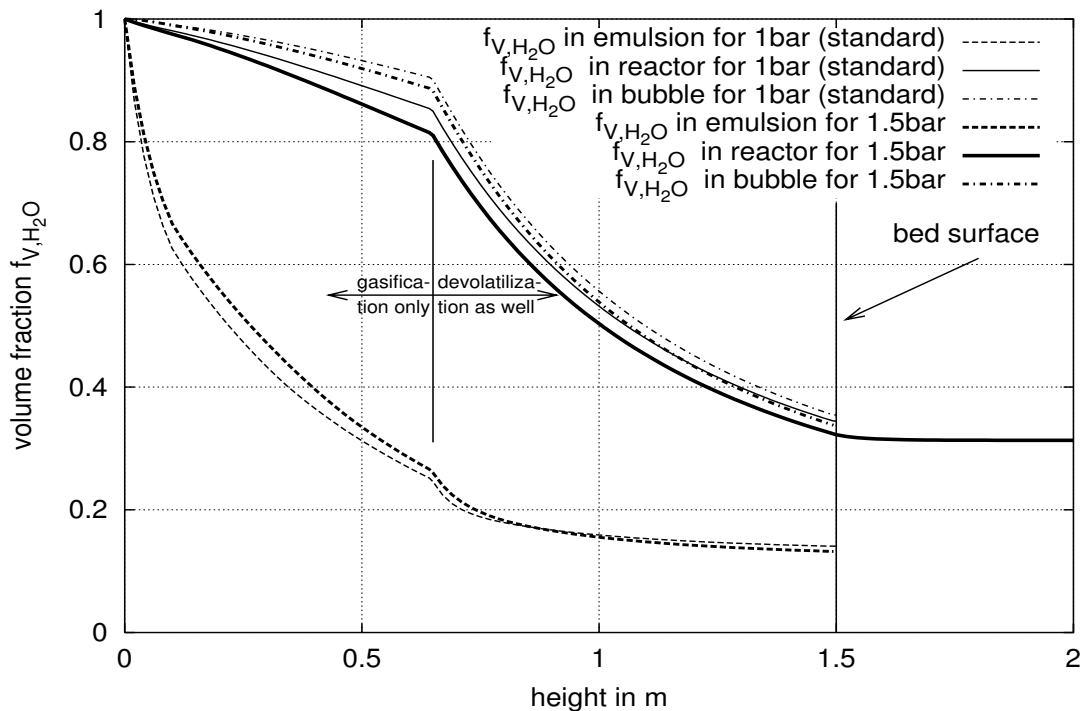


Figure 4.33: Evolution of the volume fraction of steam in the dense phase, the bubble phase and the reactor average at enhanced pressures.

Fig. 4.34 shows the carbon mass in the solid circulation flow, the carbon consumption and the water consumption. The carbon mass in the solid circulation flow decreases with higher pressure. This is a result of the enhanced steam gasification reaction rate. Therefore, the water consumption and corresponding to this, the carbon consumption are increasing. The total amount of water charged by the fuel flow (moisture and water in the volatiles) is still exceeding the consumed water mass. The increase in the water and char consumption is slowing down for increasing pressures. The product gas composition is changing, but rather slightly (refer to Fig. 4.35). The steam gasification reaction and the carbon dioxide gasification reaction show an enhanced rate, which is resulting in higher CO and H₂ fractions

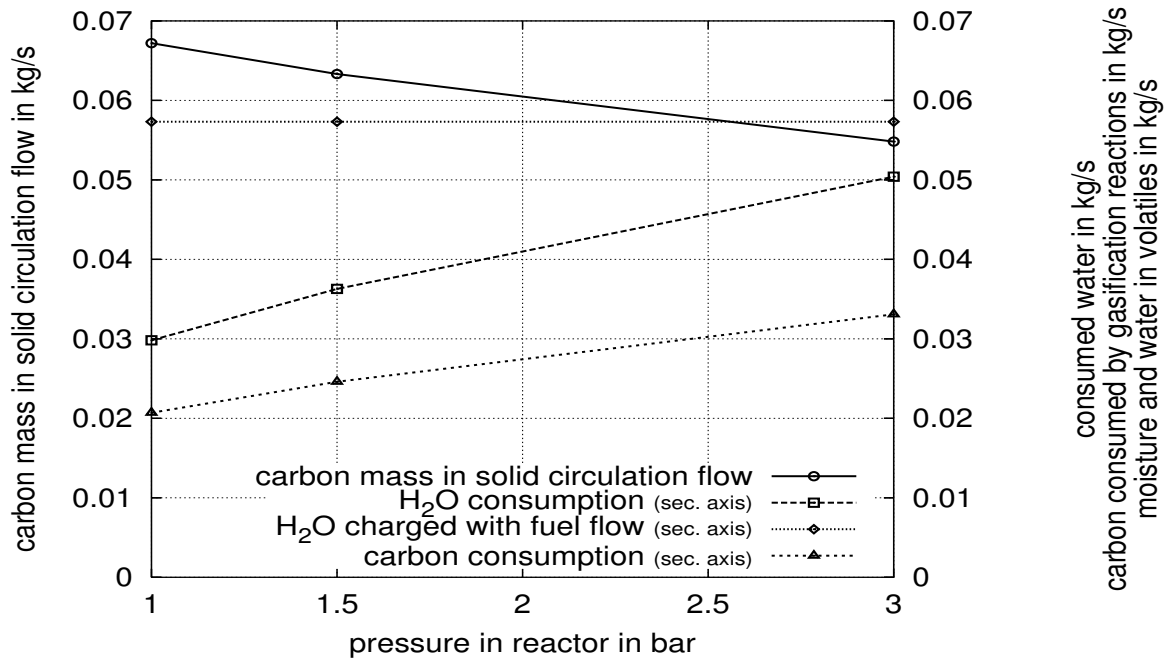


Figure 4.34: Water and carbon consumption on pressure variation. The water consumption increases continuously for a higher pressure. Corresponding to this, the carbon consumption increases, as well. Still, the consumed water does not exceed the water charged by the moisture and the water in the volatiles of the fuel flow.

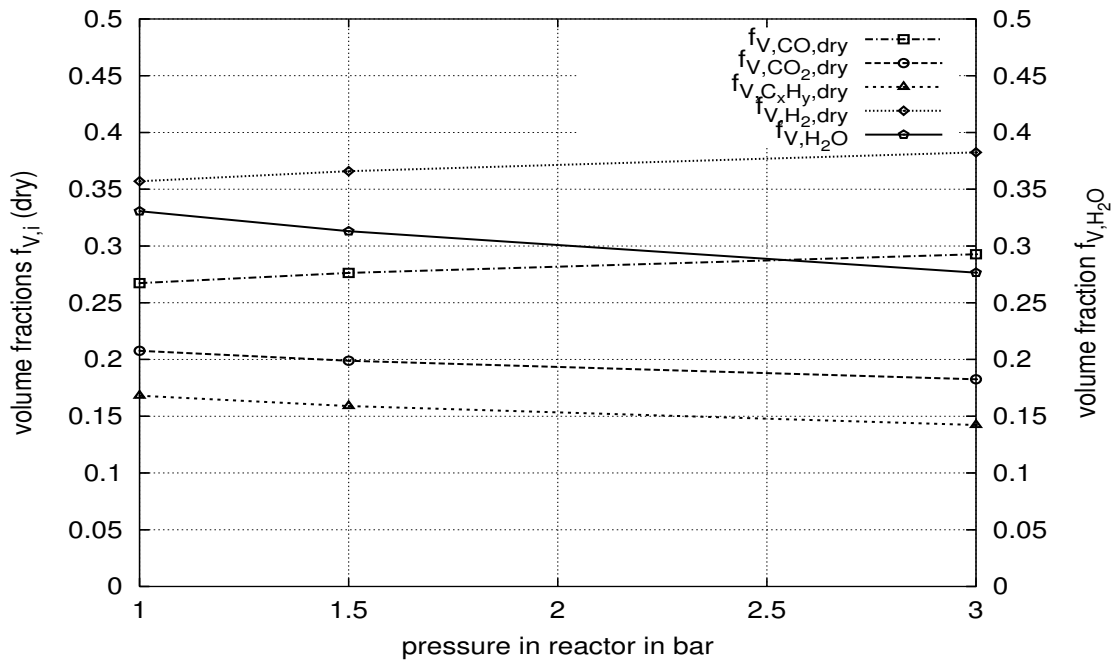


Figure 4.35: Volume fractions of product gas on enhanced pressure. The curves of the evolution of the volume fractions show nearly linear behavior in the whole range investigated. The water and carbon dioxide consumption increases. The methane decomposition by the inverse hydrogasification reaction still takes place.

in the product gas. However, the discrete relative sensitivity coefficient is not beyond 0.2 for neither of the volumetric flows in the product gas (refer to Table 4.4, line ⟨17⟩). The discrete relative sensitivity for the steam consumption is -0.47 . However, a higher pressure is not appropriate to get a rise of conversion if other possibilities as for example an elevated temperature still have potential since the construction of pressure vessels is costly in material, work and money.

pressure	1.0 bar	1.5 bar	3.0 bar
CO (dry)	26.7	27.5	29.3
CO ₂ (dry)	20.8	19.9	18.3
C _x H _y (dry)	16.8	15.9	14.2
H ₂ (dry)	35.7	36.6	38.2
H ₂ O	33.1	31.3	27.7

Table 4.7: Product gas composition in percent per volume for an enhanced pressure of 1.5 bar and 3.0 bar. The discrete relative sensitivity coefficients are calculated with the values for 1.5 bar (refer to Table 4.4 at line ⟨17⟩).

Part Load Performance

The performance of part load is computed with the following procedure. The fuel feed flow is reduced and corresponding to it, the steam flow for the bed fluidization as well. In order to fix a connection between these mass flows, β is defined as the ratio of the sum of the free water charge to the feed flow of dry fuel. The free water charge is the moisture of the fuel flow and the water charge for the fluidization flow but not the chemically fixed water in the fuel.

$$\beta = \frac{\text{steam for fluidization} + \text{moisture}}{\text{dry fuel}} = \frac{\dot{m}_f w_{wt,fl} + \dot{m}_f w_{wt,f}}{\dot{m}_f (1 - w_{wt,f})} \quad (4.7)$$

Apart from the investigation for a product gas fluidization below, $w_{wt,fl}$ is always unity. For the part load variation, the fuel flow and the fluidization steam flow is decreased stepwise. The connection of these two mass flows is Eq. 4.7. The ratio β is 0.436 until a fluidization steam flow of 300 kg/h (standard: 494 kg/h). A further reduction of the load is undertaken just by reduction of the fuel feed flow. Therefore, from this operation conditions on, β is increasing which means that the steam is in increasing excess related to the carbon charge. The values for the simulation, the product gas composition and the carbon mass discharged with the solid circulation are listed in Table 4.8. The results are sketched in figures 4.39, 4.40, 4.41 and 4.42. The carbon consumption and the water consumption stay largely the same for the whole range investigated. Both decrease just slightly with decreasing fuel flow. However, the total amount of water and carbon charged into the reactor decrease according the part load operation conditions. Therefore, the ratio of the converted water mass to the charged water mass increases with decreasing part load. This ratio stays largely constant from the beginning of the point where no further reduction of the fluidization steam is done (increasing ratio β). The total charge of water reduces further for part load operation conditions below this point since the water charged with the fuel is decreasing directly proportional to the fuel flow (refer to Fig. 4.39).

Contrary to this, the ratio of the consumed carbon mass to the charged carbon mass increases rapidly for this operation conditions. This is a result of the steam excess. In

\dot{m}_{fl} kg/s	\dot{m}_f kg/s	β	CO (dry)	CO ₂ (dry)	C _x H _y (dry)	H ₂ (dry)	H ₂ O	$\dot{m}_{C,cir}$ kg/h
0.1372	0.4690	0.4362	26.0	21.4	17.3	35.3	34.1	251.3
0.1250	0.4272	0.4362	26.4	21.0	16.9	35.6	33.4	223.4
0.1235	0.4221	0.4362	26.5	21.0	16.9	35.7	33.3	220.0
0.1111	0.3798	0.4362	27.0	20.5	16.5	36.0	32.5	192.1
0.0972	0.3323	0.4362	27.7	19.9	16.0	36.4	31.4	161.1
0.0833	0.2848	0.4362	28.5	19.2	15.5	36.8	30.1	130.8
0.0833	0.2800	0.4418	28.6	19.1	15.4	36.9	30.3	127.7
0.0833	0.2000	0.5741	30.3	17.6	14.3	37.8	34.1	77.9

compositions in percent by volume

Table 4.8: Product gas composition and carbon content on part load operation conditions.

Fig. 4.40, the carbon discharge by the solid circulation flow and the ratio of the consumed carbon to the latter are sketched. This ratio shows a similar behavior like the ratio of the consumed to the charged carbon. However, for full power reactor operation conditions both ratios are in a close proximity within 0.2 and 0.3. These small values indicate that the major part of the carbon is discharged with the solid circulation flow and combusted in the riser. Only at the very lowest part load operation condition investigated, the consumed carbon

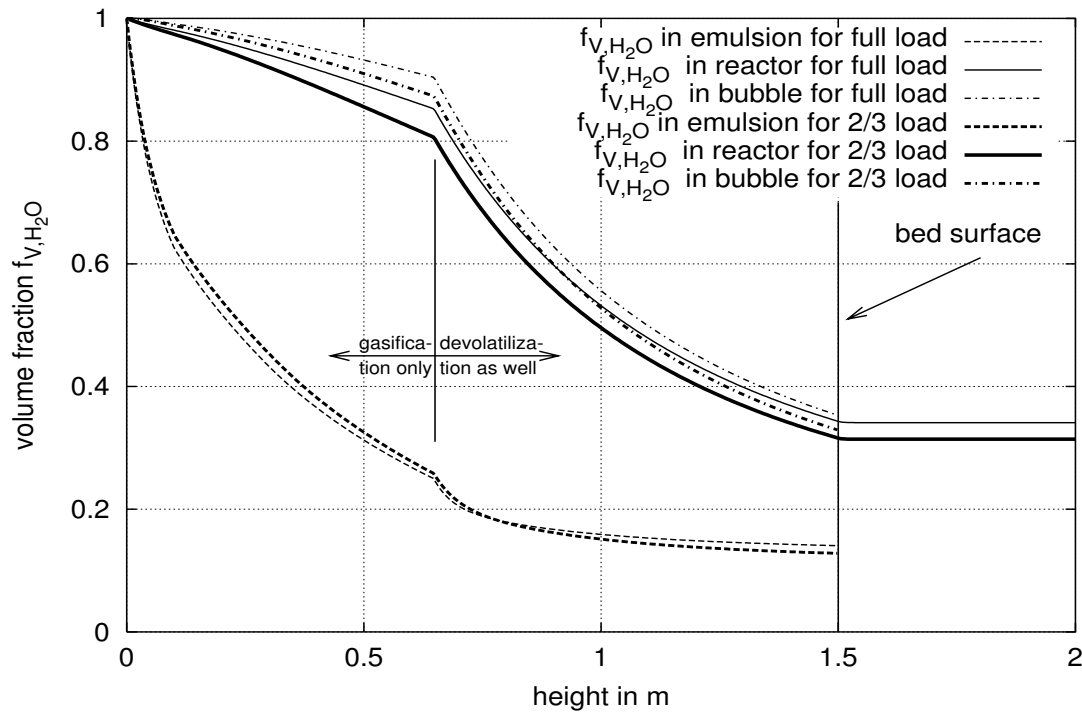


Figure 4.36: Evolution of the volume fraction of steam in the dense phase, the bubble phase and the reactor average at part load operation.

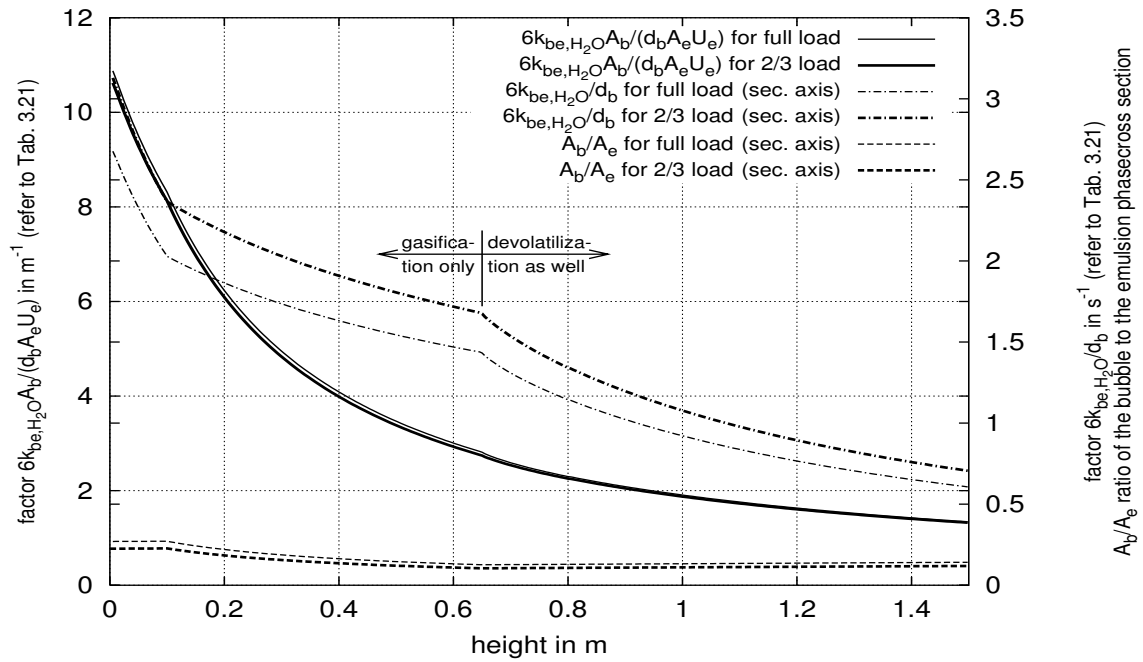


Figure 4.37: The terms $\frac{6}{d_b}k_{be}$ (in s^{-1}), $\frac{6A_b}{d_bA_eU_e}k_{be}$ (in m^{-1}), and the ratio of the cross sections of the bubble phase to the dense phase $\frac{A_b}{A_e}$ at part load operation. The first two terms are important for the mass transfer rate from the bubble to the emulsion phase (refer to Table 3.21 on page 80).

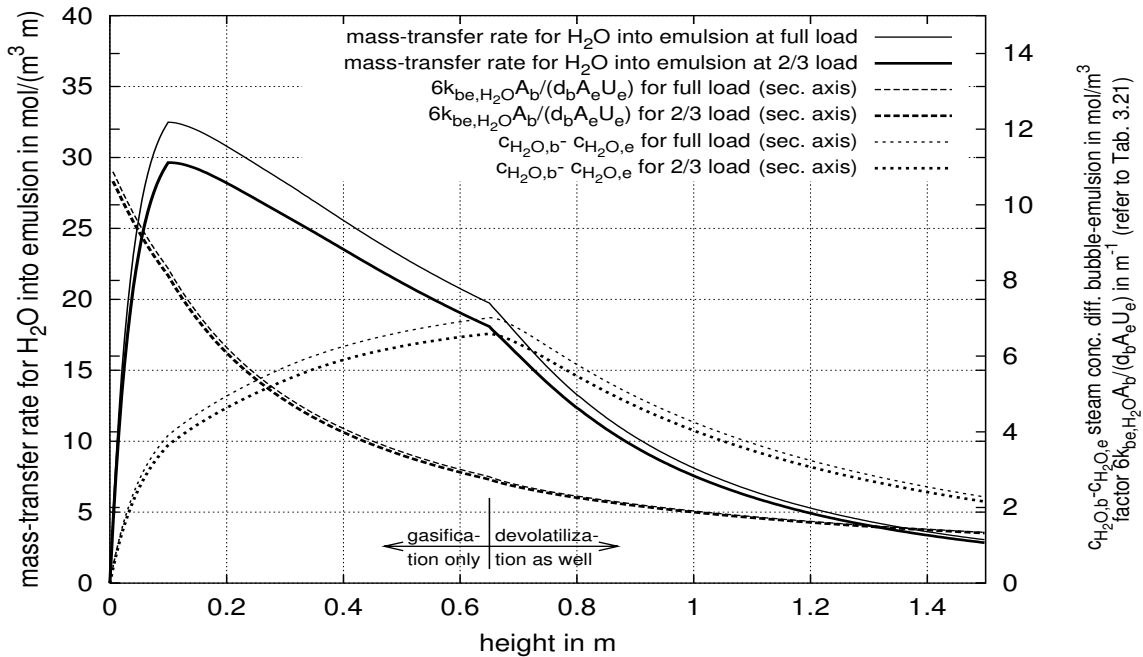


Figure 4.38: The mass transfer rate from the bubble to the emulsion phase for steam at part load operation. This is the product of the term $\frac{6A_b}{d_bA_eU_e}k_{be}$ (in m^{-1}) with the concentration difference between the bubble and the emulsion phase.

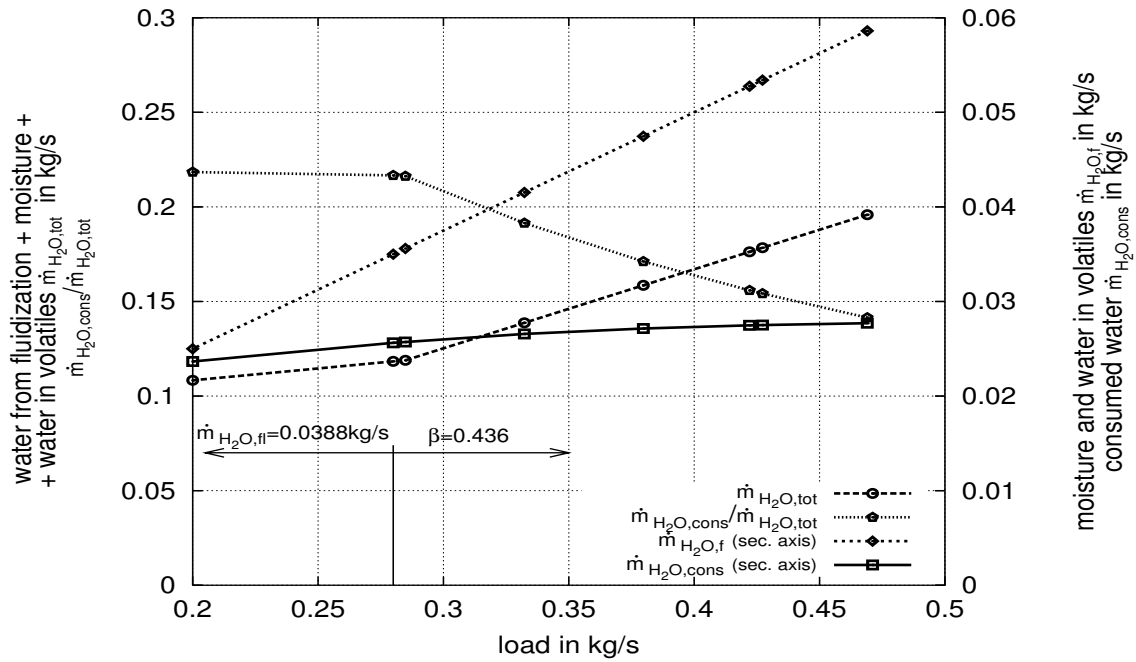


Figure 4.39: Water consumption and water charge on part load. On part load the water consumption stays relatively constant whereas the total amount of water charged into the reactor is reduced constantly by process control. So the ratio of the consumed water to the charged water increases until the point, where the fuel feed is reduced solely.

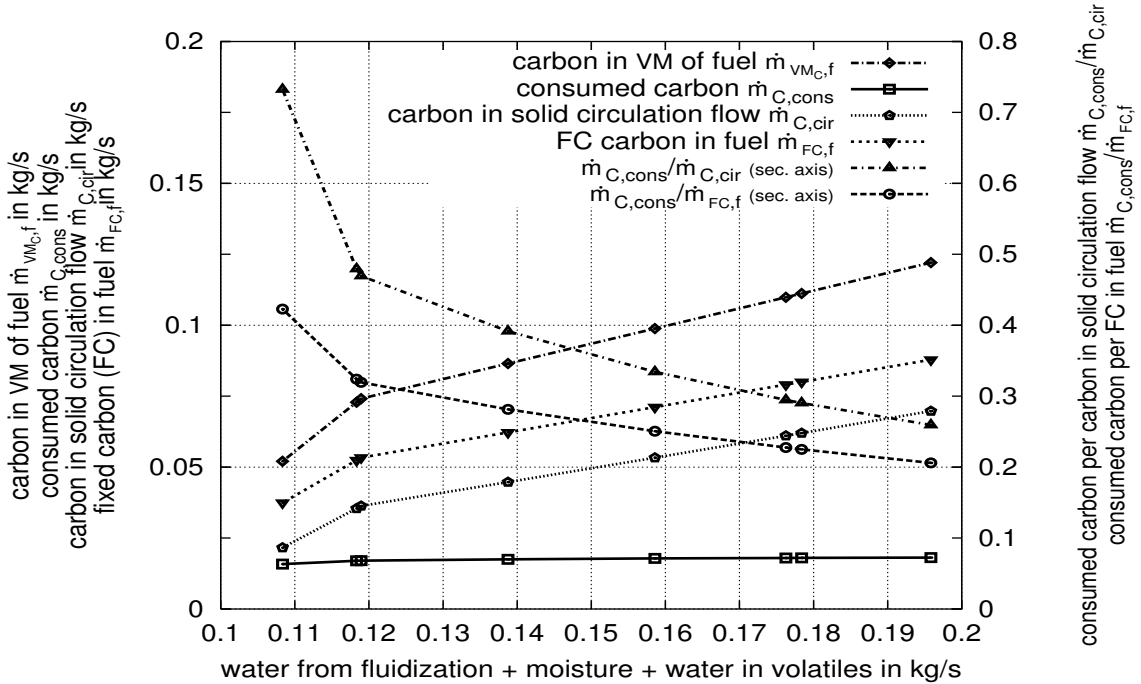


Figure 4.40: The carbon consumption on part stays largely constant as well. However, related to the carbon mass discharged by the solid circulation flow or the feed flow, the carbon consumption increases. This effect is enhanced if no more reduction of the fluidization flow is done together with a reduction of the fuel flow.

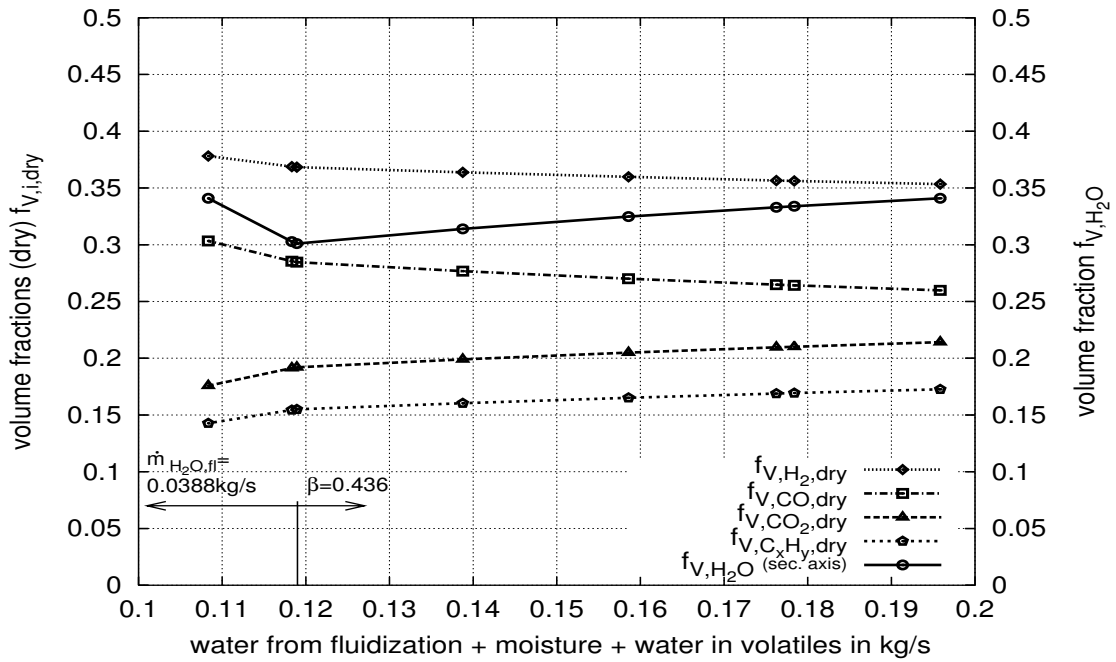


Figure 4.41: In the product gas, the fractions of C_xH_y and carbon dioxide are decreasing since this are devolatilization products and are directly proportional to the charged fuel. Contrary to this, the carbon monoxide and the hydrogen volume fraction increase due to less dilution by the other devolatilization products and steam.

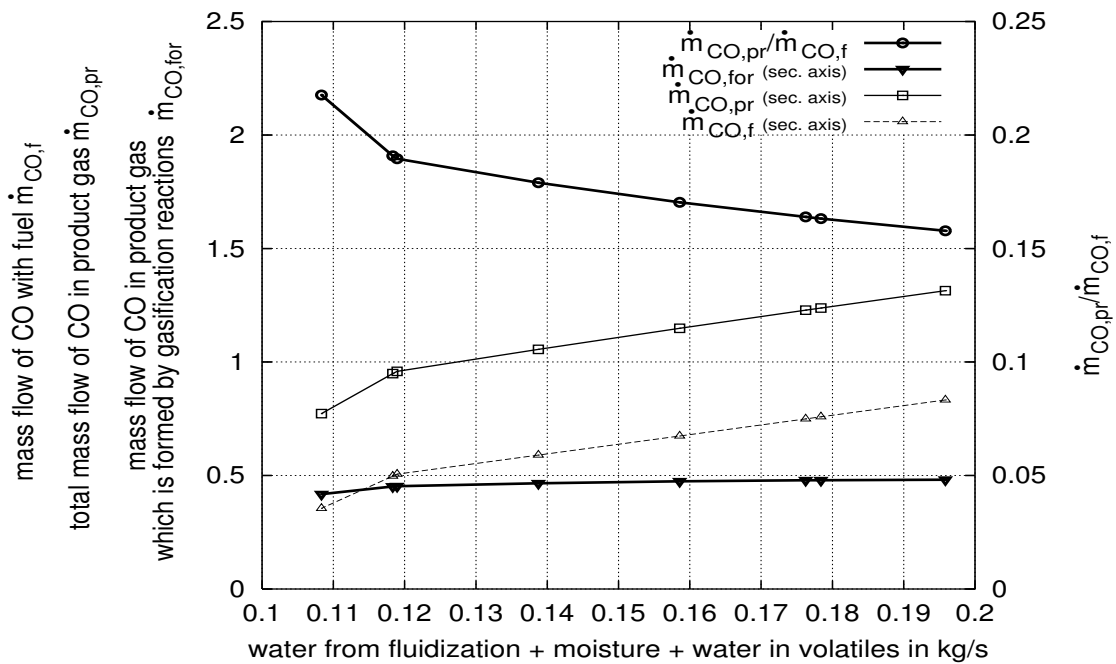


Figure 4.42: The ratio of the carbon monoxide flow in the product gas to the carbon monoxide mass flow charged with the volatile matter in the fuel shows an increasing importance of the gasification reactions. For very low fuel feed flows, the carbon monoxide content in the product gas results up to 50% of gasification reactions. A similar result is observed for hydrogen.

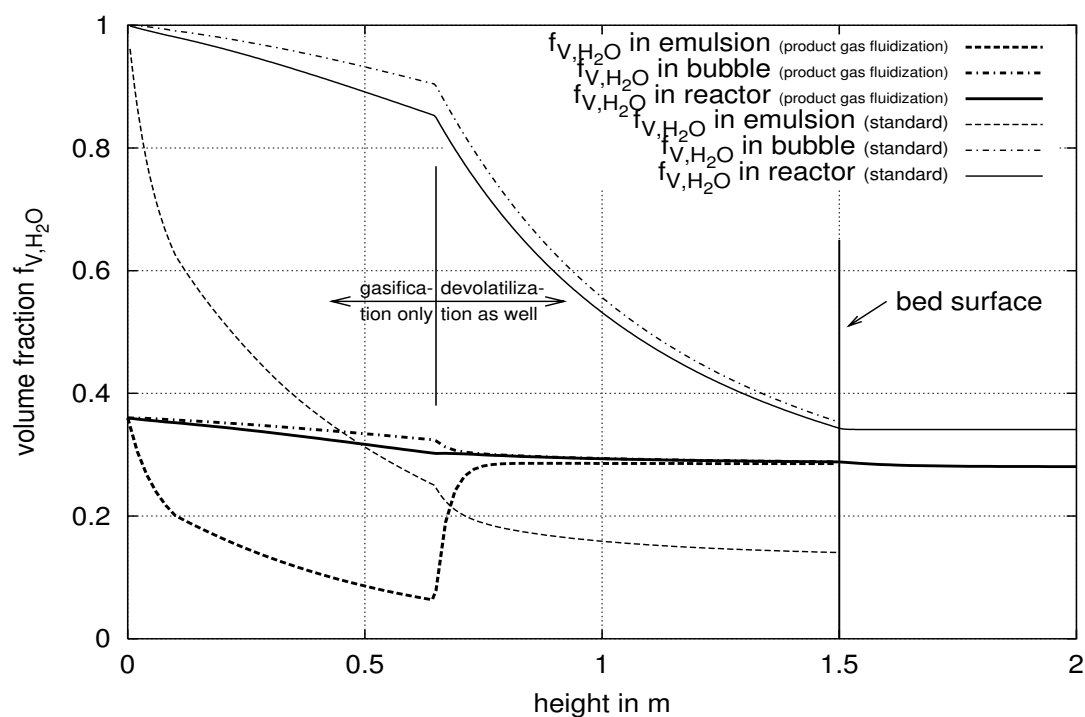
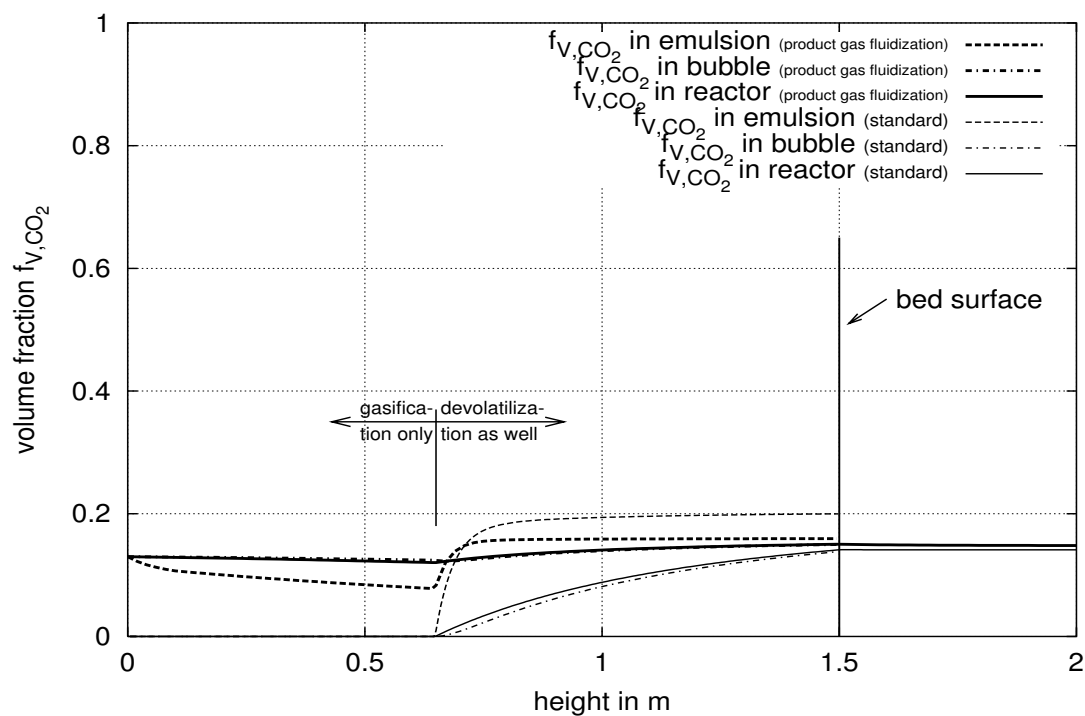
reaches about 40% of the fixed carbon and about 75% of the carbon discharged by the solid circulation flow. Still, the amount of the fixed carbon, which is burnt exceeds the amount of the fixed carbon, which is gasified considerably. The volume fractions of the product gas are listed in Table 4.8 and plotted in Fig. 4.41. The decrease of the C_xH_y and *carbon dioxide* fraction within part load operation conditions is a result of the decreasing fuel flow since their formation is due to devolatilization, only. The *water* volume fraction in the product gas is decreasing by about 4% until the point where no further fluidization steam reduction is done and increases significantly, afterwards. For the last point investigated, the water volume fraction is about the same as for full load reactor operating conditions. The product gas volume fractions for *carbon monoxide* and *hydrogen* increase for part load operation conditions. This is due to less dilution by the other devolatilization products namely C_xH_y and carbon dioxide as well as due to steam.

The mass flow of carbon monoxide in the product gas which are charged as volatile matter with the fuel is sketched in Fig. 4.42. This part is directly proportional to the fuel feed flow and is decreasing in part load operation conditions. The total mass flow of carbon monoxide in the product gas shows similar tendency. The mass flow of hydrogen and carbon monoxide in the product gas which results from gasification reactions $\dot{m}_{i,for}$ is largely constant within the whole range of part load operation (refer to Fig. 4.42) This is also coherent with the converted carbon mass (refer to Fig. 4.40). In the product gas, the mass flows of carbon monoxide and hydrogen behave similar. as the mass Therefore, the mass fractions of carbon monoxide and hydrogen in the product gas, which result from devolatilization reduce in part load operation conditions. For the lowest part load operation point, about 50% of these gases result from gasification reaction contrary to 30% for full load operation conditions. The term $\frac{6}{d_b}k_{be}$ (in s^{-1}) is enhanced at part load operation since the bubble diameter decreases due to a reduced volumetric gas flow. However, the ratio of the cross sections of the bubble to the dense phase $\frac{A_b}{A_e}$ leads to a more or less unchanged term $\frac{6A_b}{d_bA_eU_e}k_{be}$ (in m^{-1})for part load operation condition (refer to Fig. 4.37). Less steam volumetric flow in the bubble phase leads to the situation that the concentration of steam in the bubble phase changes more rapidly than for standard conditions (refer to Fig. 4.36). Hence, related to the standard, the concentration difference which is the driving force for the mass transfer is reduced at part load operation. This leads finally to a reduced mass transfer rate into the emulsion (refer to Fig. 4.38).

Product Gas Fluidization

Fluidization with gas at least containing a certain amount of product gas rather than with pure steam is done with the objective to get a higher conversion of the steam. If it is possible to reapply the product gas for fluidization without tar separation, the residence time of these is higher and the degradation can advance to an enhanced state.

For the simulation, the water content of the fuel is increased in such a way that the ratio β as defined in Eq. 4.7 is again 0.436. Table 4.9 lists the values, which are different to standard conditions. Since the product gas composition is not known in advance and it changes further with changing fluidization gas composition an iteration has to be performed to get exact results. In this work, for the composition of the fluidization gas a similar composition like the product gas composition is chosen. However, it has *not* been iterated with the product gas composition resulting from simulation. This variation is unique to get an image of the change of the conversion rates resulting from product gas fluidization. In order to get useful

Figure 4.43: H_2O volume fraction vs. reactor height for product gas fluidization.Figure 4.44: CO_2 volume fraction vs. reactor height for product gas fluidization.

fuel mass flow in ks/s	0.557
water content in kg_{wt}/kg_w	0.242
fluidization gas composition in in percent by volume	
CO	17.0
CO ₂	13.0
CH ₄	11.0
H ₂	23.0
H ₂ O	36.0

Table 4.9: Input for product gas fluidization.

Species	Gas Composition for Standard	Gas Composition for Prod- uct Gas Fluidization	$100(1 - \bar{\sigma}^{rel})$
CO	17.9	19.3	1.44
CO ₂	13.9	14.8	21.1
C _x H _y	11.2	12.1	8.45
H ₂	23.9	25.7	-0.40
H ₂ O	33.1	28.1	-0.71

Table 4.10: Results for product gas fluidization. Gas compositions in percent by volume. $100(1 - \bar{\sigma}^{rel})$ deviation of the conversion at product gas fluidization from conversion at standard conditions in percent.

results for the product gas composition, an iteration is indispensable. The results for the product gas fluidization are presented in Table 4.10. The consumed or generated amount of every species is related to standard conditions. The water conversion is decreasing by about 1%. This is a result of the steam dilution in the region up to a height of $0.65m$ compared to the standard. Since the steam gasification reaction is the most sensitive reaction, this dilution is already notable. However, since the moisture content is higher, the steam gasification reaction is enhanced in the devolatilization zone (refer to Fig. 4.43). The C_xH_y decomposition accelerates by about 8.5%. This, and the large bases of $157m_N^3$ formed hydrogen at standard operation conditions lead to the nearly negligible rate deviation from standard. The carbon conversion by carbon dioxide gasification increases significantly by 21% since carbon dioxide it is present already from the bottom of the reactor (refer to Fig. 4.44). The carbon dioxide concentration in the emulsion is lower than in the bubble similarly to the steam. However, since the reaction rate for carbon dioxide gasification is not that fast, the concentration difference between bubble and dense phase is smaller. For standard operation conditions, the change of the absolute value of converted carbon dioxide is not that important since just about $10m_N^3$ of it undergoes conversion compared to $133m_N^3$ of steam (refer to Table 4.4). However, the carbon monoxide formation increases by about 1.5%.

Generally, the product gas fluidization seems not to be extraordinary attractive concerning an enhanced conversion. However, a certain deviation of the product gas composition towards higher contents of carbon monoxide and a lower content of carbon dioxide and C_xH_y is observable. An other aspect which makes this operation mode interesting is the tar decomposition since a long residence time in regions of high temperature is necessary for their degradation. However, this point has not been investigated in this work.

4.4 Conclusion

The sensitivity analysis based on a standard reactor shows that the model parameters with the highest influence are the parameters, which describe the devolatilization composition and the frequency factor for the steam gasification. Due to the uncertainty of the former, further investigation on model parameters should start here. The plant parameters, with the highest sensitivity are the operating temperature, the bed height, and the solid circulation flow. A sensitivity analysis for the fluidization mass flow shows, that its decrease is possible without a significant reduction of the char conversion rate.

The discrete relative sensitivity of the steam conversion is in the vicinity of 9 for the operating temperature. To enhance the char conversion, an increase of this temperature is the primary choice.

For the standard reactor, one fourth of the fixed carbon undergoes conversion by gasification reactions. The residual amount is discharged by the solid circulation flow. For very low circulation flows these parts reach equivalence.

About 16% of the water charged with the fluidization mass flow, the moisture, and the volatiles in the wood is converted in the standard reactor. This is about the half of the moisture charged with the fuel flow. For 5% higher temperatures or very low solid circulation flows, the converted water mass and the water mass in moisture reach the same order of magnitude.

For part load, the char conversion stays largely constant. The char mass in the circulation flow decreases steadily until both reach the same order of magnitude at 40% load. The amounts of hydrogen and carbon dioxide which originate from gasification reactions increase from 30% for standard conditions up to 50%. Pressure variations show a disproportionate low enhancement of the gasification reaction rates. The product gas fluidization suggests an enhanced conversion of carbon dioxide. Table 5.1 gives an overview of the results for the different parameter variations.

Chapter 5

Summary

A simulation of a fluidized bed gasifier for steam gasification of wood has been done in this work. For this, a software tool has been developed in FORTRAN 90. This tool is able to handle an open reaction system with n^{th} -order rate equations and Langmuir-Hinselwood type rate equations. Five different gaseous species (CO, CO₂, CH₄, H₂, and H₂O) and char, which is supposed to consist of carbon only, have been applied in this study. Higher hydrocarbons are lumped into the methane fraction. The fluid dynamic situation in the fluidized bed has been implemented with semi-empirical equations. The bed model bases on the modified two phase theory. Because of the gas formation during gasification, a discretization of the reactor has been done in order to fulfill the fluid dynamic conditions within the whole fluidized bed.

Simulations have been performed for a geometry according to a pilot plant gasifier and further for a geometry similar to a demonstration plant. For the latter, a sensitivity analysis which bases on the design point is done. Sensitive model parameters are the parameters, which describe the devolatilization composition and the frequency factors for the gasification reactions. The sensitivity analysis shows, that the majority of the rate equations participates insignificant on the product gas composition. The significant reactions are all gasification reactions which are provided by different authors [Barrio and Hustad 2000, Barrio et al. 2000, Wang and Kinoshita 1993, Reed 1981]. These are the following chemical equations:



However, the comparison of the reaction rates for these rate equations with rate equations provided from other authors [Plante et al. 1988, Capart and Gél 1988, Groeneveld 1980, De Groot and Shafizadeh 1984] show widely scattering results. This is mainly due to the differences of the chemical properties of the woods used for the measurements.

Plant parameters which have influence on the performance of the gasifier are the bed temperature, which has the largest sensitivity at all, the bed height, and the solid circulation flow. The variation of combinations of the operation temperature and the solid circulation demonstrate the importance of a high bed temperature for an enhanced char and steam conversion. For the highest temperature where a simulation was done (1123K), the steam conversion reaches the order of magnitude of the moisture mass flow charged with the fuel flow. The volume fraction of hydrogen and carbon dioxide in the dry product gas increase

with decreasing circulation flow whereas the C_xH_y fraction and the carbon dioxide decrease. The solid circulation flow influences the char concentration in the bed since the amount of carbon withdrawn by this flow exceeds the amount of carbon which undergoes gasification by about 3 times. A reduction of this flow results in a rapid increase of the char concentration in the bed and therefore an enhanced conversion.

A higher bed ensures a longer contact time with the char. Therefore, the conversion is enhanced for higher beds. However, the significance of this effect depends also strongly on the wood distribution within the bed and the operating temperature.

Investigations for the part load operation suggest over a wide range a constant amount of steam converted. The reduction of the dry product gas volumetric flow is nearly entirely due to the reduced amount of devolatilization products. Therefore, the part of hydrogen and carbon monoxide in the product gas, which result from gasification increase from 30% for standard operation conditions to about 50% for 40% load.

The pressure variations suggest an increasing steam and char consumption. However, enhanced pressure always has disproportionate low effects on conversion since the power for the partial pressure is smaller than unity for the gasification reactions. The product gas fluidization shows a slightly enhanced carbon monoxide formation. Advantages can be expected for the tar decomposition since the larger residence time in a high temperature environment is favorable for their decomposition.

Further work should be done to extend of the reaction system to tar fractions. Also, an analysis and a more precisely modeling of the devolatilization composition seems to be indispensable. For a more accurate gasification model, it is necessary to perform a TGA for the *used* wood char type since the rate equations from literature scatter partly several orders of magnitude. Measuring the devolatilization composition is costly in work since this composition depends strongly on process parameters like the final temperature and the heating rate. The implementation of a particle model which considers heat-transfer limitations as well, can be a second step.

Operation condition	Product gas composition in percent by volume					Q_{pr} in m_N^3/h	$\dot{m}_{C,cons}$	$\dot{m}_{C,cir}$	Remarks	
	CO	CO ₂	C _x H _y	H ₂	H ₂ O					
Standard	0.171	0.141	0.114	0.233	0.341	2403.8	1.508	5.813	$\dot{m}_{fl} = 0.137$ $T = 1123K$	$\dot{m}_f = 0.469$ $\frac{\dot{m}_{cir}}{\dot{m}_f} = 50$
Part load	0.176	0.140	0.113	0.237	0.334	2202.4	1.501	5.168	$\dot{m}_{fl} = 0.125$	$\dot{m}_f = 0.427$
Part load	0.177	0.140	0.113	0.238	0.333	2177.6	1.500	5.089	$\dot{m}_{fl} = 0.124$	$\dot{m}_f = 0.422$
Part load	0.182	0.138	0.112	0.243	0.325	1972.6	1.485	4.442	$\dot{m}_{fl} = 0.111$	$\dot{m}_f = 0.380$
Part load	0.190	0.137	0.110	0.250	0.314	1741.6	1.460	3.727	$\dot{m}_{fl} = 0.097$	$\dot{m}_f = 0.332$
Part load	0.199	0.134	0.108	0.257	0.301	1509.2	1.420	3.026	$\dot{m}_{fl} = 0.083$	$\dot{m}_f = 0.285$
Part load	0.199	0.133	0.108	0.257	0.303	1492.4	1.416	2.954	$\dot{m}_{fl} = 0.083$	$\dot{m}_f = 0.280$
Part load	0.200	0.116	0.094	0.249	0.341	1210.6	1.320	1.802	$\dot{m}_{fl} = 0.083$	$\dot{m}_f = 0.200$
Product gas fluidization	0.193	0.148	0.121	0.257	0.280	2810.4	1.728	5.582	refer to pp. 124	
Pressure variation	0.190	0.137	0.109	0.251	0.313	2460.8	2.049	5.272	$p = 1.5bar$	
Pressure variation	0.212	0.132	0.103	0.277	0.276	2538.0	2.757	4.564	$p = 3.0bar$	
T and \dot{m}_{cir} variation ¹	0.169	0.141	0.115	0.229	0.346	2393.8	1.427	5.894	$T = 1123K$	$\frac{\dot{m}_{cir}}{\dot{m}_f} = 70$
T and \dot{m}_{cir} variation ¹	0.179	0.139	0.112	0.239	0.331	2424.6	1.725	5.595	$T = 1123K$	$\frac{\dot{m}_{cir}}{\dot{m}_f} = 50$
T and \dot{m}_{cir} variation ¹	0.195	0.135	0.108	0.256	0.305	2477.0	2.226	5.095	$T = 1123K$	$\frac{\dot{m}_{cir}}{\dot{m}_f} = 30$
T and \dot{m}_{cir} variation ¹	0.230	0.128	0.099	0.294	0.249	2600.2	3.363	3.958	$T = 1123K$	$\frac{\dot{m}_{cir}}{\dot{m}_f} = 10$
T and \dot{m}_{cir} variation ¹	0.241	0.122	0.103	0.286	0.248	2605.0	3.665	3.656	$T = 1173K$	$\frac{\dot{m}_{cir}}{\dot{m}_f} = 30$
T and \dot{m}_{cir} variation ¹	0.224	0.126	0.107	0.269	0.274	2545.7	3.079	4.242	$T = 1173K$	$\frac{\dot{m}_{cir}}{\dot{m}_f} = 50$
T and \dot{m}_{cir} variation ¹	0.155	0.145	0.115	0.223	0.362	2364.7	1.013	6.307	$T = 1073K$	$\frac{\dot{m}_{cir}}{\dot{m}_f} = 30$
T and \dot{m}_{cir} variation ¹	0.144	0.148	0.118	0.210	0.380	2330.8	0.717	6.604	$T = 1073K$	$\frac{\dot{m}_{cir}}{\dot{m}_f} = 50$
T and \dot{m}_{cir} variation ¹	0.138	0.149	0.120	0.204	0.389	2312.7	0.558	6.762	$T = 1073K$	$\frac{\dot{m}_{cir}}{\dot{m}_f} = 70$
T and \dot{m}_{cir} variation ¹	0.134	0.150	0.121	0.199	0.396	2301.4	0.459	6.862	$T = 1073K$	$\frac{\dot{m}_{cir}}{\dot{m}_f} = 90$

¹: Particle diameter ($d_p = 0.002m$) smaller than for standard ($d_p = 0.0133m$).

Table 5.1: Summary of the results for the parameter variation.

Nomenclature

A	m^2	cross section
$\mathcal{A}, \mathcal{B}, \mathcal{C}, \mathcal{D}, \mathcal{Q}$	—	species
ASH	kg	ash mass
a	m	particle radius
$\overline{C_1} \dots \overline{C_7}$	various units	coefficients for the NASA polinomial
CV	m^3	control volume
c	$\frac{mol}{m^3}$	concentration
c_p	$\frac{J}{molK}$	isobaric heat capacity
\bar{c}_p	$\frac{J}{molK}$	average isobaric heat capacity
c_w	—	drag coefficient
D	$\frac{m_g^2}{s}$	diffusion coefficient
D_e	$\frac{m_g^3}{s m_p}$	effective diffusion coefficient in porous particle
d	m	diameter
\bar{d}	m	average diameter
E_a	$\frac{J}{mol}$	activation energy
FC	kg	fixed carbon mass
f_{dy}	m^{-1}	decay factor
$f_{tf,b}$	—	fraction of through-flow in bubble-phase
f_V	—	volume fraction
g	$\frac{m}{s^2}$	acceleration of gravity
$H_{f^*,T}$	$\frac{J}{mol}$	formation enthalpy at operation temperature

ΔH	$\frac{J}{mol}$	reaction enthalpy
h	m	reactor height variable
J	$\frac{mol}{m^2 s}$	diffusive mole flow
K	$\frac{1}{Pa}$	adsorption equilibrium constant
K_{pb}	$\frac{1}{bar}$	adsorption equilibrium constant in terms of <i>bar</i>
k	various units	frequency factor
k_m	$\frac{m}{s}$	mass-transfer coefficient
k^e	various units	chemical equilibrium constant
L	m	bed height
M	$\frac{kg}{mol}$	molar mass
m	kg	mass
\dot{m}	kg/s	mass flow
n	mol	quantity of substance
\dot{n}	mol/s	molar flow
$\Delta_g n$	mol	change of the quantity of substance of gaseous species of a reaction
O	m^2	surface
p	Pa or bar	pressure
Δp	Pa	pressure drop within the fluidized bed height
Q	$\frac{m^3}{s}$	volumetric flow
R	$\frac{mol}{m^3 s}$	reaction rate
\mathcal{R}	$8.3144 \frac{kJ}{mol K}$	gas constant
R_{gh}	$\frac{mol}{m^3 m}$	overall conversion rate
R_{gt}	$\frac{mol}{m^3 s}$	overall reaction rate
r	m	radius variable
\bar{r}	$\frac{1}{s}$	reaction rate (definition derived from the actual solid mass $m_s(t)$)

\bar{r}	$\frac{1}{s}$	reaction rate (definition derived from the initial solid mass $m_s(t_0)$)
S	—	catalyst
$S_{f^*,T}$	$\frac{J}{molK}$	formation entropy at operation temperature
ΔS	$\frac{J}{molK}$	reaction entropy
T	K	temperature
TDH	m	transport disengaging height
t	s	time
u	$\frac{m}{s}$	velocity
\bar{u}	$\frac{m}{s}$	average velocity
$u_{b,\infty}$	$\frac{m}{s}$	single bubble rising velocity
U	$\frac{m}{s}$	superficial velocity
V	m^3	volume
VM	kg	mass of volatile matter
w	—	mass fraction
X	—	conversion
$x_1 = \frac{n_{C O_2}}{n_{C O}}$	—	devolatilization parameter
$x_2 = \frac{n_{C H_4}}{n_{C O}}$	—	devolatilization parameter
Y	—	factor Y
y	—	mole fraction

Greek Letters

α	$\frac{m}{s}$	heat-transfer coefficient
β	$\frac{kg_{wt}}{kg_{w,dry}}$	ratio of water to dry fuel
δ	—	voidage
ε	$\frac{m^3 \text{ gas}}{m^3 \text{ total volume}}$	porosity
ζ	$4m^{-1}$	decay constant
η	—	effectiveness factor

Θ	—	fractional coverage
κ	—	variation parameter
λ	$\frac{W}{mK}$	thermal heat conductivity
λ_e	$\frac{W}{mK}$	effective thermal heat conductivity in a solid particle
μ	<i>Pa s</i>	dynamic viscosity
ν	$\frac{m^2}{s}$	kinematic viscosity
$\bar{\nu}$	—	gravimetric factor
ξ	various units	parameter of the physicochemical system
Φ	$\frac{J}{m^2 s}$	thermal conductive flow
ϕ_p	—	particle sphericity
$\bar{\phi}_{i,h}, \bar{\phi}_{h,i}$	—	auxiliary variable to compute the gas viscosity
ρ	$\frac{kg}{m^3}$	density
$\bar{\sigma}^{rel}$	—	relative system response
ω	—	linear sensitivity coefficient
ω^{rel}	—	relative sensitivity coefficient
$\bar{\omega}^{rel}$	—	relative discrete sensitivity coefficient

Subscripts

<i>A</i>	active particle
<i>ad</i>	adsorption
<i>ash</i>	ash
<i>b</i>	bubble
<i>be</i>	from bubble to emulsion
<i>bm</i>	bed material
<i>bwd</i>	backward
<i>C</i>	carbon

<i>CV</i>	control volume
<i>c</i>	in terms of concentrations
<i>cat</i>	catalyst
<i>ch</i>	char
<i>cir</i>	circulation flow
<i>cons</i>	consumed
<i>cont</i>	control
<i>d</i>	dense phase
<i>des</i>	desorption
<i>dry</i>	dry
<i>dy</i>	decay
<i>e</i>	emulsion
<i>eb</i>	from emulsion to bubble
<i>eq</i>	equivalent
<i>ext</i>	external
<i>FC</i>	fixed carbon
<i>f</i>	fuel feed
<i>f*</i>	formation
<i>fb</i>	freeboard
<i>for</i>	formation
<i>fwd</i>	forward
<i>fl</i>	fluidization
<i>g</i>	gas
<i>gr</i>	gasification reaction
<i>h</i>	index variable for a specie
<i>I</i>	inert matter (sand)
<i>i, j</i>	index variable for a specie

id	ideal
int	internal
j, i	index variable for a reaction
L	bed height
l	free active sites on a certain catalyst
m	maximum number of chemical reactions in the physicochemical system
\overline{m}^*	maximum number of parameters in the physicochemical system
mf	minimum fluidization conditions
mix	mixture
N	normal conditions (273.15K and 101325 Pa)
n	reaction order
\overline{n}	maximum number of gaseous species in the physicochemical system
\overline{n}^*	maximum number of variables in the physicochemical system
o	orifice
obs	observed
p	particle
pb	in terms of partial pressures in bar
pp	in terms of partial pressures in Pa
pr	product gas
q	index variable for a bed material
R	reactor
rel	released
S	particle surface conditions
s	solid
st	standard operation conditions

TDH	transport disengaging height
t	terminal conditions
tf	through-flow
$therm$	thermodynamic
tot	total
VM	volatile matter
w	wood
wet	moisture included
waf	water and ash free
wt	water
∞	ambient conditions
0	initial conditions
Γ	total number of free surface sites on a certain catalyst
κ	result with the variation parameter
ω	after complete conversion

Superscripts

e	equilibrium
k	actual instance
$k - 1$	previous instance
$k + 1$	next instance
rel	relative

Dimensionless Groups

Ar	Archimedes Number
$DaII$	Damköhler Number

Nu	Nusselt Number
Nu_1	Nusselt Number for $d_A/d_I = 1$
Nu_∞	Nusselt Number for $d_A/d_I \gg 1$
Pr	Prandtl Number
Re	Reynolds Number
Sc	Schmidt Number
Sh	Sherwood Number
Sh_1	Sherwood Number for $d_A/d_I = 1$
Sh_∞	Sherwood Number for $d_A/d_I \gg 1$
ϕ	Thiele Modulus

List of Figures

2.1	Geldart classification	6
2.2	Physical structure of soft wood	15
2.3	Physical structure of hard wood	15
2.4	Main fractions of wood	16
2.5	Temperature dependence of the volatile composition	20
2.6	n^{th} order kinetics of steam gasification	29
2.7	n^{th} order kinetics vs. Langmuir-Hinselwood kinetics for steam gasification	29
2.8	Influence of CO ₂ partial pressure and temperature on char reactivity	31
2.9	n^{th} order kinetics of carbon dioxide gasification	31
2.10	n^{th} order kinetics vs. Langmuir-Hinselwood kinetics for CO ₂ gasification	33
2.11	Reactivity profiles for steam gasification	34
2.12	Concentration profiles during particle consumption	43
3.1	Design of the system gasifier-riser	44
3.2	Pilot plant reactor	47
3.3	Demonstration plant gasifier	48
3.4	H ₂ O volume fraction of the gases released by devolatilization	55
3.5	CO volume fraction of the gases released by devolatilization	56
3.6	CO ₂ volume fraction of the gases released by devolatilization	56
3.7	CH ₄ volume fraction of the gases released by devolatilization	57
3.8	H ₂ volume fraction of the gases released by devolatilization	57
3.9	Damköhler Number Da_{II} for steam gasification	61
3.10	Thiele Module ϕ for steam gasification	62
3.11	Effectiveness factor η for steam gasification	63
3.12	Concentration distribution from the bubble to the center of the particle	64
3.13	Sherwood Number and Nusselt Number for the particle model	66
3.14	Carbon reaction rate and evolution of the particle diameter versus time	67
3.15	Particle diameter and carbon reaction rate versus the particle conversion	69
3.16	Relative influence of heat and mass-transfer limitations on the reaction rate.	70
3.17	Effectiveness factors for heat and mass-transfer limitations	71
3.18	Wood distribution	74
3.19	Char distribution	74
3.20	Overview for the solving scheme	75
3.21	Flowsheet for the bed and the freeboard	76
3.22	Flowsheet for the differential equation solver	77
4.1	Product gas composition in pilot plant gasifier (measurement results)	83
4.2	Cross sections of the reactor and the phases	85

4.3	Volume fractions vs. reactor height	86
4.4	Velocities vs. reactor height	86
4.5	Gas flows in bubble phase and dense phase	87
4.6	Visible bubble flow, factor Y , through-flow	88
4.7	Volumetric flow of the H_2O fraction in the bubble and the dense phase	89
4.8	Volume fraction of steam versus the reactor height	90
4.9	Volume fraction of carbon monoxide versus the reactor height	91
4.10	Volume fraction of hydrogen versus the reactor height	91
4.11	Volume fraction of carbon dioxide versus the reactor height	92
4.12	Volume fraction of C_xH_y versus the reactor height	92
4.13	Species volume fraction on the particle surface	93
4.14	Overall conversion rate of the single species in the dense phase	93
4.15	Steam, carbon dioxide, and hydrogasification reactions	95
4.16	Water-gas-shift reactions and C_xH_y decomposition	95
4.17	Mass-transfer rate in from the bubble phase into the dense phase	97
4.18	Mass-transfer rates and overall conversion rates for steam	98
4.19	Consumed steam vs. the reactor height	98
4.20	Generated hydrogen vs. the reactor height	99
4.21	Consumed carbon dioxide vs. the reactor height	99
4.22	Steam concentration 10% slower steam gasification rate	104
4.23	Steam concentration for uniformly distributed wood	105
4.24	Temperature sensitivity of the steam volume fraction	107
4.25	Bed height sensitivity of the steam conversion	107
4.26	Carbon consumption on variations of T and \dot{m}_{cic}	112
4.27	Volume fractions of steam in product gas on variations of T and \dot{m}_{cic}	112
4.28	Volume fractions of H_2 and CO_2 in product gas on variations of T and \dot{m}_{cic}	113
4.29	Volume fractions of CO and C_xH_y in product gas on variations of T and \dot{m}_{cic}	113
4.30	Steam and carbon conversion on variations of T and \dot{m}_{cic}	114
4.31	Factors for the mass transfer form bubble to emulsion at enhanced pressure	116
4.32	Mass transfer rate form bubble to emulsion at enhanced pressure	116
4.33	Volume fraction of steam versus the reactor height at enhanced pressure	117
4.34	Water and carbon consumption on pressure variation	118
4.35	Volume fractions of product gas on enhanced pressure	118
4.36	Volume fraction of steam versus the reactor height at part load	120
4.37	Factors for the mass transfer form bubble to emulsion at part load	121
4.38	Mass transfer rate form bubble to emulsion at part load	121
4.39	Water consumption on part load	122
4.40	Carbon consumption on part load	122
4.41	Product gas composition on part load	123
4.42	Ratio of gasification product to devolatilization product	123
4.43	H_2O volume fraction vs. reactor height for product gas fluidization	125
4.44	CO_2 volume fraction vs. reactor height for product gas fluidization	125

List of Tables

2.1	Correlations for heat and mass-transfer for large active particles	11
2.2	Typical permeability values of wood	17
2.3	Ultimate analysis data for different biomass chars	17
2.4	Different types of pyrolysis processes	19
2.5	Influence of process parameters on the products of the devolatilization step. .	21
2.6	Langmuir-Hinselwood Kinetics of Steam Gasification	28
2.7	n^{th} order Kinetics of Steam Gasification	28
2.8	Langmuir-Hinselwood Kinetics of Carbon Dioxide Gasification	32
2.9	n^{th} order Kinetics of Carbon Dioxide Gasification	32
2.10	Time for drying, devolatilization and gasification	36
3.1	Atomic diffusion volumes	46
3.2	Viscosity for pure species	49
3.3	Summary of the equations used to calculate the bed fluid dynamic.	50
3.4	Summary of the correlations used in the freeboard.	51
3.5	Split for excess gas	53
3.6	Equations used for the calculation of the devolatilization composition	54
3.7	Equations for chemical equilibrium	59
3.8	Coefficients for chemical equilibrium	59
3.9	Used chemical kinetic equations	60
3.10	Summary of the used adsorption constants	60
3.11	Presumptions for the material properties for the particle model.	68
3.12	Volume fraction of the ambient gas used for the particle model.	68
3.13	Devolatilization composition	73
3.14	Elementary analysis of the used fuel on a water and ash free basis	73
3.15	Proximate analysis of the used wood	73
3.16	Discretization of pilot plant gasifier	73
3.17	Discretization of demonstration plant gasifier	73
3.19	Summary of the used plant parameters	78
3.20	Summary of the used model parameters	79
3.21	Differential equation system for the control volume	80
4.1	Simulation results for the pilot plant gasifier	82
4.2	Consumed water and generated gases	97
4.3	Relative discrete sensitivity coefficients for the model parameters	103
4.4	Relative discrete sensitivity coefficients for the plant parameters	109
4.5	Product gas composition on variations of T and \dot{m}_{cic}	111
4.6	Frequency factor for gasification reactions at different temperatures	115

<i>LIST OF TABLES</i>	142
4.7 Product gas composition on pressure variation	119
4.8 Product gas composition and carbon content on part load operation	120
4.9 Input for product gas fluidization	126
4.10 Results for product gas fluidization	126
5.1 Summary of the results for the parameter variation	130

Bibliography

- [Abrahamsen and Geldart 1980a] A. ABRAHAMSEN and D. GELDART – “Behaviour of gas-fluidized beds of fine powders, Part I. homogeneous expansion”, *Powder Technol.* **26** (1980), pp. 35–46.
- [Abrahamsen and Geldart 1980b] A. ABRAHAMSEN and D. GELDART – “Behaviour of gas-fluidized beds of fine powders, Part I. voidage of dense phase in bubbling beds”, *Powder Technol.* **26** (1980), pp. 47–55.
- [Bandyopadhyay and Ghosh 1996] D. BANDYOPADHYAY and A. GHOSH – “Validity of rate equation bases on langmuir-hinselwood mechanism for gasification of carbon - a reappraisal”, *Steelresearch* **67** (1996), No. 3, pp. 79–86.
- [Bandyopadhyay et al. 1991] D. BANDYOPADHYAY, N. CHAKRABORTI and A. GHOSH – “Heat and mass transfer limitations in gasification of carbon by carbon dioxide”, *Steelresearch* **62** (1991), No. 4, pp. 143–151.
- [Barrio and Hustad 2000] M. BARRIO and J. E. HUSTAD – “ CO_2 gasification of birch and the effect of CO inhibition on the calculation of chemical kinetics”, *Progress in Thermochemical Biomass Conversion* (Tirol/Austria), Sept. 2000.
- [Barrio et al. 2000] M. BARRIO, B. GØBEL, H. RISNES, U. HENRIKSEN, J. E. HUSTAD and L. H. SØRENSEN – “Steam gasification of wood and the effect of hydrogen inhibition on the chemical kinetics”, *Progress in Thermochemical Biomass Conversion* (Tirol/Austria), Sept. 2000.
- [Baskakov et al. 1978] A. BASKAKOV, B. BERG, A. RYZHKOV and FILIPPOVSKY – “Process of heat and mass transfer in a fluidized bed”, *Mass and Heat Transfer Processes in Fluidized Bed* (A. Baskakov, Ed.), Metallurgia Publishing House, Moscow, 1978.
- [Bauer et al. 1981] W. BAUER, J. WERTHER and G. EMIG – “Influence of gas distributor design on the performance of fluidized-bed reactor”, *German Chem. Eng.* **2** (1981), pp. 291–298.
- [Bettagli et al. 1995] N. BETTAGLI, U. DESIDERI and D. FIASCHI – “A biomass combustion-gasification model: Validation and sensitivity analysis”, *Journal of Energy Resources Technology* **117** (1995), pp. 329–336.
- [Bilodeau et al. 1993] J.-F. BILODEAU, N. THÉRIEN, P. PROULLX, S. CZERNIK and E. CHORNET – “A mathematical model of fluidized bed biomass gasification”, *Canadian Journal of Chemical Engineering* **71** (1993), pp. 549–557.

- [Boley and Landers 1969] C. BOLEY and W. LANDERS – “Entrainment drying and carbonization of wood waste”, Report of investigations 7282, Bureau of Mines, Washington, D.C., 1969.
- [Borelli et al. 1996] S. BORELLI, M. GIORDANO and P. SALATINO – “Modeling diffusion-limited gasification of carbons by branching pore models”, *The Chem. Eng. Journal* **64** (1996), pp. 77–84.
- [Brenan et al. 1989] K. E. BRENNAN, S. L. CAMPBELL and L. R. PETZOLD – “Numerical solution of initial-value problems in differential-algebraic equations”, *Elsevier Science Publ. Co.* (1989).
- [Brink 1978] L. BRINK – “Pyrolysis-gasification-combustion: A process for utilization of plant material”, *Applied Polymer Symposium*, No. 28, 1978, pp. 1377.
- [Bronštein et al. 1996] I. BRONŠTEIN, G. GROSCHE and E. ZEIDLER – “Teubner-Taschenbuch der Mathematik”, ch. Algebra, B.G. Teubner, Stuttgart, Leipzig, 1996.
- [Budde 1988] K. BUDDE – *Reaktionstechnik*, vol. 1, Dt. Verl. für Grundstoffindustrie, 1988.
- [Budde 1989] K. BUDDE – *Reaktionstechnik*, vol. 2, Dt. Verl. für Grundstoffindustrie, 1989.
- [Capart and Gél 1988] R. CAPART and M. GÉLUS – “A volumetric mathematical model for steam, gasification of wood char at atmospheric pressure”, *Energy from Biomass 4. Proceedings of the 3rd contractors’ meeting* (Paestum), May 1988, pp. 580–583.
- [Cerfontain et al. 1987] M. CERFONTAIN, R. MEIJER, F. KAPTEIJN and J. MOULIJN – “Alkali-catalized carbon gasification in CO/CO_2 mixtures: An extended model for the oxygen exchange and gasification reaction”, *Journal of Catalysis* **107** (1987), pp. 173–180.
- [Chen and Gunkel 1987] J.-S. CHEN and W. W. GUNKEL – “Modeling and simulation of co-current moving bed gasification reactors - part i. a non - isothermal particle model”, *Biomass* **14** (1987), pp. 51–72.
- [Darton et al. 1977] R. DARTON, R. LA NAUCE, J. DAVIDSON and D. HARRISON – “Bubble growth due to coalescence in fluidized beds”, *Trans. Instn. Chem. Eng.* **55** (1977), pp. 274–280.
- [Davidson 1977] J. DAVIDSON – “Trans. inst. chem. eng.”, *Ann. Rev. Fluid Mech.* **9** (1977), pp. 55–86.
- [Davis and Taylor 1950] R. DAVIS and G. TAYLOR – *Proc. Roy. Soc. Ser., Ser. A* **200**, 1950, pp. 375–390.
- [De Groot and Shafizadeh 1984] W. DE GROOT and F. SHAFIZADEH – “Kinetics of gasification of douglas fir and cotton weed chars by carbon dioxide”, *Fuel* **63** (1984), pp. 210–216.

- [di Blasi 1997a] C. DI BLASI – “Influences of physical properties on biomass devolatilization characteristics”, *Fuel* **76** (1997), No. 10, pp. 957–964.
- [di Blasi 1997b] C. DI BLASI – “Simulation heat, mass and momentum transfer during biomass drying”, *Developments in Thermochemical Biomass Conversion* (A. Bridgwater and D. Boocock, Eds.), Blackie Academic & Professional, London, 1997, pp. 117–131.
- [Dutta et al. 1987] DUTTA, C. Y. WEN and R. J. BELT – *Ind. Eng. Chem. Proc. Des. Dev.* **19** (1987), pp. 345–351.
- [Ergun 1952] S. ERGUN – “Fluid flow through packed columns”, *Chem. Eng. Prog.* **48** (1952), pp. 89–94.
- [Ergun 1956] S. ERGUN – “Kinetics of the reaction of carbon dioxide with carbon”, *J. Physical Chemistry* **60** (1956), pp. 480.
- [Fercher et al. 1998] E. FERCHER, H. HOFBAUER, T. FLECK, R. RAUCH and G. VERONIK – “Two years experience with the FICFB-gasification process”, *10th European Conference and Technology Exhibition* (Würzburg), June 1998, <http://www.ficfb.at/>.
- [Formisani et al. 1998] B. FORMISANI, R. GIRIMONTE and L. MANCUSO – “Analysis of the fluidization process of particle beds at high temperature”, *Chem. Eng. Sci.* **53** (1998), No. 5, pp. 951–961.
- [Froment and Bischoff 1990] G. F. FROMENT and K. B. BISCHOFF (Eds.) – *Chemical reactor analyses and design*, second Ed., John Wiley & Sons, Canada, 1990.
- [Geldart 1972] D. GELDART – “Effect of particle size and size distribution on the behaviour of gas-fluidized beds”, *Powder Tech.* **6** (1972), pp. 201–215.
- [Geldart 1973] D. GELDART – “Types of gas fluidization”, *Powder Tech.* **7** (1973), pp. 285–292.
- [Glicksman et al. 1987] L. GLICKSMAN, W. LORD and M. SAKAGAMI – “Bubble properties in large-particle fluidized beds”, *Chem. Eng. Sci.* **42** (1987), No. 3, pp. 479–491.
- [Gogolek and Grace 1995] P. GOGOLEK and J. GRACE – “Fundamental hydrodynamics related to pressurized fluidized bed combustion”, *Prog. Energy Combust. Sci.* **21** (1995), pp. 419–455.
- [Grace and Clift 1974] J. GRACE and R. CLIFT – “On the two-phase theory of fluidization”, *Chem. Eng. Sci.* **29** (1974), pp. 327–334.
- [Grace 1982] J. GRACE – “Fluidized bed hydrodynamics”, *Handbook of Multiphase Systems* (G. Hetsroni, Ed.), Washington Hemisphere Publishing, Washington, 1982.
- [Grace 1986] J. GRACE – “Contacting modes and behaviour classification of gas-solid and other two-phase suspensions”, *Can. J. Chem. Eng.* **64** (1986), pp. 353–363.

- [Groeneveld 1980] M. GROENEVELD – “Theco-current moving bed gasifier”, Ph.D. thesis, Twente University of Technology, Enschede/Netherlands, 1980.
- [Gururajan et al. 1992] V. S. GURURAJAN, P. K. AGARWAL and J. B. AGNEW – “Mathematical modeling of fluidized bed coal gasifiers”, *Trans IChemE* **70** (1992), pp. 211–238.
- [Hemati and Laguerie 1988] M. HEMATI and C. LAGUERIE – “Determination of kinetics of the wood sawdust steam-gasification of char coal in a thermobalance”, *Entropie* **142** (1988), pp. 29–40.
- [Hileman et al. 1976] F. HILEMAN, L. WOJCIK, J. FUTRELL and I. EINHORN – “Comparison of the thermal degradation products of a α -cellulose and douglas fir under inert and oxidative environments”, *Thermal Uses and Properties of Carbohydrates and Lignins Symposium* (Shafizadeh, Sarkanen and Tillman, Eds.), Academic Press, 1976, pp. 49–71.
- [Hofbauer and Rauch 2000] H. HOFBAUER and R. RAUCH – “Stoichiometric water consumption of steam gasification by the FICFB-gasification process”, *Progress in Thermochemical Biomass Conversion* (Innsbruck/Austria), Sept. 2000, <http://www.ficfb.at/>.
- [Hofbauer and Rauch 2001] H. HOFBAUER and R. RAUCH – “Hydrogen-rich gas from biomass steam gasification”, Publishable final report of project jor3-ct97-0196, Institute of Chemical Engineering Fuel and Environmental Technology/Vienna University of Technology, Vienna/Austria, 2001, <http://www.ficfb.at/>.
- [Hofbauer 2002] H. HOFBAUER – “RENET Austria”, 2002, <http://www.renet.at/>.
- [Hüttinger and Merdes 1992] K. J. HÜTTINGER and W. F. MERDES – “The carbon - steam reaction at elevated pressure: formations of product gases and hydrogen inhibitions”, *Carbon* **30** (1992), No. 6, pp. 883–894.
- [Illerup and Rathmann 1995] J. ILLERUP and O. RATHMANN – “CO₂ gasification of wheat straw, barley straw, willow and gigantesous”, Tech. report, Department of Combustion Research/Risø National Laboratory, Dec. 1995.
- [Jiang and Morey 1991] H. JIANG and R. V. MOREY – “A numerical model of a fluidized bed biomass gasifier”, *Biomass and Bioenergy* **3** (1991), No. 6, pp. 431–447.
- [Johnson 1974] J. JOHNSON – “Kinetics of bituminous coal char gasification with gases containing steam and hydrogen”, *Advances in Chemistry* **131** (1974), pp. 145.
- [Johnsson and Leckner 1995] F. JOHNSSON and B. LECKNER – “Vertical distribution of solids in a CFB-furnace”, 13th *Int. Conf. on Fluidized Bed Combustion* (New York/USA), ASME, 1995, pp. 671–679.
- [Johnsson et al. 1991] F. JOHNSSON, S. ANDERSSON and B. LECKNER – “Expansion of a freely bubbling fluidized bed”, *Powder Technology* **68** (1991), pp. 117–123.

- [Kaiser 2001] S. KAISER – “Simulation und Modellierung von Kraft-Wärme-Kopplungsverfahren auf Basis Biomassevergasung”, Ph.D. thesis, Technische Universität Wien, 2001.
- [Kantorovich and Bar-Ziv 1999] I. I. KANTOROVICH and E. BAR-ZIV – “Heat transfer within highly porous chars: a review”, *Fuel* **78** (1999), pp. 279–299.
- [Kee et al. 1993] R. KEE, F. RUPLEY and J. MILLER – “The Chemkin Thermodynamic Database”, Report SAND87-8215B, Sandia National Laboratories, Livermore/California, 1993.
- [Knight 1976] J. KNIGHT – “Pyrolysis of pine sawdust”, *Thermal Uses and Properties of Carbohydrates and Lignins Symposium* (Shafizadeh, Sarkanen and Tillman, Eds.), Academic Press, 1976, pp. 158.
- [Koufopoulos et al. 1991] C. KOUFOPANOS, N. PAPAYANNAKOS, G. MASCHIO and A. LUCCHESI – “Modelling of the pyrolysis of biomass particles. studies on kinetics, thermal and heat-transfer effects.”, *Can.J.Chem.Eng.* **69** (1991), pp. 907–915.
- [Kunii and Levenspiel 1991] D. KUNII and O. LEVENSPIEL – *Fluidization engineering*, second Ed., Butterworth-Heinemann, Boston, 1991.
- [Laine et al. 1963] N. R. LAINE, F. VASTOLA and P. WALKER – *J. Physical Chemistry* **37** (1963), pp. 2030.
- [Larfeldt et al. 2000] J. LARFELDT, B. LECKNER and M. MELAAEN – “Modeling and measurements of the pyrolysis of large wood particles”, *Fuel* **79** (2000), pp. 1637–1643.
- [Leckner et al. 1992] B. LECKNER, G. I. PALCHONOK and B. Å. ANDERSSON – “Representation of heat and mass transfer of active particles”, *The IEA-FBC Mathematical Modeling Meeting* (Turku/Finland), 1992.
- [Leckner et al. 1998] B. LECKNER, G. I. PALCHONOK and B. Å. ANDERSSON – “Heat and mass transfer to a single particle in fluidized bed”, ch. Representation of Heat and Mass Transfer of Active Particles, Chalmers Reproservice, Göteborg, 1998.
- [Lédé 1994] J. LÉDÉ – “Reaction temperature of solid particles undergoing an endothermal volatilization. application to the fast pyrolysis of biomass”, *Biomass and Energy* **7** (1994), No. 1–6, pp. 49–60.
- [Li and van Heiningen 1991] J. LI and A. VAN HEININGEN – “Kinetic of gasification of black liquor char by steam”, *Engineering Chemistry and Research* **30** (1991), No. 7, pp. 1594–1601.
- [Liliedahl and Sjöström 1997] T. LILIEDAHL and K. SJÖSTRÖM – “Modelling of char-gas reaction kinetics”, *Fuel* **76** (1997), No. 1, pp. 29–37.

- [Löffler 2001] G. LÖFFLER – “A modeling study an fuel-nitrogen conversion to NO and NO_2 related to fluidized bed combustion”, Ph.D. thesis, Technische Universität Wien, 2001.
- [Maschio et al. 1992] G. MASCHIO, C. KOUFOPANOS and A. LUCCHESI – “Pyrolysis, a promising route for biomass utilization”, *Biosource Technology* **42** (1992), pp. 219–231.
- [Maschio et al. 1994] G. MASCHIO, A. LUCCHESI and C. KOUFOPANOS – “Study of kinetic and transfer phenomena in the pyrolysis of biomass particles”, *Advances in Thermochemical Biomass Conversion* (A. Bridgwater, Ed.), Blackie Academic & Professional, London, 1994, pp. 977–985.
- [Mathews et al. 1997] J. P. MATHEWS, P. G. HATCHER and A. W. SCARONI – “Particle size dependence of coal volatile matter: is there a non-maceral-related effect?”, *Fuel* **76** (1997), No. 4, pp. 359–362.
- [Melaen and Grønli 1997] M. MELAAEN and M. GRØNLI – “Modelling and simulation of moist wood drying and pyrolysis”, *Developments in Thermochemical Biomass Conversion* (A. Bridgwater, Ed.), Blackie Academic & Professional, London, 1997, pp. 132–146.
- [Menster and Ergun 1973] M. MENSTER and S. ERGUN – “A study of the carbon dioxide carbon reaction by oxygen exchange”, *USBM Bull.* **664** (1973).
- [Moilanen and Mühlen 1996] A. MOILANEN and H.-J. MÜHLEN – “Characterization of gasification reactivity of peat char in pressurized conditions”, *Fuel* **75** (1996), No. 11, pp. 1279–1285.
- [Moilanen et al. 1993] A. MOILANEN, K. SAVIHARJU and T. HARJU – “Steam gasification reactivities of various fuel chars”, *Advances in Thermochemical Biomass Conversion* (A. Bridgwater, Ed.), Blackie Academic & Professional, London, 1993, pp. 131–141.
- [Moilanen et al. 1994] A. MOILANEN, K. SAVIHARJU and T. HARJU – “Steam gasification reactivities of various fuel chars”, *Advances in Thermochemical Biomass Conversion* (A. Bridgwater, Ed.), Blackie Academic & Professional, London, 1994, pp. 131–140.
- [Mühlen 1983] H.-J. MÜHLEN – “Zum Einfluß der Produktgase auf die Kinetik der Wasserdampfvergasung in Abhängigkeit von Druck und Temperatur”, Ph.D. thesis, GHS Essen, 1983.
- [Palchonok 1998] G. I. PALCHONOK – “Heat and mass transfer to a single particle in fluidized bed”, Ph.D. thesis, Chalmers University of Technology, Sweden, 1998.
- [Peters and Bruch 2001] B. PETERS and C. BRUCH – “A flexible and stable method for simulating the thermal decomposition of wood particles”, *Chemosphere* **42** (2001), pp. 481–490.

- [Petzold 1982] L. PETZOLD – “A description of dassl: A differential/algebraic system solver”, *Proceedings of the IMACS World Congress* (Montreal/ Canada), 1982.
- [Plante et al. 1988] P. PLANTE, C. ROY and E. CHORNET – “ CO_2 gasification of wood charcoals derived from vacuum and atmospheric pyrolysis”, *Can. J. Chem. Eng.* **66** (1988), pp. 307–312.
- [Pober and Bauer 1977] K. POBER and H. BAUER – “The nature of pyrolytic oil from municipal solid waste”, *Fuels From Waste*, Academic Press, New York, 1977, pp. 73–86.
- [Raveendran and Ganesh 1998] K. RAVEENDRAN and A. GANESH – “Adsorption characteristics and pore development of biomass pyrolysis char”, *Fuel* **77** (1998), No. 7, pp. 769–781.
- [Reed 1981] T. B. REED – *Biomass gasification*, Noyes Data Corporation, New Jersey, 1981.
- [Reid et al. 1986] R. C. REID, J. M. PRAUSSINITZ and B. E. POLING – *The properties of gases and liquids*, fourth Ed., McGraw-Hill Book Company, 1986.
- [Rensfelt et al. 1978] E. RENSFELT, G. BLOMKUIST, S. EKSTROM, B. ESPENÄS and L. L. – “Basic gasification studies for development of biomass medium-btu gasification processes”, *Energy from Biomass and Wastes*, No. 27, IGT, Aug. 1978, pp. 466–494.
- [Richard et al. 1982] J. RICHARD, M. CATHONNET and J. ROUAN – “Gasification of charcoal: Influence of water vapor”, *Fundamentals of Thermochemical Biomass Conversion* (1982), pp. 589–599.
- [Risnes et al. 2000] H. RISNES, L. SØRENSEN and J. HUSTAD – “ CO_2 reactivity of char from danish wheat, norwegian spruce and longyear coke”, *Progress in Thermochemical Biomass Conversion* (Tirol/Austria), Sept. 2000.
- [Ross et al. 2000] D. ROSS, C. HEIDENREICH and D. ZHANG – “Devolatilisation times of coal particles in a fluidised-bed”, *Fuel* **79** (2000), pp. 873–883.
- [Saastamoinen 1994] J. SAASTAMOINEN – “Model for drying and pyrolysis in an updraft biomass gasifier”, *Advances in Thermochemical Biomass Conversion* (A. Bridgewater, Ed.), Blackie Academic & Professional, London, 1994, pp. 186–200.
- [Schaller 1995] W. SCHALLER – “Strom aus Biomasse - das Forschungsprojekt TINA”, *Erneuerbare Energie* (1995), No. 3, <http://www.aee.at/verz/artikel/biomass2.html>.
- [Schuster et al. 2001] G. SCHUSTER, G. LÖFFLER, K. WEIGL and H. HOFBAUER – “Biomass steam gasification - an extensive parametric modeling study”, *Biore-source Technology* **77** (2001), pp. 71–79, <http://www.ficfb.at/>.
- [Sit and Grace 1981] S. SIT and J. GRACE – “Effect of bubble interaction on interphase mass transfer in gas fluidized beds”, *Chem. Eng. Sci.* **36** (1981), pp. 327–335.

- [Smidt 2000] S. SMIDT – “Lexikon Waldschädigende Luftverunreinigungen”, Aktualisierte fassung der fbva-berichte nr. 199 (1997), Forstliche Bundesversuchsanstalt Waldforschungszentrum, 2000.
- [Sørensen et al. 1996] L. SØRENSEN, J. SAASTAMOINEN and J. HUSTAD – “Evolution of char reactivity data by different shrinking-core models”, *Fuel* **75** (1996), No. 11, pp. 1294–1300.
- [Squires 1961] A. SQUIRES – “Devolatilisation times of coal particles in a fluidised-bed”, *Trans.Inst.Chem.Eng.* **39** (1961), No. 3.
- [Srinivasalu Gupta and Bhatia 2000] J. SRINIVASALU GUPTA and S. K. BHATIA – “A modified discrete random pore model allowing for different initial surface reactivity”, *Carbon* **38** (2000), pp. 47–58.
- [Stoltze et al. 1993] S. STOLTZE, U. HENRIKSEN, T. LYNGBECH and O. CHRISTENSEN – “Gasification of straw in large-sample tga”, *Nordic Seminar on Solid Fuel Reactivity* (Gothenburg/Sweden), Chalmers University of Technology, Nov. 1993.
- [Stoltze et al. 1994] S. STOLTZE, U. HENRIKSEN, T. LYNGBECH and O. CHRISTENSEN – “Gasification of straw in large-sample tga, part ii”, *Nordic Seminar on Biomass Gasification and Combustion* (Trondheim/Norway), NTH, Jun. 1994.
- [Stull and Prohet 1971] D. STULL and H. PROHET (Eds.) – *JANAF Thermodynamic Tables*, National Standard Reference Data Series NSRDS-NBS 37, 1971.
- [Tancredi et al. 1996a] N. TANCREDI, T. CORDERO, J. RODRÍGUEZ-MIRASOL and R. J.J. – “CO₂ gasification of eucalyptus wood chars”, *Fuel* **75** (1996), No. 13, pp. 1505–1508.
- [Tancredi et al. 1996b] N. TANCREDI, T. CORDERO, J. RODRÍGUEZ-MIRASOL and J. RODRÍGUEZ – “CO₂ gasification of eucalyptus wood chars”, *Fuel* **75** (1996), No. 13, pp. 1505–1508.
- [Taylor et al. 1978] S. TAYLOR et al. – *La madera*, Editorial Blume, Barcelona, 1978.
- [The Chemical Rubber Co. 1977] THE CHEMICAL RUBBER CO. (Ed.) – *CRC handbook of chemistry and physics*, 58th Ed., CRC Press, Boca Raton/Florida, 1977.
- [Tillman 1978] D. TILLMAN – *Wood as an energy resource*, Academic Press, New York, 1978.
- [Timpe and Hauserman 1992] R. TIMPE and W. HAUSERMAN – “The catalytic gasification of hybrid poplar and common cattail plant chars”, *Energy from Biomass and Wastes XVI*, March 1992, pp. 903–919.
- [Toomey and Johnstone 1952] R. TOOMEY and H. JOHNSTONE – “Gaseous fluidization of solid particles”, *Chem.Eng.Prog.* **48** (1952), pp. 220–226.
- [Turn et al. 1998] S. Q. TURN, C. M. KINOSHITA, D. M. ISHIMURA and J. ZHOU – “The fate of inorganic constituents of biomass in fluidized bed gasification”, *Fuel* **77** (1998), No. 3, pp. 135–146.

- [VDI-GVC 1997] VDI-GVC (Ed.) – *VDI-Wärmeatlas: Berechnungsblätter für den Wärmeübergang*, Springer, Heidelberg, 1997.
- [Wang and Kinoshita 1993] Y. WANG and M. KINOSHITA – “Kinetic model of biomass gasification”, *Solar Energy* **51** (1993), No. 1, pp. 19–25.
- [Weimer and Clough 1981] A. WEIMER and D. CLOUGH – “Modeling a low pressure steam-oxygen fluidized bed coal gasifying reactor”, *Chem. Eng. Sci.* **16** (1981), pp. 549–568.
- [Werther 1978] J. WERTHER – “Effect of gas distributor on the hydrodynamics of gas fluidized beds”, *German Chem. Eng.* **1** (1978), pp. 166–174.
- [Werther 1983] J. WERTHER – “Hydrodynamics and mass-transfer between the bubble and emulsion phases in fluidized beds of sand and cracking catalyst”, *Fluidization IV* (New York/USA) (D. Kunii and R. Toei, Eds.), Engineering Foundation, 1983, pp. 93–101.
- [Whitty 1997] K. WHITTY – “Pyrolysis and gasification behavior of black liquor under pressurized conditions”, Report 97-3, Åbo Akademi, Department of Chemical Engineering, 1997.
- [Yates 1983] J. G. YATES – *Fundamentals of fluidized-bed chemical processes*, Butterworth, London/UK, 1983.
- [Zanzi et al. 1994] R. ZANZI, K. SJÖSTRÖM and E. BJÖRNBOM – “Rapid pyrolysis of wood with application to gasification”, *Advances in Thermochemical Biomass Conversion* (A. Bridgwater, Ed.), Blackie Academic & Professional, London, 1994, pp. 977–985.